A molecular line and continuum study of water maser sources

Timothy Jenness
St. John's College

A dissertation submitted for the degree of Doctor of Philosophy in the University of Cambridge

June 1996

Preface

This dissertation is the result of work undertaken at the Mullard Radio Astronomy Observatory, Cambridge between October 1992 and September 1995, and includes nothing which is the outcome of work done in collaboration. It has not, nor has any similar dissertation, been submitted for a degree, diploma or other qualification at this, or any other, university. This dissertation does not exceed 60 000 words in length.

First of all I find it extremely hard to write things like this so I apologise in advance, especially if I am too sarcastic...

To begin with I would like to thank Paul Scott, my supervisor, for those discussions on motor racing in the coffee room, for accompanying me on my holiday to the Grand Canyon (maybe I mean VLA?) and for putting up with me during those times when I was more interested in becoming a UNIX hacker than getting my research finished. Thanks also to Rachael Padman for useful discussions on this project as well as for heated debates concerning the relative merits of VMS versus UNIX; it's a shame her DEC Alpha is not running a decent operating system. I would also like to thank her for thinking I am going to be able to do a good job programming for the JCMT over the next three years (as long as I don't damage the UNIX version of SPECX *too* much!) Thanks also to John Richer for discussions on DBMEM and for trying to convince me that I should program in C++.

One person who does need to be singled out is Dave Titterington, MRAO's computer system manager. He has managed to keep the computers going *despite* the switch to Solaris 2, and he has had to put up with me asking him to install new software fairly regularly. I'm sure I will find out just how much work is involved when I start at the Joint Astronomy Centre.

I have really enjoyed my time at MRAO, the highlight of which was the holiday in Leiden – thanks for putting up with us Anja. I would also like to take this opportunity to apologise to those people who

have experienced my driving; I'm sure Oliver will never forget the experience! Thanking all my fellow students will be long and boring for the reader but two people deserve a mention: John for not needing much in the way of encouragment to become a UNIX and LaTeX hacker (the COFFEE program signifies time well-spent!), and Kate for giving me a kick whenever I was lacking motivation. Thanks also to Frossie for keeping me sane with those late night e-mails from Hawaii over the past two months.

Finally thanks to my family for putting up with me for 24 years. I hope Hawaii isn't too far away for a visit.

Contents

List of Figures

List of Tables

Units

Where possible SI units have been used throughout this thesis. Some unusual units, common in astronomy, are listed in the table below. B1950 coordinates have been used throughout this dissertation.

Solar mass	$M_\odot$	1.989×10^{30} kg
Solar luminosity	$L_\odot$	3.826×10^{26} W
parsec	pc	3.09×10^{16} m
Astronomical Unit	AU	1.50×10^{11} m
arcsecond	arcsec	4.85×10^{-6} rad
square arcsecond	arcsec^2	2.35×10^{-11} sr
jansky	Jy	1×10^{-26} W m^{-2} Hz^{-1}

Chapter 1

Introduction

The first interstellar molecule detected at radio wavelengths was the hydroxyl radical, OH (Weinreb *et al*. 1963). The simultaneous detection of four OH lines, corresponding to the rotation levels of this molecule splitting into four states, provides information on the population distribution; significant deviations from thermal equilibrium populations (Weaver *et al*. 1965) required an alternative explanation for the line formation mechanism and led to theories invoking stimulated emission (Litvak *et al*. 1966; Perkins *et al*. 1966) and masers.

The second maser molecule to be discovered was water. Cheung *et al*. (1969) detected the 22-GHz $6_{16} \rightarrow 5_{23}$ transition with a 20 foot radio telescope at Hat Creek Observatory. Given that the antenna temperature was 60 K for a line 600 K above ground, maser emission was suspected. This hypothesis was confirmed by Knowles *et al*. (1969) who used an 85 foot radio telescope to place much more stringent limits on the source size. Observations of W49 detected lines as strong as 1700 K and, with an upper limit on the source size of $0\farcs7$, indicated a lower limit on the brightness temperature of 50 000 K; this was far too large to be from a thermal source since water molecules dissociate at a few thousand degrees. Subsequent interferometer observations of OH and water maser sources (Moran *et al*. 1968, 1973; Burke *et al*. 1970) detected sources only milli-arcseconds across, corresponding to brightness temperatures in excess of 10^{10} K, confirming that these sources were not thermally excited.

In the next few years many water masers, and OH masers, were found in red giants and supergiants (e.g. Engels *et al*. 1986; Benson *et al*. 1990) and in star-forming regions (Genzel & Downes 1977). Whereas the excitation mechanism of masers in late-type stars is fairly well established (Cooke & Elitzur 1985; Chapman & Cohen 1986), the morphology of water masers in star-forming regions is, in general, more complex, as the regions are characterised by possessing many maser spots displaying no overall structure (Genzel 1986).

The most luminous maser in the Galaxy is W49 N with a total luminosity of order of 1 $L_{\odot}$; a sin-

gle spot in this source had an isotropic luminosity of 0.08 $L_\odot$ in a linewidth of 3.6 km s^{-1} (Walker *et al*. 1982). One of the most well-studied maser sources is W51 M. Genzel *et al*. (1981) made VLBI observations of the central maser spot. Single dish observations show that this source has a very complicated structure – maser components are visible with velocities as high as 100 km s^{-1} relative to the host molecular cloud with a general trend that the "low velocity" features ($v < 50$ km s^{-1}) are much stronger than the "high velocity" features ($v > 50$ km s^{-1}). The VLBI observations identified many maser spots all within a source of less than 0.01 pc in diameter. Further VLBI observations allowed proper motion studies of individual features to be made. This led to the result that the "high velocity" features had small transverse motions whereas the "low velocity" features had large transverse motions. This indicates that in fact there may be *no* "low velocity" masers in W51 M, with all the masers possessing velocities of at least 50 km s^{-1}. The change in intensity with velocity in the single dish spectrum is then explained by preferential amplification perpendicular to the direction of motion, which is not surprising since water masers require large, velocity coherent, gain paths. These features have been reasonably well explained by dissociative shock models (Elitzur *et al*. 1989).

In general the association of compact H II regions, OH masers and high velocity flows has been well established in regions of O and B star formation. Studies have shown, however, that, unlike OH masers, water masers are separated from UC H II regions by a small distance (Forster & Caswell 1989). A link has also been shown to exist between molecular mass outflows and the presence of a water maser (Bally & Lada 1983; Felli *et al*. 1992), although higher resolution images of the outflow structure were missing from these studies. This made it hard to decide where abouts on the outflow the water maser was excited.

Recent observations at the James Clerk Maxwell Telescope (JCMT) and elsewhere have identified a class of very deeply embedded, possibly protostellar, sources which are not associated with any of the traditional indicators of star formation, such as H II regions and near-infrared emission, but which *do* lie close to otherwise isolated H_2O masers.

A good example of a source showing this behaviour can be found in S106 (Richer *et al*. 1993). They reported a bright submm continuum source approximately 20 arcsec to the west of S106 IR. Fig. 1.1 shows a 450 μm image of this source and shows that a water maser, detected by Stutzki *et al*. (1982) and with increased positional accuracy by Kawabe (unpublished), is associated directly with S106-FIR. This maser is within 8 mpc of the embedded core. The presence of the water maser and the high inferred density, of more than 10^7 cm^{-3}, lead Richer *et al*. (1993) to suggest that this source is a very young self-luminous protostellar object.

Perhaps an even more striking source is that found in M17 SW (Hobson *et al*. 1993; 1994). The M17 SW molecular cloud core is adjacent to the M17 H II region, at a distance of 2.2 kpc (Chini *et al*. 1980). The region has been observed extensively in radio, infrared and optical wavelengths and appears to be an excellent example of triggered star formation. The northern condensation has three deeply embedded sources (labelled FIR1 to FIR3 from north to south) each of which has a mass of approximately 350 $M_\odot$. Three water masers have also been detected in this region (Jaffe *et al*. 1981;

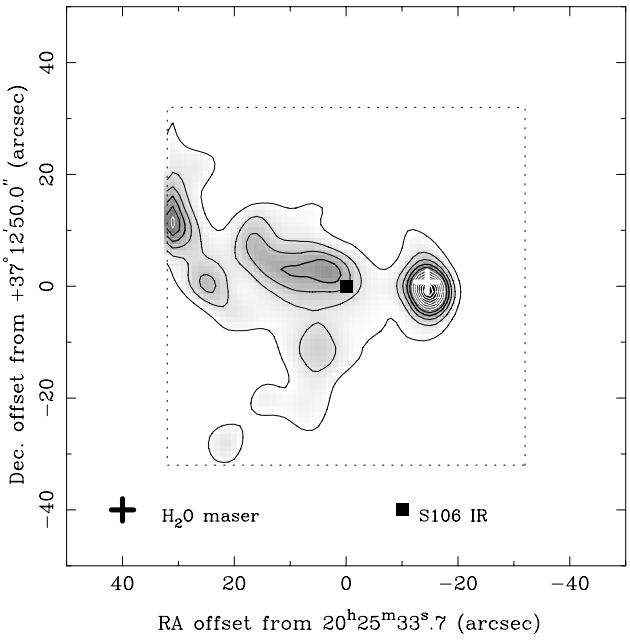

Figure 1.1
450-μm image of S106-FIR (Fig. reproduced from Richer *et al*. 1993)

Massi *et al*. 1988), the relative positioning of which matches extremely well with the positions of the FIR cores as can be seen in Fig. 1.2 (unreliable pointing for the submm map meant that that map was shifted such that the northern maser was coincident with FIR1). With this pointing shift applied, the masers are no further than 0.04 pc from the exciting sources.

This thesis describes a search, based on catalogues of known water maser positions, for new deeply embedded cores similar to those found in S106 and M17. In addition to millimetre molecular line and submm continuum observations, 22 GHz and 8 GHz radio observations have been made of a number of the sources in order to obtain more accurate maser positions and to search for any associated compact H II regions. Observing sources such as these in less active star forming regions (e.g. Tofani *et al*. 1995) should provide a cleaner environment in which to examine the maser excitation and the ongoing process of star formation.

This thesis can essentially be divided into three parts.

Chapters 2 and 3 deal directly with the observations and data reduction. Chapter 2 discusses the scientific criteria used in the source selection and then describes the observational techniques used to obtain the data. Chapter 3 presents that data, in tabular form followed by maps, and then presents parameters derived directly from those observations, e.g. mass, luminosity and temperature.

Chapter 4 uses the data presented in the previous chapter and discusses the global properties of the sample before, in chapter 5, discussing in detail those sources for which a significant amount of new data have been obtained.

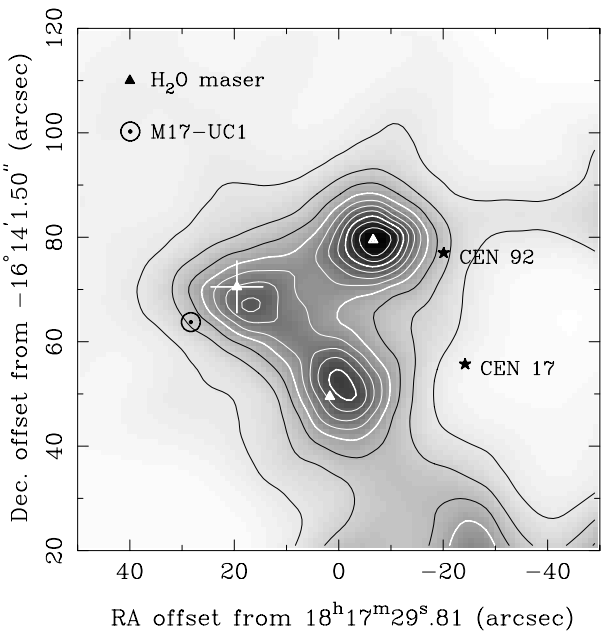

Figure 1.2
The northern condensation of M17 SW at 800 μm. Also shown are the three known H_2O masers, the stars CEN 17 and CEN 92, and the UC H II region M17-UC1. The map has been shifted such that the source FIR1 is aligned with the relevant water maser. (Fig. reproduced from Hobson *et al*. 1993)

Finally, chapter 6 discusses the origin of the water maser emission in these sources and relates it to the properties of the embedded cores.

Since only some sources are discussed in detail, all of the observational data obtained from a literature search on the sources in the sample can be found in Appendix B. Whilst not all this data has been used explicitly, much of it was necessary in, for example, constructing the spectral energy distributions seen in Fig. 4.1.

As can be seen below, a reference list can be found at the end of each chapter. A full list of all references used in this work can be found in the bibliography after the appendices.

References

Bally J., Lada C. J., 1983, *ApJ*, 265, 824
Benson P. J., *et al*., 1990, *ApJS*, 74, 911
Burke B. F., Papa D. C., Papadopoulos G. D., Schwartz P. R., Knowles S. H., Sullivan W. T., Meeks M. L., Moran J. M., 1970, *ApJ*, 160, L63
Chapman J. M., Cohen R. J., 1986, *MNRAS*, 220, 513
Cheung A. C., Rank D. M., Townes C. H., Thornton D. D., Welch W. J., 1969, *Nature*, 221, 626
Chini R., Elsässer H., Neckel T., 1980, *A&A*, 91, 186
Cooke B., Elitzur M., 1985, *ApJ*, 295, 175
Elitzur M., Hollenbach D. J., McKee C. F., 1989, *ApJ*, 346, 983
Engels D., Schmid-Burgk J., Walmsley C. M., 1986, *A&A*, 167, 129
Felli M., Palagi F., Tofani G., 1992, *A&A*, 255, 293
Forster J. R., Caswell J. L., 1989, *A&A*, 213, 339

Genzel R., 1986, in *Masers, Molecules and Mass Outflows in Star Forming Regions*, ed. Haschick A. D., p. 233, Haystack Observatory, Westford, MA
Genzel R., Downes D., 1977, *A&AS*, 30, 145
Genzel R., *et al*., 1981, *ApJ*, 247, 1039
Hobson M. P., Padman R., Scott P. F., Prestage R. M., Ward-Thompson D., 1993, *MNRAS*, 264, 1025
Hobson M. P., Jenness T., Padman R., Scott P. F., 1994, *MNRAS*, 266, 972
Jaffe D. T., Güsten R., Downes D., 1981, *ApJ*, 250, 621
Knowles S. H., Mayer C. H., Cheung A. C., Rank D. M., Townes C. H., 1969, *Science*, 163, 1055
Litvak M. M., McWhorter A. L., Meeks M. L., Zeiger H. J., 1966, *Phys. Rev. Lett*., 17, 821
Massi M., Churchwell E., Felli M., 1988, *A&A*, 194
Moran J. M., *et al*., 1973, *ApJ*, 185, 535
Moran J. M., Burke B. F., Barrett A. H., Rogers A. E. E., Carter J. C., Ball J. A., Cudaback D. D., 1968, *ApJ*, 152, L98
Perkins F., Gold T., Salpeter E. E., 1966, *ApJ*, 145, 361
Richer J. S., Padman R., Ward-Thompson D., Hills R. E., Harris A. I., 1993, *MNRAS*, 262, 839
Stutzki J., Ungerechts H., Winnewisser G., 1982, *A&A*, 111, 201
Tofani G., Felli M., Taylor G. B., Hunter T. R., 1995, *A&AS*, 112, 299
Walker R. C., Matsakis D. N., Garcia-Barreto J. A., 1982, *ApJ*, 255, 128
Weaver H., Williams D. R. W., Dieter N. H., Lum W. T., 1965, *Nature*, 208, 29
Weinreb S., Barrett A. H., Meeks M. L., Henry J. C., 1963, *Nature*, 200, 829

Chapter 2

Source selection and observations

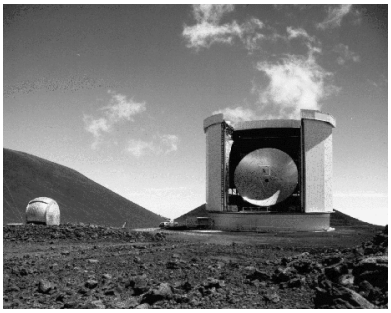

In this chapter I discuss how the sample of water masers was selected and the origin of the scientific criteria used. Also I discuss the observational techniques and the telescopes used to obtain the data.

2.1 Source selection

The first task was to list all of the known water maser sources. This work was made much easier by the existence of the first Arcetri Atlas, by Comoretto *et al*. (1990), who had already reported a complete literature search for pre-1989 detections and found 526 maser sources. This meant that my literature search could be concentrated on detections after 1989. A complete list of those references which have been searched can be found in table 2.1 which also contains the updated Arcetri Atlas of Brand *et al*. (1994). The combined Atlas does account for all the other references in the table, and also includes a few that I had missed, but at the time of the initial search the updated atlas did not exist and so the additional references in the table account for the sample I was working from. The stellar maser catalogue (Benson *et al*. 1990) has been included in the table for completeness only, as the masers in this catalogue have already been selected as belonging to evolved stars and would not be relevant for this work. Also it must be noted that the 'new' detections listed in the table are not unique and some sources are repeated in the various references. The Arcetri Atlas is not just a list of sources but is also a list of observations. All the masers listed in the Atlas were re-observed using the Medicina 32-m telescope, which has a beam size of 114 arcsec at 22-GHz, and a sensitivity of approximately 10 Jy. The variable nature of water masers is highlighted by the fact that only 203 of the 526 masers previously detected were confirmed.

Before *IRAS* no systematic method of searching for water masers had been used so detections relied on observers looking at regions of interest in the hope of finding a water maser. Table 2.1 shows that

Table 2.1. Maser references.

	Basis of detection	Number found
Brand *et al*. (1994)	*All* H_2O masers post 1988 and pre-1994	192
Comoretto *et al*. (1990)	*All* H_2O masers pre-1989	526
Benson *et al*. (1990)	Stellar masers	368
Felli *et al*. (1992)	CO outflows	56
Churchwell *et al*. (1990)	UC HII regions	56
Palla *et al*. (1991)	IRAS colours	44
Scalise *et al*. (1989)	IRAS colours	23
Braz *et al*. (1989)	IRAS colours	8
Kömpe *et al*. (1989)	IRAS sources in S247/252	5
Tereby *et al*. (1992)	IRAS + NH_3 cores	3

most of the recent new detections of water masers have been selected by use of the *IRAS* point source catalogue (Beichman *et al*. 1988). Surveys such as these have a number of problems:

1. Observing a large number of sources selected from *IRAS* (most samples have more than 200 sources) requires a lot of telescope time, even without very deep integrations. Although a large sample is desirable, limited observing time usually results in a detection limit of a few janskys, so that very weak or variable masers are not detected.

2. The very fact that the *IRAS* catalogue is being used necessarily means that the maser sources are already associated with *IRAS* sources. Very cold, deeply embedded objects with no near-by *IRAS* sources, such as VLA 1623 (the prototypical Class 0 object, André *et al*. 1993), would not be included in such a sample since 10 or 20 K black bodies peak at wavelengths greater than 100 μm and would not be detected by *IRAS*.

Given the large number of known water maser sources the next task was to select those sources which, notwithstanding the bias against isolated VLA 1623-type objects, were most likely to contain deeply embedded protostellar cores.

Given current receiver technology it is unreasonable to attempt to observe all water maser sources using the JCMT. Taking into account the usual overheads (e.g. pointing and calibration) it takes approximately 20 to 30 minutes to make a submm continuum map with UKT14 (see §2.2.1). In order to observe all 700 known water masers approximately 37 nights of telescope time would be required. The maximum observing time that could reasonably be expected to be allocated would be 6 shifts and this means that the sample needs to be reduced to approximately 100 sources.

2.1.1 Source colour selection

Water masers arise in two distinct types of systems. They are present in the hot envelopes of late-type stars (i.e. giant stars), and in star-forming regions. The first step in reducing the sample size is to

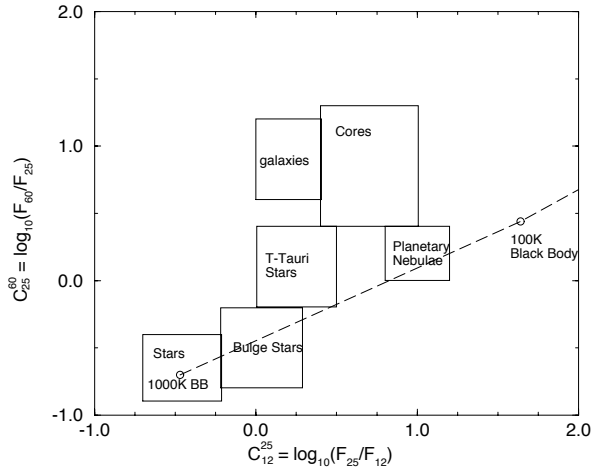

Figure 2.1
IRAS colours for some objects of known type.

separate these two types. *IRAS* fluxes can be used to separate the warmer stellar objects (those with 25 and 12 μm fluxes greater than the 60 and 100 μm fluxes) from the cooler deeply embedded objects (those with 25 and 12 μm fluxes less than the 60 and 100 μm). *IRAS* colours are defined such that

$$C_n^m = \log_{10}\left(\frac{f_m}{f_n}\right)$$

where m or n can be $12, 25, 60$ or 100 μm and f_i is the flux at wavelength i. These colours have been calculated with no *IRAS* colour corrections applied (see Neugebauer *et al*. 1984). When these colours are analysed, different source types are found to occupy different regions of colour-colour space (Emerson 1987; Harris *et al*. 1988). Fig. 2.1 shows the source colours for objects of known type (taken from Emerson 1987) along with those of two ideal blackbodies. The region of interest for this thesis is the section labelled 'cores' and it is here that most of the selected sources were expected to lie.

This empirical method for determining object type has been put on a statistical footing by Palagi *et al*. (1993) who reclassified the masers in the original Arcetri Atlas according to their *IRAS* fluxes as being associated with either evolved stars (STAR) or young star-forming regions (SFR). This was achieved by performing a multivariate analysis (Murtagh & Heck 1987), which can simultaneously make use of all four *IRAS* fluxes, so that any bias introduced by an arbitrary colour selection (i.e. only using three of the four *IRAS* fluxes) can be removed.

Principal component analysis

To start with, Palagi *et al*. (1993) performed a principal component analysis (Murtagh & Heck 1987) on those sources from the first Arcetri Atlas which had an *IRAS* point source association and no upper limits in any of the four *IRAS* bands, in order to find the colour combination most able to separate the sources into two distinct groups. This resulted in a sample size for the analysis of 246.

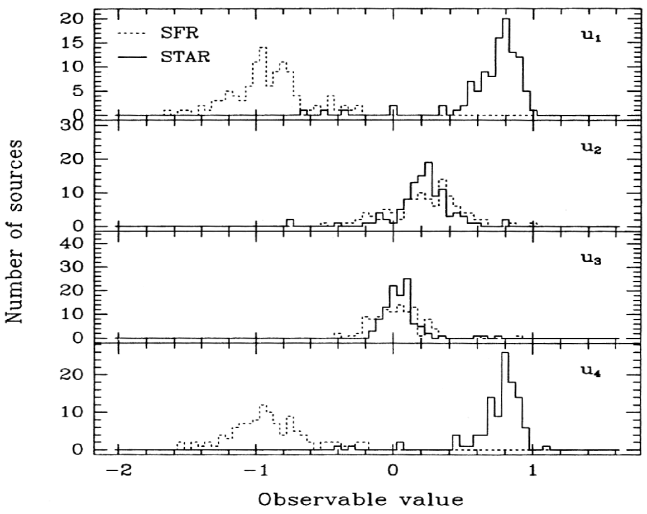

Figure 2.2
Distribution of the observables $u_1 \ldots u_4$ of sources with a good identification as SFR or STAR, taken directly from Fig. 2 of Palagi *et al*.(1993).

Table 2.2. Boundary definitions of STAR and SFR from the analysis of Palagi *et al*. (1993).

	STAR	SFR
u_1	$+0.1 \rightarrow +1.4$	$-2.4 \rightarrow -0.3$
u_2	$-1.8 \rightarrow +0.8$	$-1.2 \rightarrow +1.2$
u_3	$-1.4 \rightarrow +0.5$	$-1.0 \rightarrow +1.3$
u_4	$+0.0 \rightarrow +1.2$	$-2.0 \rightarrow -0.1$

This analysis in the three dimensional colour-colour space provided three new observables, u_1, u_2 and u_3. u_1 shows the largest separation of the two samples (i.e. maximises the sample variance) whereas u_2 and u_3 show very little difference between the two samples and are perpendicular to u_1 (Fig. 2.2). The results of the analysis are as follows:

$$u_1 = +0.510[f_{12}] - 0.137[f_{25}] + 0.403[f_{60}] - 0.776[f_{100}]$$

$$u_2 = -0.533[f_{12}] + 0.522[f_{25}] + 0.857[f_{60}] - 0.846[f_{100}]$$

$$u_3 = +0.473[f_{12}] - 1.057[f_{25}] + 1.244[f_{60}] - 0.660[f_{100}]$$

where $[f_n] = \log(f_n)$.

Linear discriminant analysis

From the 246 sources in the sample used for the principal component analysis, a subsample of 214 sources with good morphological identifications as either SFR or STAR was extracted. Knowing that there were two distinct classes of source (x_{STAR} and x_{SFR}), with standard deviations σ_{STAR} and σ_{SFR} respectively, they constructed an observable called "linear discriminant" which was a linear combination

of the observed fluxes and which maximised the quantity

$$\left| \frac{< x_{\rm STAR} > - < x_{\rm SFR} >}{\sqrt{\sigma_{\rm STAR}\sigma_{\rm SFR}}} \right|$$

They found that the linear discriminant among STAR and SFR regions is given by

$$u_4 = 0.226[f_{12}] + 0.501[f_{25}] - 0.324[f_{60}] - 0.403[f_{100}]$$

which can be expressed as a linear combination of the other three observables:

$$u_4 = 1.105u_1 + 0.016u_2 - 0.600u_3$$

Fig. 2.2 shows that u_1 and u_4 convey much the same information and separate the sample much better than u_2 or u_3 (see also table 2.2).

Selecting only the SFR sources from the updated Arcetri Atlas left me with a sample of 409 sources. This was still too large so further criteria were used to make the sample more manageable.

2.1.2 Further selection criteria

The timing of the first JCMT observing run meant that only sources with right ascensions greater than 18 h and less than 08 h were observable. This constraint did not reduce the sample by very much since the updated Arcetri Atlas only contains 92 water masers outside this range, of which only 18 are of type SFR (approximately 4% of the total number of SFR sources).

Well-studied sources such as M17 SW (e.g. Hobson *et al*. 1993) and S106 (e.g. Richer *et al*. 1993), and regions such as Taurus and ρ Oph, for which considerable data already exist, were removed from the sample at this point. Some sources in Orion were kept in the sample since removal of these would have left nothing to observe in half of a JCMT shift.

Since the sample is still very large a decision was taken to include only those sources with an actual or kinematic distance less than 5 kpc. As discussed in chapter 1, water masers are sometimes found to possess velocities in excess of 50 km s^{-1} with respect to the host molecular cloud. It should be considered carefully whether water maser velocities can be used to determine kinematic distances. What is really needed is the molecular cloud velocity, but this is not available for all sources; in these cases it is necessary to rely on water maser observations to determine distance. The kinematic distances used to determine this sample were those published in the Arcetri Atlas and were based upon water maser velocities. Initially this was the only information available and sources were selected using these values in the hope that most of the masers were low velocity. Although the error in the distance estimate using maser velocities could be as much as 50 per cent, this is still alright in most cases and does not affect the sample to a great degree. In fact all but two of the sources observed possess masers with velocities smaller than 25 km s^{-1} relative to the host molecular cloud (§4.2.2), and half have distances determined from other, more reliable, lines (table 3.7). Generally the sources selected in this sample have

weak, low-velocity masers with simple spectra, so the use of maser velocity to calculate kinematic distance should not be a significant source of error. High-velocity masers are usually associated with extremely strong and complicated maser sources (e.g. W51, Genzel *et al*. 1981) which have already been removed from the sample.

A cut-off distance of 5 kpc was arbitrarily chosen to keep the sample size manageable and also have a reasonably good resolution in the continuum maps. For example, at 5 kpc a diffraction-limited 7 arcsec 450 μm continuum map would have a spatial resolution of 0.17 pc. Sources which did not have a distance quoted in the Arcetri Atlas or in a paper immediately referenced by the Atlas had to be removed from the sample unless it was obvious that they were nearby (e.g. in Orion). A search through all references for each of the ∼350 SFR sources in order to find a distance was not feasible.

Once all these criteria were applied the sample was reduced to 115 sources. In addition IRAS 17441−2910 was observed. This source is not only outside the right ascension range specified above but is also at a distance of 10 kpc. It was included because of a spare few hours at the start of an observing run in 1994 May where the main sample was not visible at a low enough airmass and another source was required to 'fill in.' IRAS 17441 was the only source of type SFR in the available R.A. range which possessed a reasonably large galactic lattitude offset from the Galactic Centre, and therefore may have been closer to us than the Galactic Centre.

A list of the 115 sources in the complete sample (plus IRAS 17441) can be found in table 2.3. The numbering system used in the table to identify the maser sources is based on that used by Palagi *et al*. (1993) with additional sources being slotted in to the system, using letters to suffix the nearest number, as they were found.

Table 2.3: The sample of H_2O masers closer than 5 kpc of type SFR.

No.	IRAS Association	Name/Region	Observed
3	00117+6412		
5	00338+6312	L1287	*
7	00342+6347		
8	00379+6248		
8b	00420+5530		*
10	00468+6527		
11	00494+5617	NGC281–west	
17	01134+6429		
23		W3(1)	
24	02219+6152	W3(2)	
25		W3(3)	
26	02232+6138	W3(OH)	
30	02333+5930		

continued on next page

continued from previous page

No.	IRAS Association	Name/Region	Observed
33	02461+6147		
36	02593+6016	S201	
38	03035+5819	HHL5 / AFGL437	*
39	03101+5821		
40	03211+5446	BFS 31	
44	03258+3104	HH 7–11 (B)	
45	03259+3105	HH 7–11 (A)	
46	03262+3108	HH 6	*
48	03353+5550		
65b	04579+4703	IRAS SSSC	
68c	05274+3345	AFGL 5142	*
68d	05302−0537	Ori A–west	*
69		Ori KL	
70	05329−0508	OMC(2)2	
71	05329−0512	OMC2	
72	05338−0647	HH 1	
73	05358+3543	S231	
76	05373+2349	HH 4	*
77	05375−0731	L1641–south 3	*
82	05413−0104	L1630	*
83	05435−0011	HH 19–27	
87b	05553+1631		
91		Mon R2	*
92	06053−0622	Mon R2 IRS 3	*
96	06084−0611	GGD 12–15	*
99	06103−0612	GGD 16–17	*
104b	06291+0421		*
112	06437+0009		
115b	07180−2356	L1660	
117	07225−2428	HHL–50	
119	07277−1821	S305	
198	17441−2910[1]		*
216	18032−2137		*
227	18089−1732	AFGL 5451	*
234		W33 cont	

continued on next page

[1] at a distance of 10 kpc

continued from previous page

No.	IRAS Association	Name/Region	Observed
236	18117−1753	W33A	*
237b	18134−1942		
243	18141−1615		
244		G14.45–0.11	*
245	18144−1723		
246	18153−1651		
249	18159−1648		
250	18162−2048	GGD 27–28	*
251	18164−1631		*
258	18182−1433		
261b	18236−1205		
262	18244−1155		
263	18248−1158	G19.61–0.23A	
265	18253−1130	G20.08–0.14	
271	18273+0113	GGD 29 / Serpens	*
272	18276−1431		
273	18282−0951	RCW 169	
276d	18316−0602	AFGL 7009S	*
277	18317−0757	G23.96+0.15	
309		W43(M2)	
315	18455−0149		*
331b	18507+0121		
332	18507+0110	W44	
334	18515+0157		
334b	18517+0121		
338	18537+0749	S76 E	*
339	18538+0216		
344	18556+0136	G35.2–0.74	
347	18592+0108	W48	*
352b	19045+0813		
361c	19092+0841		
362	19095+0930	OH43.8–0.1	
380	19255+2133	K 3–35	
385b	19374+2352	IRAS SSSC	*
387b	19388+2357	IRAS SSSC	
389	19442+2427	S87	*

continued on next page

continued from previous page

No.	IRAS Association	Name/Region	Observed
406b	20050+2720		
406c	20056+3350	IRAS SSSC	*
407	20081+3122	ON1	
409b	20126+4104		
412b	20188+3928		
413	20198+3716	ON2S	
414		ON2N / G75.78+0.34	
414c	20227+4154		
418	20275+4001	AFGL 2591	*
418b	20286+4105		
421		W75 N	
422		W75 S(1)	
424		W75 OH	
425		W75 S(3)	
431	20489+4410	Pelican	
435b	21007+4951	L988-A	*
435c	21078+5211	Cyg. OB7	*
443b	21391+5802	LDN1121 / S131	
446		HH 32-35[1] / Bs40[3]	*
447		Bs40[2] / NGC 7129	*
448	21418+6552	LkHα234	*
449	21432+4719	HHL 73	*
459	22142+5206		*
462	22176+6303	S140 IRS 1	
465b	22198+6336	L1204-A	*
471	22475+5939	S146	*
472	22506+5944	IRAS SSSC	*
475	22528+5936		*
476	22539+5758	S147	*
479	22566+5830	S152	*
489	23138+5945	S157 / GL3057	*
498	23314+6033		*

Of the 116 sources in the sample, 44 (Mon R2 and MonR2 IRS3 were counted as one observation) were observed (indicated by a * in table 2.3). These sources were chosen at random during the observing run from the above list. It was not possible to observe all the sources since only 5 shifts were allocated for this project and for some of the time the weather was good enough for 450 μm data to be

taken; this reduced the amount of time available to observe the sample at 850 μm.

Fig. 2.3 shows the distance distribution of the observed sources. The distance histogram (Fig. 2.3a) peaks at 1.5 and 4.0 kpc but since this is an angle averaged distribution it is not clear that this figure is showing spiral arm structure. Although the sample is small, comparing Fig. 2.3c with H I data (Mihalas & Binney 1981) and first quadrant CO data (Dame & Thaddeus 1985), shows that the spatial distribution of the observed sources corresponds well with the Galactic spiral arm structure (c.f. §4.2 in Palagi *et al*. 1993). Fig. 2.4 shows the *IRAS* colour-colour plot of the observed sources. Although PC analysis is better at selecting sources than a simple colour-colour diagram, since it utilises all the *IRAS* fluxes, it is a good check for the method that, as expected, the *IRAS* colours of the observed sources correspond roughly to the 'cores' region of Emerson (1987). This result shows that colour selections are good enough a discriminator for the purposes of this project. Also marked on the colour-colour plot is the colour criterion for ultra-compact H II (UC H II) regions used by Wood & Churchwell (1989).

2.2 Observations

As many sources as possible, from the sample of 115, were observed in the submm continuum to search for embedded objects. Submm continuum observations are especially sensitive to cool dust ($T \sim 40$ K) which is expected to surround forming stars. Along with molecular line observations this information enabled me to determine various parameters of the embedded cores such as hydrogen column density, temperature and mass (see §3.2 for the mathematical details).

Since some of the maser positions were very inaccurate (up to ± 30 arcsec), 15 of the more interesting sources were observed with the Very Large Array to find accurate maser positions (± 0.2 arcsec) and any association with UC H II regions. Evolving stars are expected to blow away neutral material and surround themselves with ionized gas (a Strömgren sphere) which will emit in the radio as Bremsstrahlung. Combined with the Ryle Telescope observations (and other published information) this allowed me to distinguish optically thin free-free emission ($I_\nu \approx$ constant) from optically thick free-free emission ($I_\nu \propto \nu^2$) or ionized winds ($I_\nu \propto \nu^{0.6}$, Panagia & Felli 1975).

A summary of all the observations carried out for this work can be found in table 2.4.

2.2.1 The James Clerk Maxwell Telescope

The James Clerk Maxwell Telescope (JCMT) is a 15-m submm telescope capable of observing in the range 1300 to 350 μm. At these wavelengths, the sky transmission is determined largely by the amount of water in the atmosphere, and hence necessitates the positioning of telescopes of this type on high, dry sites. The JCMT is situated on the dormant volcano Mauna Kea, Hawaii at an altitude of over 4000 m, and is operated by the Royal Observatory, Edinburgh on behalf of the Particle Physics and Astronomy Research Council of the United Kingdom, The Netherlands Organization for Pure Research and the National Research Council of Canada. The wavelengths at which observations are made, how-

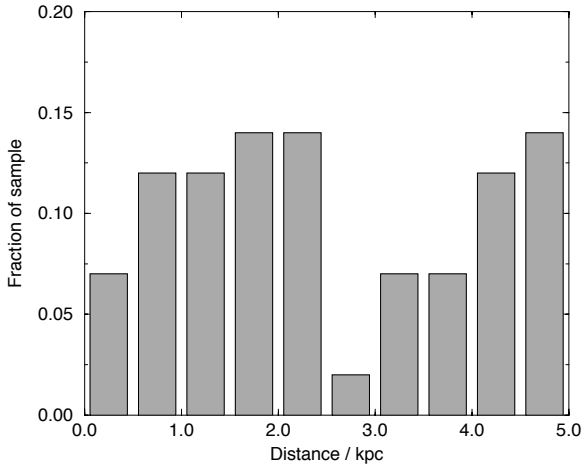

(a)

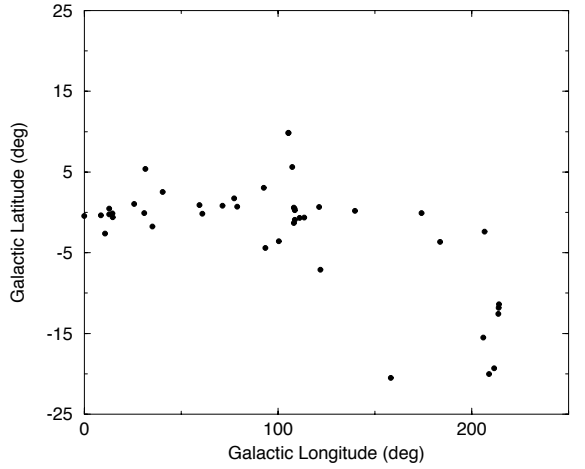

(b)

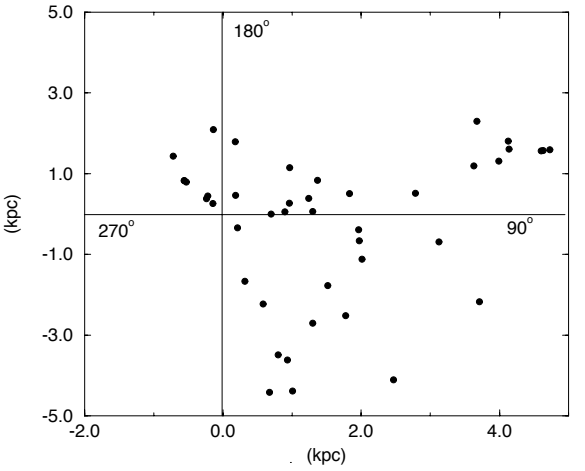

(c)

Figure 2.3. Distances and Galactic distribution of observed sources.

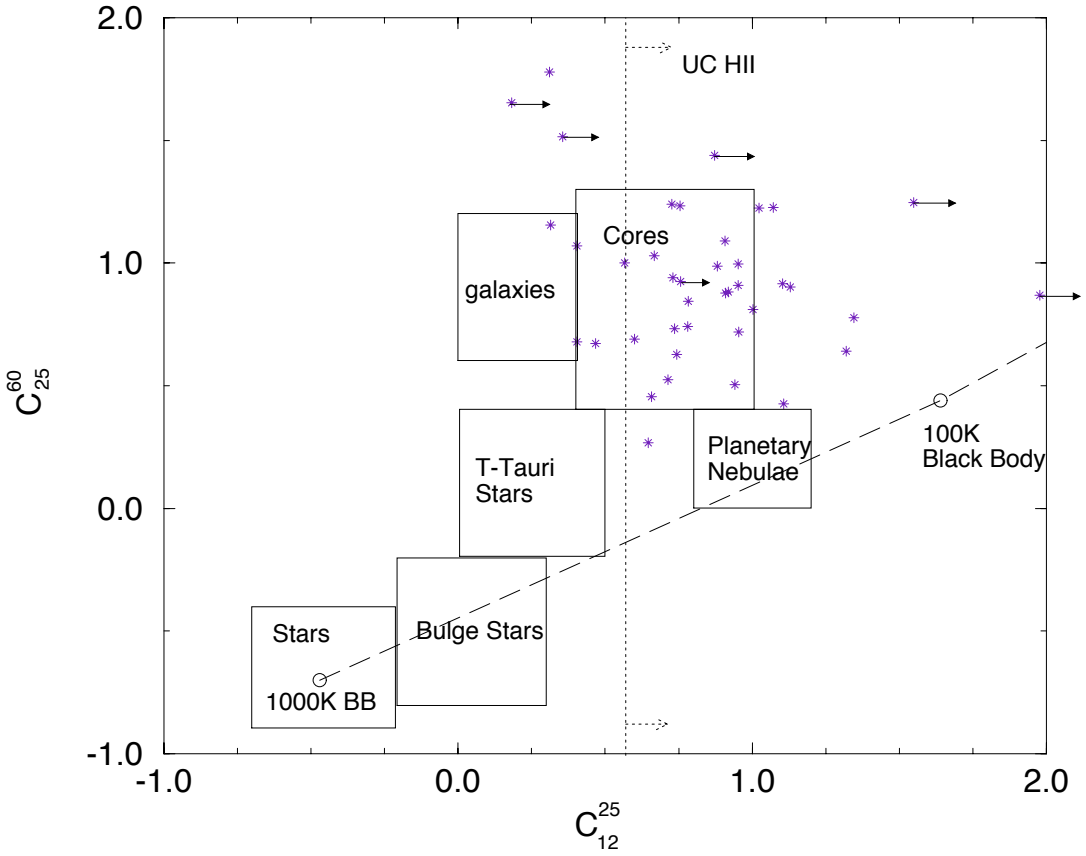

Figure 2.4. *IRAS* colours of the observed sources.

Table 2.4. Summary of observations carried out for this dissertation. A cross indicates an observation has been made. The number in the high resolution 450 μm column indicates the number of observations averaged into each map. For the symmetric top molecules the number indicates the integration time in seconds.

	850 μm	800 μm	450 μm (lo-res)	450 μm (hi-res)	8 GHz	15 GHz	^{12}CO	C^{18}O	CS	CH_3CN CH_3CCH	CH_3CCH CH_3OH	H_2O
00338+6312	×										1080	
00420+5530	×				×		×	×		1200		×
03035+5819	×						×					
03262+3108	×							×				
05274+3345	×											
05302−0537	×											
05373+2349	×											
05375−0731	×											
05413−0104	×											
06053−0622	×											
06084−0611	×											
06103−0612	×											
06291+0421	×											
17441−2910	×			2				×	×			
18032−2137	×		×	1				×		2700	2700	
18089−1732	×		×									
18117−1753	×		×									
G14.45-0.11	×		×		×		×	×				×
18162−2048	×	×	×									
18164−1631	×		×	2			×	×	×	2100	2160	
18273+0113	×	×	×	2	×		×	×	×	3000		×
18316−0602		×	×		×					3000	1980	×
18455−0149	×		×	1	×			×	×	2400		×
18537+0749	×		×									
18592+0108	×		×									
19374+2352		×	×	1	×	×	×	×	×	3000		×
19442+2427	×		×									
20056+3350		×	×	1	×	×		×	×	3000	3000	×
20188+3928		×	×	2	×	×	×	×	×	4800	5700	×
20275+4001	×		×							2400	540	
21007+4951	×		×		×	×						×
21078+5211	×	×	×	1	×	×	×	×	×	2400	3600	×
HH 32-35		×	×									
21418+6552	×	×	×									
21432+4719		×			×	×	×					×
22142+5206	×							×				
22198+6336	×			3		×	×	×	×	3600	2400	
22475+5939		×		1				×			5610	
22506+5944	×				×	×				3330		×
22528+5936	×				×							×
22539+5758	×				×							×
22566+5830	×											
23138+5945	×											
23314+6033	×			2	×	×	×	×		3480		×

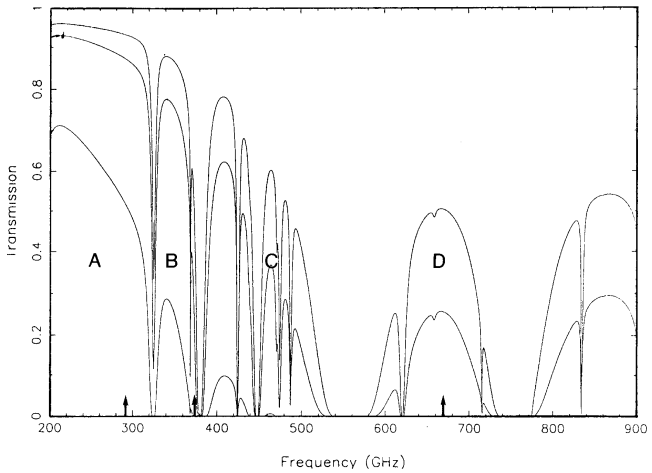

Figure 2.5. Zenith sky transmission on Mauna Kea. The three different traces denote the transmission under good (0.5 mm precipitable water; upper trace), average (1.0 mm; middle trace) and poor (5.0 mm; lower trace) observing conditions. The arrows denote the centre frequencies of the three most commonly used UKT14 continuum filters: 270 GHz (1100 μm), 370 GHz (800 μm) and 670 GHz (450 μm) while the letters refer to the different heterodyne receiver bands.

ever, are still governed by atmospheric transmission (Fig. 2.5). There is high transmission for $\lambda > 1$ mm, below which there are four main 'windows' centred near 800, 600, 450 and 350 μm. Both line and continuum observations are made in these windows or at the longer wavelengths. A summary of all the observing parameters can be found in table 2.5.

Continuum observing procedure

Cool dust emits radiation in the form of a modified black body (§3.2.2). Whilst this emission peaks in the mid- or far-infrared, significant emission also occurs at submm and millimetre wavelengths. In the millimetre sky transmission is extremely good but the larger beam and contamination from radio continuum (free-free) emission offset this gain. In the high frequency windows (450- and 350-μm) the continuum flux is much stronger and the beam size is small but these wavelengths suffer from low transmission and are only usable under the best weather conditions on Mauna Kea. A good compromise is the 800 μm atmospheric window. This window is less sensitive to the weather and is free of contamination from Bremsstrahlung emission.

The submm continuum data presented in chapter 3 were taken at the JCMT in 1993 September and 1994 August. All the data were taken using UKT14, a single-element ^{3}He-cooled Ge:In:Sb bolometer (Duncan *et al.* 1990), and the continuum backend. The sources were mapped in an 'on-the-fly' observing mode, where the telescope was continuously scanned in azimuth whilst using the secondary mirror to chop in the azimuth direction so that atmospheric contributions can be minimised; several scans at different elevations were used to make the final maps. Fig. 2.6 shows how the two beams move across

Table 2.5. Observing parameters

JCMT Continuum:

Date	Wavelength (μm)	Beam FWHM (arcsec)	Raster	Sampling (arcsec)	Chop throw (arcsec)	Aperture (mm)	Integration time/pt (s)	Calibration Accuracy (%)
Sept. 1993	850	18	37×25	5	60	65	1.0	20
Sept. 1993	800	17	37×25	5	60	65	1.0	20
Sept. 1993	450	18[a]	23×15	5	40	65	1.0	25
Aug. 1994	450	7	29×17	2	30	27	3.0	30

[a]with non-diffraction-limited aperture

		Rest Frequency (GHz)	Beam FWHM (arcsec)	Grid	Sampling (arcsec)	Off position in RA (arcsec)	Integration time/pt (s)	Bandwidth (MHz)	Velocity Resolution (km s^{-1})
JCMT Spectral Line:									
May 1994	^{12}CO $J = 2 \rightarrow 1$	230.5380	21	7×7	10	1200	30	250	0.2
May 1994	C^{18}O $J = 2 \rightarrow 1$	219.5603	21	5×5	10	1200	120	250	0.2
Aug 1994	C^{18}O $J = 2 \rightarrow 1$	219.5603	21	5×5	10	1800	120	250	0.2
Aug 1994	CS $J = 5 \rightarrow 4$	244.9357	21	3×3	10	1800	60	250	0.2
Jun 1995	CH_3CCH $J_K = 14_0 \rightarrow 13_0$	239.2523	21	-	-	180BM	2400	500	0.8
Jun 1995	CH_3CCH $J_K = 20_0 \rightarrow 19_0$	341.7411	14	-	-	180BM	2400	500	0.5
Jun 1995	CH_3CN $J_K = 13_0 \rightarrow 12_0$	239.1379	21	-	-	180BM	2400	500	0.8
Jun 1995	CH_3OH $J_{K_+K_-} = 7_{12} \rightarrow 6_{12}$	341.4156	14	-	-	180BM	2400	500	0.5
VLA Spectral Line:									
July 1994	H_2O $6_{16} \rightarrow 5_{23}$	22.23508	0.4	-	-	-	10	6.25	2.6

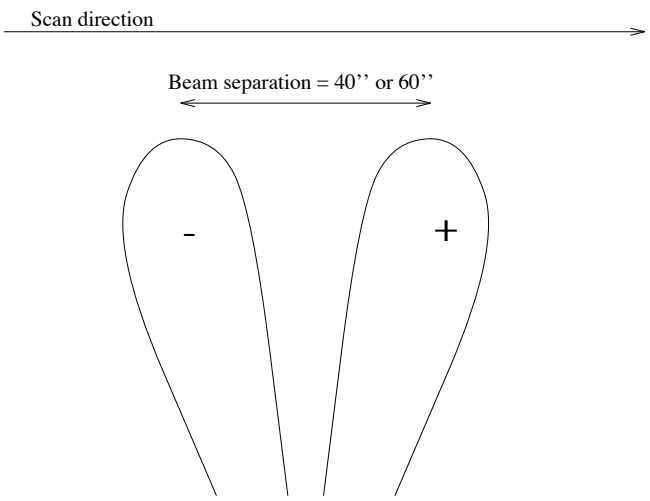

Figure 2.6
Dual beam scanning mode of the JCMT.

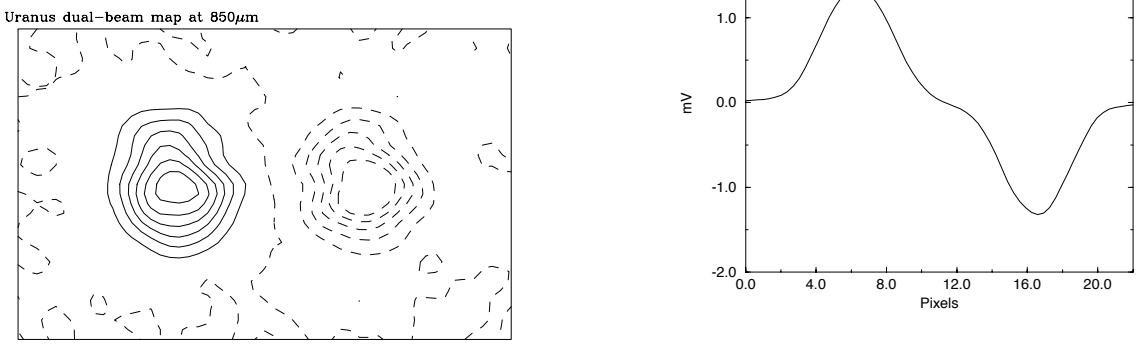

Figure 2.7. A dual beam map of a point source plus a cut to show the plus and minus beams.

the sky and Fig. 2.7 shows the dual-beam map of a point source (in this case Uranus at 850 μm) before processing. The 800/850-μm raster scans covered an area of approximately 1.5×1.5 arcmin^2 around each source, which was a few times greater than the uncertainties in position of even the least accurately measured masers.

Observations were made at either 850 or 800-μm, and at 450-μm, but because of time constraints not all the sources were mapped in two wavelengths. For the first night the 800-μm filter was used but on subsequent nights it was found that the narrower 850 μm filter gave better quality maps.

Throughout the observations the telescope pointing accuracy was better than 2 arcsec although problems with atmospheric 'anomalous refraction' limited the absolute positions of the 450-μm data (especially for IRAS 23314+6033) to probably no better than 4 arcsec. Since we were mainly interested in photometry, the sources were initially mapped with a 17 arcsec focal plane aperture. High-resolution 450-μm diffraction-limited maps, having a beam size of 7 arcsec, were made of some of the sources in 1994 August. Uranus was observed at each wavelength to map the beam and measurements

were made of Uranus (our primary calibrator) and secondary calibrators, from the JCMT calibrator list (Sandell 1994), through the night to check the calibration. The atmospheric opacity was calculated from the Caltech Submillimeter Observatory τ values for 225 GHz (Stevens & Robson 1994), and checked against my own photometry.

The dual-beam maps were processed using the software package NOD2 (Emerson *et al*. 1979). The first stage is to correct each map for the atmospheric transmission (i.e. compensate for telescope elevation (airmass) and the zenith optical depth (τ)). Bad pixels and the uniform offsets were then removed from the dual-beam map before the data was restored to an approximately equivalent single-beam map using a fourier filter technique (algorithm RESTOR). These azimuth-elevation maps were then interpolated onto an RA-Dec grid using a sinc interpolation (algorithm CONVERT). Fluxes were obtained from the maps generated by NOD2 by summing pixels in a circular aperture (using the ANM image processing software package) and comparing the resulting sum with that obtained from a planet map of known flux density.

Maps were also made using the dual-beam maximum entropy algorithm DBMEM, which treats the reconstruction of the map from the dual-beam data as a direct linear inversion problem resulting in a map which has been deconvolved from the beam (Richer 1992). Since most of the data have only a modest signal-to-noise ratio (typically 5 to 10 per pixel), I do not expect any significant resolution enhancement by using this method; however the algorithm has other convincing advantages, such as enforced positivity and proper treatment of correlations in the two-dimensional data. Thus I have chosen to present DBMEM reconstructions of the data (chapter 3); the DBMEM reconstructions have been smoothed with Gaussians (FWHM of 12 arcsec for the 800/850-μm maps and 3 arcsec for the 450-μm maps) to suppress high-spatial-frequency noise structure.

Whilst running DBMEM it was noticed that the final flux in the map was very sensitive to the estimated noise value given to the program for low signal-to-noise data. This is a well-known problem of MEM reconstructions from total power observations (e.g. Cohen 1991; Wu 1993) and is caused by the entropy term in the minimizing function pushing the solution towards the input model. This means that although there may be two solutions with the same χ^2 consistent with the noisy data, one peaking above the data and one below, the entropy term will always bias the solution towards the lower value. For large signal to noise data the effect of the entropy term is small and the measured flux is within a few per cent of the actual flux. Significant errors in the photometry of poor signal-to-noise chopped data were not noticed in the initial testing of DBMEM (Richer 1992) although those tests were aimed mainly at comparing source structure. This problem was investigated by running DBMEM with different signal-to-noise data sets from the first observing run and specifying different noise estimates. The HISTORIC algorithm from the MEMSYS software package was used throughout, which uses a stopping criteria of χ^2 equal to the number of data points, since this gave the best looking maps and was a good compromise between no deconvolution (as used in NOD2) and the MEMSYS CLASSIC algorithm (which gave very spiky maps since it pushes the deconvolution much further). Flux was measured for the different noise estimates by using a standard 80 arcsec photometry aperture throughout, and

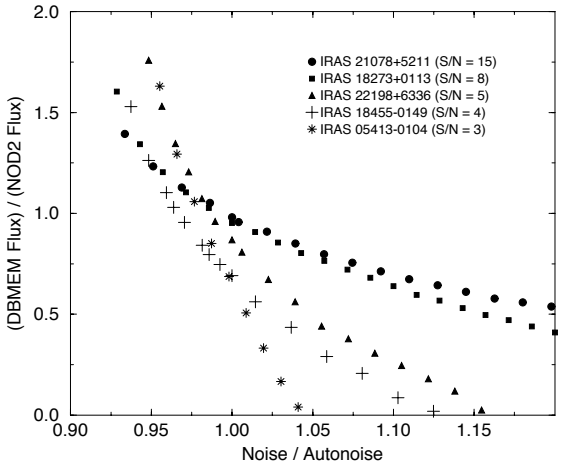

Figure 2.8
Plot of flux versus the noise estimate of the dual beam map. The axes have been scaled so that different data can be compared.

then scaled by the NOD2 value so that different data sets could be compared. Fig. 2.8 shows how the source flux varies with estimated noise. The estimated noise used for each run has been scaled by the 'actual' noise value as calculated by DBMEM. The graph shows that for the high signal-to-noise data a change in the specified noise of 20 per cent can result in the measured flux of the source dropping by 50 per cent. For the low signal-to-noise data a variation in estimated noise of 5 per cent can result in no source being detected at all – this is saying that the input data is consistent with the input model of a flat field. In all but the very low signal-to-noise data however, good flux agreement with that using the standard NOD2 method can be obtained if the noise calculated by DBMEM is used. Of course it must always be remembered that single beam measurements are required to constrain the *total* flux of a source and neither NOD2 nor DBMEM can provide this information from a dual-beam map.

Millimetre spectral line observations

Millimetre spectral line observations were made during 1994 May and August using the common-user heterodyne Receiver A2 (Davies *et al*. 1992) and the Digital Autocorrelation Spectrometer (DAS) (Bos 1988; Dent & Matthews 1995) with a bandwidth of 250 MHz over 2048 channels. This gave a frequency resolution of 0.156 MHz, equivalent to a velocity resolution of approximately 0.2 km s^{-1}.

I observed the ^{12}CO and C^{18}O $J = 2 \rightarrow 1$ rotational transitions which have rest frequencies of 230.5380 and 219.5603 GHz respectively, and also CS $J = 5 \rightarrow 4$ at 244.9357 GHz. The maps were made in position-switching mode, in which measurements at a grid of positions were compared with a fixed reference or 'off' position chosen, as far as possible, to contain little or no emission at velocities of interest. Off-position offsets of 1200 arcsec in right ascension were used throughout except in the case of G14.45-0.11 where 1800 arcsec seemed to be preferable for the C^{18}O and 2400 arcsec for the ^{12}CO observations to make sure that the off position was looking at 'blank' sky. An off-position offset of 1800 arcsec was used for the mapping observations made in 1994 August.

At these frequencies the JCMT has a beam FWHM of 21 arcsec and it was decided to use fully-sampled grids with 10 arcsec by 10 arcsec spacing. Time constraints meant that only two sources could be observed with grids larger than 7×7 pixels (L1204A and IRAS 23314+6033). Spectra were obtained for 15 of the sources.

In 1995 June observations were performed to search for the symmetric-top molecules methyl cyanide (CH_3CN) and propyne (CH_3CCH), and the asymmetric-top methanol (CH_3OH). Observing symmetric-tops has the advantage that many transitions are observed *simultaneously* and it is only the relative peaks of the transitions which determine the temperature and *not* the absolute calibration (which is a real problem when dealing with other high density tracers such as CS). The properties of the symmetric-top molecules are described in table 2.6 and §3.2.3. Fortuitously the methyl cyanide $J = 13 \rightarrow 12$ and propyne $J = 14 \rightarrow 13$ transitions are very close in frequency and it is possible to observe these lines simultaneously with a DAS bandwidth of 500 MHz. The $K = 5$ transition of propyne is not visible in this case since it merges with the $K = 0$ transition of methyl cyanide, but this is not a problem since the five transitions up to and including $K = 4$ are enough to determine a reliable temperature and the ability to also observe methyl cyanide far outweighs this loss. The high J propyne transitions were observed with receiver B3i (Cunningham *et al*. 1992) and for these observations methanol was close enough in frequency to appear in the passband of the 500 MHz DAS mode.

The spectra were observed in beam-switching mode where the secondary mirror moves on and off the source, at a frequency of 1 Hz, to subtract out the atmospheric contributions. Since the secondary mirror is chopping in azimuth the off position is not constant but rotates around with the sky. This technique is only usable for compact sources (i.e. smaller than the chop throw in extent) where the line emission is not thought to be extended. Symmetric top molecules such as propyne and methyl cyanide are observable with this technique because they have very low abundances (Wang *et al*. 1993) and the objects being observed were known to be compact cores.

The observations were calibrated regularly using the standard ambient and cold loads, and the pointing was checked every few hours by observing standard JCMT pointing sources. All maps and spectra presented in this dissertation use the T_A^* temperature scale. This is related to brightness temperature by $T_R = T_A^*/\eta_b$ (see Kutner & Ulich 1981), where $\eta_b = \eta_c \eta_{fss}$ and is estimated to be approximately 0.7. All data analysis was done using the standard SPECX software. Linear baselines were removed and each set of data was read into a separate SPECX data-cube for further processing. All the maps have been velocity-scaled with respect to the local standard of rest (LSR).

2.2.2 The Very Large Array

The Very Large Array (VLA) is a 27-element array capable of operating at a wide range of frequencies and resolutions and can be used in 4 different configurations (A to D) to examine different angular scales. For example, D-array is the most compact (1 km largest baseline) and therefore has the lowest angular resolution, i.e. largest synthesised beam, but is also sensitive to the most extended emission.

Table 2.6. Parameters of symmetric top molecules (Kuiper *et al*. 1984; Poynter & Pickett 1985).

CH_3CN	$\mu = 1.30 \times 10^{-29}$ Cm	CH_3CCH	$\mu = 2.60 \times 10^{-30}$ Cm
	A = 158275 MHz		A = 158590 MHz
	B = 9203 MHz		B = 8546 MHz

	K	ν (GHz)	$S_{J+1,K\rightarrow J,K}$	E_u (K)		K	ν (GHz)	$S_{J+1,K\rightarrow J,K}$	E_u (K)
$J = 13 \rightarrow 12$	0	239.137	13.00	80.34	$J = 20 \rightarrow 19$	0	341.741	20.00	172.23
	1	239.133	12.92	87.50		1	341.734	19.95	179.43
	2	239.119	12.69	108.96		2	341.715	19.80	201.02
	3	239.096	12.31	144.73		3	341.682	19.55	237.01
	4	239.064	11.77	194.80		4	341.637	19.20	287.39
	5	239.023	11.08	259.18		5	341.578	18.75	352.17
	6	238.972	10.23	337.87	$J = 14 \rightarrow 13$	0	239.252	14.00	86.12
	7	238.912	9.23	430.87		1	239.248	13.93	93.32
	8	238.844	8.08	538.18		2	239.234	13.71	114.92
						3	239.211	13.36	150.92
						4	239.179	12.86	201.31

Table 2.7. Properties of VLA B configuration for snapshot observations.

Band	Frequency (GHz)	θ_{syn} ($''$)	θ_{max} ($''$)		
K	22.235	0.4	3.5	Maximum antenna separation	11.4km
X	8.4	0.9	10.0	Minimum antenna separation	0.21km

On the other hand A-array, with a 36 km largest baseline, has sub-arcsecond resolution but also resolves out extended emission, a property of interferometers. For these observations B-array was used because it was the next array available. The VLA is part of the National Radio Astronomy Observatory, USA, which is operated by Associated Universities, Inc., under cooperative agreement with the National Science Foundation.

For these observations the VLA was in configuration B (run number AJ239) and 6 hours were allocated on 1994 July 3 starting at 17^h30 LST. Details of B array can be found in table 2.7 and see also Fig. 2.9 for the configuration. Note that the values in that table are for single snapshot observations, as used in this run, and the range of angular scales is therefore smaller than for a full observation by about 60%. This is because the *uv* coverage is patchy and not circularly symmetric. For a full observation the coverage is complete and a more or less circular beam can be synthesised.

Integration times of only 10 seconds were used (to limit time smearing) but this does generate a large amount of data in spectral line mode since each source was observed for a duration of approximately 7 minutes. 3C48 was used as the primary flux calibrator and was observed for 5 minutes at the end of the run. No other calibrator was available because of RA constraints. Phase was calibrated regularly for both K- and X- bands at least every third source (table 2.8) for approximately 2 min each time. Reference pointing was also used to maximize the gain at 22GHz (VLA Observational Status Report 1993). The pointing was checked whenever the antennas moved further than 10 degrees from

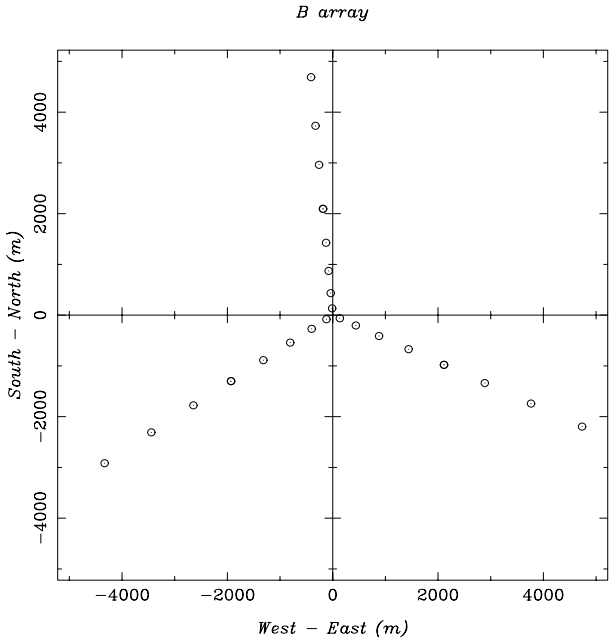

Figure 2.9
VLA B array configuration.

Table 2.8. VLA calibrators for AJ239.

1730−130		phase & pointing
1829−106		phase
1801+010		phase
1932+204		phase
2013+340		phase & pointing
2005+403		phase & pointing
2030+547		phase
2200+420		phase & pointing
2146+608		phase & pointing
0012+610		phase
0134+329	3C48	flux

a reference position.

All the reduction of the VLA data was done with the NRAO package AIPS (Astronomical Image Processing Software) release 15JUL93, using the AIPS Cookbook (Greisen 1994) for the reduction method. The continuum and line data follow the same initial method of analysis with the spectral line observations calibrated using the 'Channel 0' information (which is the average of the middle 75% of the observed band). The data was first flagged using the AIPS tasks QUACK (which removes the first data point from each observation) and UVFLG (which removes suspect antennas from the dataset). For the 8 GHz observations it was necessary to remove IF 1 for antennas 16, 22 and 24 and for the 22 GHz observations antenna 22 was removed. All the maps were made and cleaned using the MX task.

8.4-GHz continuum

X-band (8-GHz) continuum observations were made to see if ultra-compact continuum sources were associated with the masers. A bandwidth of 50 MHz was used at a frequency of 8.4149 GHz. X-band was chosen because its sensitivity for flat spectrum sources is 4 times better than for K-band. The total integration time per source was approximately 7 min, giving an rms noise level of approximately 0.1 mJy beam^{-1}. For snapshot observations this configuration has a synthesized beam size of 0.9 arcsec and resolves out any structure greater than approximately 10 arcsec in extent.

Water maser line

The H_2O $6_{16} \rightarrow 5_{23}$ maser transition, at 22.235 GHz rest frequency (K-band), was observed during the same VLA run as that used for the 8-GHz data to find accurate positions of the water masers, improving on single-dish measurements. Since we knew the LSR velocity of these maser lines from earlier observations, a small bandwidth of 6.25 MHz was chosen. With Hanning smoothing in dual-IF mode 2AC, 32 channels were available giving a channel spacing/width of 195 kHz (approximately 2.6 km s^{-1}). Since the masers were expected to be very strong and our bandwidth was so small, bandpass calibration was not thought necessary. Reference pointing was used though to try to maximize the antenna gain. Total integration time per source was approximately 7 min and this gave an rms noise of approximately 15 mJy beam^{-1} channel^{-1}.

2.2.3 The Ryle Telescope

Six of the sources were observed at 15.4 GHz in 1994 June and July using part of the Ryle Telescope (Jones 1991), an east-west earth-rotation aperture synthesis telescope with eight 13-m dishes on a 4.6-km longest baseline at Cambridge operated by the Mullard Radio Astronomy Observatory. Five antennas were used, with a maximum spacing of 108-m, giving a synthesized beamwidth of 30×30 cosecδ arcsec^2. Additional observations were made in 1995 April with the RT in a more extended configuration giving a maximum resolution of 1×1 cosecδ arcsec^2. The measurements consisted of a single

run of either 3 or 12 h depending on the observed source intensity. Data processing used the local packages POSTMORTEM and ANMAP.

References

André P., Ward-Thompson D., Barsony M., 1993, *ApJ*, 406, 122
Beichman C. A., Neugebauer G., Habing H. J., Clegg P. E., Chester T. J. (eds), 1988, *Infrared Astronomical Satellite (IRAS) Catalogs and Atlases*, The Joint IRAS Science Working Group, NASA RP–1190
Benson P. J., *et al*., 1990, *ApJS*, 74, 911
Bos A., 1988, The DAS: System Description, Tech. Rep. 187, Netherlands Foundation for Radio Astronomy
Brand J., *et al*., 1994, *A&AS*, 103, 541
Braz M. A., Scalise Jr. E., Gregorio Hetem J. C., *et al*., 1989, *A&AS*, 77, 465
Churchwell E., Walmsley C. M., Cesaroni R., 1990, *A&AS*, 83, 119
Cohen J. G., 1991, *AJ*, 101, 734
Comoretto G., *et al*., 1990, *A&AS*, 84, 179
Cunningham C. T., Hayward R. H., Wade J. D., Davies S. R., Matheson D. N., 1992, *Int. J. Infrared Millim. Waves*, 13, 1827
Dame T. M., Thaddeus P., 1985, *ApJ*, 297, 751
Davies S. R., Cunningham C. T., Little L. T., Matheson D. N., 1992, *Int. J. Infrared Millim. Waves*, 13, 647
Dent W. R. F., Matthews H. E., 1995, *User's guide to the DAS*, Joint Astronomy Centre, Hilo, HI, http://www.jach.hawaii.edu/JCMT/das-guide/das-guide.html
Duncan W. D., Robson E. I., Ade P. A. R., Griffin M. J., Sandell G., 1990, *MNRAS*, 243, 126
Emerson D. T., Klein U., Haslam C. G. T., 1979, *ApJ*, 76, 92
Emerson J. P., 1987, in *Star Forming Regions*, eds Peimbert M., Jugaku J., p. 19, IAU Symp. No. 115, Reidel, Dordrecht
Felli M., Palagi F., Tofani G., 1992, *A&A*, 255, 293
Genzel R., *et al*., 1981, *ApJ*, 247, 1039
Greisen E. (ed.), 1994, *AIPS Cookbook (15JUL94)*, NRAO, Socorro, New Mexico
Harris S., Clegg P., Hughes J., 1988, *MNRAS*, 235, 441
Hobson M. P., Padman R., Scott P. F., Prestage R. M., Ward-Thompson D., 1993, *MNRAS*, 264, 1025
Jones M., 1991, in *IAU Colloq. 131, Radio Interferometry: Theory, Techniques and Applications*, eds Cornwell T. J., Perley R., p. 395, Astron. Soc. Pac., San Francisco
Kömpe C., Joncas G., Baudry A., Wouterloot J. G. A., 1989, *A&A*, 221, 295
Kuiper T. B. H., Rodriguez Kuiper E. N., Dickinson D. F., Turner B. E., Zuckerman B., 1984, *ApJ*, 276, 211
Kutner M. L., Ulich B. L., 1981, *ApJ*, 250, 341
Mihalas D., Binney J., 1981, *Galactic Astronomy*, p. 531, W. H. Freeman, San Francisco, 2nd edn.
Murtagh F., Heck A., 1987, *Multivariate Data Analysis*, Astrophysics & Space Science Library, Reidel, Dordrecht
Neugebauer G., *et al*., 1984, *ApJ*, 278, L1
Palagi F., Cesaroni R., Comoretto G., Felli M., Natale V., 1993, *A&AS*, 101, 153
Palla F., Brand J., Cesaroni R., Comoretto G., Felli M., 1991, *A&A*, 246, 249
Panagia N., Felli M., 1975, *A&A*, 39
Poynter R. L., Pickett H. M., 1985, *Applied Optics*, 24, 2335, http://spec.jpl.nasa.gov/
Richer J. S., 1992, *MNRAS*, 254, 165
Richer J. S., Padman R., Ward-Thompson D., Hills R. E., Harris A. I., 1993, *MNRAS*, 262, 839
Sandell G., 1994, *MNRAS*, 271, 75
Scalise Jr. E., Rodríguez L. F., Mendoza-Torres E., 1989, *A&A*, 221, 105
Stevens J. A., Robson E. I., 1994, *MNRAS*, 270, L75
Tereby S., Vogel S. N., Myers P. C., 1992, *ApJ*, 390, 181
Wang T. Y., Wouterloot J. G. A., Wilson T. L., 1993, *A&A*, 277, 205

Wood D. O. S., Churchwell E., 1989, *ApJS*, 69, 831

Wu N., 1993, in *The restoration of HST images and spectra – II*, eds Hanisch R. J., White R. L., p. 58, Space Telescope Science Institute, http://iris.stsci.edu/proceedings/wun.html

Chapter 3

Observational data and preliminary analysis

In this chapter I present the observational data and a preliminary analysis of those data in order to estimate physical conditions in the maser's host molecular clouds. The properties of the sample as a whole will be presented in chapter 4.

3.1 Observational data

The entire data set observed for this thesis is summarized below:

- **JCMT submm continuum**: Table 3.1 (p.32), Figs 3.1 (p.38) and 3.2 (p.45)
  The 850 μm source sizes were found for the deconvolved DBMEM maps and are therefore sensitive to the signal-to-noise of each map. Sizes less than 10 arcsec are probably consistent with point sources in the 18 arcsec JCMT beam. Maps were fitted with elliptical Gaussians using the ANM plotting package.
- **RT 15-GHz continuum**: Table 3.2 (p.33), Fig. 3.6 (p.51)
- **VLA 8-GHz continuum**: Table 3.3 (p.33), Fig. 3.7 (p.52)
  The VLA radio continuum sources were fitted to elliptical Gaussians by the JMFIT package within AIPS.
- **JCMT heterodyne observations**: Tables 3.4 (p.34) and 3.5 (p.35), Figs 3.3 (p.47), 3.4 (p.49) and 3.5 (p.50)
- **VLA H_2O maser observations**: Table 3.6 (p.37)

Table 3.1. JCMT continuum data: Observed submm fluxes integrated over the map. The position given is that of the 800/850-μm source. Each source was mapped once except for the 850-μm maps of Mon R2 and IRAS 17441(mapped twice) and some high resolution 450-μm maps (the number of maps made of each source at this wavelength is indicated after a / following the flux density).

IRAS	Submm source		Name		Flux densities (Jy)				850-μm size		
Association	R.A.(1950)	Dec.(1950)			850 μm	800 μm	450 μm		Maj	Min	PA
							Lo-res	Hi-res	(″)	(″)	(deg)
00338+6312	00 33 52.8	63 12 22	L1287		17				18	10	93
00420+5530	00 42 05.7	55 30 31			5.7				30	20	80
03035+5819	03 03 33.5	58 19 09	HHL 5/GL437		11				30	10	110
03262+3108	03 26 05.6	31 08 16	HH 6		5.6				12	12	90
05274+3345	05 27 29.7	33 45 38	GL 5142		21				12	13	90
05302−0537	05 30 14.8	−05 37 56	Orion A-west		3.3				28	15	42
05373+2349	05 37 21.4	23 49 18	HH 4		2.1				18	16	78
05375−0731	05 37 31.0	−07 32 04	L1641.S3		6.5				14	9	75
05413−0104	05 41 18.9	−01 04 11	L1630		2.3				14	8	136
06053−0622	06 05 19.9	−06 22 44	MonR2 IRS3		21				41	15	63
06084−0611	06 08 23.7	−06 11 06	GGD 12–15	FIR2	36				16	14	90
06084−0611	06 08 25.6	−06 10 53	GGD 12–15	FIR1	-				24	15	115
06103−0612	06 10 23.4	−06 12 45	GGD 16–17		2.6				14	14	90
06291+0421	06 29 10.0	04 21 35			<5.4						
17441−2910	17 44 09.2	−29 10 59			11			54/2	24	12	76
18032−2137	18 03 18.6	−21 37 52		FIR2	49		390	320/1	14	12	32
	18 03 23.2	−21 37 36		FIR1	20		123		16	16	
18089−1732	18 08 56.4	−17 32 15	GL 5451		17		200		11	9	80
18117−1753	18 11 44.1	−17 52 57	W33 A		45		240		25	15	90
	18 14 18.6	−16 26 49	G14.45-0.11	FIR1	3.6		25		16	11	14
	18 14 15.3	−16 27 12		FIR2	5.7		37		36	18	30
	18 14 17.4	−16 27 17		FIR3	2.4		18		23	14	10
18162−2048	18 16 13.0	−20 48 47	GGD 27–28		21	24	130		18	11	90
18164−1631	18 16 21.8	−16 31 21			22		100	90/2	22	18	27
18273+0113	18 27 17.5	01 13 15	GGD 29		13	17	80	60/2	16	12	170
18316−0602	18 31 40.2	−06 02 06	GL7009S			28	180		14	12	130
18455−0149	18 45 34.8	−01 48 51			4.1		26	17/1	18	15	90
18537+0749	18 53 46.1	07 49 19	S76 E		33		215		20	12	115
18592+0108	18 59 13.8	01 09 03	W48		50		250		20	16	133
19374+2352	19 37 27.8	23 52 49				7.1	55	30/1	13	12	152
19442+2427	19 44 16.0	24 28 36	S87	FIR1	6.5		18		24	13	94
	19 44 14.0	24 28 12		FIR2	17		110		33	14	40
20056+3350	20 05 35.8	33 50 56				6.2	48	33/1	17	12	54
20188+3928	20 18 50.4	39 28 19		FIR2		21	144	130/2	24	19	35
	20 18 50.0	39 28 45		FIR1		9.8	48		29	14	120
20275+4001	20 27 35.9	40 01 14	GL 2591		19		170		22	15	96
21007+4951	21 00 45.1	49 51 17	L988-A		1.7		10		46	28	95
21078+5211	21 07 46.8	52 10 21			18	>13	110	113/1	9	9	
	21 41 51.5	65 49 37	HH32–35[1]			5.2	30		10	10	
21418+6552	21 41 57.8	65 53 08	LkHα234		3.4	4.2	60		11	11	
21432+4719	21 43 15.2	47 18 58	HHL 73			<1.1					
22142+5206	22 14 14.4	52 06 37			<1.2						
22198+6336	22 19 50.0	63 36 26	L1204-A		5.2			35/3	12	8	100
22475+5939	22 47 31.8	59 39 50	S 146	FIR1		2.0			15	10	160
	22 47 29.8	59 38 59		FIR2		6.5		16/1	26	15	90
22506+5944	22 50 39.2	59 44 47			8.1				15	8	80
22528+5936	22 52 48.6	59 36 58			<3.1						
22539+5758	22 54 00.7	57 59 06		FIR1	5.7						
	22 53 56.4	57 58 36		FIR2	6.8				29	17	27
22566+5830	22 56 39.8	58 31 47	S152	FIR1	7.2				9	9	
	22 56 38.4	58 31 04		FIR2	6.8						
23138+5945	23 13 51.7	59 45 47	S157/GL3057	FIR1	3.5				30	16	30
	23 13 53.5	59 45 24		FIR2	5.9						
23314+6033	23 31 23.2	60 33 52			3.9			15/2	23	13	115

Table 3.2. 15-GHz RT observations. For IRAS 20188+3928 the second extended source to the south-east had a peak brightness of 3.9 mJy beam $^{-1}$. The main detections for the low resolution maps were all centered on the submm continuum source within the positional errors of the RT.

	Source position		Beam	Flux	Size
	R.A.	Dec.	(arcsec)	(mJy)	(arcsec)
19374+2352	submm		30	75	-
20056+3350	submm		30	3	slightly extended
20188+3928	submm		30	28	-
20188+3928	20 18 58	39 26 4	30	14.5	120×120
20188+3928	20 18 50.7	39 28 17	1.1×1.9	26	-
20188+3928	20 18 50.9	39 28 38	1.1×1.9	2.8	-
21007+4951	submm		30	<0.6	
21078+5211	21 07 47	52 10 45	5.5	118	35×45
21432+4719			30	<0.6	
22198+6336			30	<0.6	
22506+5944			5	<1.0	
23314+6033	23 31 24	60 33 35	19×10	19	40×25

Table 3.3. VLA 8-GHz continuum observations.

	R.A.	Dec.	Flux	Size		
	(1950)	(1950)	(mJy)	Maj($''$)	Min($''$)	PA(deg)
00420+5530			<0.3			
G14.45−0.11			<0.3			
18273+0113	18 27 17.44	01 13 15.6	2.8	<0.6	<0.6	
	18 27 17.75	01 13 12.4	2.2	<0.3	<0.3	
	18 27 17.11	01 13 20.0	1.2	<0.3	<0.3	
18316−0602	18 31 40.14	-06 02 05.7	3.8			
18455−0149			<0.3	1.1	0.9	172
19374+2352	19 37 27.80	23 52 51.4	79.3	0.8	0.6	37
20056+3350	20 05 35.69	33 50 56.2	0.93			
	20 05 35.79	33 50 56.7	0.60			
20188+3928	20 18 50.71	39 28 17.1	24.1	1.2	0.95	5
	20 18 50.77	39 28 19.1	2.2	<0.36	<0.36	
	20 18 50.92	39 28 38.7	3.4	<0.36	<0.36	
21007+4951			<0.3			
21078+5211			<0.3			
21432+4719			<0.3			
22506+5944	22 50 38.85	59 44 42.3	1.7			
22528+5936			<0.3			
22539+5758	22 53 55.99	57 58 41.1	2.6			
23314+6033			<0.3			

Table 3.4. JCMT heterodyne data: Carbon monoxide, carbon monosulphide and methanol line data.

	^{12}CO $J = 2 \rightarrow 1$			C^{18}O $J = 2 \rightarrow 1$			CS $J = 5 \rightarrow 4$			CH_3OH	Evidence
	v_{LSR} (km s^{-1})	Δv_{eq} (km s^{-1})	T_A^* (K)	v_{LSR} (km s^{-1})	Δv_{eq} (km s^{-1})	T_A^* (K)	v_{LSR} (km s^{-1})	Δv_{eq} (km s^{-1})	T_A^* (K)	T_A^* (K)	of outflow
00338+6312										0.20	
00420+5530	−52	4.2	17.3	−51.8	2.0	4.3					
03035+5819	−40	4.7	56.3								
03262+3108				8.3	1.5	3.8					
17441−2910				18.5	3.5	10.6	18.2	4.5	4.0		
18032−2137				34	4.6	10.5				0.96	Yes
G14.45−0.11	42.3	9.5	15.3	40.5	2	7.6					No
18164−1631	15.9	6.5	21.6	18	3	4.6	17.2	3.5	3.0	0.26	in ^{12}CO
18273+0113	10.4	7	14.3	8.3	2	4.8	9.8	2.9	1.4		in^{12}CO
18316−0602										0.86	
18455−0149				81.5	2.2	5.7	81.8	2.4	1.4		
19374+2352	35.4	7.3	15.7	37	3.3	3.9	36.7	4.16	2.2		Maybe
20056+3350				9	3	4	9	3.5	1.9	<0.06	
20188+3928	4.7	8.5	27.5	1.5	2.6	6.2	2.2	3.2	4.1	0.16	Yes
20275+4001										0.45	
21078+5211	−5.5	3	35.4	−6.6	2.4	4.7	−6.8	3.9	4.2	1.0	Maybe
21432+4719	3		<1								
22142+5206				−37.6	1.5	3.5					
22198+6336	−10.5	6	13.8	−11	2	4.4	−10.5	3	0.9	0.16	Yes
22475+5939				−51	3.1	1.8				<0.06	
23314+6033	−45	5	28	−45	2	4.3					Yes

Table 3.5. Methyl cyanide and propyne line data. Upper limits are 2σ.

		18032−2137		18164−1631		18273+0113		18316−0602		18455−0149		19374+2352		20056+3350	
		T_A^*/K	Δν/MHz	T_A^*	Δν	T_A^*	Δν	T_A^*	Δν	T_A^*	Δν	T_A^*	Δν	T_A^*	Δν
CH_3CN	K=0	0.315	4.80	0.075	1.87	<0.034		0.215	5.50	0.045	2.57	<0.028		<0.024	
	1	0.270		0.050				0.185		<0.026					
	2	0.197		0.033				0.136							
	3	0.158		0.035				0.130							
	4	0.081		0.020				0.105							
	5	0.090		<0.034				0.066							
	6	0.050						0.060							
	7	<0.036						0.028							
	8							0.015							
CH_3CCH	0	0.770	3.10	0.235	2.25	<0.048		0.289	3.10	<0.026		0.081	2.60	0.113	2.60
$J = 14 \rightarrow 13$	1	0.680		0.196				0.247				0.045		0.092	
	2	0.399		0.120				0.175				0.032		0.032	
	3	0.374		0.085				0.148				0.028		0.041	
	4	0.092		0.025				0.045				0.014		<0.024	
CH_3CCH	0	0.203	3.50	<0.054				0.155							
$J = 20 \rightarrow 19$	1	0.180						0.129							
	2	0.132						0.063							
	3	0.157						0.062							
	4	0.029						<0.040							
	5	<0.050													

Table 3.5 *continued* Methyl cyanide and propyne line data. Upper limits are 2σ.

		20188 FIR1		20188 FIR2		20275+4001		21078+5211		22198+6336		22475 FIR1		22475 FIR2	
		T_A^*/K	Δν/MHz	T_A^*	Δν	T_A^*	Δν	T_A^*	Δν	T_A^*	Δν	T_A^*	Δν	T_A^*	Δν
CH_3CN	K=0	<0.032		<0.036		0.158	3.30	0.165	3.82	<0.024					
	1					0.150		0.145							
	2					0.110		0.090							
	3					0.135		0.095							
	4					0.086		0.018							
	5					0.053		0.019							
	6					0.066		<0.034							
	7					0.049									
	8					<0.030									
CH_3CCH	0	<0.032		<0.036		0.306	2.60	0.312	3.00	<0.024					
$J = 14 \rightarrow 13$	1					0.252		0.268							
	2					0.145		0.129							
	3					0.102		0.127							
	4					0.030		0.048							
CH_3CCH	0	<0.062		0.088	2.0	<0.14		0.120	3.50	<0.064		<0.046		<0.046	
$J = 20 \rightarrow 19$	1			0.033				0.129							
	2			0.085				0.065							
	3			0.068				0.052							
	4			0.052				0.050							
	5			<0.060				0.034							

Table 3.5 *continued* Methyl cyanide and propyne line data. Upper limits are 2σ.

		22506+5944		23314+6033		00338+6312		00420+5530	
		T_A^*/K	Δν/MHz	T_A^*	Δν	T_A^*	Δν	T_A^*	Δν
CH_3CN	K=0	<0.026		<0.028				<0.040	
CH_3CCH	0	0.050	2.85	<0.028				<0.040	
$J = 14 \rightarrow 13$	1	0.039							
	2	<0.026							
CH_3CCH	0					<0.046			
$J = 20 \rightarrow 19$									

Table 3.6. VLA 22-GHz Spectral Line Observations.

	R.A. (1950)	Dec. (1950)	Flux (Jy)	v_{LSR} (km s^{-1})
00420+5530	00 42 06.15	55 30 23.8	0.45	−45
G14.45−0.11			<0.05	
18273+0113	18 27 17.44	01 13 15.6	0.74	35
18316−0602	18 31 40.15	−06 02 05.4	109	45
			0.23	74
18455−0149	18 45 34.86	−01 48 51.2	1.01	82
19374+2352	19 37 27.69	23 52 52.2	0.19	34
20056+3350	20 05 35.70	33 50 55.8	0.46	10
	20 05 35.76	33 50 55.8	0.28	2
20188+3928	20 18 49.79	39 28 46.7	3.20	7
	20 18 50.81	39 28 37.6	0.21	4
21007+4951	21 00 44.70	49 51 15.2	0.07	−1
21078+5211	21 07 46.65	52 10 22.8	6.53	−5
21432+4719			<0.05	
22506+5944	22 50 38.66	59 44 52.6	21.6	−53
	22 50 38.36	59 44 54.5	2.16	−53
	22 50 38.74	59 44 53.3	5.26	−53
22528+5936			<0.05	
22539+5758			<0.05	
23314+6033	23 31 22.73	60 33 54.2	0.14	−54

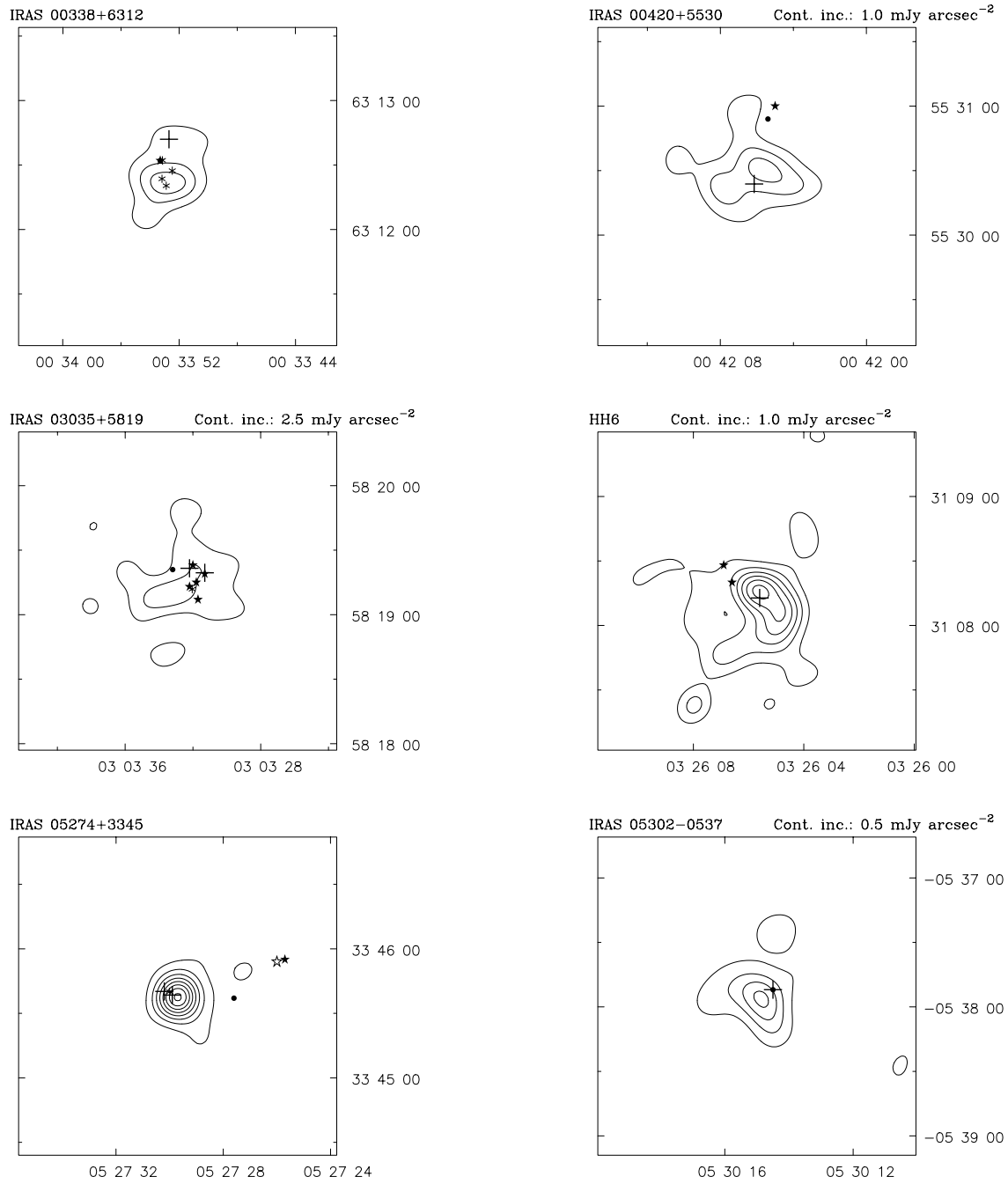

Figure 3.1. 850-μm continuum maps. For these maps the following key for the symbols is used: Cross – water maser, filled circle – *IRAS* source, asterisk – radio source, filled star – near-infrared source, open star – far-infrared source and filled square – OH maser. All the maps have been re-convolved with a 12-arcsec Gaussian. These continuum maps have linear contours every 5 mJy arcsec^{-2} (excluding the zero level contour) unless otherwise stated. The size of the cross gives no indication of the accuracy of the position.

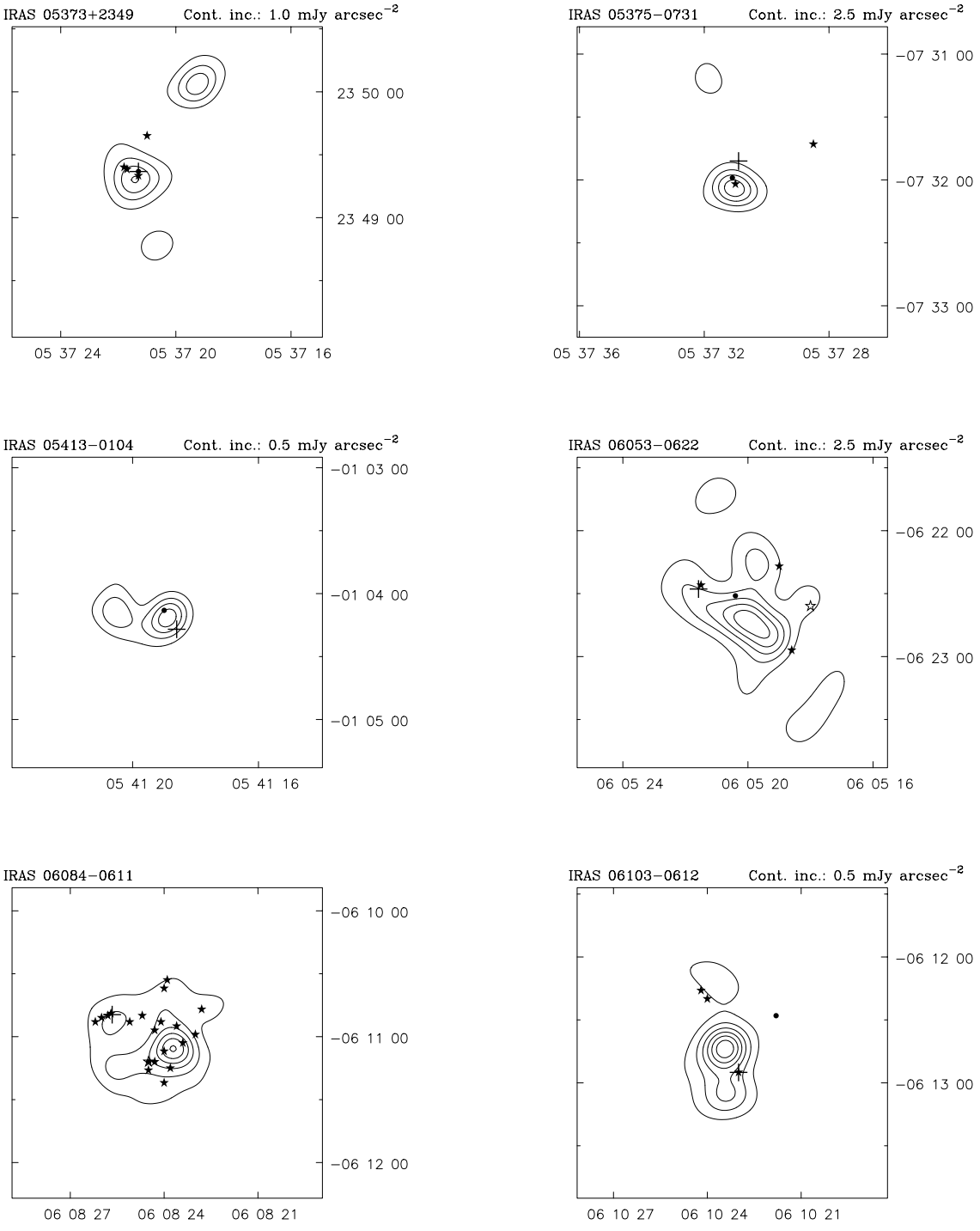

Figure 3.1 *continued* 850-μm continuum maps.

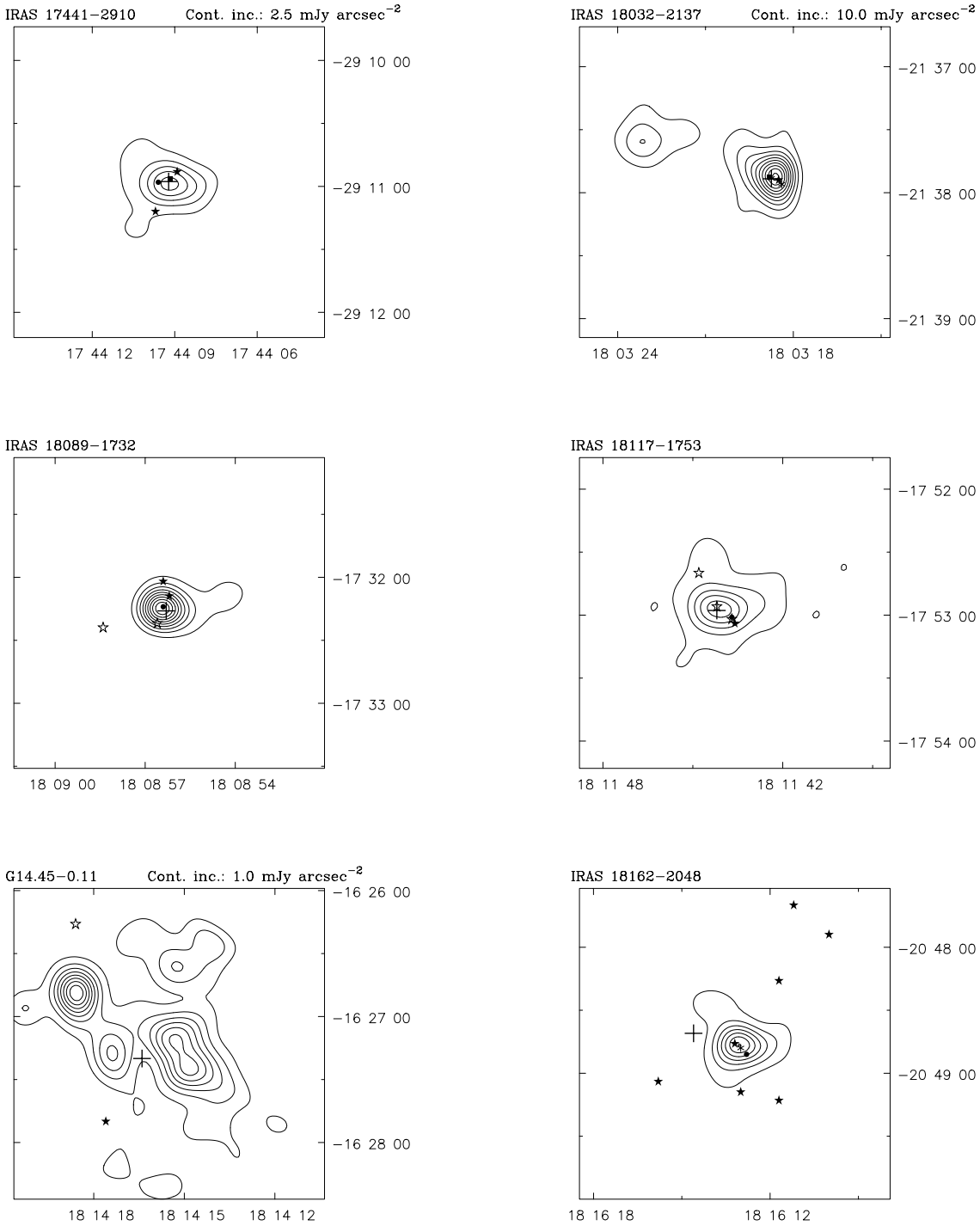

Figure 3.1 *continued* 850-μm continuum maps.

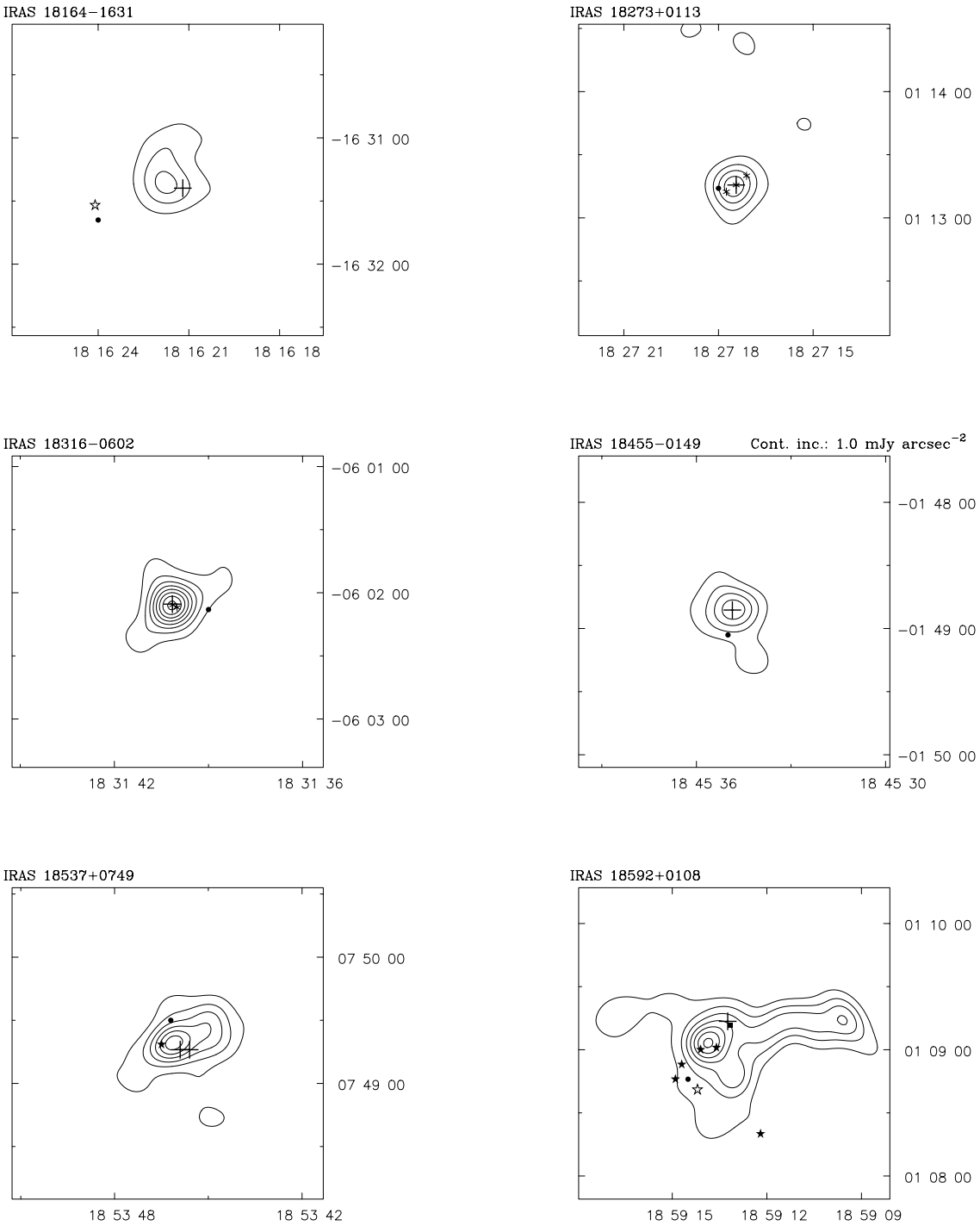

Figure 3.1 *continued* 850-μm continuum maps.

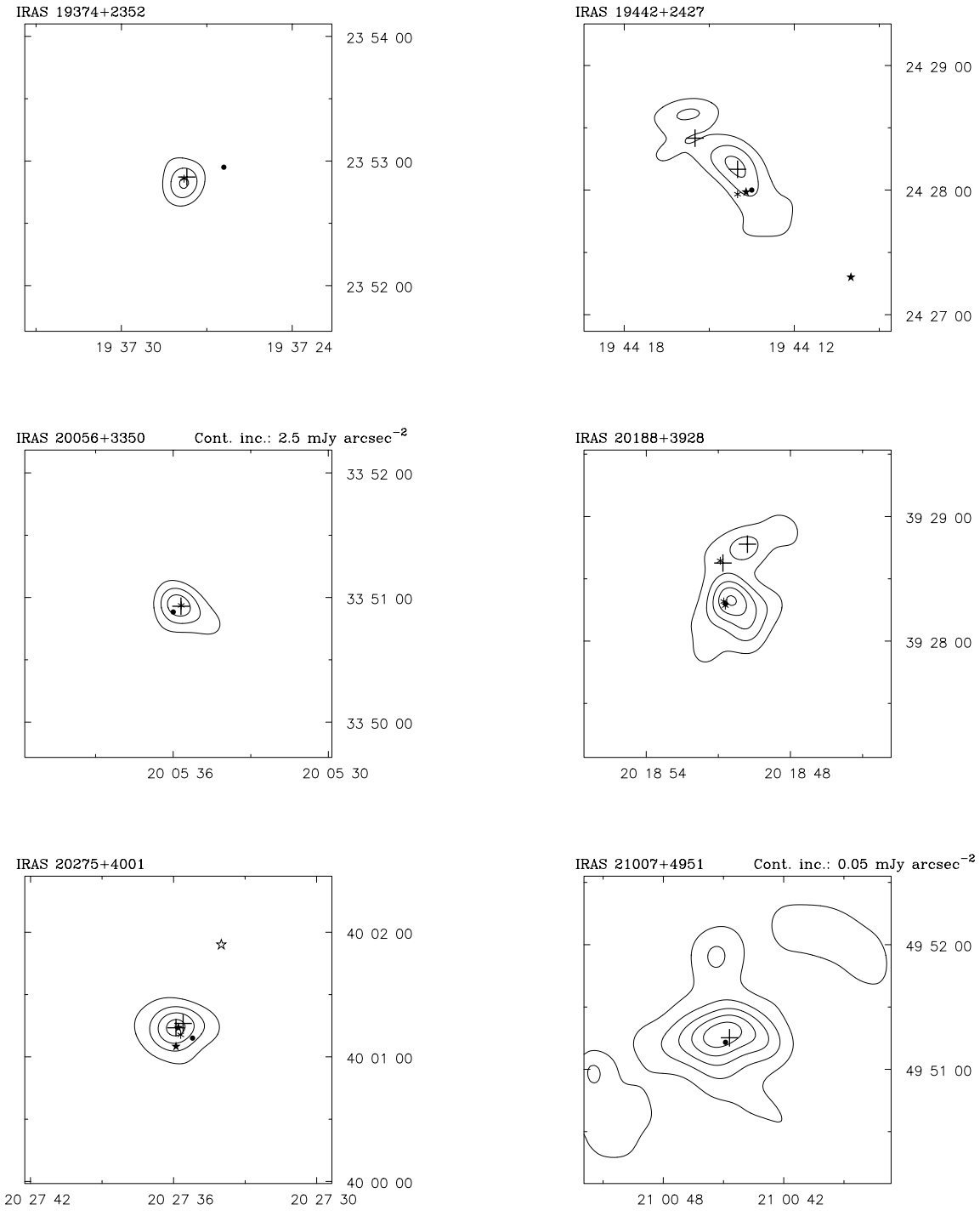

Figure 3.1 *continued* 850-μm continuum maps.

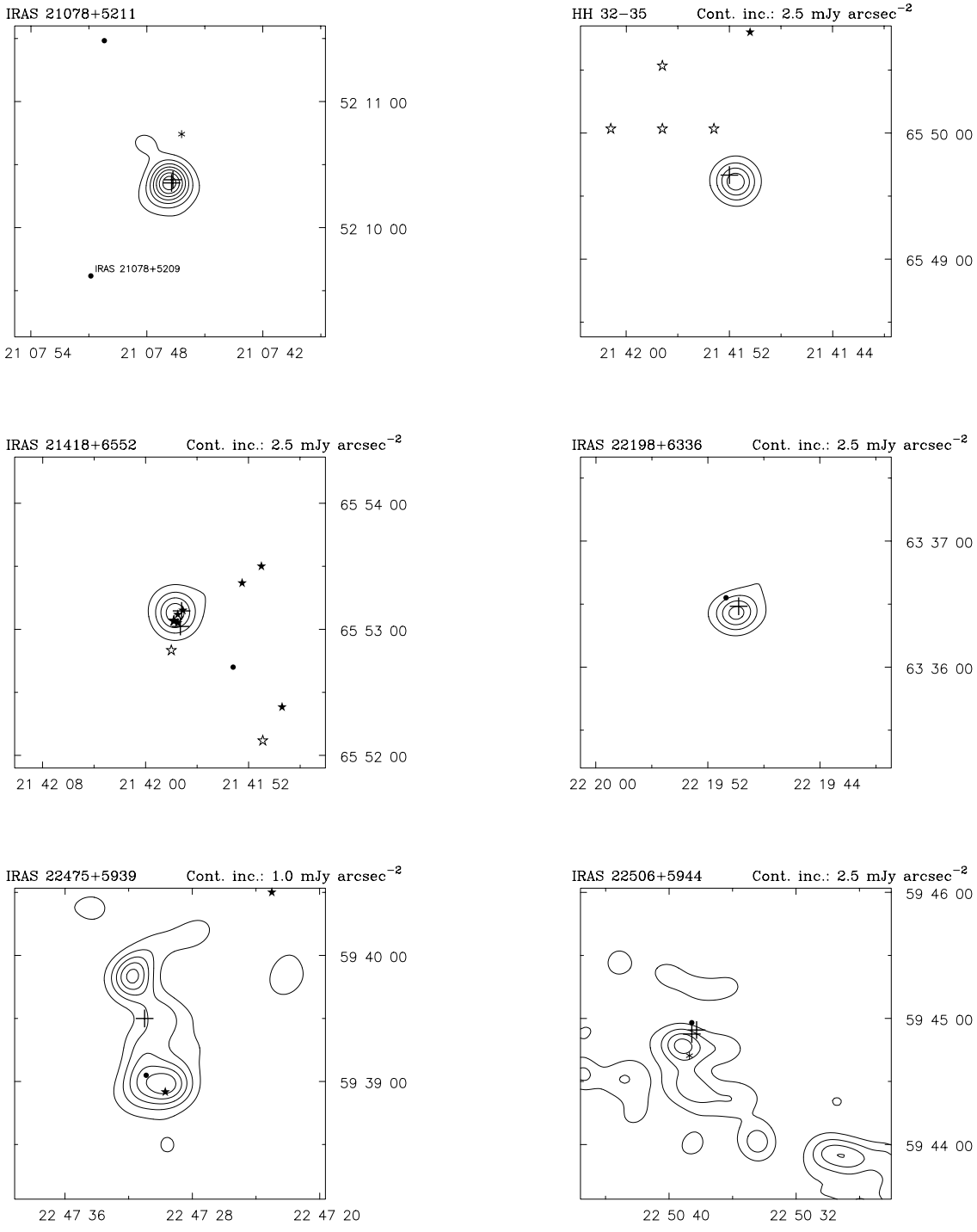

Figure 3.1 *continued* 850-μm continuum maps.

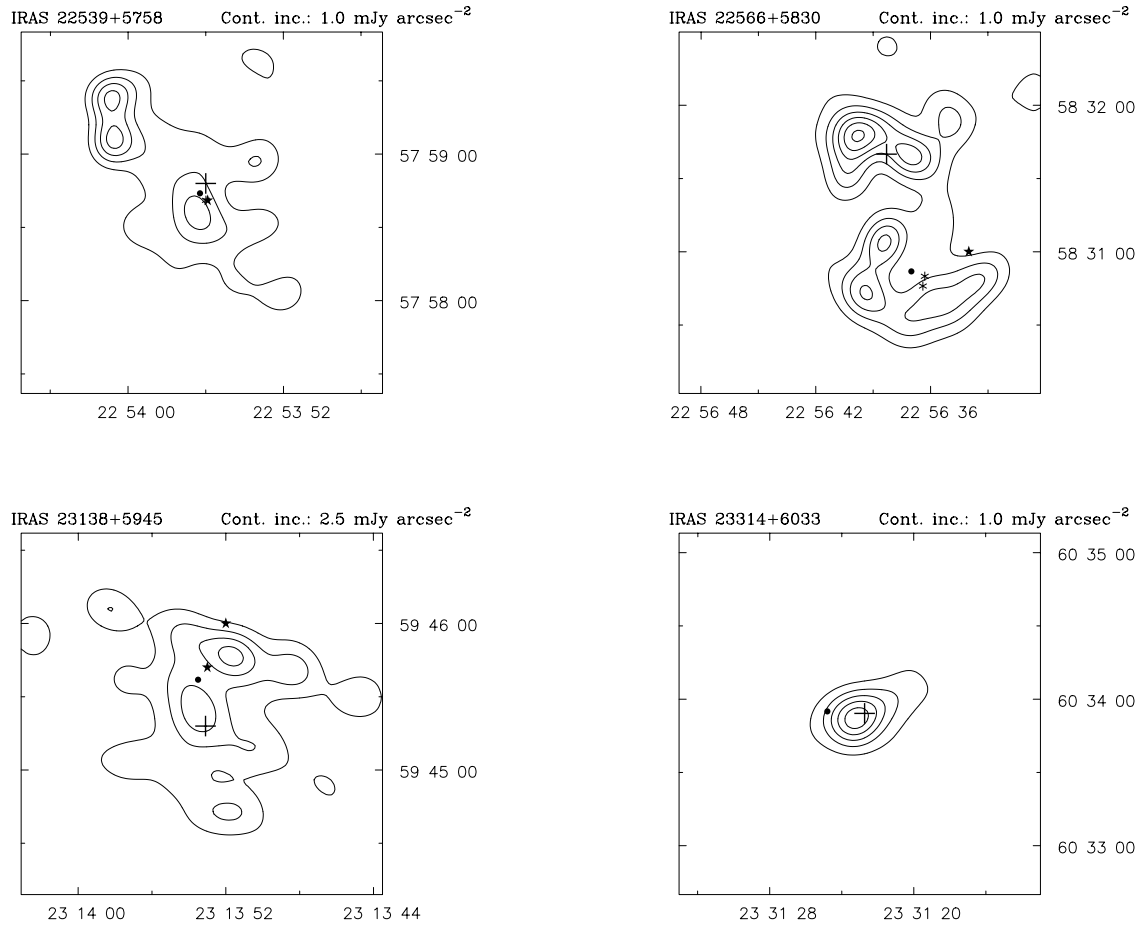

Figure 3.1 *continued* 850-μm continuum maps.

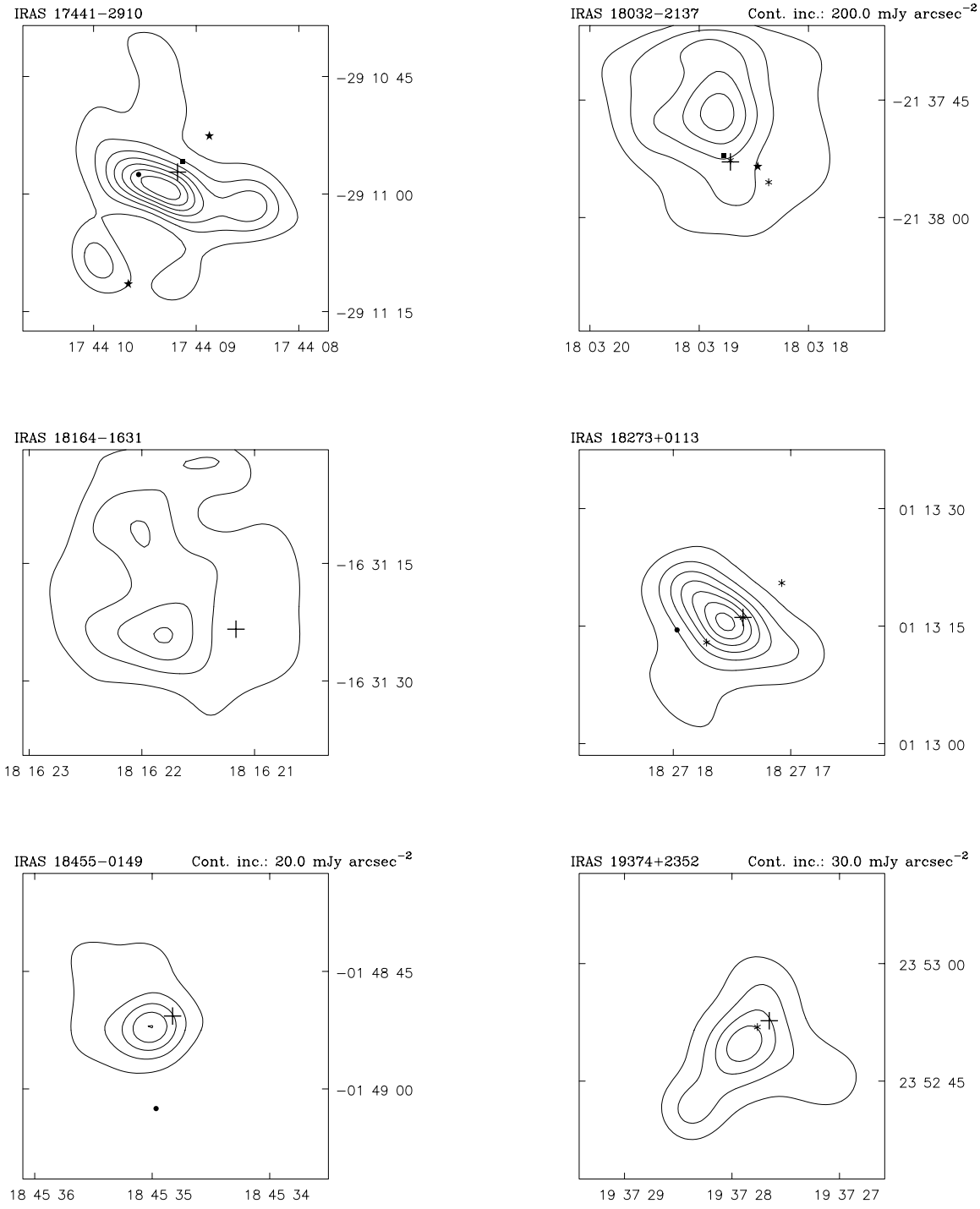

Figure 3.2. 450-μm high-resolution continuum maps. Contours are every 50 mJy arcsec^{-2} (excluding the zero level contour) unless specified otherwise.

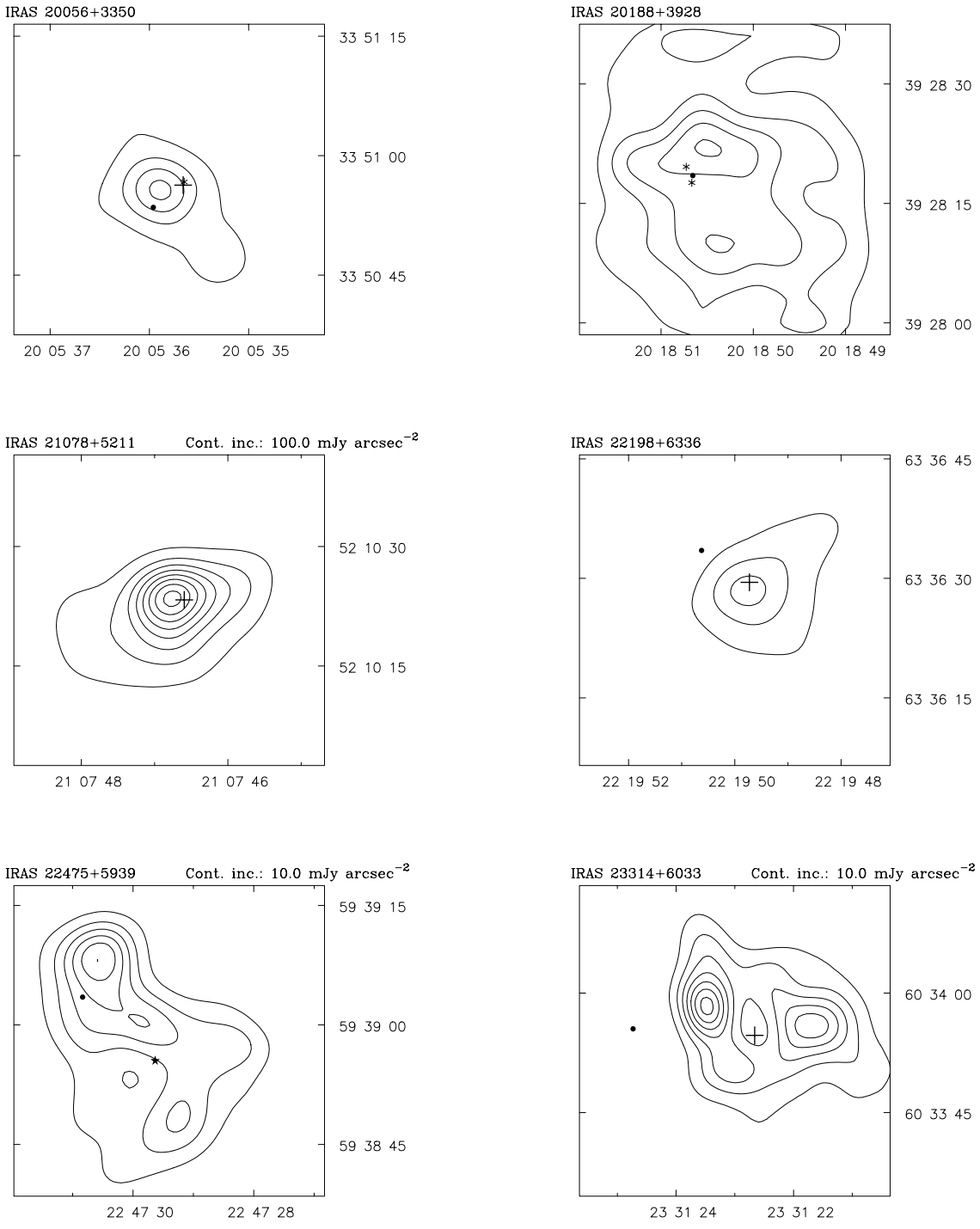

Figure 3.2 *continued* 450-μm high-resolution continuum maps.

a)

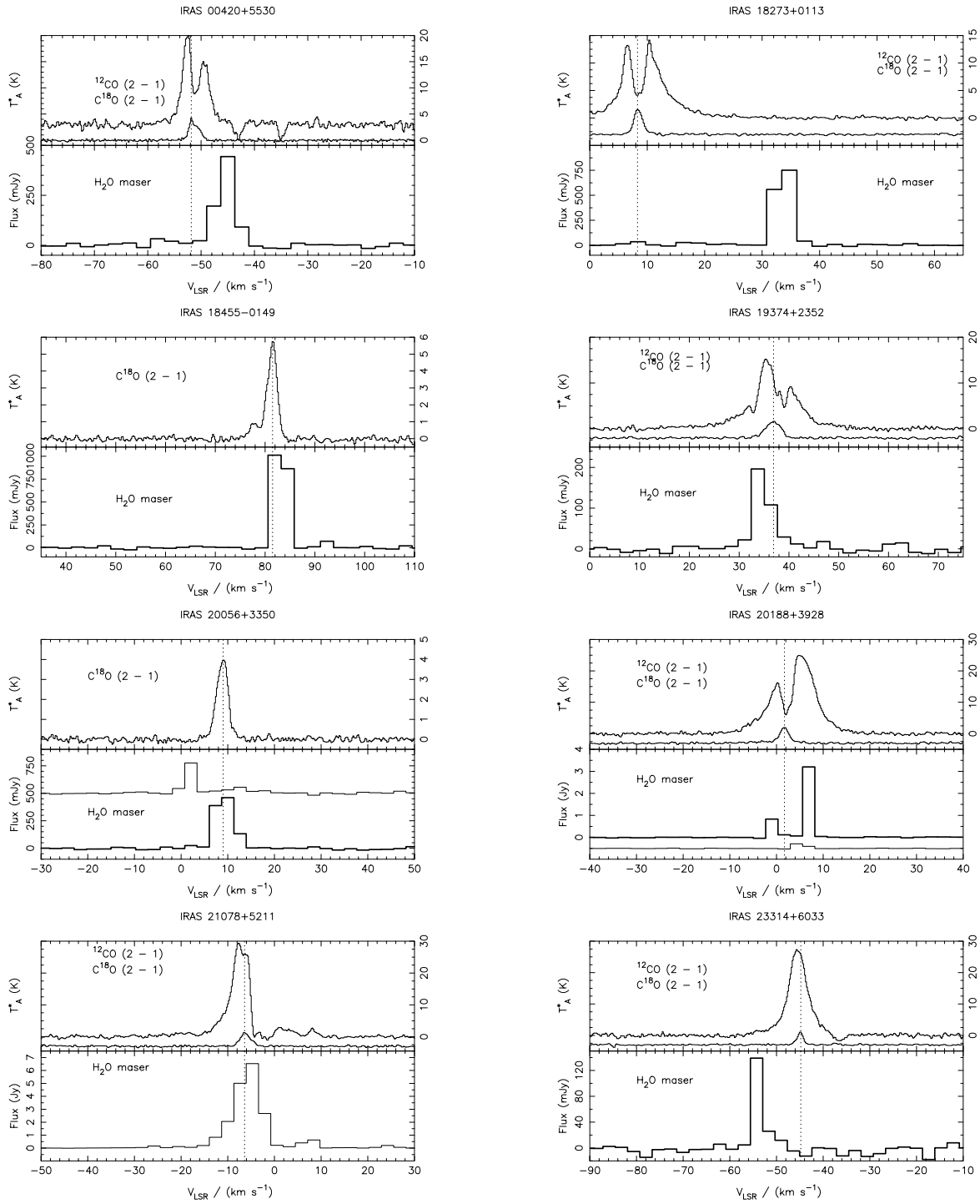

Figure 3.3. Sample spectra: (a) Sources with maser and CO spectra

b)

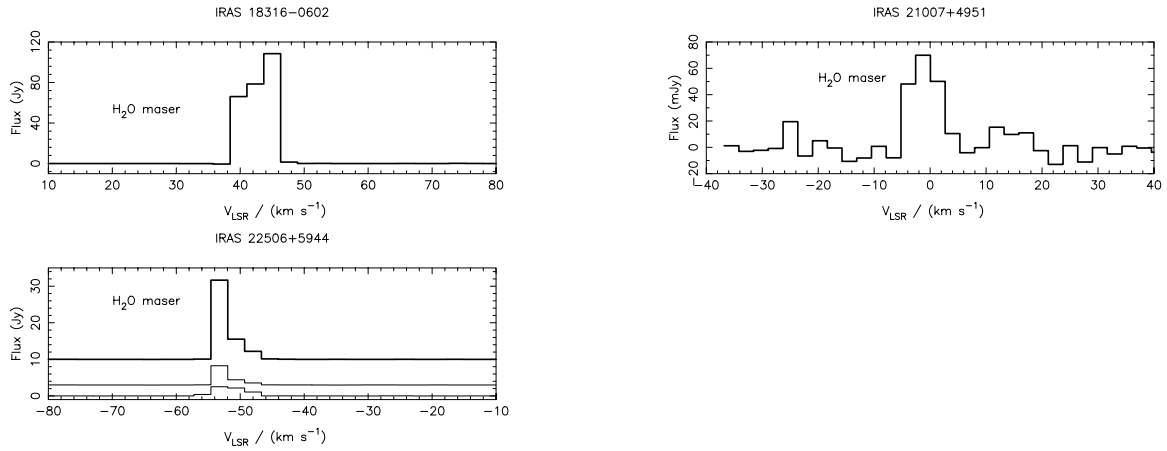

c)

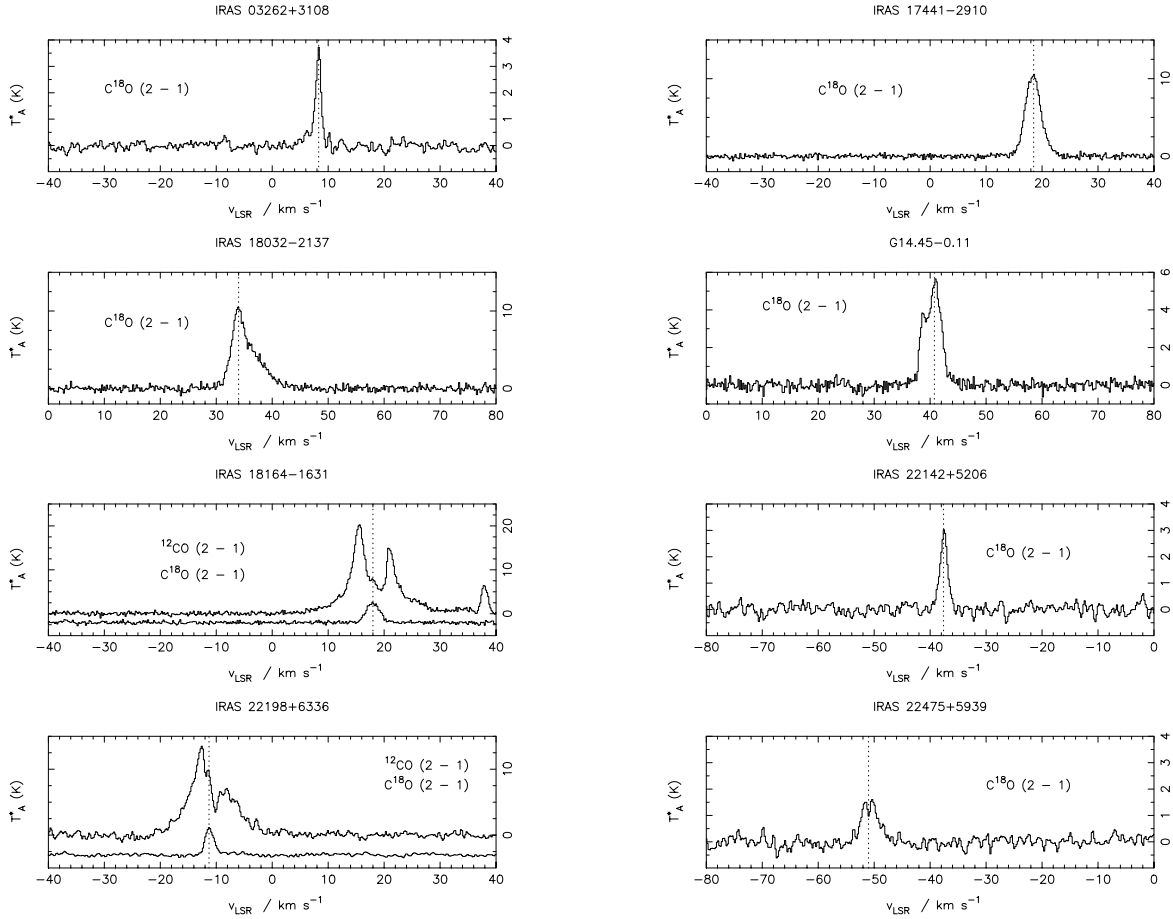

Figure 3.3 *continued* Sample spectra: (b) Sources with maser spectra only, (c) Sources with only CO spectra available.

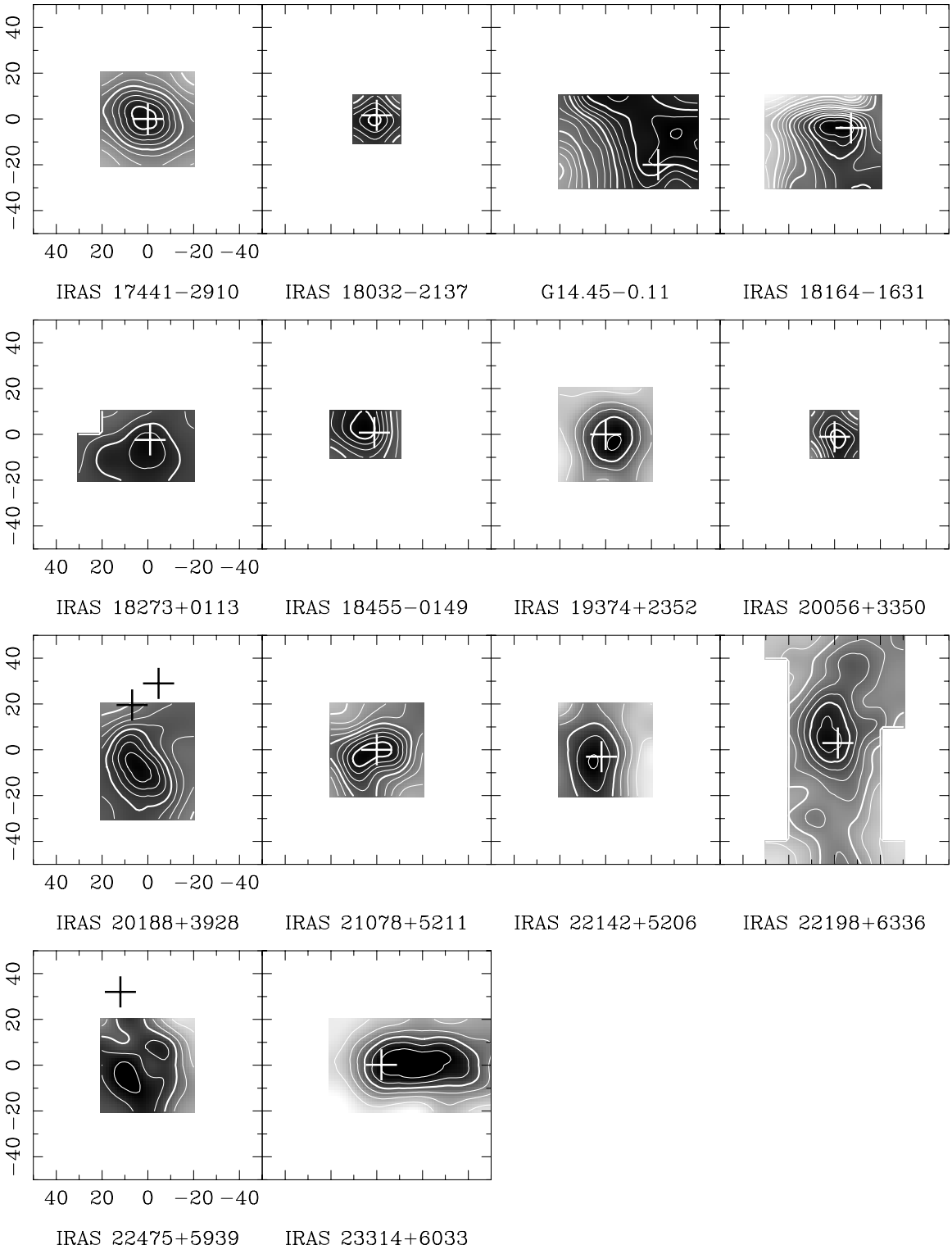

Figure 3.4. $C^{18}O$ maps of integrated intensity. Contours levels are at 1.0 K km s^{-1} except for 17441−2910, 18032−2137 and 19374+2352, which have contour levels of 3.0 K km s^{-1}. For clarity only the water masers are shown without any indication of positional errors. Map centres are as listed in Table 3.1.

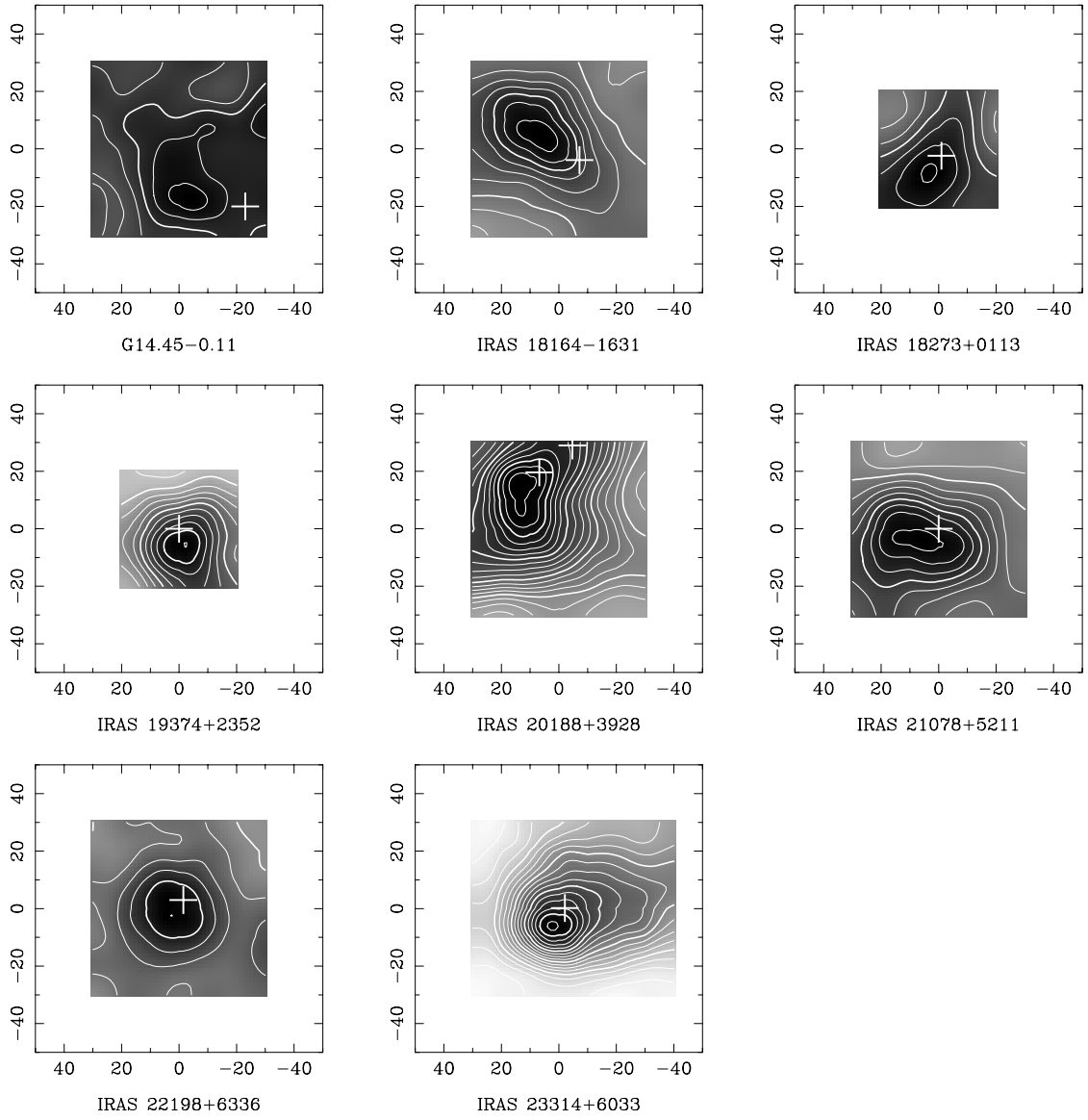

Figure 3.5. ^{12}CO maps of integrated intensity. Contours levels are at 10.0 K km s^{-1}. For clarity only the water masers are shown. The crosses give no indication of the positional errors of the masers which are all better than 5 arcsec. Map centres are as listed in Table 3.1.

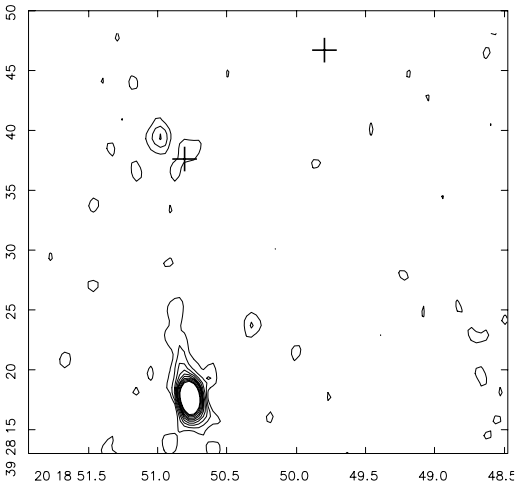

IRAS 20188+3928
Contours are every 0.5 mJy beam^{-1} beginning at 0.5 mJy beam^{-1}

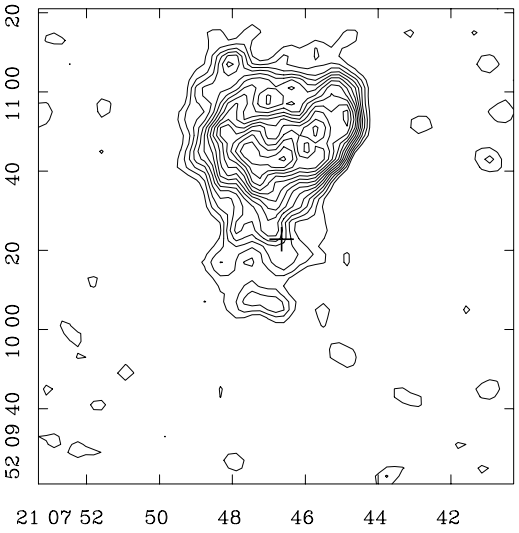

IRAS 21078+5211
Contours are every 0.31 mJy beam^{-1} beginning at 0.31 mJy beam^{-1}

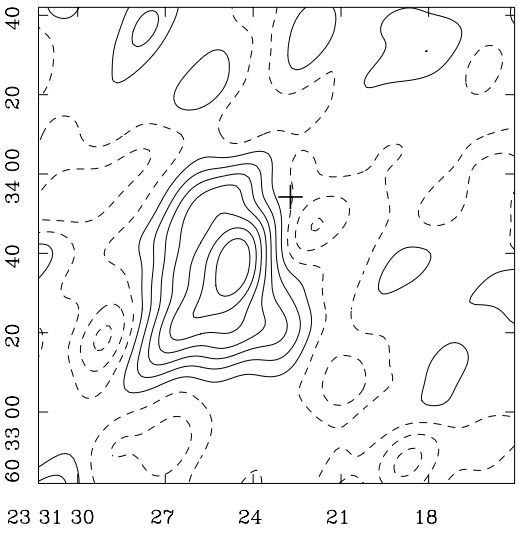

IRAS 23314+6033
Contours are every 0.66 mJy beam^{-1} beginning at -1.5 mJy beam^{-1}

Figure 3.6. RT high-resolution maps. Water masers are indicated by crosses.

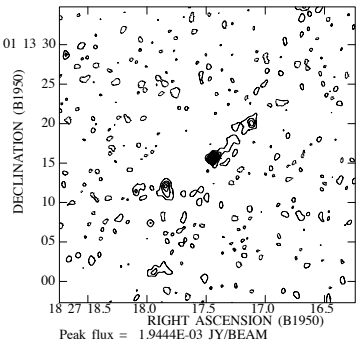

a) IRAS 18273+0113

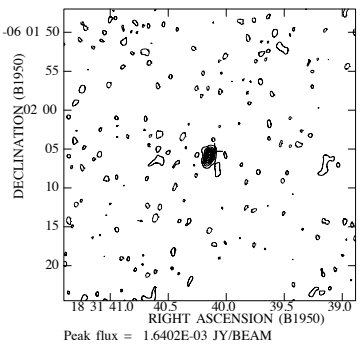

b) IRAS 18316–0602

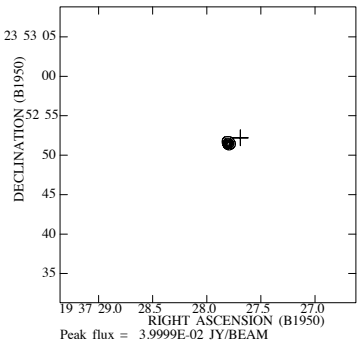

c) IRAS 19374+2352

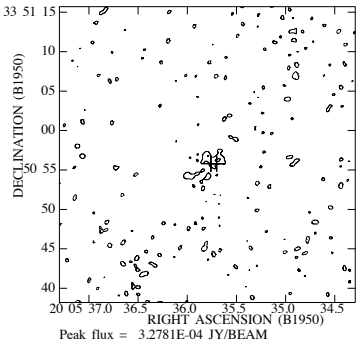

d) IRAS 20056+3350

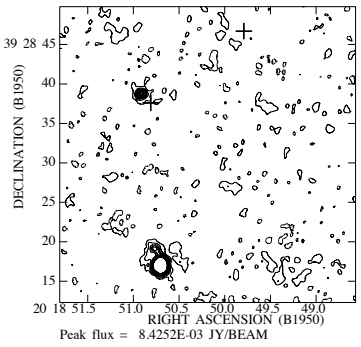

e) IRAS 20188+3928

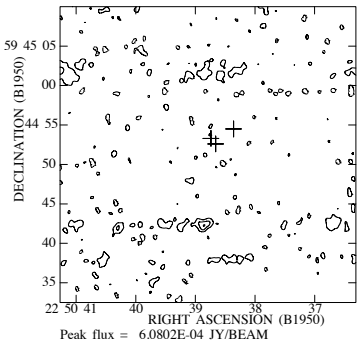

f) IRAS 22506+5944

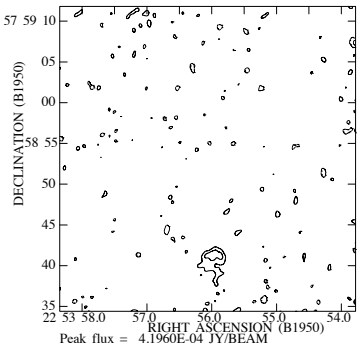

g) IRAS 22539+5758

Figure 3.7. VLA 8-GHz continuum maps of the detected sources. Our water maser positions are marked with crosses. Contour levels are every 5 mJy beam^{-1} for (c), 0.2 mJy beam^{-1} for (a), (b), (e) and (f) and 0.15 mJy beam^{-1} for (d) and (g). The noise level for these maps is approximately 0.1 mJy beam^{-1}.

3.2 Derived parameters

I now go on to derive estimates of the physical conditions in the vicinity of the maser sources using the data presented in the previous section. The global properties of these data are discussed in the following chapter and in detail, for some sources, in chapter 5. So that the origin of these numbers can be appreciated a small digression is required into the theory of radiative transfer.

3.2.1 Radiative transfer

The equation governing the transfer of radiation of specific intensity I_ν (in units of W m^{-2} Hz^{-1} sr^{-1}) along a path s through a medium can be written

$$\frac{dI_\nu}{ds} = -\kappa_\nu I_\nu + \varepsilon_\nu, \tag{3.1}$$

where ε_ν and κ_ν are the emission and absorption coefficients of the medium, respectively. This equation may be integrated for the case of incident radiation, I_o passing through a homogeneous cloud of length L and temperature T,

$$\int_{I_o}^{I_\nu} \frac{dI}{\frac{\varepsilon_\nu}{\kappa_\nu} - I} = \kappa_\nu \int_0^L ds \tag{3.2}$$

obtaining an emergent intensity of

$$I_\nu = I_o e^{-\tau} + (1 - e^{-\tau})\Sigma_\nu, \tag{3.3}$$

where the source function, Σ_ν, is given by $\Sigma_\nu = \varepsilon_\nu/\kappa_\nu$ and the optical depth $\tau = \kappa_\nu L$.

3.2.2 Continuum emission from dust

In the case of radiative transfer through dust the absorption coefficient is best written as the dust number density times the dust absorption cross-section i.e. $\kappa_\nu = n(\text{dust})\sigma(\nu)$. Unlike the case for line radiation described in subsection 3.2.3 the absorption coefficient is independent of temperature. For wavelengths smaller than the typical grain size the dust cross-section is equal to the geometric limit of twice the physical cross-section. At wavelengths longer than the typical grain size, the cross-section falls as $\sigma \propto \lambda^{-\beta}$, with $\beta \approx 1$ the observed law in the optical and near-infrared, and $\beta = (1 \rightarrow 2)$ in the far-infrared and millimeter range (see e.g. Emerson 1988). The theoretical limit at long wavelengths for crystalline materials is $\beta = 2$, but the precise value of β depends on the grain material and can be as high as 4.

Using equation (3.3) and assuming the emission comes from an homogeneous cloud of uniform dust temperature T_d, the observed brightness distribution of an object, $I_\nu(\Omega)$, is given by a grey-body spectrum:

$$I_\nu(\Omega) = (1 - e^{-\tau_\lambda(\Omega)}) B_\nu(\nu, T_d), \tag{3.4}$$

where background emission, I_o, has been neglected and $B_\nu(\nu,T)$ is the Planck function and is equal to the source function using Kirchoff's law. The Planck function can be written in terms of the Rayleigh-Jeans brightness temperature, J,

$$B_\nu(\nu,T) = \frac{2kJ(\lambda,T)}{\lambda^2} \tag{3.5}$$

$$J(\lambda,T) = \left(\frac{h\nu}{k}\right)\frac{1}{\exp(h\nu/kT)-1}. \tag{3.6}$$

To derive gas masses it has been assumed that the gas column density is proportional to the dust optical depth. This relation must be calibrated on a representative set of objects and it must then be assumed that this relation holds for all molecular clouds. Adopting the Hildebrand (1983) assumptions, the dust optical depth can be written as

$$\tau_\lambda = 8.3\times10^{-4}\left(\frac{\lambda}{400\ \mu\mathrm{m}}\right)^{-\beta}\left[\frac{N(\mathrm{H}+\mathrm{H_2})}{10^{26}\ \mathrm{m}^{-2}}\right] \tag{3.7}$$

$$= \left(\frac{\lambda_c}{\lambda}\right)^{\beta}, \tag{3.8}$$

where solar metallicities have been assumed and λ_c, the critical wavelength, is that at which the optical depth is 1. For submm continuum observations the emission is optically thin for all but the densest protostellar condensations (e.g. emission at 350 μm is expected to be optically thin for visual extinctions less than 5000 mag). Under this assumption equation (3.4) reduces to

$$I_\nu(\Omega) = B_\nu(\nu,T_d)\tau_\lambda(\Omega). \tag{3.9}$$

By integrating this over solid angle and using equation (3.7), an estimate of the gas mass associated with a total dust flux of $S_\nu = \int I_\nu(\Omega)d\Omega$ can be obtained:

$$\frac{M_{tot}}{\mathrm{M}_\odot} = 7.2\left(\frac{S_\nu}{\mathrm{Jy}}\right)\left(\frac{\lambda}{400\ \mu\mathrm{m}}\right)^{2+\beta}\left(\frac{D}{\mathrm{kpc}}\right)^2\left[\frac{J(\lambda,T_d)}{\mathrm{K}}\right]^{-1}, \tag{3.10}$$

where D is the distance to the source and this equation has been corrected for the cosmic abundance of helium (c.f. Richer 91).

3.2.3 Line emission from molecular clouds

The bulk of the molecular gas in regions of star formation is generally cool ($T \leq 100$ K) and the only quantum levels which are thermalized, other than nuclear spin transitions and the electronic fine structure lines of some atoms, are the molecular rotational ladders. Since the most abundant molecule in molecular clouds, hydrogen, is homopolar and cannot undergo electric dipole transitions, polar trace molecules must be used to find the properties of clouds.

Two types of molecules have been used for this thesis. Linear diatomic molecules, such as carbon monoxide, with their simple rotational ladders are good density probes, and symmetric top molecules,

such as propyne (CH_3CCH), with several radiatively uncoupled energy ladders, act as good thermometers. The rotational levels are characterized by the total angular momentum quantum number, J, and the component of J along the principal axis, K, and there are $(2J+1)$ K states per J level. In order to conserve angular momentum the selection rules for these transitions is ($\Delta J = 0, \pm 1, \Delta K = 0$) and radiative transitions between K-levels are forbidden. This means that the relative populations between K-levels depend primarily on the kinetic temperature of the colliding particles. For diatomic molecules K is always zero and the problem is much simplified.

For line radiation, let us a consider a two level system with populations n_u and n_l and degeneracies g_u and g_l, where u and l signify the upper and lower states. The emission and absorption coefficients are then related to the Einstein A and B coefficients through

$$\varepsilon_\nu = \frac{h\nu_{ul}}{4\pi} A_{ul} n_u \phi(\nu) \tag{3.11}$$

$$\kappa_\nu = \frac{h\nu_{ul}}{c} (n_l B_{lu} - n_u B_{ul}) \phi(\nu) \tag{3.12}$$

where $\phi(\nu)$ is the line shape function and gives the fraction of photons emitted with frequencies $\nu \rightarrow \nu + d\nu$, and is normalised such that $\int \phi(\nu) d\nu = 1$. For consistency with the Planck radiation law the Einstein A and B coefficients must satisfy

$$B_{lu} g_l = B_{ul} g_u \tag{3.13}$$

$$A_{ul} = \frac{8\pi h \nu_{ul}^3}{c^3} B_{ul}, \tag{3.14}$$

and defining the excitation temperature, $T_{\rm ex}$ of the transition with Boltzmann statistics by

$$\frac{n_u}{n_l} = \frac{g_u}{g_l} \exp\left(\frac{-h\nu_{ul}}{kT_{\rm ex}}\right), \tag{3.15}$$

allows the emission and absorption coefficients to be rewritten as

$$\varepsilon_\nu = \frac{hc}{4\pi} A_{ul} n_u(\nu) \tag{3.16}$$

$$\kappa_\nu = \frac{A_{ul} c^3}{8\pi \nu_{ul}^3} \frac{g_u}{g_l} \left[1 - \exp\left(-\frac{h\nu_{ul}}{kT_{\rm ex}}\right)\right] n_l(\nu), \tag{3.17}$$

where the populations have now been written as number density per unit velocity interval using the Doppler relation, $d\nu = c/\nu \, d\nu$. Using equations (3.15), (3.16) and (3.17) the source function can now be written as

$$\Sigma_\nu = \frac{2h\nu^3}{c^2} \left[\exp\left(\frac{h\nu_{ul}}{kT_{\rm ex}}\right) - 1\right]^{-1}. \tag{3.18}$$

In full thermodynamic equilibrium (a very rare occurrence in molecular clouds) all the levels are thermalized at the gas kinetic temperature ($T_{\rm ex} = T_{\rm kin}$) and Kirchoff's Law applies. For this assumption the source function is then equal to the Planck function B_ν (equation 3.5).

With this information it is now possible to apply these equations to astrophysical systems. The general solution of the radiative transfer problem for a given temperature and velocity structure is extremely difficult, requiring the self-consistent solution of level populations and the radiative transfer equation. Approximate numerical methods have been employed, such as the large velocity gradient model of Goldreich & Kwan (1974), but in this thesis no such modeling is used and the line data are analysed assuming the optically thick and thin limits and local thermodynamic equilibrium.

For $\tau \gg 1$ equation (3.3) reduces to $I_\nu = B_\nu(\nu, T_{\rm ex})$ and the object appears as a black body of temperature $T_{\rm ex}$. The observed line temperature $T_R = \lambda^2 I_\nu/(2k)$ then gives an estimate of the excitation temperature, which is normally a lower limit to the kinetic temperature,

$$T_{\rm ex} = \frac{h\nu}{k}\frac{1}{\ln[1+(h\nu/kT_R)]}. \tag{3.19}$$

For $\tau \ll 1$ the probability of a photon being absorbed within the cloud is small. Neglecting the background radiation I_ν, the emergent line intensity from a homogeneous cloud of optical depth $\tau = \kappa L$ is then given by,

$$I_\nu = \frac{2kT_R}{\lambda^2} = \tau_\nu \Sigma_\nu = \varepsilon L. \tag{3.20}$$

Substituting in for ε (equation 3.16) one can obtain an expression for the line intensity:

$$T_R(\mathrm{v}) = \frac{hA_{ul}\lambda^2 c}{8\pi k} N_u(\mathrm{v}), \tag{3.21}$$

where $N_u(\mathrm{v}) = Ln_u(\mathrm{v})$ is the column density per unit velocity interval in the upper state. Therefore in the optically thin limit the observed line intensity is simply proportional to the population in the upper state and the spontaneous emission rate from the upper to the lower state. This lower limit to the population of the upper state is independent of the excitation temperature.

The rotational electric dipole moment μ_e determines the coupling of the molecule to the radiation field through the Einstein A coefficient, and is given by

$$A_{ul} = \frac{16\pi^3}{3\varepsilon_0 hc^3}\mu_e^2 \frac{S_{ul}}{g_u}\nu_{ul}^3, \tag{3.22}$$

where S_{ul} is the oscillator strength. Substituting for the Einstein A coeficient and integrating equation (3.21) over velocity allows the column density in the upper state to be written as

$$N_u^{column} = \left(\frac{3\varepsilon_0 k}{2\pi^2\mu_e^2\nu_{ul}}\right)\frac{g_u}{S_{ul}}\int T_R(\mathrm{v})d\mathrm{v}. \tag{3.23}$$

Integrating this expression over solid angle then gives the *total* number of molecules in the upper state of

$$N_u^{total} = \left(\frac{3\varepsilon_0 kD^2}{2\pi^2\mu_e^2\nu_{ul}}\right)\frac{g_u}{S_{ul}}\int\int T_R(\Omega,\mathrm{v})d\mathrm{v}d\Omega. \tag{3.24}$$

To obtain the total number of these molecules in the cloud the fractional population of the upper state must be estimated. By employing Boltzmann statistics

$$\frac{N_u}{N_{tot}} = \frac{g_u e^{-E_u/kT_{\rm ex}}}{Z}, \tag{3.25}$$

where Z is the partition function. Substituting this into equation (3.23) gives the total column density for the molecule of

$$N_{tot}^{column} = \left(\frac{3\varepsilon_0 k}{2\pi^2 \mu_e^2 \nu_{ul}}\right) \frac{Z}{S_{ul}} e^{E_u/kT_{\rm ex}} \int T_R(\nu) d\nu. \tag{3.26}$$

At this point my treatment of diatomic and symmetric top molecules diverges slighlty and will be dealt with separately.

Linear diatomic molecules

Since for linear diatomic molecules the angular momentum is quantized according to $L^2 = J(J+1)\hbar^2$ the energy levels can be written as

$$E_J = \frac{J(J+1)\hbar^2}{2I} = BhJ(J+1) \tag{3.27}$$

where I is the principal moment of inertia, $B = h/8\pi^2 I$ is the rotational constant and it is assumed that no molecular distortion occurs. The energy difference between transitions is then

$$\Delta E_{J+1\rightarrow J} = 2Bh(J+1), \tag{3.28}$$

and hence the frequencies of the transitions are directly related to the $J = 1 \rightarrow 0$ frequency by $\nu_{J+1\rightarrow J} = (J+1)\times\nu_{10}$. The energy levels can now be written in terms of this frequency,

$$E_J = \frac{J(J+1)h\nu_{10}}{2} = \frac{J(J+1)kT_0}{2}, \tag{3.29}$$

where $T_0 = h\nu_{10}/k$ is the energy of the $J = 1$ level above ground state.

Assuming that local thermodynamic equilibrium (LTE) is applicable (i.e. $T_{\rm ex}(J) = T_{\rm kin} \forall J$) and with this knowledge of energy levels, it is now possible to estimate a partition function.

$$Z = \sum_{J=0}^{\infty} (2J+1) e^{-J(J+1)T_0/2T_{\rm ex}} \tag{3.30}$$

$$\approx \frac{2T_{\rm ex}}{T_0} \quad \text{for} \quad T_{\rm ex} \gg T_0 \tag{3.31}$$

For these simple molecules the oscillator strength is given by

$$S_{J+1\rightarrow J} = J+1, \tag{3.32}$$

and substituting this and equations (3.29) and (3.31) into equation (3.26) gives a final estimate for the total column density in a particular molecular species of

$$N_{All\ states}^{column} = \left(\frac{3\varepsilon_0 k^2}{h\pi^2\mu_e^2\nu_{10}^2}\right)\frac{T_{\rm ex}e^{(J+1)(J+2)T_0/2T_{\rm ex}}}{(J+1)^2}\int T_R(\nu)d\nu, \tag{3.33}$$

where frequencies have been written in terms of ν_{10}, and the total number of molecules is then,

$$N_{All\ states}^{total} = \left(\frac{3\varepsilon_0 k^2 D^2}{h\pi^2\mu_e^2\nu_{10}^2}\right)\frac{T_{\rm ex}e^{(J+1)(J+2)T_0/2T_{\rm ex}}}{(J+1)^2}\int\int T_R(\Omega,\nu)d\nu d\Omega. \tag{3.34}$$

Symmetric top molecules

The energy levels of a symmetric top molecule are given by

$$E_{J,K} = BhJ(J+1)+h(A-B)K^2, \tag{3.35}$$

where A and B are the rotational constants. The LTE partition function is given by Herzburg (1945) as:

$$Z = \frac{5.34\times10^{15}}{\sigma}\left[\frac{T^3}{B^2A}\right]^{1/2} \tag{3.36}$$

$$= 0.523T^{3/2} \quad \text{for propyne} \tag{3.37}$$

$$= 0.486T^{3/2} \quad \text{for methyl cyanide,} \tag{3.38}$$

where $\sigma = 3$ reflects the symmetry of the molecule. The oscillator strength is

$$S_{J+1,K\to J,K} = \frac{(J+1)^2-K^2}{J+1}, \tag{3.39}$$

which reduces to the same value as that for the diatomic molecule when $K = 0$.

Rewriting (3.26) by taking the natural logarithm leads to

$$\ln\left(\frac{2\pi^2}{3\varepsilon_0 kc}\frac{N_{tot}}{Z}\right) = \ln\left(\frac{\int T_R(\nu)d\nu}{\mu_e^2\nu^2 S_{ul}}\right)+\frac{E_u}{kT_{\rm Rot}}, \tag{3.40}$$

where velocities have been converted to frequencies via the Doppler equation and $T_{\rm Rot}$ is the rotational temperature which equals $T_{\rm kin}$ in LTE. Plotting known transitions on a 'rotation diagram' (i.e. plotting $\ln(\int T_R(\nu)d\nu/\mu_e^2\nu^2 S_{ul})$ against E_u) yields a straight line of gradient $1/T_{\rm Rot}$ and intercept proportional to N_{tot}/Z. Any deviation from a straight line suggests that either the LTE assumption is not valid or multiple temperature components are present in the beam. Rotation diagrams and spectra for the sources in which propyne or methyl cyanide was detected are shown in Fig. 3.8.

3.2.4 Visual extinction

Hydrogen column densities, and hence visual extinction, were derived assuming standard ratios relative to H_2 of 1.6×10^{-7} for $C^{18}O$ (Stutzki & Güsten 1990), 1.6×10^{-9} for CS (Snell *et al*. 1984), 1.1×10^{-9} for propyne (Churchwell & Hollis 1983) and 1.4×10^{-10} for CH_3CN (Churchwell & Hollis 1983).

These column densities have then been converted to an equivalent visual extinction, A_V, using the calibration of Bohlin *et al*. (1978)

$$N(\mathrm{H}+2\mathrm{H_2}) \approx 1.8\times10^{25}\left(\frac{A_V}{\mathrm{mag}}\right)\mathrm{m}^{-2}, \tag{3.41}$$

but it must be remembered that this calibration has only been determined for low values of A_V.

3.2.5 Distances

Calculation of masses and luminosity depend critically on the accuracy of the distance measurements (e.g. equation 3.10). In general, kinematic distances have been used and whilst this method is prone to errors, for example in the use of the water maser velocity instead of molecular cloud velocity for half the sources and ambiguities between the near and far estimates, it is usually the only information on distances available for a source (see §2.1.2).

The distance reference codes used in table 3.7 are as follows:

1. Wouterloot *et al*. (1993)
2. Palla *et al*. (1991)
3. Arcetri Atlas (Comoretto *et al*. 1990)
4. Torrelles *et al*. (1992)
5. Tofani *et al*. (1995)
6. Wilking *et al*. (1989)
7. Wouterloot & Walmsley (1986)
8. Forster & Caswell (1989)
9. Genzel & Downes (1977)
10. Jaffe *et al*. (1981)
11. McCutcheon *et al*. (1991)
12. Henkel *et al*. (1986)
13. Lada *et al*. (1984)
14. Felli *et al*. (1992)
15. Miralles *et al*. (1994)
16. Blair *et al*. (1978)

a) CH_3CCH $J = 14 \rightarrow 13$

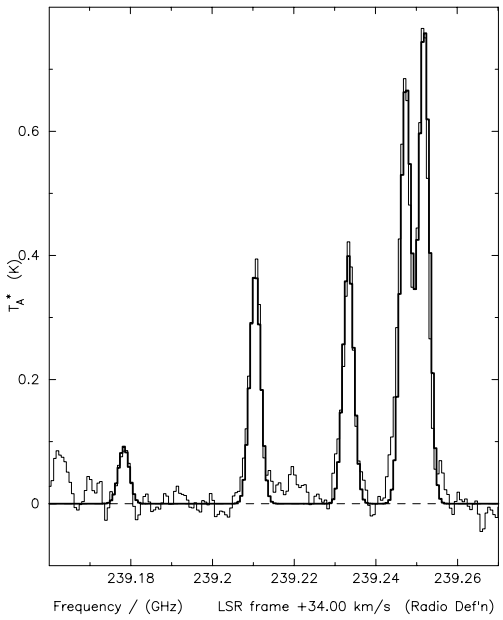

b) CH_3CN $J = 13 \rightarrow 12$

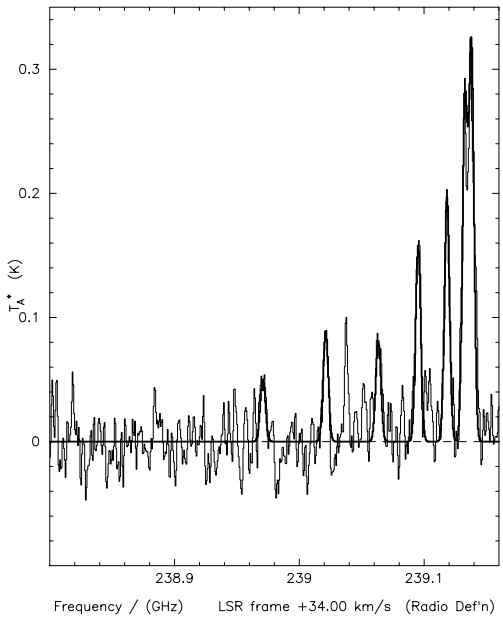

c) CH_3CCH $J = 20 \rightarrow 19$

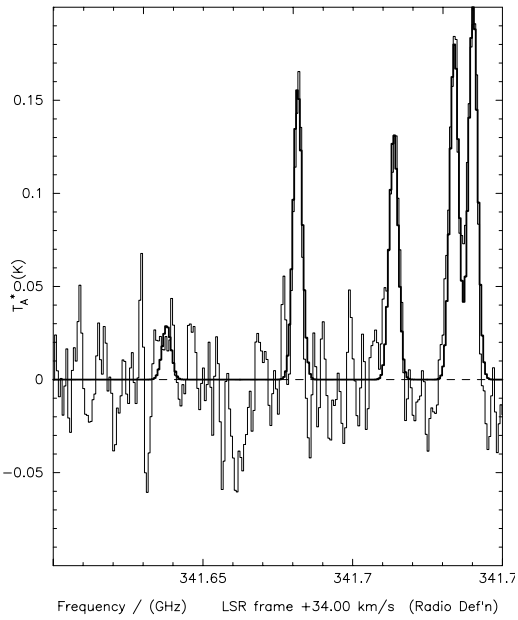

d) Rotation diagram

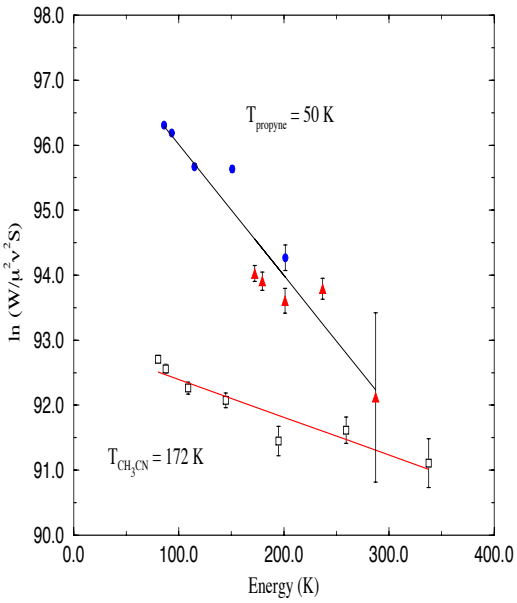

Figure 3.8. Rotation diagram and spectra for IRAS 18032−2137.

a) CH_3CCH $J = 14 \rightarrow 13$

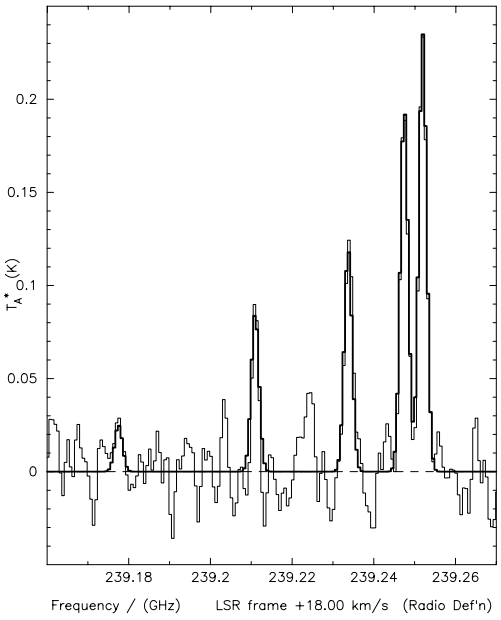

b) CH_3CN $J = 13 \rightarrow 12$

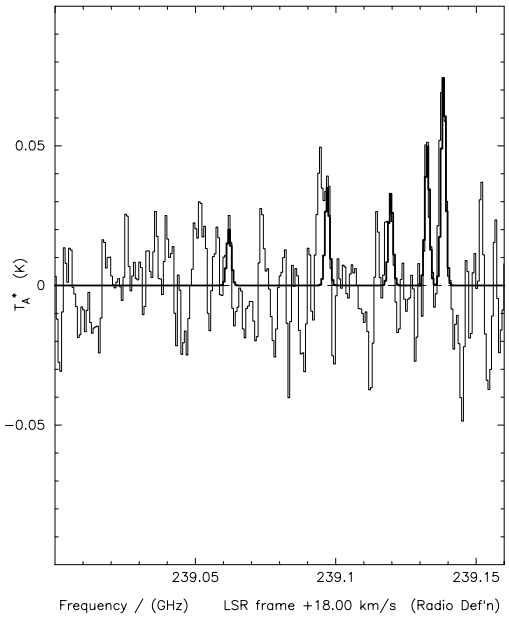

c) Rotation diagram

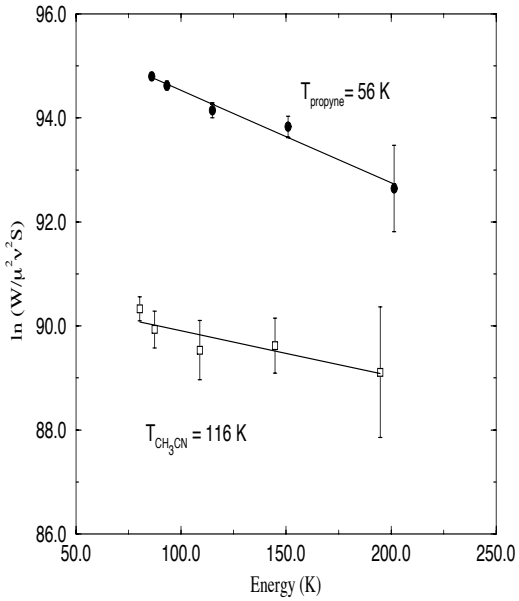

Figure 3.8 *continued* Rotation diagram and spectra for IRAS 18164−1631.

a) CH_3CCH $J = 14 \rightarrow 13$

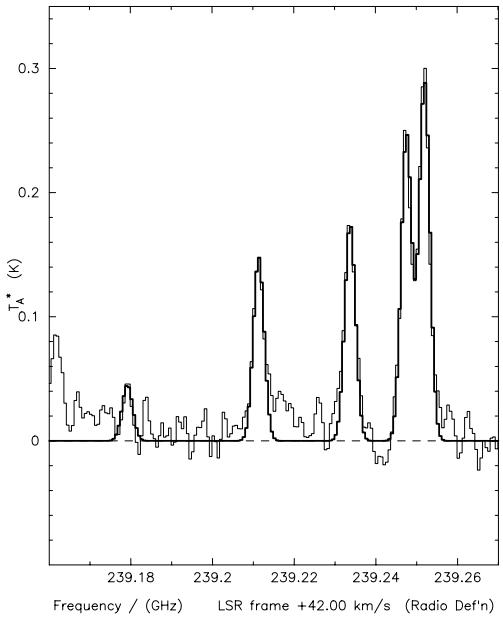

b) CH_3CN $J = 13 \rightarrow 12$

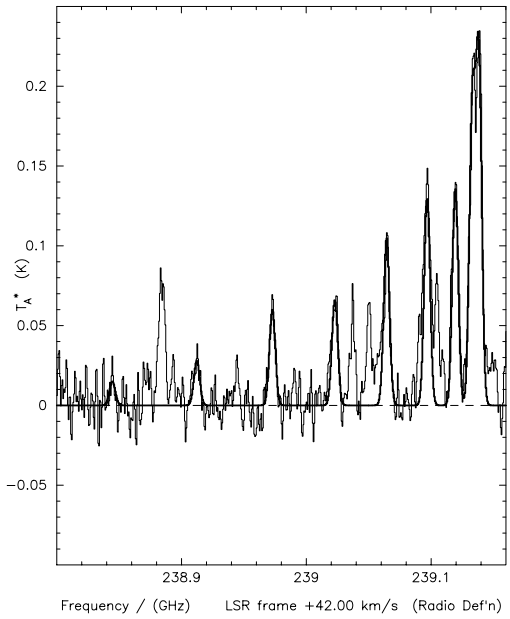

c) CH_3CCH $J = 20 \rightarrow 19$

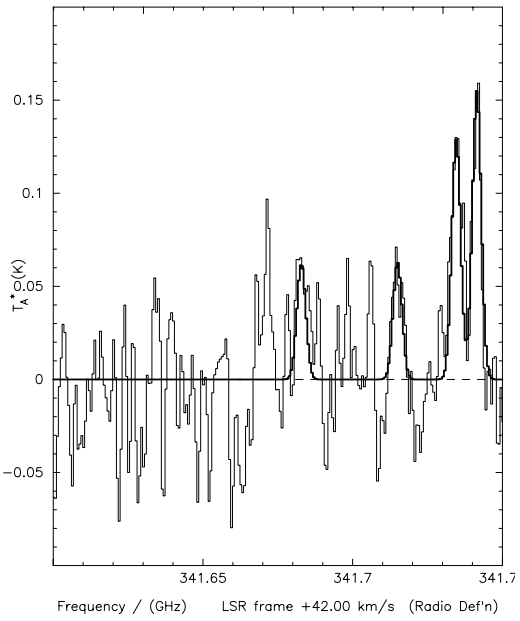

d) Rotation diagram

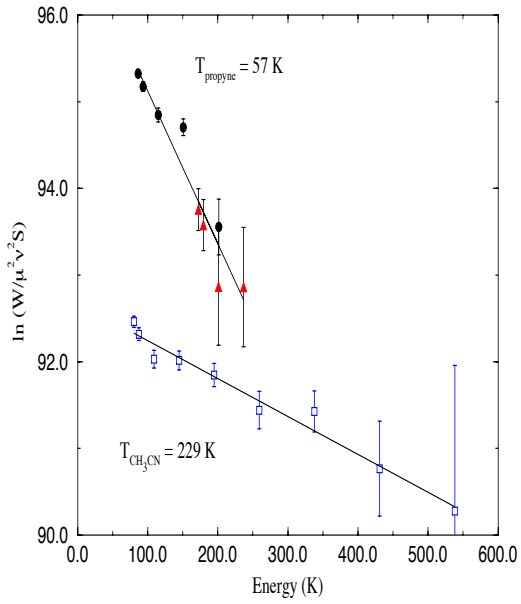

Figure 3.8 *continued* Rotation diagram and spectra for IRAS 18316−0602.

a) CH_3CCH $J = 14 \rightarrow 13$ b) Rotation diagram

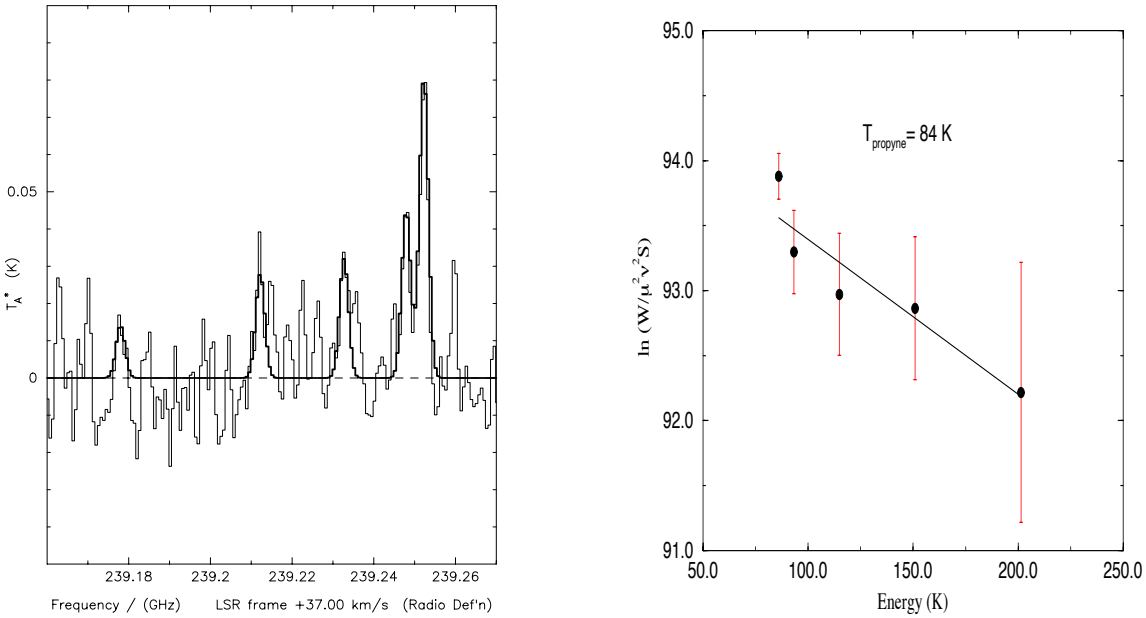

Figure 3.8 *continued* Rotation diagram and spectrum for IRAS 19374+2352.

a) CH_3CCH $J = 14 \rightarrow 13$ b) Rotation diagram

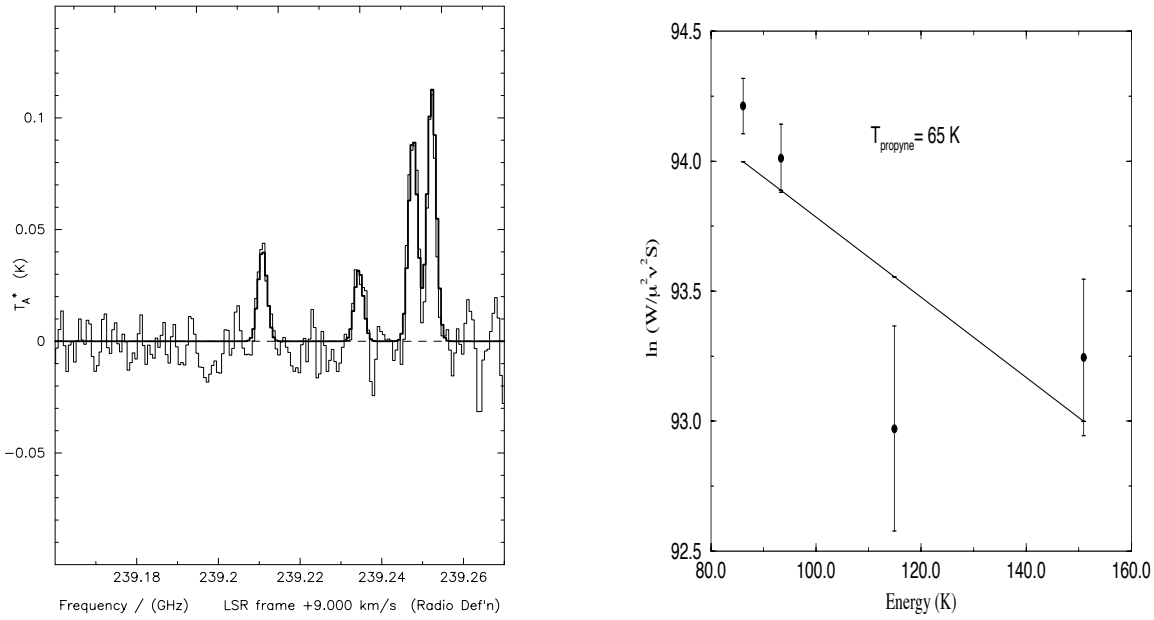

Figure 3.8 *continued* Rotation diagram and spectrum for IRAS 20056+3350.

a) CH_3CCH $J = 14 \rightarrow 13$

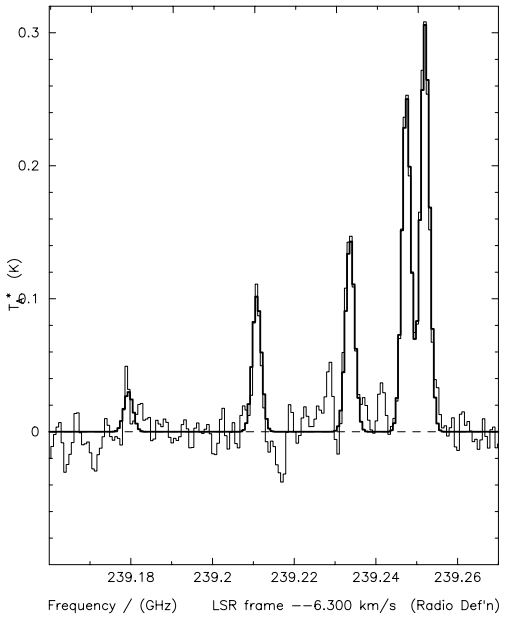

b) CH_3CN $J = 13 \rightarrow 12$

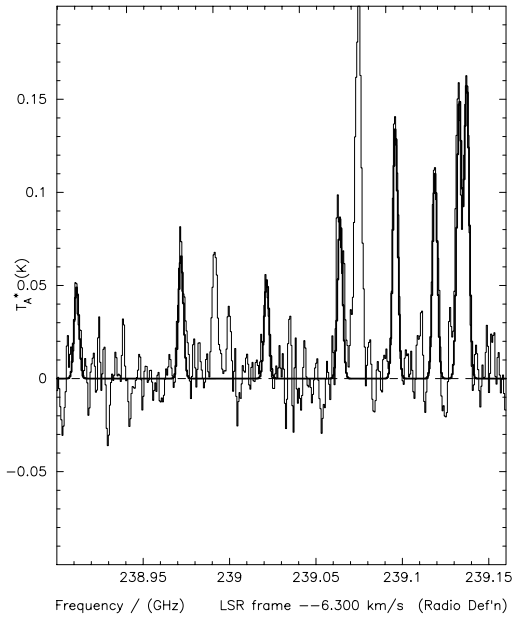

c) Rotation diagram

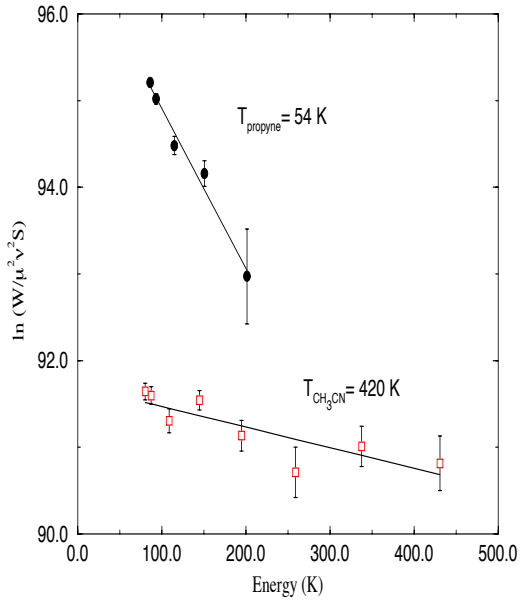

Figure 3.8 *continued* Rotation diagram and spectrum for IRAS 20275+4001.

a) CH_3CCH $J = 14 \rightarrow 13$

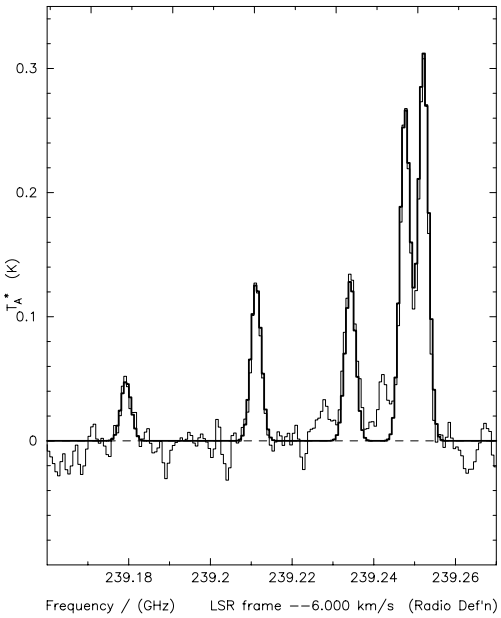

b) CH_3CN $J = 13 \rightarrow 12$

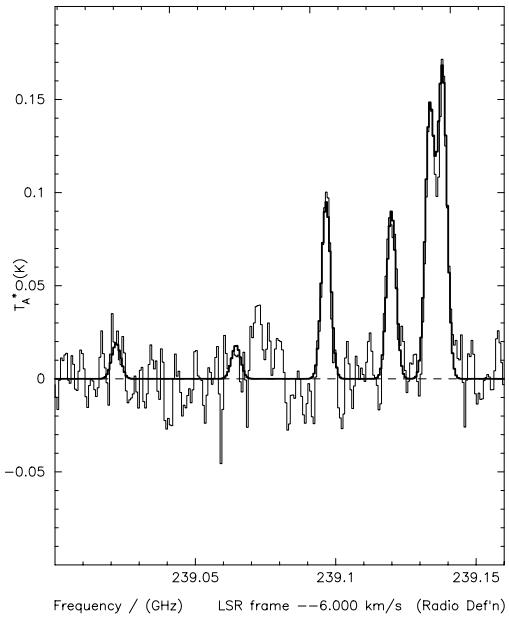

c) CH_3CCH $J = 20 \rightarrow 19$

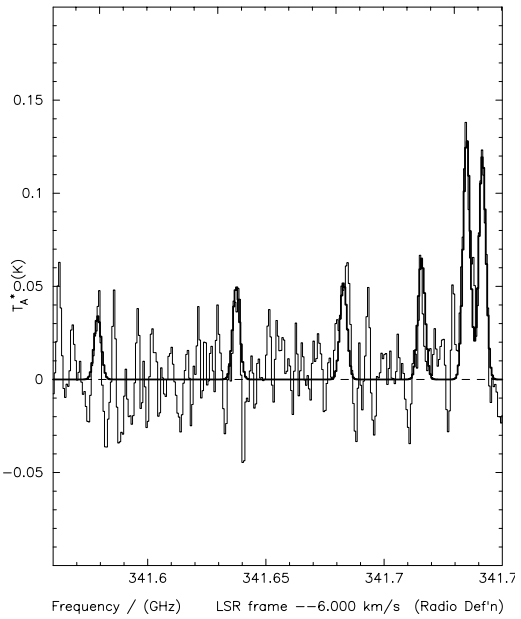

d) Rotation diagram

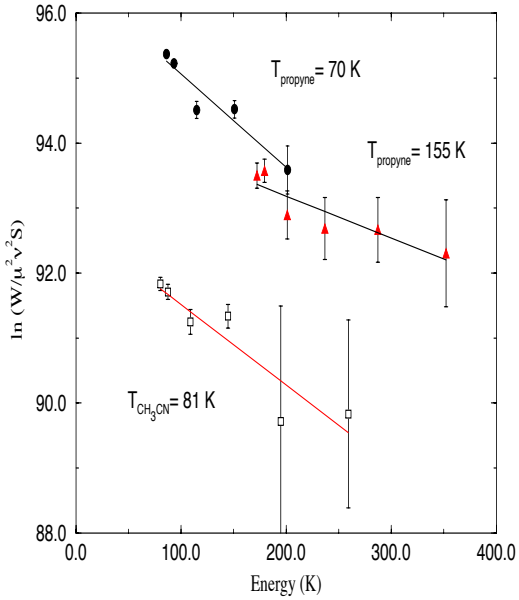

Figure 3.8 *continued* Rotation diagram and spectra for IRAS 21078+5211.

a) CH_3CCH $J = 20 \rightarrow 19$

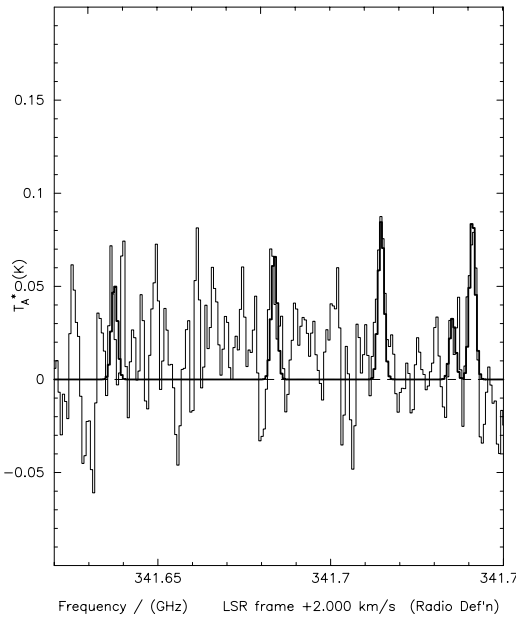

b) Rotation diagram

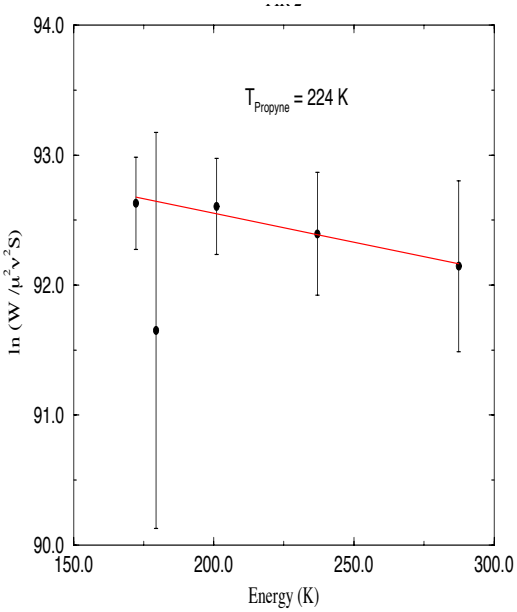

Figure 3.8 *continued* Rotation diagram and spectra for IRAS 20188+3928.

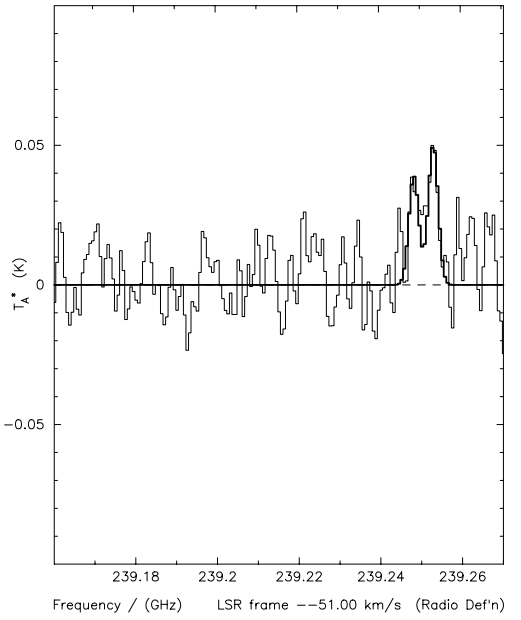

Figure 3.9
CH_3CCH $J = 14 \rightarrow 13$ spectrum for IRAS 22506+5944

Table 3.7. Parameters derived from the SEDs

	Distance	NIR SED	$T_{\rm d}$	λ_c	Ω	$M_{\rm dust}$	A_V	$\log\left(\frac{L_{\rm FIR}}{L_\odot}\right)$	$T_{\rm NIR}$	$R_{\rm NIR}$
	(kpc)	Class	(K)	(μm)	(arcsec^2)	($M_\odot$)	(mag.)		(K)	(AU)
00338+6312	1.60[1]	II-D	30	46	330	96	261	3.27	1600	0.32
00420+5530	4.33[2]	II-D	29	19	920	518	69	3.98	2300	0.14
03035+5819	1.50[3]	I	35	28	750	91	124	3.64	125	328
03262+3108	0.50[3]	UN	20	46	410	12	261	1.42	-	-
05274+3345	1.80[4]	II-D	29	91	320	319	726	3.61	1100	0.06
05302−0537	0.50[5]	UN	23	73	100	73	522	2.50	-	-
05373+2349	2.10[1]	II-D	32	10	770	39	26	3.10	900	1.88
05375−0731	0.45[6]	O	28	82	100	5	621	1.78	-	-
05413−0104	0.50[7]	UN	24	28	260	4	124	1.35	-	-
06053−0622	0.95[6]	II-D	60	19	1810	49	69	4.65	800	1.90
06084−0611	1.00[3]	II-D	44	100	250	90	837	3.90	1300	0.01
06103−0612	1.00[3]	I	28	46	110	13	261	2.23	-	-
06291+0421	1.60[1]	UN	35	46	120	35	261	3.17	-	-
17441−2910	10.00[8]	II-D	46	73	100	2249	522	5.49	-	-
18032−2137	4.47[3]	II-D	36	100	480	3403	837	5.07	1200	0.75
18089−1732	3.58[3]	II-D	43	100	130	605	837	4.68	-	-
18117−1753	4.50[9]	I	38	100	360	2637	837	5.07	-	-
G14.45−0.11	3.73[3]	UN	48	19	440	183	69	4.71	-	-
18162−2048	1.70[3]	I	38	19	2200	192	69	4.18	-	-
18164−1631	2.30[10]	UN	32	28	1530	436	124	4.12	-	-
18273+0113	0.40[3]	O	26	55	500	12	341	2.02	-	-
18316−0602	3.00[11]	UN	33	64	500	833	428	4.38	-	-
18455−0149	4.79[3]	UN	32	10	1500	397	26	4.11	-	-
18537+0749	2.33[3]	I	40	100	290	563	837	4.51	-	-
18592+0108	3.08[3]	I	43	46	1260	1353	261	5.23	1200	0.44
19374+2352	4.30[2]	UN	34	19	740	413	69	4.26	-	-
19442+2427	2.30[12]	I	42	37	610	264	188	4.50	-	-
20056+3350	2.08[3]	UN	37	19	580	76	69	3.72	-	-
20188+3928	3.20[11]	UN	30	73	510	1174	522	4.29	-	-
20275+4001	2.00[13]	II-D	55	48	340	162	278	4.84	500	57
21007+4951	0.70[14]	UN	21	28	230	6	124	1.28	-	-
21078+5211	1.30[15]	UN	38	37	540	74	188	3.72	-	-
HH 32-35	1.00[3]	UN	20	55	230	34	341	1.88	-	-
21418+6552	1.90[3]	II-D	40	10	940	39	26	3.63	1500	0.54
21432+4719	0.90[3]	UN	28	10	200	2	26	1.42	-	-
22142+5206	2.83[3]	I	39	10	200	18	26	3.26	-	-
22198+6336	1.30[1]	O	31	28	380	34	124	2.92	-	-
22475+5939	4.20[16]	II-D	50	10	500	103	26	4.58	1300	0.38
22506+5944	4.99[3]	UN	26	46	390	1105	261	4.01	-	-
22528+5936	4.89[3]	UN	35	10	220	60	26	3.50	-	-
22539+5758	3.82[3]	II-D	35	19	420	183	69	3.97	1300	0.42
22566+5830	4.86[3]	I	43	19	680	485	69	4.87	-	-
23138+5945	4.44[3]	II-D	43	10	1250	284	26	4.67	-	-
23314+6033	4.50[1]	UN	38	28	240	264	124	4.30	-	-

Table 3.8. Parameters derived from line observations.

	$C^{18}O$			CS		CH_3CCH			CH_3CN			
	$M_{gas}/M_\odot$	N_{col} (10^{19} m^{-2})	A_V (mag)	N_{col} (10^{17} m^{-2})	A_V (mag)	T_{Rot} (K)	N_{col} (10^{17} m^{-2})	A_V (mag)	T_{Rot} (K)	N_{col} (10^{16} m^{-2})	A_V (mag)	$\log\left(\frac{L_{H_2O}}{L_\odot}\right)$
00420+5530		9.88	34									−6.08
03262+3108		6.55	23									
17441−2910	10^4	42.6	150	7.68	27							
18032−2137FIR2	1010	57.2	200			50^{+5}_{+5}	$38.4^{+13.1}_{+10.2}$	194	172^{+33}_{-24}	$14.6^{+6.7}_{-4.9}$	58	
G14.45−0.11		17.5	61									
18164−1631	276	18.4	64	4.62	16	56^{+6}_{-5}	$8.2^{+3.3}_{-2.4}$	41	116^{+47}_{-26}	$0.9^{+0.8}_{-0.5}$	4	
18273+0113	5	11.2	38	1.73	6							−7.89
18316−0602						57^{+7}_{-6}	$14.9^{+8.9}_{-5.7}$	75	229^{+15}_{-14}	$16.7^{+3.1}_{-2.7}$	66	−3.85
18455−0149	565	19.4	67	1.43	5							−5.56
19374+2352	840	18.4	64	4.92	17	84^{+25}_{-16}	$2.7^{+2.4}_{-1.3}$	14				−6.40
20056+3350	64	17.5	61	3.14	11	65^{+105}_{-25}	$3.8^{+14.8}_{-3.2}$	19				−6.45
20188+3928FIR2	660	18.1	63	5.60	19	224^{+37}_{-27}	$3.7^{+1.4}_{-1.1}$	19				−5.56
20275+4001						54^{+5}_{-5}	$12.1^{+5.0}_{-3.6}$	61	420^{+150}_{-86}	$15.7^{+8.4}_{-6.1}$	62	
21007+4951												−8.30
21078+5211	80	19.0	66	8.06	28	70^{+14}_{-11}	$13.8^{+10.3}_{-6.2}$	70	81^{+21}_{-14}	$3.8^{+3.5}_{-1.9}$	15	−5.71
21078+5211						155^{+50}_{-30}	$6.0^{+5.6}_{-3.1}$	30				
22142+5206	117	7.03	24									
22198+6336	108	11.1	38	1.15	4							
22475+5939FIR2	343	7.60	26									
22506+5944												−4.35
23314+6033	540	7.95	28									−6.69

References

Blair G. N., Davis J. H., Dickinson D. F., 1978, *ApJ*, 226, 435
Bohlin R. C., Savage B. D., Drake J. F., 1978, *ApJ*, 224, 132
Churchwell E., Hollis J. M., 1983, *ApJ*, 272, 591
Comoretto G., *et al*., 1990, *A&AS*, 84, 179
Emerson J. P., 1988, in *Formation and Evolution of Low Mass Stars*, eds Dupree A. K., Lago M. T. V. T., p. 21, Kluwer Academic Publishers, Dordrecht
Felli M., Palagi F., Tofani G., 1992, *A&A*, 255, 293
Forster J. R., Caswell J. L., 1989, *A&A*, 213, 339
Genzel R., Downes D., 1977, *A&AS*, 30, 145
Goldreich P., Kwan J., 1974, *ApJ*, 189, 441
Henkel C., Haschick A. D., Güsten R., 1986, *A&A*, 165, 197
Herzberg G., 1945, *Infrared and Raman Spectra*, New York: Van Nostrand Reinhold
Hildebrand R. H., 1983, *QJRAS*, 24, 267
Jaffe D. T., Güsten R., Downes D., 1981, *ApJ*, 250, 621
Lada C. J., Thronson, Jr. H. A., Smith H. A., Schwartz P. R., Glaccum W., 1984, *ApJ*, 286, 302
McCutcheon W. H., Dewdney P. E., Purton C. R., Sato T., 1991, *AJ*, 101, 1435
Miralles M. P., Rodríguez L. F., Scalise E., 1994, *ApJS*, 92, 173
Palla F., Brand J., Cesaroni R., Comoretto G., Felli M., 1991, *A&A*, 246, 249
Richer J. S., 1991, *Molecular line and continuum studies of high-mass star formation*, Ph.D. thesis, University of Cambridge
Snell R. L., Scoville N. Z., Sanders D. B., Erickson N. R., 1984, *ApJ*, 284, 176
Stutzki J., Güsten R., 1990, *ApJ*, 356, 513
Tofani G., Felli M., Taylor G. B., Hunter T. R., 1995, *A&AS*, 112, 299
Torrelles J. M., Gomez J. F., Anglada G., Estalella R., Mauersberger R., Eiroa C., 1992, *ApJ*, 392, 616
Wilking B. A., Mundy L. G., Blackwell J. H., Howe J. E., 1989, *ApJ*, 345, 257
Wouterloot J. G. A., Walmsley C. M., 1986, *A&A*, 168, 237
Wouterloot J. G. A., Brand J., Fiegle K., 1993, *A&AS*, 98, 589

Chapter 4

Sample analysis

This chapter will present statistical results for the sample as a whole as opposed to the source by source discussion of the next chapter. Using the observational data from this dissertation and the literature (see Appendix B for a complete list of the data used) it has been possible to find quantities such as luminosity and mass for each of the sources in the sample.

4.1 Spectral energy distributions

In the last ten to fifteen years a classification system for the evolutionary state of young stars has been developed on the basis of the shape of their spectral energy distributions (e.g. Lada & Wilking 1984). Spectral energy distributions (SEDs) have been constructed for all the sources using my own continuum data, presented in the previous chapter, and observations from the literature, presented in Appendix B. The spectral classification system can be summarised as follows:

- Class 0 sources (André *et al*. 1993) are characterised by having no emission at wavelengths less than about 12 μm, and a high ratio of submm to bolometric luminosity. They are still in the main accretion phase, have strong collimated molecular outflows and generally possess radio continuum indicative of shock excitation. This puts constraints on the SED such that a class 0 should have a spectral energy distribution resembling that of a grey-body of T$<$ 30 K. The *IRAS* bias of the maser sample reduces the chance of finding an object such as the 'classic' class 0 object VLA 1623 (André *et al*. 1993) which has no *IRAS* point source associated with it. Class 0 objects are thought to be at a very early stage where the young star is just beginning to form but where most of the matter is in the surrounding dust and not in the central object. The presence of molecular outflows suggests that these sources have 'cored-apple' structures where matter is

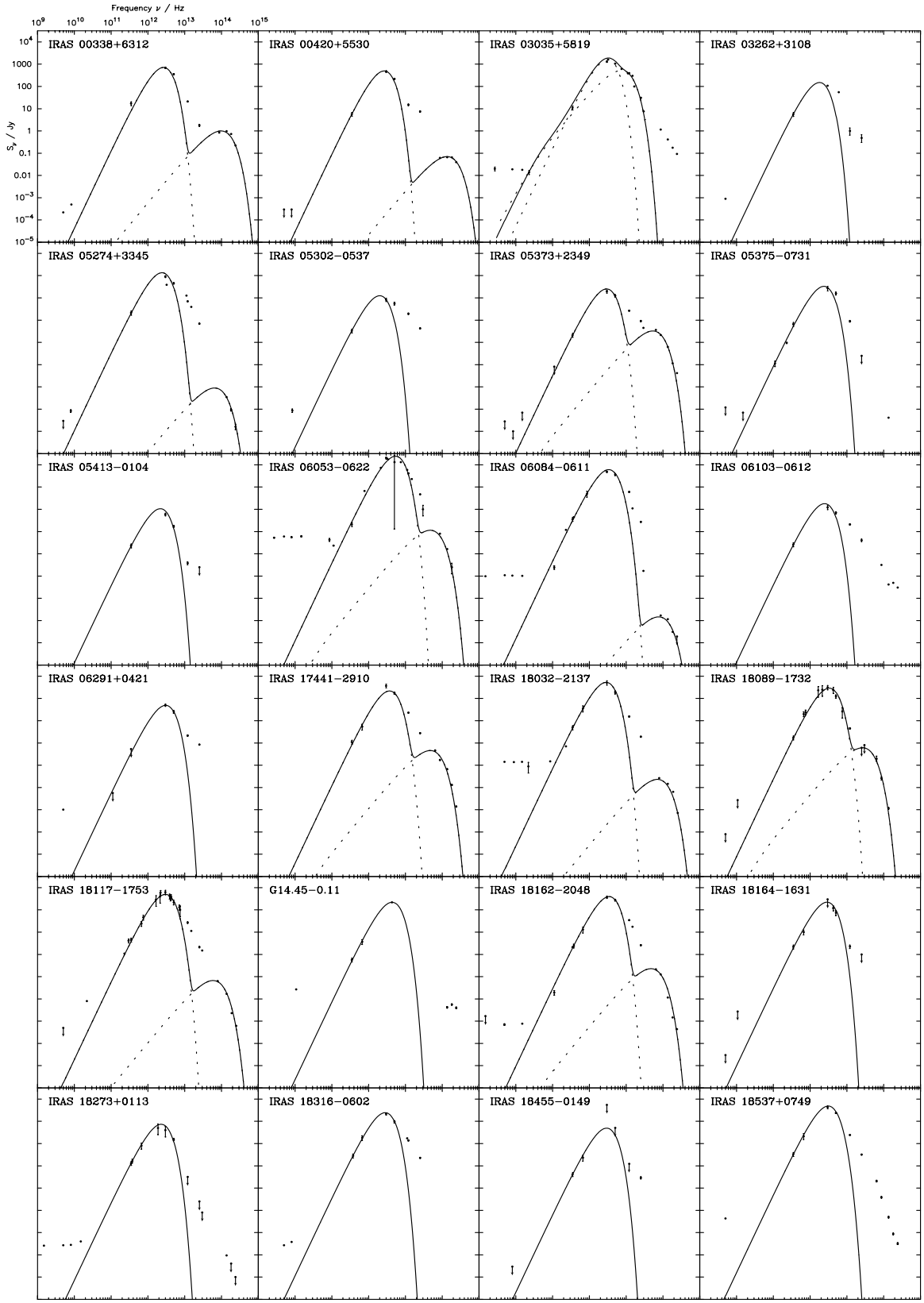

Figure 4.1. SEDs for the first 24 sources.

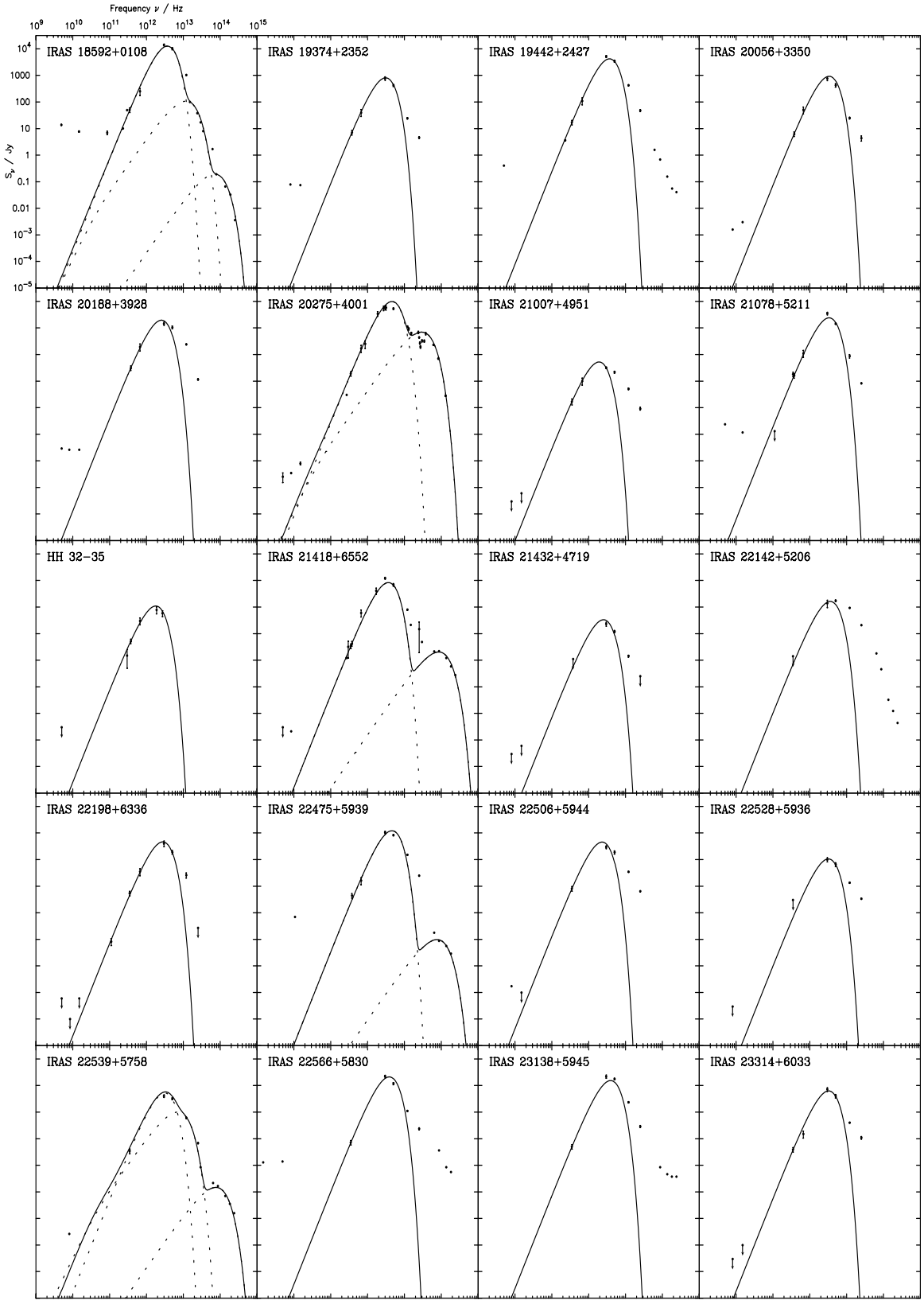

Figure 4.1 *continued* SEDs for the remaining sources.

accreting onto the central object via a thick accretion disk and the bipolar outflow has blown through the dust perpendicular to the disk. An example of a class 0 SED from this sample is IRAS 18273+0113 which also possesses radio continuum, a molecular outflow and evidence for a near infra-red source (15 mag. in K, >18 mag. in J, Eiroa & Casali 1992).

- SEDs of class I sources are broader than a single temperature grey-body and suggest the presence of a range of temperatures from 50 to $\sim$ 1000 K. This spectrum can not be fitted by the single temperature fit used in this dissertation but that type of fit can still give a good idea of the dust luminosity (since the two long wavelength *IRAS* fluxes would be fitted), mass, size and the lower end of the dust temperature range and therefore still gives a reasonably good way of comparing these sources with the other classes. A full radiative transfer calculation (e.g. Adams & Shu 1986) shows that class I spectra can be modelled by the isothermal collapse of a slowly rotating core which results in flattened disc-like structures and the formation of cavities (with a radius of approximately 100 AU) around the central star. These models suggest that class I sources are in the process of building up mass by the accretion of circumstellar matter.

- Next is a double peaked SED known as class II-D. These SEDs are fitted, generally, extremely well by a two component model, consisting of cool greybody ($T_d \approx 50$ K) and a much warmer black body component ($T \approx 1000$ K). In this sample good examples of II-D spectra can be found in IRAS 18089-1732 and IRAS 06084-0611. Adams, Lada & Shu (1987) have shown that this type of SED can be modelled by a combination of emission from a stellar photosphere plus a disc (the warm component) and a residual infalling shell (the cooler component).

- Class II sources are broad, hot SEDs which have peak emission in the near-infrared. They can be explained simply by combination of emission from a stellar photosphere plus a disc. The *IRAS* colour selection for sources which are stronger in 100 or 60 μm than 12 or 25 μm means that no class II sources are present in my sample.

- Class III objects are the most evolved, having SEDs characteristic of the emission from stellar photospheres. These objects are also too evolved to be present in this sample.

Table 4.1 shows how my sample divides up using this classification system. Immediately noticeable is that 18 of the sources (40%) have an unknown classification because of a complete lack of near-infrared data. This is unfortunate but extensive observations of the unclassified sources, with telescopes such as UKIRT or the smaller TIRGO, was not possible (5 nights were allocated to this project on the TIRGO telescope but unfortunately all nights were lost due to bad weather). More than half of the remaining sources have II-D spectra indicating that most of the sources are fairly well evolved. The very small number of class 0 candidates is possibly not surprising given the insensitivity of *IRAS* to 20 K cores. Ever since *IRAS* the fashionable method for finding H_2O maser sources has been to use the *IRAS* PSC and search in a particular colour-colour region of the survey. The vast majority of masers in the Arcetri atlas are associated with *IRAS* sources and hence the Arcetri atlas would not be

NIR class	#
O	3
I	9
II-D	14
Unknown	18

Radio spectrum	#
Thermal	10
Rising	6
Falling	1
<1 mJy	12
Undetermined	9
Unknown	5

Table 4.1
Number of each SED class and radio spectral type in the sample

expected to contain many class 0 sources, *even if it is assumed water masers are as prevalent in class 0 sources as they are in more evolved objects*. This problem would only be rectified if an unbiased survey of the Galactic plane for 22 GHz H_2O masers was conducted, which is as yet an unreasonable proposition, or an instrument such as *ISO* could use its 200 μm capability to search for cooler objects than those to which *IRAS* was sensitive, and those objects could then be searched for maser emission.

4.1.1 Greybody fits

Since only a few sources have complete spectral coverage for their SEDs, especially at wavelengths less than 12 μm, a complicated numerical analysis is unwarranted (for example, the bolometric temperature (Myers & Ladd 1993), mean frequency (Ladd *et al*. 1993) or the ratio of submm luminosity to bolometric luminosity (André *et al*. 1993)). The far-infrared parts of the SEDs are the most complete, because of *IRAS*, and this part of the spectrum has been analysed using a single temperature greybody fit.

Dust temperatures can be found by fitting a greybody (§3.2.2) to the SED by assuming the dust emission to be from a homogeneous cloud at a constant dust temperature $T_{\rm d}$, and solid angle Ω. By varying a subset of the four parameters (T_d, Ω, λ_c, β), a least-squares fit of the predicted fluxes to those observed can then be performed. The fit is subject both to statistical errors implicit in the measured continuum fluxes, and to the systematic errors associated with comparing fluxes from observations made with different beam sizes and observing techniques. The lack of more complete submm information for all the sources makes it impossible to determine the value of β from the fit alone. For this work β has been fixed at 1.5, the value usually found in protostellar cloud core regions (André *et al*. 1993; Krügel & Chini 1994), as opposed to 2.0, the theoretical limit for crystalline solids favoured by Gordon (1995). There are essentially two remaining free parameters; the dust temperature constrains the frequency of the peak emission and the product $\Omega\lambda_c^{1.5}$, for $\lambda_c \lesssim 100$ μm such that the FIR emission is optically thin, constrains the flux scale. This fitting of the product $\Omega\lambda_c^{1.5}$ means that there are many solutions of Ω and λ_c consistent with the data and table 3.7 shows only one valid combination – a smaller source size than that shown in the table hence implies a larger column density.

The large *IRAS* bias of this sample (only two sources do *not* have an *IRAS* counterpart) and the colour selection criteria applied to the sample means that it is not surprising that the dust fits result in temperatures ranging from 30 to 60 K. Sources with upper limits in the submm are unconstrained by

the fitting procedure but their luminosities can still be estimated (most of the energy is emitted at *IRAS* wavelengths) although only upper limits can be found for the masses.

Unfortunately the *IRAS* point sources can not definitely be associated with the submm cores (Fig. 4.3) even though both wavelengths should be sampling warm dust. This is entirely due to the large beam of the *IRAS* satellite, which is 2 arcmin FWHM at 100 μm. For example, if a compact core was embedded on the edge of extended emission, *IRAS* would probably place the point source somewhere between the centre of the diffuse emission and the compact core. Of course this interpretation makes it hard to justify the use of *IRAS* flux data for the construction of SEDs where the submm core and the *IRAS* source do not coincide. For these sources it has been assumed that a large fraction of the *IRAS* flux is due to the point source. Correction for extended emission is not possible and it is believed that this error will not affect the derived luminosities too much. Sources which have more than one submm core within the *IRAS* beam really need other infra-red observations to apportion the *IRAS* flux to individual components. Where this data has not been available the *IRAS* flux has been used since even a 50 per cent error in this value will still give luminosities accurate to within an order of magnitude. Derived temperatures are less sensitive to these errors and should be correct to better than 10 per cent.

In the subsequent analysis $L_{\rm FIR}$ refers to the luminosity derived from the single component fit and not from the raw data points directly. In effect this means that $L_{\rm FIR}$ is a measure of the luminosity at wavelengths longer than about 50 μm. As has already been stated above this value is a good approximation of the total infra-red luminosity since the sample has already been *IRAS* selected to have peak *IRAS* fluxes at 100 or 60 μm.

4.1.2 Radio spectra

Table 4.1 also shows information on the radio fluxes of sources in the sample. The radio data are much more complete than the near infra-red data with 39 sources (88 per cent) having at least one radio observation available.

Of the sources with detected radio emission at more than one frequency, 10 (25%) have optically thin flat thermal spectra. The six sources with spectra rising with frequency are either due to a real effect from an ionized wind or optically thick H II region or, at least in some cases, are caused by the observations being sensitive to different angular scales and resolving out flux. A good example of this can be found with IRAS 21078+5211, which has a falling spectrum. This source was observed with the Ryle Telescope at 15 GHz in the extended configuration, which is sensitive to scales less than about 1 arcmin, in 1995 April. The RT detected a diffuse H II region, similar in structure to that found at 5 GHz by McCutcheon *et al.* (1991), having an integrated flux of 118 mJy. 15 GHz observations have also been performed by Miralles *et al.* (1994) using the VLA in D-array, which is only sensitive to structure smaller than 45 arcsec in snapshot mode, and they detected only 31 mJy. This result suggests that this source is very extended and has no compact emission. This is confirmed with my 8-GHz VLA B-array observations of this source which detected less than 0.3 mJy on scales less than about

20 arcsec, and highlights the danger of performing photometry with an interferometer.

As would be expected in a sample selected in a search for very young objects, 30 per cent of the sources have no detected radio continuum (< 1mJy). Their UC HII regions may be too small to be visible, infalling matter is quenching the ionization, they may simply be too young to possess an O or B star, or they may not be massive enough to form an O or B star. Class 0 objects should be too young to have formed main-sequence stars and would not be expected to have any radio continuum due to this mechanism. The fact that class 0 sources such as *IRAS* 16293 and VLA 1623 do possess radio continuum suggests that an alternative form of excitation is required (e.g. shock excitation). It is even possible that some of these class 0 sources are in fact class I sources which are being observed through the surrounding disk.

4.2 Source comparisons

Following the procedures outlined in the previous section, information on spectral class, circumstellar mass, dust temperature, far-infrared luminosity, Lyman-photon luminosity and hence stellar luminosity, hydrogen column density and source size were all calculated for the sample. Along with information such as water maser luminosity and velocity offset of the maser from the molecular cloud, the data were examined for any significant correlations.

4.2.1 Position offsets

The most striking result of these data is that the water masers and submm peaks lie very close to one another. Fig. 4.3 shows the position of the water maser, radio and *IRAS* sources relative to the submm continuum peak for each source whereas Fig. 4.4 shows the actual offsets of the submm and *IRAS* sources from the masers for all sources. Fig. 4.5 shows the cumulative distribution of the separation between the water masers and submm peaks and the water masers and *IRAS* point sources, in parsecs.

Since the x and y offsets should each be approximately Gaussian distributed if they are purely due to pointing errors, the separation was quantified using a χ^2 statistic such that

$$\chi^2 = \sum_{i=1}^{N} \left[\left(\frac{|\, x_i \,| - \varepsilon}{\sigma_{x_i}} \right)^2 + \left(\frac{|\, y_i \,| - \varepsilon}{\sigma_{y_i}} \right)^2 \right], \qquad \varepsilon \geq 0, \tag{4.1}$$

where N is the number of sources each with offsets (x_i, y_i) and error σ_i, and ε is the separation specified from a given model. For the *IRAS* data the x and y axes were rotated to align with the major and minor axes of the *IRAS* error ellipse; for the submm data the errors were circular and the R.A. and dec axes were chosen. A model is consistent with the data if its χ^2 is less than the number of degrees of freedom. For N x and y offsets fitting one parameter there are $2N - 1$ degrees of freedom. χ^2 was calculated for different ε and the minimum value then indicates the most likely separation of the two objects. It is

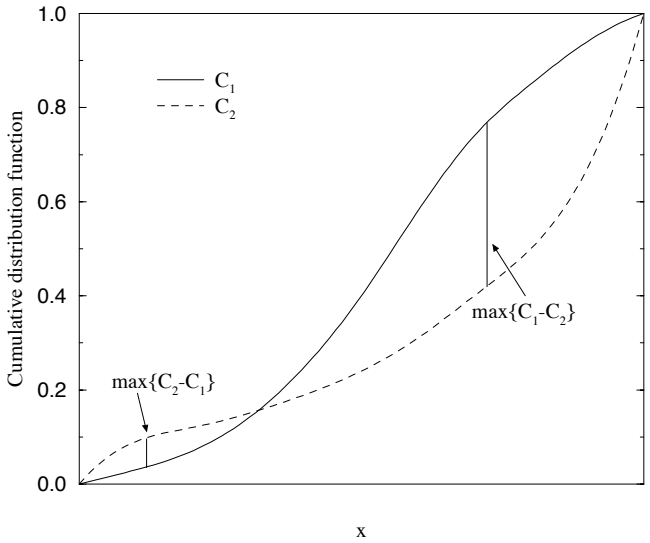

Figure 4.2
Illustration of the Kolmogorov–Smirnov and Kuiper tests. For the two cumulative distribution functions C_1 and C_2, the KS statistic K is given by the length of the longer of the two lines marking points of maximum difference between the curves, whereas the Kuiper statistic D is defined as the sum of the lengths of the two marked lines (Figure reproduced from Sleath (1995)).

probably a more useful result to determine the distance *within* which the objects lie rather than the radius *on* which the objects lie. In an attempt to quantify this value, the χ^2 statistic was modified slightly such that the contribution to χ^2 was zero when the data point was within a given radius (i.e. $\chi^2(i) = 0$ when $(\mid x_i \mid -\varepsilon) < 0$ and similarly for y_i). Since this formulation of χ^2 now becomes monotonically decreasing with increasing ε, it is no longer possible to *minimize* the χ^2. The minimum separation is now found by increasing ε until $\chi^2 < 2N - 1$. This formulation produces a larger ε than the more usual χ^2 statistic, since the small separation data points with small errors are no longer contributing, but does mean that the resulting statistic is consistent with the number of degrees of freedom. The main problem with this method is that it relies on the *absolute* value of χ^2 and is therefore sensitive to the accuracy of the assumed errors.

An alternative approach is to derive a model for the distibution of masers and then compare this with the actual distribution of the data. If N masers are distributed uniformly on the surface of a sphere of radius R, the fraction of the total number of masers detected within a projected radius r is given by

$$\frac{N(r)}{N} = \left(\frac{r}{R}\right)^2. \tag{4.2}$$

Similarly, the expected cumulative distribution for N masers distributed uniformly within a sphere of radius R is given by

$$\frac{N(r)}{N} = 1 - \left[1 - \left(\frac{r}{R}\right)^2\right]^{\frac{3}{2}}. \tag{4.3}$$

It is now possible to compare these two models with the data by using either a Kolmogorov–Smirnov (KS) test (Press *et al*. 1992) or Kuiper test (Kuiper 1962), resulting in a single number, *viz*. the probability of the two distributions being identical.

Both the Kolmogorov–Smirnov and Kuiper tests are based on comparisons of the cumulative distribution functions (C_1 and C_2) of two data sets (or one data set and a theoretical model) with N_1 and

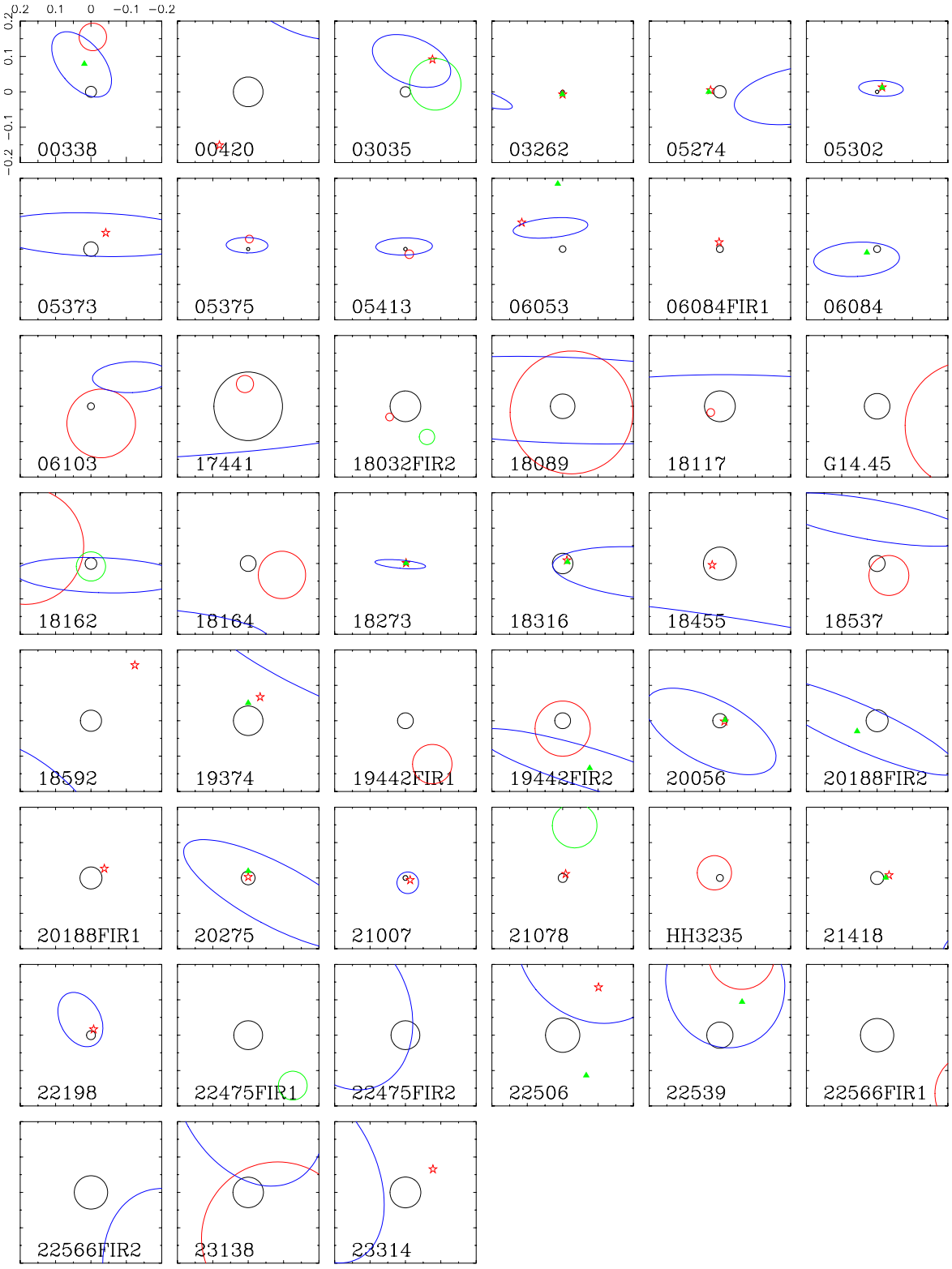

Figure 4.3. Distribution of maser, *IRAS* and radio sources relative to the submm peak. Offsets are in parsecs. *IRAS* error ellipses are 2σ; other error circles are 1σ. Submm cores are at the centre (black), maser sources are red, *IRAS* sources are blue and radio sources are green. Symbols indicate sources with error bars too small to be plotted.

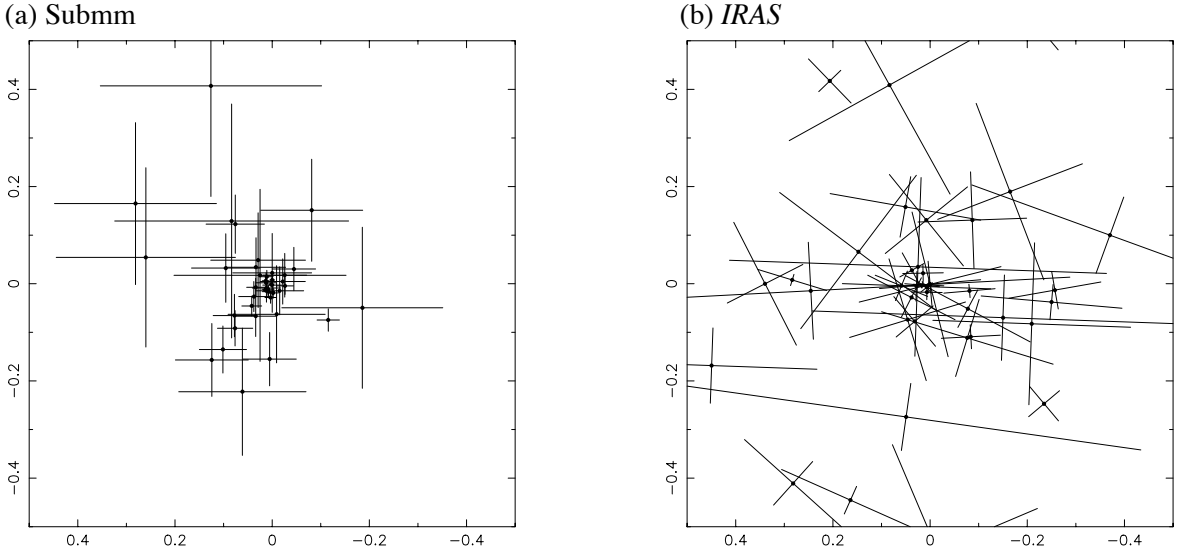

Figure 4.4. A more detailed look at the maser offsets in parsecs. All error bars are 1σ.

N_2 points respectively. The KS statistic is then defined as

$$K = \max_{-\infty<x<\infty} |C_1(x) - C_2(x)|,$$

whereas the Kuiper statistic is defined as

$$D = K_+ + K_- = \max_{-\infty<x<\infty} \{C_1(x) - C_2(x)\} + \max_{-\infty<x<\infty} \{C_2(x) - C_2(x)\}$$

(see Fig. 4.2), i.e. whereas the KS test measures the maximum absolute deviation between the distributions, the Kuiper test is the sum of the maximum differences above and below between C_1 and C_2. The significance of the (easily) measured value of these statistics is then calculated as,

$$\text{Probability(data identical)} = Q_{\rm K}\left(K\left[\sqrt{N_0} + 0.12 + 0.11/\sqrt{N_0}\right]\right)$$

for the KS test, where

$$Q_{\rm K}(\lambda) = 2\sum_{j=1}^{\infty}(-1)^{j-1}{\rm e}^{-2j^2\lambda^2} \qquad \text{and} \qquad N_0 = \frac{N_1 N_2}{N_1 + N_2},$$

and for the Kuiper test,

$$\text{Probability(data identical)} = Q_{\rm D}\left(D\left[\sqrt{N_0} + 0.155 + 0.24/\sqrt{N_0}\right]\right)$$

where

$$Q_{\rm D}(\lambda) = 2\sum_{j=1}^{\infty}(4j^2\lambda^2 - 1){\rm e}^{-2j^2\lambda^2}.$$

The KS test is the most widely used technique for comparing two unbinned data sets, but has the disadvantage of being more sensitive to values of x around the median (such that $C(x) = 0.5$) than to the extremes of the data. This results in the test being good at picking out shifts in the median value of the distribution, but rather less useful for finding spreads. In contrast, the Kuiper test is equally sensitive over all values of x, with the inevitable drawback that it is then more prone to giving misleading answers due to outliers. The tests do however complement each other in their respective sensitivity ranges.

One problem with the algorithm, as implemented, is that it takes no account of the errors on each point. For this reason only those sources with the smallest errors were included in the KS analysis, whereas all the data was included for the χ^2 analysis. A χ^2 test should always give a smaller value for the 'best fit' radius than the KS test because an attempt is being made to fit three dimensional data by using a two dimensional model – the sources in the centre and on the edge will be pulling the χ^2 in opposite directions and will result in a 'best fit' radius somewhere between the two extremes. This difference has been quantified using a computer simulation. An (x,y) data set was generated which had the expected theoretical distribution; this data then underwent a χ^2 test with the result that χ^2 is minimised at $\varepsilon = 0.38R$ for a uniform spherical distribution, and at $\varepsilon = 0.44R$ for a shell distribution.

Calculating χ^2 for the submm and maser data, assuming zero separation, returns a reduced value (i.e. $\chi^2_R = \chi^2/(2N-1)$) of 2.5. This is much larger than one and indicates that the data are not consistent with submm cores and water masers being coincident. Minimizing χ^2 for different ε results in a most likely separation of 0.012 pc. The reduced χ^2 is still fairly large, a value of 1.5, but it is possible that this is reflecting an underestimate in the assumed pointing errors (for this analysis pointing errors of 2 arcsec for the compact submm sources and 5 arcsec for the extended sources have been adopted). The modified χ^2 test returns a larger value for the separation and predicts that the data are consistent with all the maser emission arising within a projected radius of 0.018 pc (3700 AU) centred on the submm continuum peak. Sources with large separations have extended submm sources (Mon R2, S146, L1287, HHL5 and W48) with less-well defined peaks, and are active sites of star-formation, presumably with two or more sources of heating. Higher resolution single beam or interferometric observations of these sources would be required in order to resolve out this extended emission and see if compact sources are responsible for these maser sites, and it is not surprising that these sources have the worst association. Discarding the source with the largest contribution to χ^2, Mon R2, reduces this radius from 0.018 pc to 0.010 pc (2000 AU). Conversely the compact sources have extremely good associations; the very small separations indicate that these masers are occurring at localised sites of star formation.

Fig. 4.6 shows the cumulative distribution for those sources with separations less than 0.05 pc (i.e. the most compact submm sources which tend to have comparable errors. This accounts for approximately 50 per cent of the sample). Also plotted on the figure are the predicted distributions for a shell model (solid line) and for uniform spherical model (broken lines). A KS test on this data shows that there is only a 0.3 per cent chance that the best shell model is consistent with the data. On the other

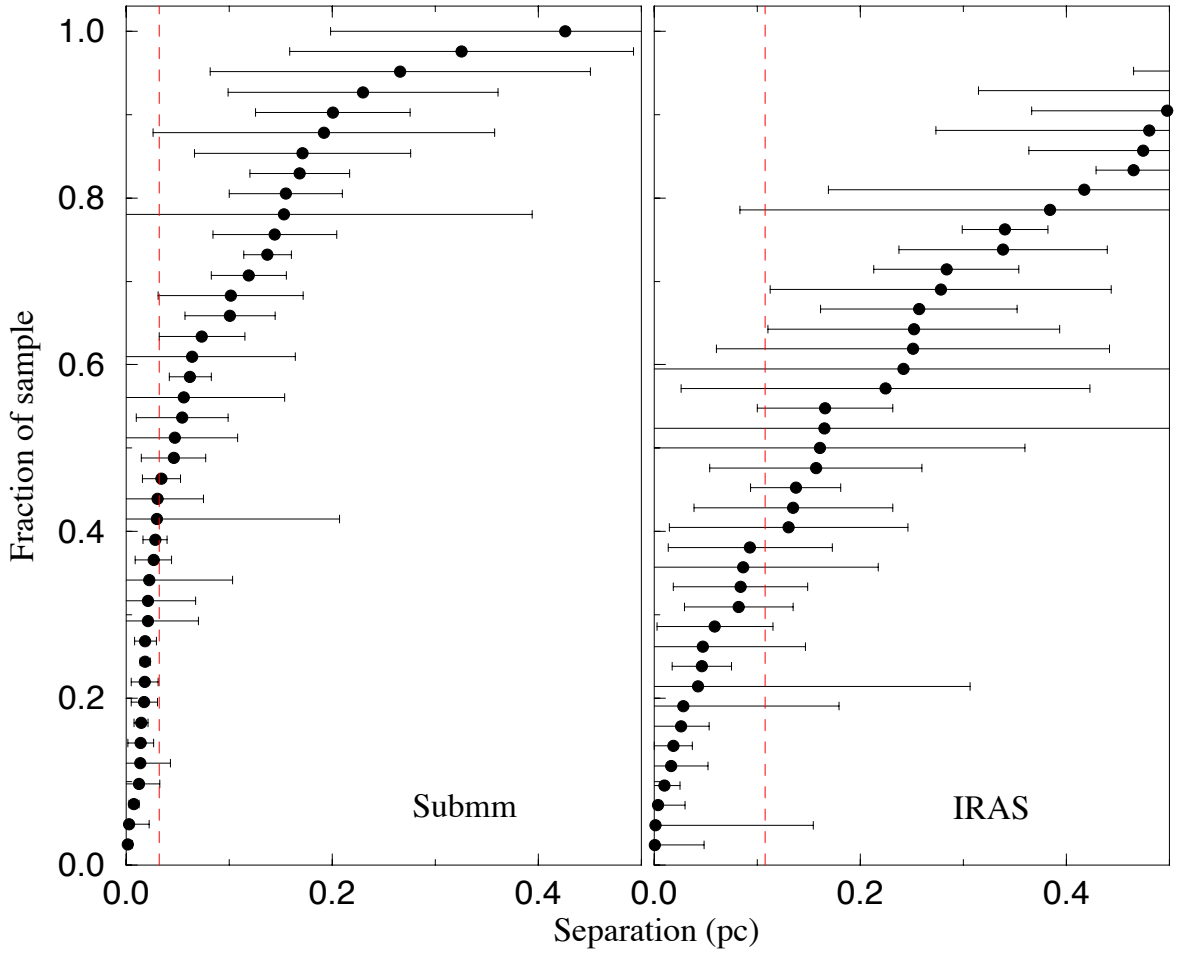

Figure 4.5. Cumulative distribution of maser separation from submm, and *IRAS* sources. The error bars are 1σ and the *IRAS* errors are a combination of the x and y errors. The dashed vertical line indicates the minimum separation consistent with all the data.

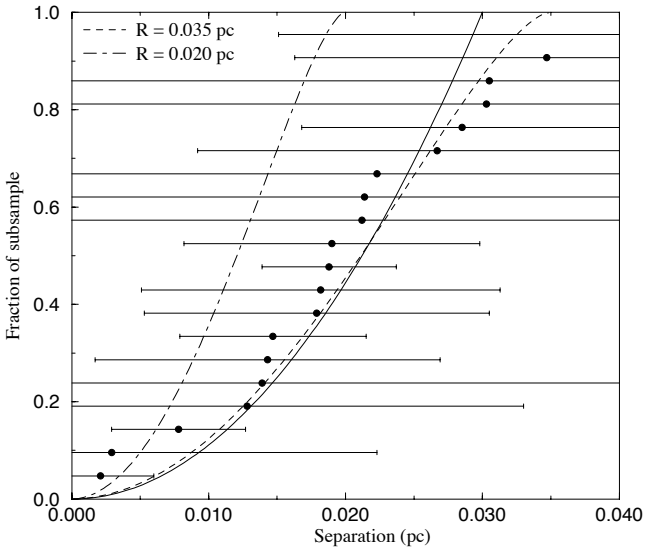

Figure 4.6
Cumulative distribution of maser separation from the submm sources compared with expected distributions. Only the nearest 50 per cent are included (c.f. Fig. 4.5). The broken lines show the expected distribution for a spherical model. The solid line is the expected distribution for a shell model with radius 0.03 pc. The two points with separations larger than 0.04 pc are not visible.

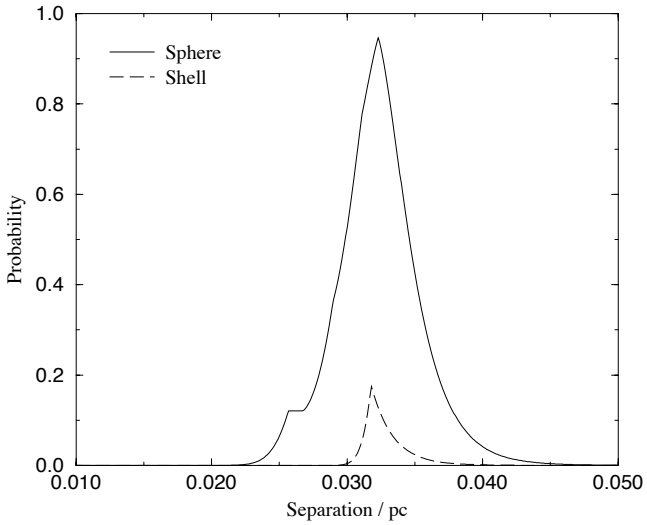

Figure 4.7
Result of KS test on separation of masers from submm sources. The solid line is the test for a spherical model and the dashed line is for a shell model.

hand there is a 77 per cent probability that the masers are uniformally distributed within a sphere of radius 0.035 pc; this model is shown by a dashed line in Fig. 4.6. If only the data within 0.04 pc is selected (19 data points) the fit improves tremendously. Fig. 4.7 shows that there is a 96 per cent probability that these water masers are uniformally distributed within a sphere of radius 0.0323 pc (6000 AU). The shell model is clearly inconsistent with the data. Performing a Kuiper test on these data shows that there is only a 77 per cent probability of the two sets being equivalent but the position of this maximum probability does agree with the KS result. If the result from the χ^2 test (0.012 pc) is scaled by the factor predicted from the computer simulation, the resulting radius, of 0.0316 pc, is in extremely good agreement with the radius derived from the KS analysis. It seems clear that even though the KS test uses a subset of the data (with zero errors on each point) this method still gives a result comparable with the χ^2 technique which uses all of the available data including errors.

For the *IRAS* data the reduced χ^2 value, assuming positional coincidence between the *IRAS* sources and the water masers, is 4, and makes this hypothesis untenable. χ^2 is minimized for an *IRAS*-maser separation of 0.022 pc but the reduced χ^2 value of 3.6 means that it is extremely unlikely that there is any association at this distance. Performing the modified χ^2 test on the *IRAS* data shows that the data are consistent with the *IRAS* point sources being within 0.11 pc (10 arcsec) of the masers and within 0.08 pc (6 arcsec) of the submm sources. Given the large *IRAS* beam and the positional accuracy of the satellite this result is consistent with an association but does show that better data, in the form of mid-infrared observations, are desirable to improve on these figures. Sources with particularly bad associations are IRAS 03262, 18032, 21078 and 21418 and these sources were not included in the analysis. Using a KS test there is no evidence to suggest that the masers are uniformly distributed within, or on, a sphere near to the *IRAS* sources. *IRAS* is sensitive to the properties of the star forming region as a whole, allowing the water maser to be classified as STAR or SFR, but, unsurprisingly, can not be used to investigate the small scale properties of masers.

The comparison of the radio and maser data shows that for some objects the offset is very small, less than 1 arcsec, and for a few sources the offset is very large, greater than 1 arcmin. Generally the large offset emission is very diffuse and the small offset radio emission is from UC H II regions. As for the submm sources, the more compact the emission is, the better the association, although UC H II regions are usually offset by about an arcsecond from water masers (e.g. Forster & Caswell 1989). Performing a χ^2 test on the radio data shows that once the sources with separations greater than 5σ are removed the data are consistent with the masers being within 0.016 pc of the radio sources. Whilst this value is comparable with that obtained for the submm continuum the number of sources associated with compact radio emission in this sample is small (18 sources). Comparing the observed distribution with theoretical models indicates that there is no evidence whatsoever that the masers are uniformally distributed within, or on, a sphere near to the radio continuum sources. A general result, also seen by Tofani *et al.* (1995), is that for this sample UC H II are very rare even though masers are present. This is because the dynamical lifetime of UC H II regions is so short that they are not present in much of the sample, either because the sources have evolved into large cometary H II regions or are too young to possess an UC H II region.

In this sample more than 90 per cent of the water masers had an associated submm source and the positional coincidence is better for this type of source than for *IRAS* or radio H II regions. Although UC H II regions do show very good positional agreement with the maser they are much less common in this sample than submm sources. In conclusion, water masers in star forming regions are good tracers for submm cores.

4.2.2 Velocity offsets

Fig. 4.8 shows the distribution of water maser velocity relative to the molecular cloud. The distribution favours low velocity over high velocity masers with only two sources possessing masers with relative velocities greater than 25 km s^{-1}. The velocity distribution is approximately Gaussian with a FWHM

of 15 km s^{-1}. ^{12}CO spectra suggest that molecular clouds have velocity widths of at least 10 km s^{-1} FWHM so that the vast majority of water masers have velocities consistent with the progenitor cloud. This result is consistent with that of Tofani *et al*. (1995) who also found that the maser velocities are within v_{blue} and v_{red} of the molecular cloud. This is a very different results to that found in sources with very luminous masers, such as W51 (Genzel *et al*. 1981), which have many high velocity maser features with relative velocities up to 100 km s^{-1}. In contrast the sources in this sample have very simple maser spectra with usually fewer than 5 components, are low luminosity and are low velocity. This could be due to a sensitivity problem. The strongest masers in W51 are low velocity, although the low velocity components have the largest proper motions, and it could simply be that the high velocity components for sources in this sample are too weak to be detected.

Comparing the maser velocities with maser separation from the submm continuum (Fig. 4.9) indicates that high velocity masers have small separations and low velocity masers have larger offsets. This is consistent with an expanding shell producing the masers. Although only those sources with a separation of less than 0.2 pc have been included in this analysis, i.e. two thirds of the sample, the earlier statistical analysis suggesting that the masers are randomly distributed within a sphere of radius 0.032 pc suggests that the data are not really good enough for this kind of analysis. Indeed, if only those sources are included which were used for the KS analysis in the previous section, no correlation of separation with velocity is seen. This may, in part, be due to large variations observed in the velocity of the strongest component – an average velocity has been used in Fig. 4.9 – which makes it extremely difficult to find a correlation unless masers only ever have a single component.

4.2.3 Sample properties

Fig. 4.10 shows histograms of the derived parameters. They show that the sample consists of sources covering a large range of parameter space. The column density of hydrogen nuclei has been converted to visual extinction, A_V, by using the calibration $N(H + 2H_2) = 1.8 \times 10^{25} A_V$ m^{-2} (Bohlin *et al*. 1978) which is just a scaling factor. Large values of A_V (or column density) are probably unreliable from this simple fit and recent work suggests that this A_V calibration factor could be as much as four times too large (Casanova *et al*. 1995; Clayton & Mathis 1988) implying smaller values for A_V. Many of the fits with large values of A_V are implying that a two component fit would be a better approximation since these sources have SEDs slightly wider than a simple blackbody.

A point worth noting is that many class II-D sources have $A_{V(fit)} > 500$ mag which is equivalent to approximately 150 mag extinction in J (Mathis 1990). Class II-D objects have near-infrared sources visible in J, and, by definition, the source must still be visible through this extinction. Since the continuum observations produce an angle averaged column density, a more reliable measure of the line-of-sight column density can be derived from line observations. For example, IRAS 18032 has an extinction of 1000 mag from the dust fit but only 200 mag from the C^{18}O observations. Unfortunately a visual extinction of 200 mag, equivalent to 60 mag extinction in J, is still too large for a near-infrared source to be visible. The only way to reconcile a J extinction of 60 mag and the detection of a near-

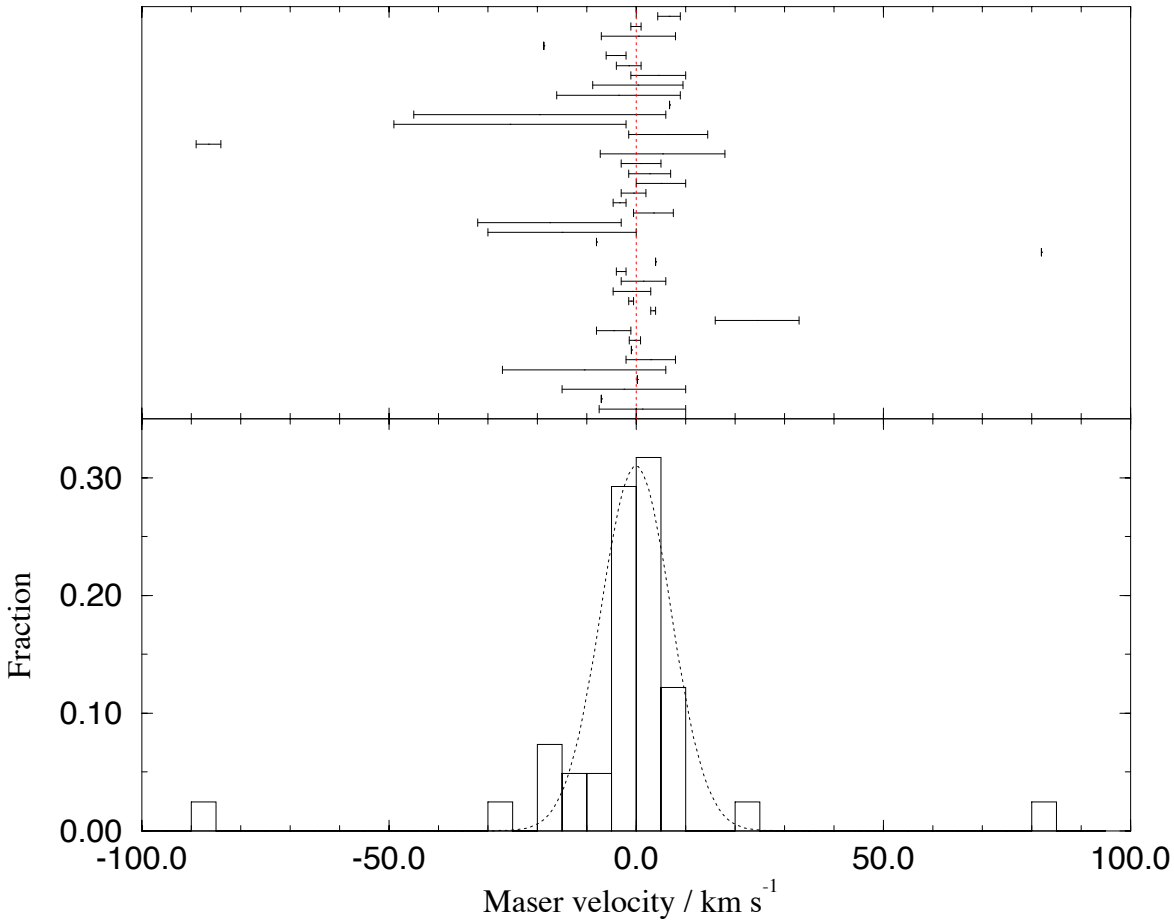

Figure 4.8. Velocity of water masers relative to the molecular cloud. The curve on the lower plot is a Gaussian of FWHM 15km s^{-1}.

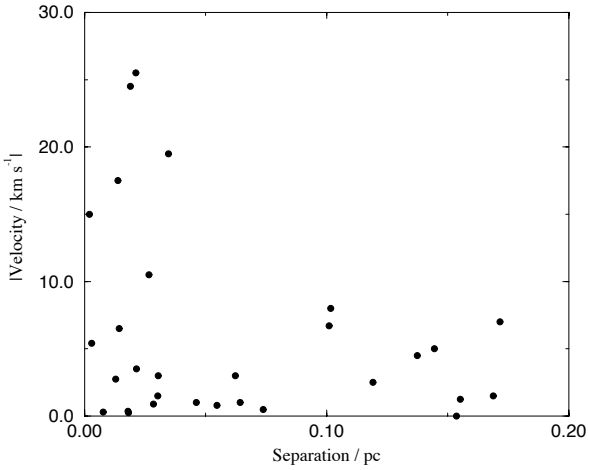

Figure 4.9
Maser velocity against separation from submm continuum source. For clarity errors on the separations have not been shown.

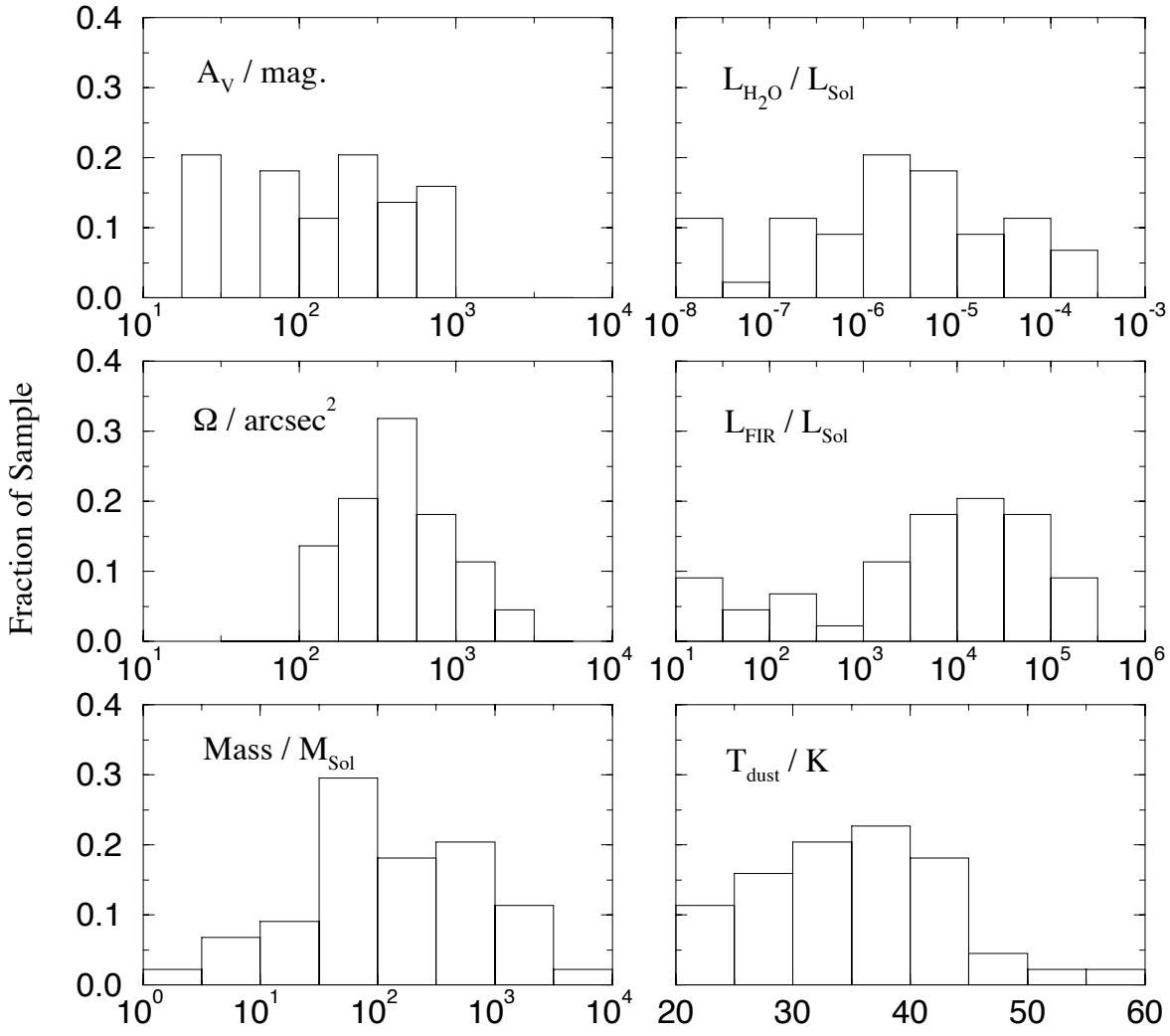

Figure 4.10. Histograms of global sample properties.

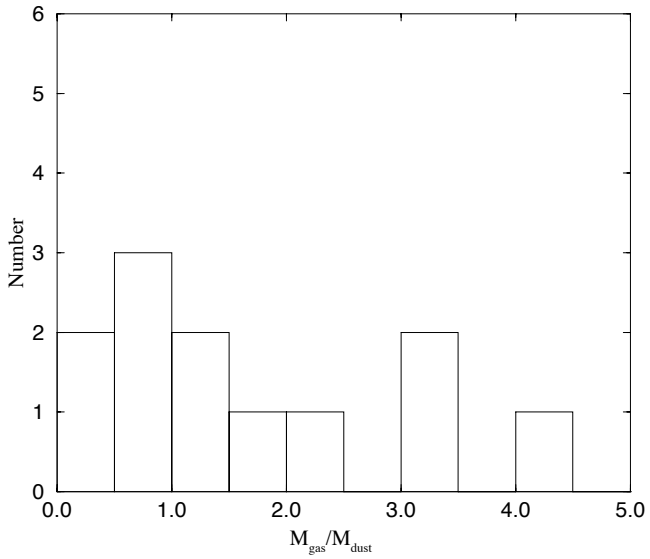

Figure 4.11
Histogram of ratio of masses derived from gas and masses derived from dust

infrared source is to invoke an orientation effect. A class II-D object still has an appreciable accretion disk and if the orientation of the disk is close to the plane of the sky the central star would be visible in the near-infrared. Submm observations would also detect the molecular material in the disk and imply a large column density simply because the central region of the disk is much smaller than the beam. This is *especially* true for sources, such as IRAS 18032, which are a few kpc away. A disk structure would also explain why the average column density derived from the continuum data is so much larger than the line-of-sight column. Another explanation is that the sources have a clumpy structure. The near-infrared source could be visible between clumps where the extinction is much less than the average measured by the large beam.

Masses have also been calculated using the $C^{18}O$ observations (see table 3.8). Of the sources detected in the submm continuum which also have $C^{18}O$ data, the calculated masses agree, within a factor of two, in 50 per cent of cases. All but one, IRAS 22142 which is undetected in the continuum, agree within a factor of four (see Fig. 4.11). IRAS 18032 was only partially mapped so it is not surprising that the mass derived from the line observations is 0.3 of the mass determined from the continuum observations. The IRAS 22198 mass included emission from the outflow and so is an overestimate of the core mass. Dust masses have used the calibration of Hildebrand (1983) whereas more recent reviews of dust opacity suggest that these masses should be $\sim$ 50 per cent larger (Gordon 1995). Gas masses have been derived assuming local thermodynamic equilibrium (LTE), that the $C^{18}O$ line is optically thin and that the assumed abundance of 1.6×10^{-7} relative to H_2 (Stutzki & Güsten 1990) is correct for all sources. An excitation temperature of 50 K was also assumed for the sources which had no propyne observations. In fact if the sources were slightly optically thick or had higher excitation temperatures the mass would be increased so these values are really lower limits (especially in sources which have not been fully mapped) and masses derived by these two independent methods are therefore consistent. It should also be noted that whereas $M_{\rm gas} \propto T_{\rm ex}$, $M_{\rm dust} \propto 1/T_{\rm d}$ (where the proportionalities are

only approximate) and that the dust temperatures used are the *fitted* values and the gas temperatures used are from propyne observations where available.

Since estimates for the mass of each core and upper limits to the source sizes are available, it is a simple matter to estimate the density. Assuming a uniform sphere which is the same size in the z direction as it is on the sky, the density is given as $\rho = 3M/(4\pi R^3)$. Whilst this underestimates the peak density dramatically (for example isothermal spheres at the point of collapse have an inverse square density law) this method does provide a lower limit to the maximum density. Using this technique all of the sources in the sample have mean densities greater than 10^5 cm^{-3} and 75 per cent have densities greater than 10^6 cm^{-3}. Some sources with particularly low apparent densities, e.g. IRAS 23314+6033, reflect the fact that there are two sources within the beam.

Of the 16 sources observed for high temperature gas, propyne and methyl cyanide, 7 sources were strong enough to allow rotational temperatures to be calculated (table 3.8). Only 4 of those were strong enough in methyl cyanide to obtain temperatures. In all cases the propyne observations were sensitive to low temperature gas, $\sim$ 50 K, agreeing with the fitted dust temperatures. Three of the sources detected in methyl cyanide indicated temperatures greater than 170 K. This suggests that the bulk of the propyne emission comes from a cool, extended halo surrounding a dense, hot core responsible for the methyl cyanide emission. This result has been found before, for example in Orion, SGR B2 and DR21 (Churchwell & Hollis 1983; Wang *et al*. 1993) and various reasons have been suggested. Wang *et al*. (1993) favour the conclusion that the methyl cyanide and propyne are in different spatial locations, whereas Wouterloot & Hollis (1983) favour the two molecules co-existing but the methyl cyanide emission being dominated by that from a warm dense region and the propyne emission dominated by a cool, extended halo. I favour the second explanation: methyl cyanide requires a large density to be thermalized (20 times larger than the propyne transition requires) and it is more likely that only the dense, hot regions have enough molecules in the upper state to be visible. The gas further out will be cooler and also less dense; even if there is more methyl cyanide in the cooler halo this will not be detected. One source does not fit in to this model; IRAS 21078 has rotational temperatures of 71 and 82 K (for propyne $J = 14 \rightarrow 13$ and methyl cyanide respectively), twice the fitted dust temperature, and 171 K for propyne $J = 20 \rightarrow 19$. In this case there is not enough methyl cyanide present in the hot core to be visible and the emission is dominated by the cooler gas. The propyne is excited such that the high J transitions are only thermalised in the core and not in any halo emission, as suggested above.

The relationship between the detection of propyne and the existence of a H II region can also be investigated. Of the sources which had detectable propyne seven sources had compact radio emission and two had none. One of these was IRAS 21078 which does have a large H II region but does not seem to be associated with the submm core (§5.6). For those sources in which propyne was not detected, five had no radio and three had compact radio sources. IRAS 00338 is extremely weak (0.3 mJy), and GGD 29 has a strong radio jet.

The hypothesis that the sources with detectable propyne also have H II regions is supportable, al-

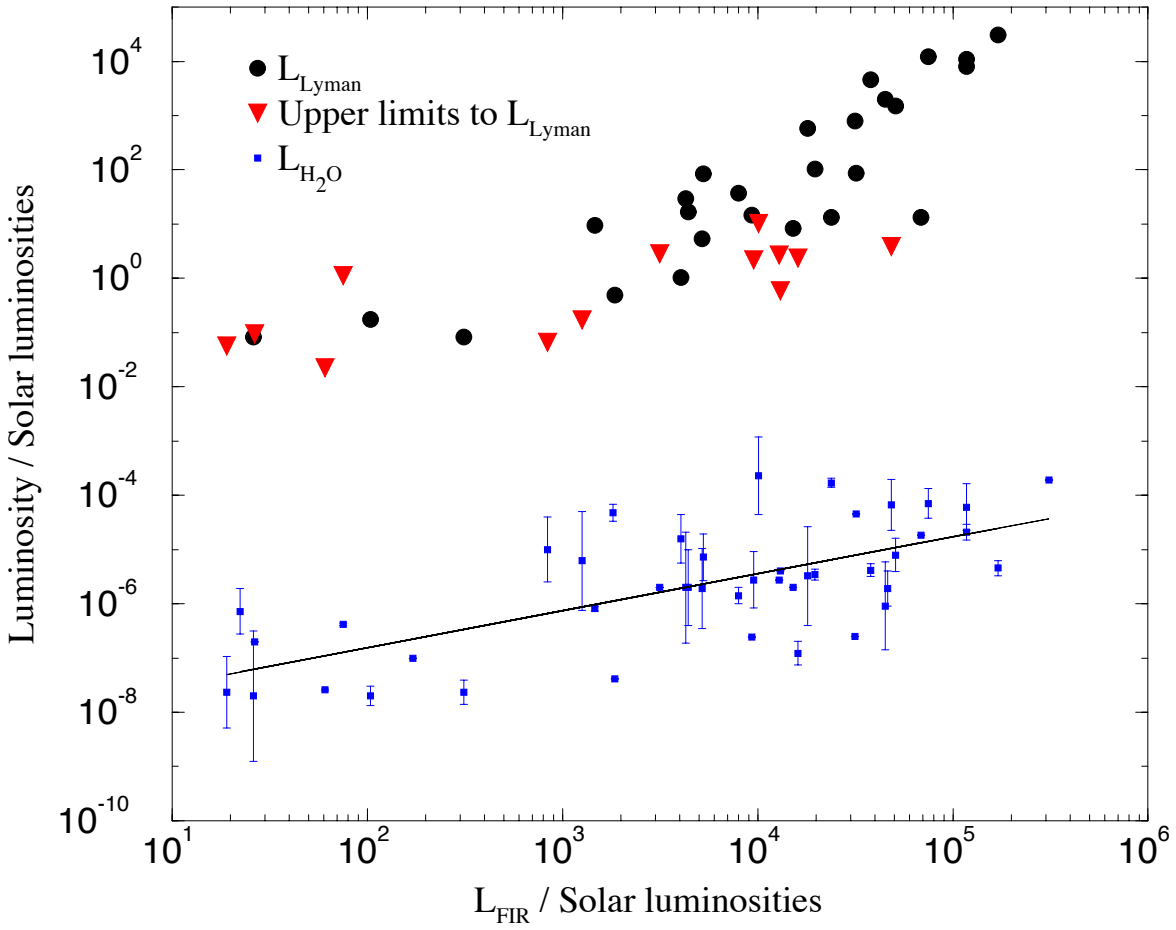

Figure 4.12. Lyman photon luminosity and water maser luminosity against far infrared luminosity. The vertical lines in the water maser data are not error bars but show the maximum and minimum values observed.

though not clear cut, and is not altogether surprising if the propyne emission arises from the region near to the ionized gas.

4.2.4 Luminosity comparisons

Fig. 4.12 shows how the inferred Lyman luminosity and isotropic water maser luminosity compare with the far-infrared luminosity. The Lyman luminosity, which is directly proportional to the thermal radio flux, does seem to be correlated with the luminosity seen in the dust (with a correlation coefficient of 0.87). If this Lyman flux is then converted to stellar type (§A.4) the reason for this correlation becomes clear. Fig. 4.13 shows that for most of the sources with detected radio continuum $L_{\rm star} \approx L_{\rm FIR}$. This indicates that in these cases the luminosity seen in the dust can be *entirely* accounted for by a single O or B star at the centre. Sources just below the line $L_{\rm star} = L_{\rm FIR}$ either have energy available

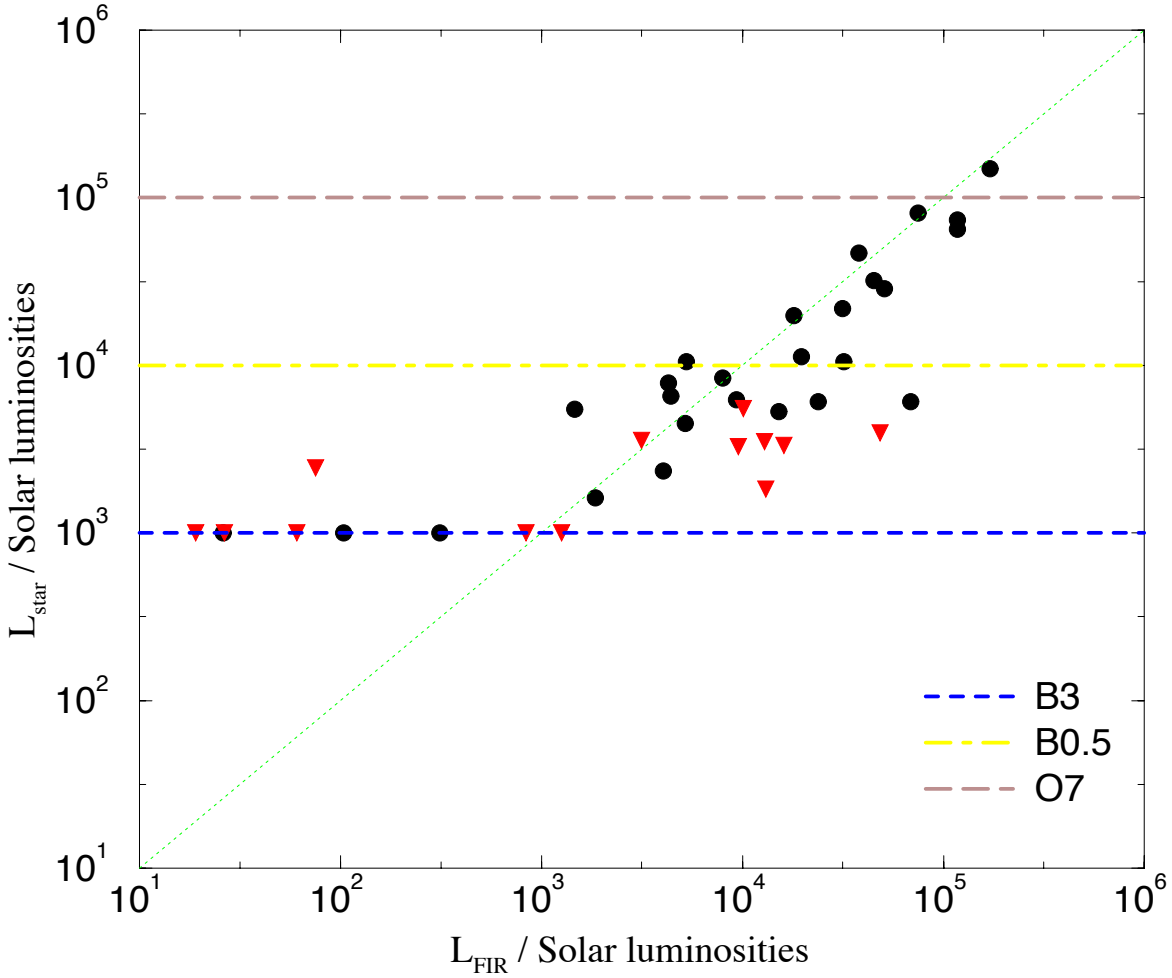

Figure 4.13. Stellar luminosity against far-infrared luminosity. The diagonal line is $L_{\rm FIR} = L_{\rm star}$. The horizontal lines show the luminosity associated with certain stellar types. Filled circles are sources detected at radio wavelengths and triangles indicate upper limits.

from other mechanisms, such as gravitational energy if the object is still collapsing, as well as the stellar component or the embedded star is not yet main-sequence. As sources move further below this line no radio continuum is detected suggesting that the main energy source is still accretion. All of the sources detected in the radio continuum which have $L_{\rm FIR} > 1000$ L$_\odot$have predicted $L_{\rm star}$ within an order of magnitude of the observed value suggesting that in these objects at least 10 per cent of the luminosity seen in the dust is accounted for by the existence of at least a B3 star.

HH6 and IRAS 18273+0113 have an excess of radio continuum (equivalent to a B3 star) suggesting that only 10% of the star's energy is absorbed by the dust. The greybody fits to HH6 and IRAS 18273 suggest that these sources have visual extinctions of approximately 300 mag. implying that 90% of the energy from a central B3 type star escapes due to anisotropic emission. Line observations suggest a slightly more realistic visual extinction of about 30 mag. These sources are right on the limit

of the Panagia (1973) analysis and are really consistent with a central object less luminous than a B3 star suggesting that the radio emission comes from another mechanism.

Fig. 4.12 also shows that the maser luminosity is related to the far-infrared luminosity by a power law. The best regression fit line for my sample is given by,

$$\frac{L_{\mathrm{H_2O}}}{\mathrm{L}_\odot} = 7 \times 10^{-9} \left(\frac{L_{\mathrm{FIR}}}{\mathrm{L}_\odot} \right)^{\frac{2}{3}}, \tag{4.4}$$

whereas Palagi *et al.* (1993) (hereafter PCC) report

$$\frac{L_{\mathrm{H_2O}}}{\mathrm{L}_\odot} = 5 \times 10^{-10} \left(\frac{L_{\mathrm{FIR}}}{\mathrm{L}_\odot} \right)^{1.1}, \tag{4.5}$$

for sources in the first Arcetri atlas and Felli *et al.* (1992) (hereafter FPT) report

$$\frac{L_{\mathrm{H_2O}}}{\mathrm{L}_\odot} = 1.1 \times 10^{-9} \left(\frac{L_{\mathrm{FIR}}}{\mathrm{L}_\odot} \right)^{1.01}, \tag{4.6}$$

for a sample of molecular outflows. The analyses of PCC and FPT used the *IRAS* luminosity as opposed to a fitted luminosity but this should not make a significant difference to the results. The fact that the power-law relation found in my sample is different to that reported by others must reflect the small size of the sample: The PCC sample included 125 sources and FPT included 56. These results show a general trend that the water maser luminosity increases with the total energy available in the region but is approximately 10 orders of magnitude smaller. Although the relation holds over more than 5 orders of magnitude of far-infrared luminosity, the huge variation in maser luminosity (sometimes a variation of 3 orders of magnitude in a few months) and large scatter about the line of best fit (the correlation coefficient is approximately 0.7 in all three samples) indicates that when more energy is present in a system more energy is available to power a water maser.

If the scale is magnified though, the correlation becomes less clear, and in fact suggests there are two distinct distributions; sources with $L_{\mathrm{FIR}} > 1000$ $\mathrm{L}_\odot$ and sources with $L_{\mathrm{FIR}} < 1000$ $\mathrm{L}_\odot$. The high L_{FIR} sources have mean water maser luminosities of 10^{-5} $\mathrm{L}_\odot$ whereas the low FIR luminosity sources have mean water maser luminosities of 10^{-7} $\mathrm{L}_\odot$. This is almost certainly a feature of the data set being too small since there is a distinct lack of sources with $100 < L_{\mathrm{FIR}}/\mathrm{L}_\odot < 1000$ and PCC do not show this effect at all.

It should also be checked that these data are all due to water masers and not just thermal emission. All of the sources detected by my observations with the VLA were point-like and this places a limit on the size of these objects at less than 0.2 arcsec. The Rayleigh-Jeans brightness temperature of $S_\nu/\Omega = 2\mathrm{k}T_\mathrm{b}/\lambda^2$ can be written in the more useful form of

$$\left(\frac{T_\mathrm{b}}{\mathrm{K}} \right) = 2.6 \times 10^3 \left(\frac{S_\nu}{\mathrm{Jy}} \right) \left(\frac{\theta}{\mathrm{arcsec}} \right)^{-2}. \tag{4.7}$$

For the weakest source detected by my VLA observations, L988-A with a flux density of 0.07 Jy at a distance of 0.7 kpc, the brightness temperature is > 4500 K. This is still consistent with thermally

excited emission, whereas the strongest detection from the VLA observations, GL7009S, has $T_b > 6.8 \times 10^6$ K which does seem to imply maser emission.

Using a more probable value for the size of a maser spot of $R_{\rm maser} = 10^{11}$ m (Genzel 1986; Elitzur *et al*. 1989), and rewriting equation (4.7) in terms of the actual source dimension,

$$\left(\frac{T_{\rm b}}{\rm K}\right) = 3.458 \times 10^{31} \left(\frac{S_\nu}{\rm Jy}\right) \left(\frac{\lambda}{\rm cm}\right)^2 \left(\frac{D}{\rm kpc}\right)^2 \left(\frac{R_{\rm maser}}{\rm m}\right)^{-2}, \qquad (4.8)$$

a 22-GHz maser with a flux density of 1 Jy at a distance of 1.0 kpc would have a Rayleigh-Jeans brightness temperature, $T_{\rm b}$, of 5×10^9 K. Once the extremely small size is assumed then even the weakest maser detected by my VLA observations, L988-A, has a brightness temperature of 2×10^8 K which shows that thermal emission cannot be responsible.

Selection effects

It is also possible that this correlation is entirely due to a selection effect. The high luminosity sources are simply those at the largest distance from us – i.e. at large distances it is only possible to see bright sources, and weak objects at large distances are not detected. This should not be a problem in this case for a number of reasons. The sample was selected from the existence of a maser with kinematic distance less than 5 kpc and not by the existence of a maser above a given flux density (because no flux-limited survey of water maser sources exists covering a reasonably large area *and* the masers are so variable that a flux-limiting sample is meaningless). The fact that the vast majority of these sources has an associated FIR flux indicates that the sample is not biased by the FIR data (mostly from *IRAS*). The main problem with the FIR data is that some of the sources do not seem to be directly associated with the *IRAS* point source even though they do have an embedded core. In these cases the FIR luminosity could be incorrect by an order of magnitude; luckily most sources do not have this problem and any correlation would not be affected by such bad points.

The apparent correlation between the maser and FIR luminosities could have been influenced in a number of ways:

i. if large errors were present in the estimated source distances,
ii. in the selection of the source sample, and
iii. by the variability in the maser luminosities.

These will be discussed in turn.

i. Distance errors Although the ratio of luminosities is independent of assumed distance, errors in the distances could introduce an apparent correlation e.g. consider a sample of *identical* sources, all at the same *true* distance, but observed with errors in the distance estimates. This would

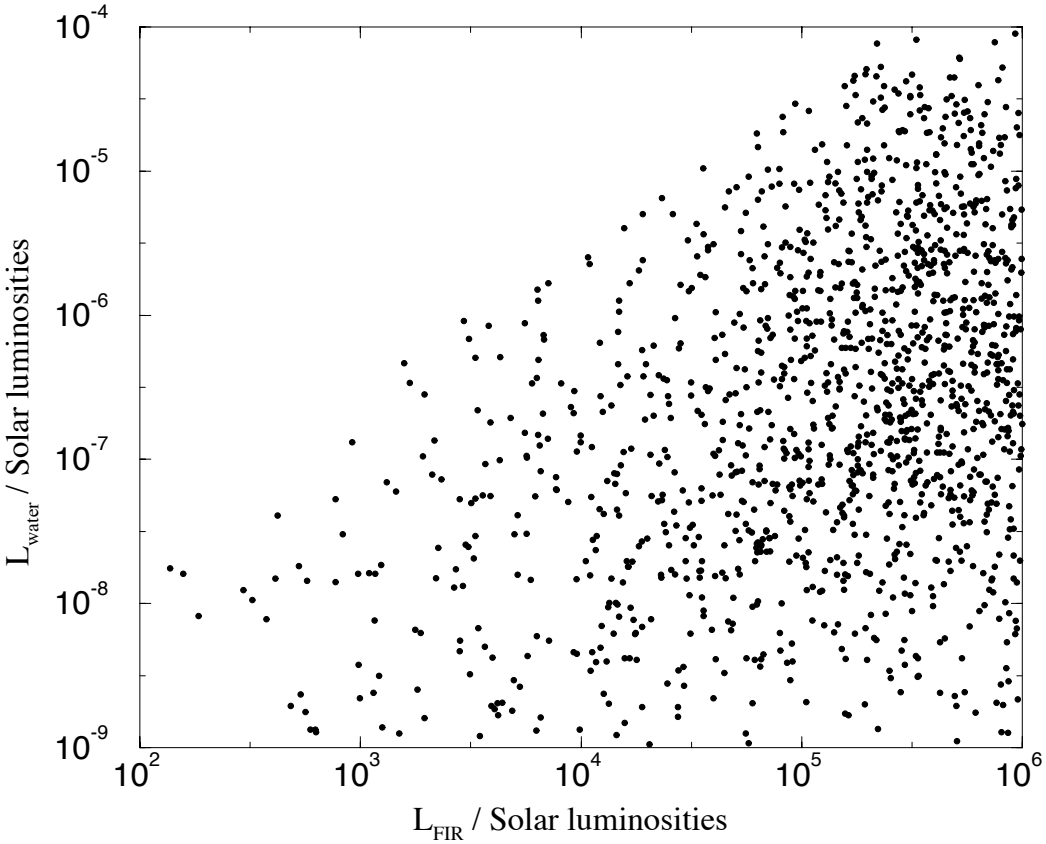

Figure 4.14. Water maser luminosity against FIR luminosity for a randomly generated sample of sources.

produce a perfect correlation in the luminosities, albeit for a pathological original source population. Since, however, the observed correlation extends over a range of some five orders of magnitude in FIR luminosity and over more than two and a half magnitudes in maser luminosities, to produce the observed correlation would have required completely unrealistic distance errors i.e. errors considerably exceeding an order of magnitude. I conclude that distance errors are unlikely to have been a significant factor.

ii. Sample selection A Monte Carlo simulation has been carried out in which 10 000 sources were generated each having a randomly ascribed distance (up to 5 kpc), maser luminosity (in the range $10^{-9} < L_{\mathrm{H_2O}}/\mathrm{L}_\odot < 10^{-4}$) and FIR luminosity (in the range $10 < L_{\mathrm{FIR}}/\mathrm{L}_\odot < 10^6$). Sources were then selected which had a water maser flux within a given range (using the known distance to the source) and finally selected by those which had a detectable FIR integrated intensity. The results of this Monte-Carlo simulation are shown in Fig. 4.14. The upper limit of this plot is

entirely due to the removal of high luminosity masers with weak FIR sources from the sample (i.e. those sources with FIR flux below a certain value have been removed). Removing the FIR flux constraint leads to a scatter plot with no apparent correlation.

This indicates that whilst it is possible to generate a plot similar to Fig. 4.12 from a random sample, this requires that the upper limit to detectable water maser flux is constrained as well as the lower limit, which has not been done for the observed sample.

iii. Maser variability It is well known that the luminosity of an individual water maser can vary by three or four orders of magnitude over relatively short timescales. In practice, this implies that the masers will have been included in the sample only if they happened to be emitting relatively strongly within the last few years. The observed correlation is then essentially between maximum (or near maximum) maser luminosity and FIR luminosity (which is, of course, a reasonable result on physical grounds). Since FIR emission was detected from *all* the masers in the sample, it is not obvious how a spurious correlation could have been introduced.

To summarize, although it does not seem to be possible to ascribe the observed luminosity correlation to spurious factors, it is clear that my result is at best a tentative one (although supported by other studies). The result does however fit in with the suggestion that maser activity is present at all stages of the evolution of FIR cores, the lack of an *observed* maser in particular cases being attributable to maser variability and/or the effects of beaming.

References

Adams F. C., Shu F. H., 1986, *ApJ*, 308, 836
Adams F. C., Lada C. J., Shu F. H., 1987, *ApJ*, 312, 788
André P., Ward-Thompson D., Barsony M., 1993, *ApJ*, 406, 122
Bohlin R. C., Savage B. D., Drake J. F., 1978, *ApJ*, 224, 132
Casanova S., Montmerle T., Feigelson E. D., André P., 1995, *ApJ*, 439, 752
Churchwell E., Hollis J. M., 1983, *ApJ*, 272, 591
Clayton G. C., Mathis J. S., 1988, *ApJ*, 327, 911
Eiroa C., Casali M. M., 1992, *A&A*, 262, 468
Elitzur M., Hollenbach D. J., McKee C. F., 1989, *ApJ*, 346, 983
Felli M., Palagi F., Tofani G., 1992, *A&A*, 255, 293
Forster J. R., Caswell J. L., 1989, *A&A*, 213, 339
Genzel R., 1986, in *Masers, Molecules and Mass Outflows in Star Forming Regions*, ed. Haschick A. D., p. 233, Haystack Observatory, Westford, MA
Genzel R., *et al*., 1981, *ApJ*, 247, 1039
Gordon M. A., 1995, *A&A*, 301, 853
Hildebrand R. H., 1983, *QJRAS*, 24, 267
Krügel E., Chini R., 1994, *A&A*, 287, 947
Kuiper N. H., 1962, *Proc. Koninklijke Nederlandse Akademie van Wetenschappen, ser. A*, 63, 38
Lada C. J., Wilking B. A., 1984, *ApJ*, 287

Ladd E. F., Lada E. A., Myers P. C., 1993, *ApJ*, 410, 168
Mathis J. S., 1990, *Ann. Rev. Astron. Astrophys.*, 28, 37
McCutcheon W. H., Dewdney P. E., Purton C. R., Sato T., 1991, *AJ*, 101, 1435
Miralles M. P., Rodríguez L. F., Scalise E., 1994, *ApJS*, 92, 173
Myers P. C., Ladd E. F., 1993, *ApJ*, 413, L47
Palagi F., Cesaroni R., Comoretto G., Felli M., Natale V., 1993, *A&AS*, 101, 153
Panagia, 1973, *AJ*, 78, 929
Press W. H., Teukolsky S. A., Vetterling W. T., Flannery B. P., 1992, *Numerical Recipes in* FORTRAN, Cambridge University Press, Cambridge, 2nd edn.
Sleath J. P., 1995, *A new model of spiral galaxies based on propagating star formation*, Ph.D. thesis, University of Cambridge
Stutzki J., Güsten R., 1990, *ApJ*, 356, 513
Tofani G., Felli M., Taylor G. B., Hunter T. R., 1995, *A&AS*, 112, 299
Wang T. Y., Wouterloot J. G. A., Wilson T. L., 1993, *A&A*, 277, 205

Chapter 5

Detailed source analysis

This chapter will discuss in detail the sources for which the largest amount of data, as presented in chapter 3, has been obtained. Each section will begin with a short summary of previous observations and will then move on to discuss how the new observations contribute to our understanding of the structure and kinematics of each source. Maps already presented in chapter 3 are not repeated in this chapter.

5.1 IRAS 18164−1631

This infrared source was discovered by Jaffe *et al*. (1982) at 70 μm and subsequently detected by *IRAS* at 25- and 60-μm. Recent observations have not detected any radio continuum (<0.3 mJy at 6 cm; Hughes & MacLeod 1994).

CO observations (Stier *et al*. 1982) show a large (9 arcmin) source centred on the *IRAS* source, with a velocity of 20 km s^{-1}. CS $J = 7 \rightarrow 6$ observations (Plume *et al*. 1992) detected a line but reported no evidence of visible wings. Ammonia has been detected approximately 80 arcsec from the *IRAS* position (with no direction specified) and a rotation temperature of 18 K derived (Wouterloot *et al*. 1988). The water maser was detected by Jaffe *et al*. (1981) and has a broad ($\sim$ 2 km s^{-1} wide) line centred at 26 km s^{-1} (LSR). The maser was observed once in 1979 November, with an antenna temperature of 28 K, and again in 1980 April, with an antenna temperature of 22 K (approximately 30 Jy). Observations for the Arcetri Atlas failed to detect the line (<10.9 Jy).

My 850 μm continuum observation shows a weak source with extended emission to the north. The high-resolution image shows that this extended emission is due to two sources, but there is still a substantial background. The *IRAS* source is approximately 40 arcsec to the south east and is not associated directly with the submm cores which are outside the error ellipse. The SED is fitted extremely well by

Figure 5.1. IRAS 18164−1631

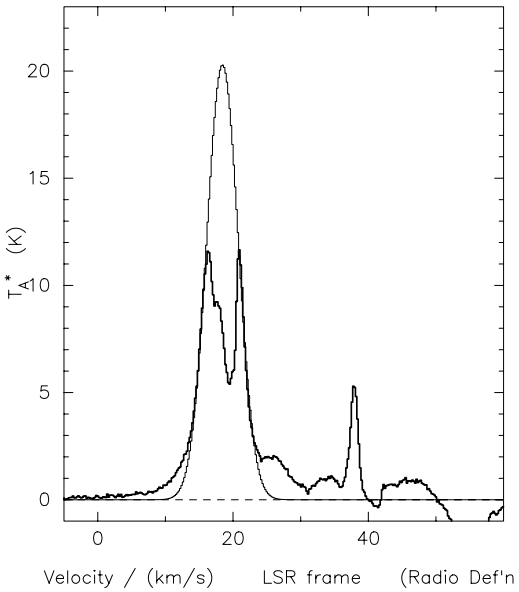

(a) Average ^{12}CO spectrum with fitted Gaussian (width = 5.4 km s^{-1} at 18.4 km s^{-1}).

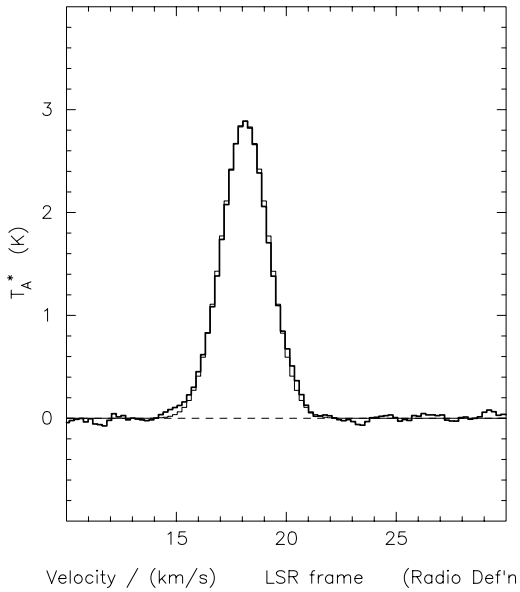

(b) Average C^{18}O spectrum with fitted Gaussian (width = 2.5 km s^{-1} at 18.1 km s^{-1}.)

a single temperature, 32 K, greybody curve and the calculated luminosity agrees with the value quoted in Jaffe *et al.* (1982). The large offset between the FIR peak and the submm cores suggests that the FIR fluxes used for the SED are overestimates and include substantial contributions from extended warm dust chopped out by the submm observing technique. The poor positional accuracy of the water maser observations of Jaffe *et al.* (1981), of 6 arcsec, makes it impossible to say much about the relationship between the maser and the submm emission, although it is clear that the weaker submm source is not responsible for the maser emission.

The average CO spectra are shown in Fig. 5.1. The ^{12}CO spectrum shows complicated structure towards the red end which is probably due to a foreground or background cloud. The emission feature at 38 km s^{-1} strengthens from the north west to the south east corner of the map (Fig. 5.2) and seems to be unrelated to the continuum or other line maps. This is convincing evidence that this feature is not associated with the submm continuum and suggests that it may indeed be associated with the *IRAS* source which is also to the south east. The negative feature at 50 km s^{-1} is due to contamination from a source in the reference beam. The main CO emission feature shows strong absorption in the line centre with blue- and, probably, red-shifted wings. The emission peak is centred between the two submm sources and extends from the north east to the south west. The C^{18}O column peaks on the southern submm source and there is an extremely abrupt drop off in emission 5 arcsec to the north in the vicinity of the weaker northern source. Interestingly the linewidths are actually widest on the weaker source. All the C^{18}O lines are Gaussian and there is no evidence for wings. Comparing the mass derived from the gas with that derived from the dust is unreasonable since the dust and gas emission seem to arise

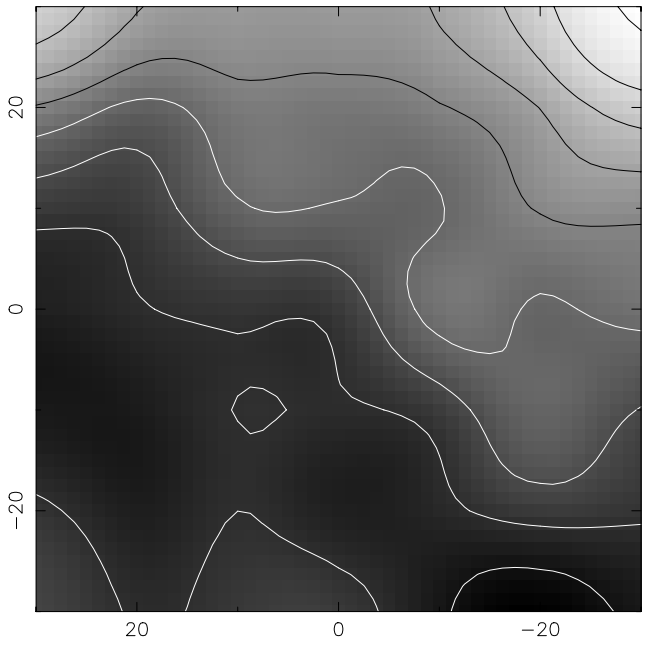

Figure 5.2
IRAS 18164−1631 ^{12}CO integrated intensity map between 36 and 40 km s^{-1}. Coordinates are in arcsec offsets from the submm core.

from different areas, although the southern continuum source is the main contributor to both. The CS spectra (Fig. 5.3a) are broad and show evidence for wings, contrary to the results of Plume *et al*. (1992); the higher excitation 7-6 transition may not be thermalised in the outflow. In common with the C^{18}O data the widest lines are associated with the northern submm source whereas the column density peak (Fig. 5.3b) is associated with the southern submm source.

Symmetric top observations give rotational temperatures of 56 K from propyne and 116 K from methyl cyanide. These values are much higher than the temperature derived from the ammonia observations. The abundance of methyl cyanide relative to propyne is 10 times lower than 'expected' – this is good evidence for the methyl cyanide emission arising from a central hot core although there may also be some contribution arising from warm gas located behind shocks.

5.2 IRAS 18455−0149

This source was first detected as part of a maser survey of 2 square degrees of the Galactic plane (Matthews *et al*. 1985). Subsequently reported as an extremely weak *IRAS* point source it was only detected at 12 μm.

My continuum observations show that the 850 μm source is essentially point-like with weak extended structure to the north east. High-resolution 450 μm observations show that this source does indeed consist of a compact core, approximately 5 arcsec diameter (0.1 pc at 4.79 kpc), with weak emission to the north east. The three *IRAS* upper limits make it impossible to fit a SED but the possible extremes have been shown in Fig. 5.4. The lowest possible temperature, constrained by the submm

Figure 5.3. IRAS 18164−1631

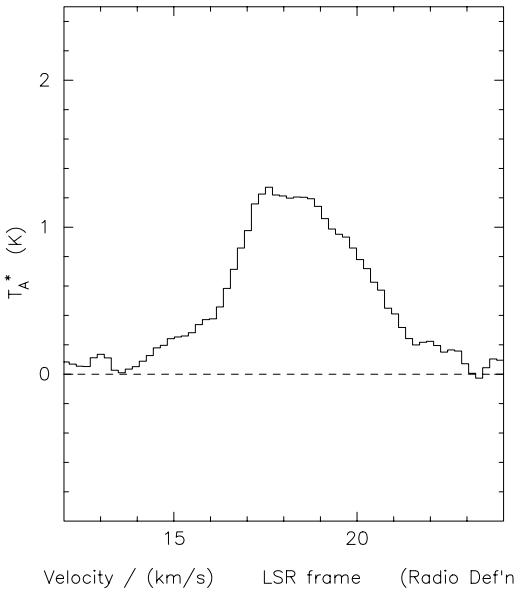

(a) Average CS spectrum.

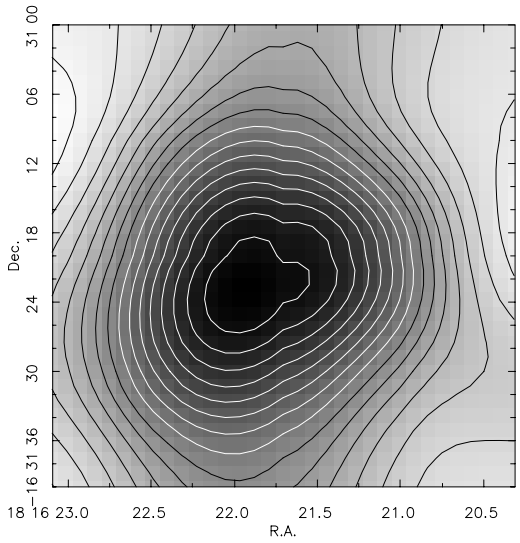

(b) CS $J = 5 \rightarrow 4$ integrated intensity map.

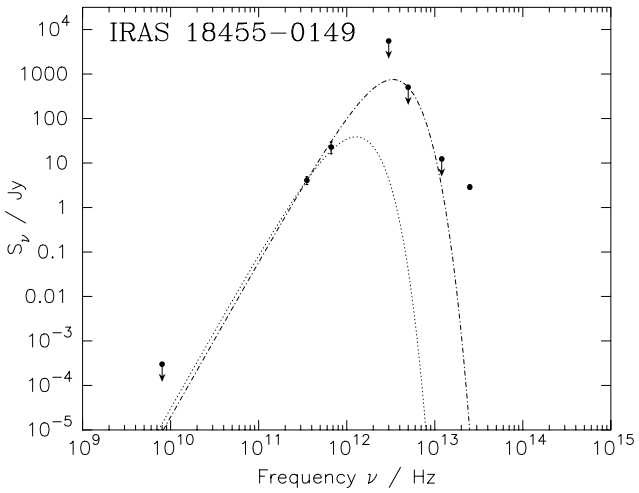

Figure 5.4
SED of IRAS 18455. The dotted line is $\beta = 1.5$, $T_{\rm d} = 14$ K, $\Omega = 490$ arcsec^2 and $\lambda_c = 47$ μm, and the dot-dashed line is $\beta = 1.5$, $T_{\rm d} = 42$ K, $\Omega = 43$ arcsec^2 and $\lambda_c = 85$ μm.

observations, is 14 K (giving a mass of 1300 $M_\odot$ and a luminosity of 437 $L_\odot$) and the upper limit, constrained by the *IRAS* points, is 42 K (giving a mass of 280 $M_\odot$ and a luminosity of 2.24×10^4 $L_\odot$). No compact radio emission was detected.

Line observations show that whilst the CS map is centred on the submm core as expected, the $C^{18}O$ integrated intensity map peaks approximately 5 arcsec to the north east. Without mapping a larger region it is difficult to know whether this offset is real. Average spectra are shown in Fig. 5.5 and it is obvious that better signal-to-noise is required for the CS lines. The secondary peak in the $C^{18}O$ data, at 77 km s^{-1}, does vary across the map but more integration time is required see this variation in detail. It is expected that the gas mass derived from the $C^{18}O$ is an underestimate to the actual mass simply

Figure 5.5. IRAS 18455−0149

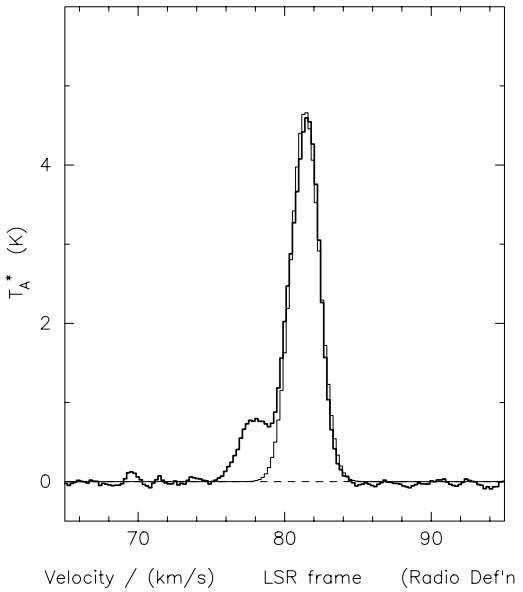

(a) Average $C^{18}O$ spectrum with fitted Gaussian (width = 2.3 km s^{-1} at 81.4 km s^{-1}).

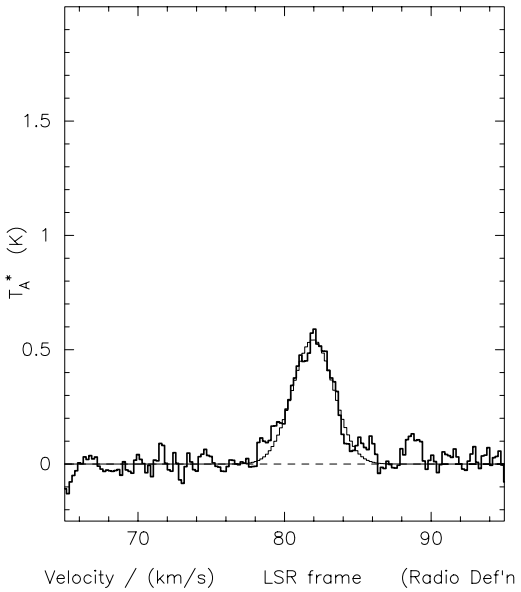

(b) Average CS spectrum with fitted Gaussian (width = 3.3 km s^{-1} at 81.9 km s^{-1}.)

because of the limited region mapped in this line – this mass is consistent with the values derived from the dust in the previous paragraph. The CS abundance relative to $C^{18}O$ is 10 times lower than normally expected; it is not clear whether this is due to chemical effects or, more likely, that the CS is only thermalized in a small dense core and the CO is more diffuse. A marginal detection of one transition of methyl cyanide places an upper limit on the kinetic temperature of 50 K (using the 3σ upper limit for the K=1 line).

The water maser has only been observed three times previously: in 1981 (1.6 Jy), 1982 (3.5 Jy) (Matthews *et al*. 1985) and in 1989 (Comoretto *et al*. 1990) (<4.4 Jy). My VLA observations detected a weak maser (1 Jy) with a velocity identical to that of the molecular material; this is 6 km s^{-1} slower, with respect to the molecular material, than the maser detected in 1982. The maser is less than 1 arcsec (0.02 pc) from the submm continuum peak.

5.3 IRAS 19374+2352

This *IRAS* point source, with good detections in all four wavebands, has not otherwise been observed in continuum. The maser has been observed once in 1989 March (Palla *et al*. 1991), when a single component at a velocity of 39 km s^{-1} and with a flux density of 33 Jy was seen. This source has also been searched for methanol but with a negative result (Schutte *et al*. 1993). The POSS image of this region shows no evidence for dust and simply shows foreground stars.

Figure 5.6. IRAS 19374+2352

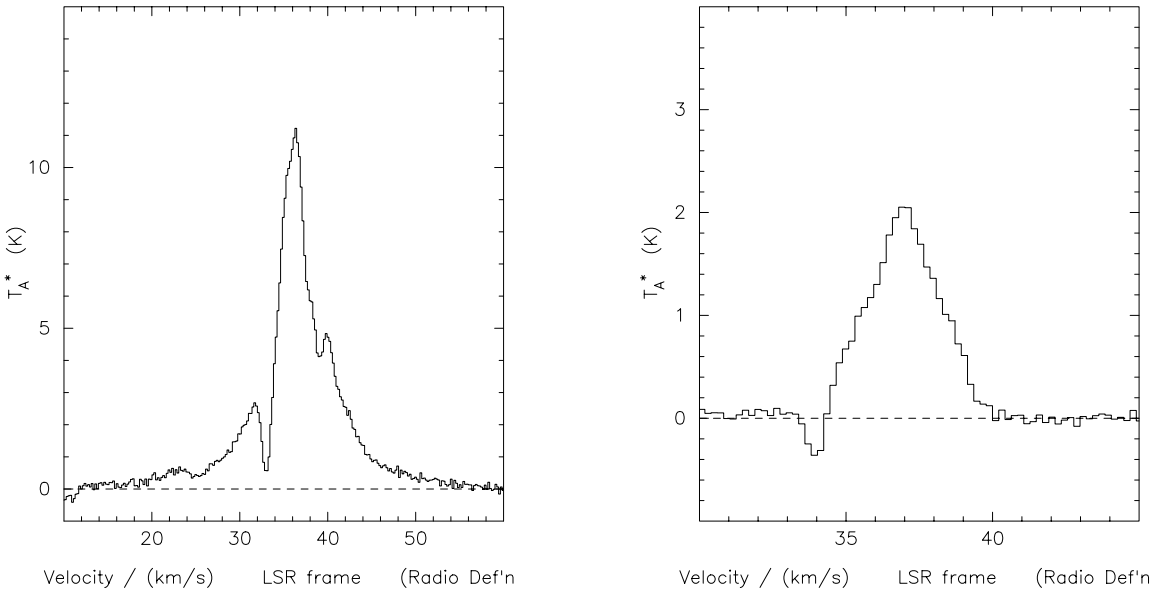

(a) Average ^{12}CO spectrum

(b) Average C^{18}O spectrum.

My submm continuum observations show a slightly extended (12 arcsec; 0.25 pc) 800 μm map which resolves into two sources at 450 μm. The south eastern object is very weak and it is not possible to separate the flux of this object from the main component. The observed source size constrains the mean density to be at least 10^6 cm^{-3}. The fit to the SED is good and all but the 12 μm *IRAS* flux are fitted. Radio continuum observations with the VLA resolve a strong compact source 0.015 pc in diameter. Assuming the H II region is expanding at a velocity of 10 km s^{-1} this size implies a dynamical lifetime of approximately 1000 yr. The RT observations confirm that there is no extended flux which had been resolved out by the VLA observations so that all the radio flux is within this source and the spectral index is consistent with thermal bremmsstrahlung emission. Both the radio flux density and the FIR luminosity are consistent with that produced by a B0 to B0.5 star.

Line observations in ^{12}CO, C^{18}O and CS all show maximum integrated emission and the widest lines within 5 arcsec of the submm core. The ^{12}CO line is fairly weak ($T_{\rm Max} = 16$ K) so it is probably not safe to assume that this emission is optically thick. Both the ^{12}CO and C^{18}O maps show a negative feature at 33 km s^{-1} (Fig. 5.6) and this must be due to contamination in the reference beam. The average ^{12}CO spectrum shows strong indication of wings so outflowing material is almost certainly present even if channel maps show no evidence of this. Propyne has been detected with a fairly warm temperature of 84 K. The derived column density agrees extremely well with that derived from the CS, $A_V \approx 15$, but it is likely that the bulk of the C^{18}O gas is not at this high temperature. The derived gas mass is twice that calculated from the dust but this may, in part, be due to the adoption of the rotation temperature found from the propyne observations.

The water maser is located within 2 arcsec of the compact radio emission and within 3 arcsec of

the submm peak. It is now much weaker than in 1989, falling from 33 Jy to 0.19 Jy in five years. The change in velocity, of 5 km s^{-1} indicates that this may not be the same component as observed previously.

5.4 IRAS 20056+3350

This *IRAS* point source, with good detections in all four wavebands, has not otherwise been observed in continuum. A 1.5 K ^{13}CO (1-0) line has been detected, with a 4.4 arcmin beam, and a mass of 56 $M_{\odot}$ inferred (for a distance of 1 kpc) (Casoli *et al*. 1986). This source was also detected as part of a survey of *IRAS* sources for HCO^+ cores (Richards *et al*. 1987). It has also been searched for methanol but with a negative result (Schutte *et al*. 1993). The water maser has been detected three times previously (Brand *et al*. 1994). In all cases a single broad, approximately 3 km s^{-1}, line has been detected. In 1989 January an 80 Jy line was seen at 10.4 km s^{-1}; in 1992 January the maser was at 8.4 km s^{-1} and the flux density varied from 111 Jy to 124 Jy in one day.

The 800 μm submm continuum observations reveal a compact core with a hint of extended structure to the south west. This structure also shows up in the high-resolution map and may be due to a weak continuum source. The main source is essentially point like in these maps. Low-resolution RT observations detected 3 mJy at 15 GHz but there was some contribution from structure on scales of approximately 30 arcsec. The VLA map shows marginal evidence for radio continuum at 8 GHz and it is likely that at least 50 per cent of the flux detected by the RT has been resolved out by the VLA. This means that it is not possible to determine a spectral index. The SED fit to the mid-infrared and submm data is extremely good with all except the 12 μm flux value fitted.

No ^{12}CO observations were made of this source and only a small (3×3) map in C^{18}O. These observations show that the source is still concentrated on the submm peak. There is some absorption on the red- side of the spectrum (Fig. 5.7) and this is probably from foreground gas. CS observations (on a 5×5 grid) show that the source is very compact – one beamwidth from the central peak no line is visible – and does show an extension to the south west similar to that seen in the continuum (Fig. 5.8). Propyne was detected but the temperature determination is poor because of the abnormally weak K=2 line. The CS to propyne column density ratio is consistent with other abundance determinations but these molecules are four times less abundant relative to C^{18}O and are probably concentrated towards the core. Having said this, the mass determination from C^{18}O gives extremely good agreement with the value obtained from the continuum measurements, 64 and 76 $M_{\odot}$ respectively for a source distance of 2.08 kpc – these values are smaller than that reported by Casoli *et al*. (1986) but the beam area for those observations was 170 times larger.

The VLA observations detected two water masers close (<1 arcsec; 0.01 pc) to the submm core and aligned with the weak radio continuum. These masers are at different velocities: the strongest line is broad and at the cloud velocity (it is not possible to say whether red- and blue-shifted components are smeared out by the large channel width) whereas a weaker blue-shifted component is visible at

Figure 5.7. IRAS 20056+3350

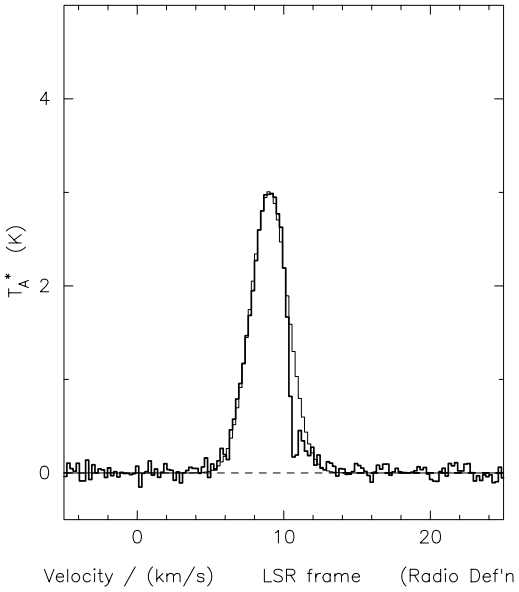

(a) Average $C^{18}O$ spectrum with fitted Gaussian (width = 3.0 km s^{-1} at 9 km s^{-1})

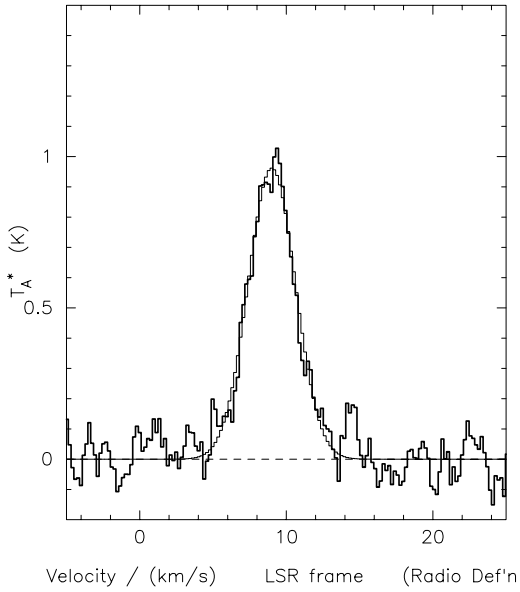

(b) Average CS spectrum with fitted Gaussian (width = 3.8 km s^{-1} at 9 km s^{-1})

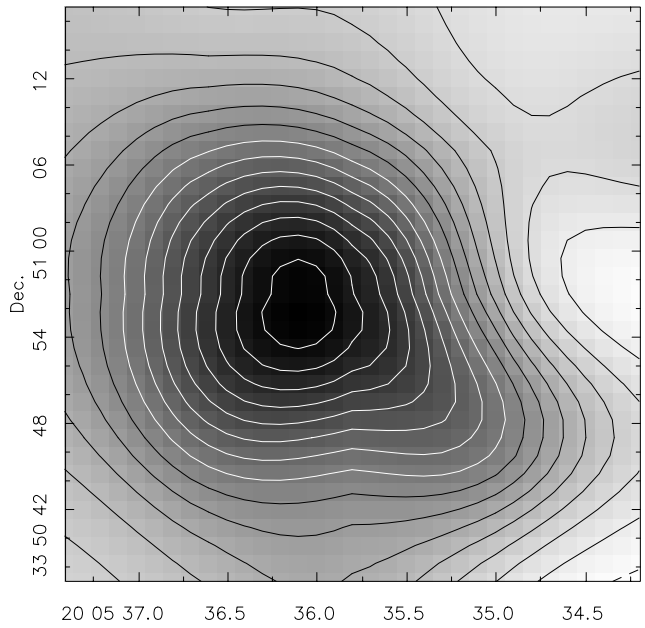

Figure 5.8
IRAS 20056+3350 CS integrated intensity map.

2 km s^{-1}. This maser is now 250 times weaker than it was in 1992.

5.5 IRAS 20188+3928

Previous observations of this source have identified two compact H II regions (McCutcheon *et al*. 1991; hereafter MDPS) and a molecular outflow (Little *et al*. 1988; hereafter LBC). The *IRAS* source is associated with the southern radio source and has good detections in all four *IRAS* bands. Odenwald (1989) suggests that a single star, visible on the POSS plates, is responsible for this *IRAS* emission and MDPS suggest that the 5-GHz radio continuum and the FIR luminosity can be accounted for by a B0 star.

My line and continuum observations extend our knowledge of this source. The 800 μm continuum map shows that IRAS 20188 consists of at least two embedded cores (FIR1 and FIR2). The strong southern compact H II region reported by MDPS is associated with FIR2, but the weaker radio source to the north is between FIR1 and FIR2 (Fig. 5.9). Since the *IRAS* fluxes cannot distinguish the two submm cores, the temperature derived from the SED fit can only be a weighted average of the actual dust temperature in the cores. From the low-resolution 450- and 800-μm data FIR2 has a steeper spectrum than FIR1 but it is possible that both sources have submm spectra consistent with $\beta = 1$ given the reasonably large calibration errors expected for these fluxes. At a distance of 3.2 kpc (MDPS), and assuming a dust temperature of 30 K (the fitted value) and a dust index of 1.0, the masses of FIR1 and FIR2 are 260 and 560 $M_\odot$ respectively. The high-resolution 450 μm map shows that the extended structure in FIR2 is due to two continuum sources, FIR 2a and 2b. Both sources are extended east-west and unresolved north-south, and it is likely that higher resolution images will resolve FIR2b, and possibly 2a, into two dust cores. The *IRAS* source and the main radio continuum source are coincident with FIR2a, the strongest submm component.

Using the compact RT array, the northern and southern sources were too close to be separated, but unrelated extended radio emission was detected almost 3 arcmin to the south-east of the *IRAS* position. This emission is probably part of the large (10×7 arcmin^2) radio source visible on the NRAO 5-GHz survey (Condon & Broderick 1985). The NRAO and RT maps are shown in Fig. 5.10.

High-resolution 8-GHz radio continuum images from the VLA (Fig. 5.11a) show the two radio continuum sources seen by MDPS, but in much more detail. The southern source resolves into a strong, 24 mJy, resolved component of approximately 0.015 pc diameter, and a weaker, 2 mJy, unresolved component 2 arcsec to the north. The northern source is also unresolved and this places an upper limit on the size of 0.36 arcsec (5.6 mpc). Combining the VLA, RT and MDPS observations, both radio sources have flat spectra consistent with thermal Bremsstrahlung emission. Under these conditions it is then possible to calculate the electron density (and hence the mass of ionised hydrogen) of the main radio source: 24 mJy in a source of radius 7.5 mpc (1500 AU) requires an electron density of 4.3×10^4 cm^{-3} and thence 0.002 $M_\odot$ of ionised hydrogen. Similar parameters can be obtained for the northern radio source: A lower limit can be found for the source size if it is assumed

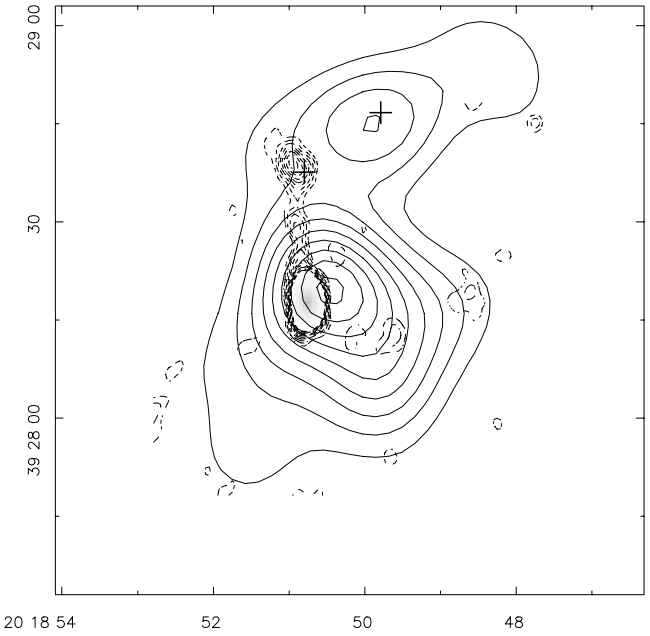

Figure 5.9
IRAS 20188+3928 800 μm (contours) plus 15 GHz continuum (greyscale plus dashed contours).

Figure 5.10. IRAS 20188+3928

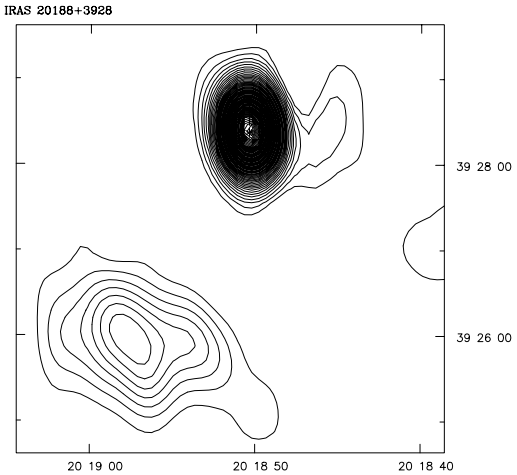

(a) Low-resolution 15 GHz continuum. Contours are every 0.5 mJy beam^{-1}.

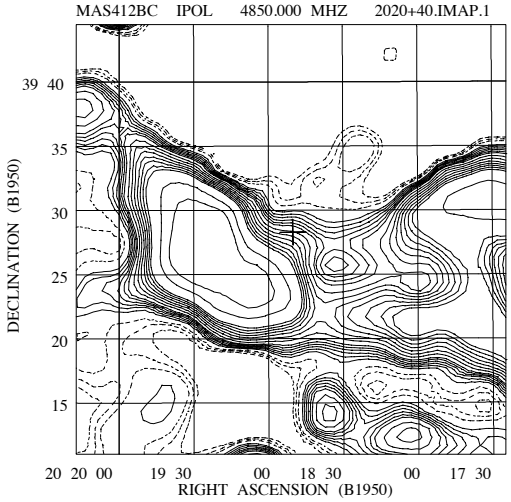

(b) NRAO 5-GHz survey map. Contours are every 10 mJy beam^{-1} up to 100 mJy beam^{-1} as well as 150 and 200 mJy beam^{-1}.

Figure 5.11. IRAS 20188+3928

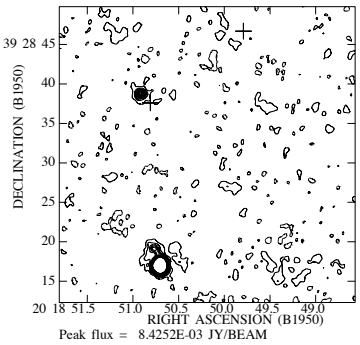

(a) 8 GHz VLA continuum. 0.9 arcsec beam. Contours are every 0.2 mJy beam^{-1}.

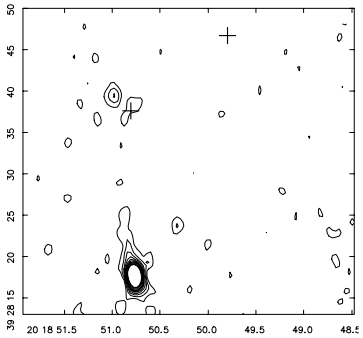

(b) 15 GHz high-resolution continuum. 1.1×1.9 arcsec^2 beam. Contours are every 0.5 mJy beam^{-1}.

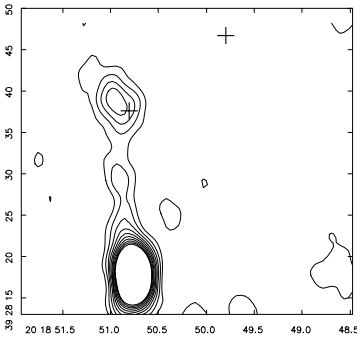

(c) 15 GHz medium-resolution continuum. 3×4.5 arcsec^2 beam. Contours are every 0.5 mJy beam^{-1}(1.5σ).

that the emission becomes optically thick ($\tau = 1$) at the lowest frequency for which data exists. This indicates that the source radius is between 300 AU (assuming an upper limit to the turnover frequency of 5 GHz) and 575 AU (the upper limit measured from the 8 GHz map) and implies that the source becomes optically thick between 5- and 2.7-GHz. A radius of 2 mpc has been adopted for the remainder of this discussion and implies that the electron density is 1.2×10^5 cm^{-3} and the mass of H II is 10^{-4} M$_\odot$.

The high-resolution RT map (Fig. 5.11b) also resolves the two continuum sources and shows evidence for extended emission from the southern source towards the UC H II region. On removing the long baseline *uv*-data and making an intermediate resolution map (Fig. 5.11c), a ridge of radio emission is seen connecting the two radio sources, although the lowest contour is just above the noise level. This connection means that it is highly unlikely that the two radio sources are unrelated. The VLA in B array at 8-GHz is not sensitive to structure larger than 10 arcsec so it is not surprising that this ridge was not seen in my high-resolution map. The 5-GHz map of MDPS shows evidence for this extension although no connection is seen.

The most plausible explanation is that this is an optically thin radio jet from a high-mass star. Although a large enough region was mapped, a counterpart radio source to the south was not seen. The northern radio source is simply indicating the bow shock ploughing into the external medium and the weak source visible on the 8 GHz map just to the north of the southern source is evidence of recent mass ejection. This jet is highly collimated; with a length of 0.33 pc and diameter of 800 AU this suggests an opening angle of less than 1 degree with a position angle of 6 degrees. Assuming the jet is in the plane of the sky, since no other information is available, and that it is moving with a velocity of 300 km s^{-1}, not unreasonable for jets from high-luminosity stars (e.g. other sources in this maser sample: IRAS 18162−2048 (Martí *et al*. 1993; 1995); LkHα234 (Ray *et al*. 1990); IRAS 20275+4001

(Poetzel *et al*. 1992)), the dynamical lifetime of the radio jet is approximately 1000 yrs. This means that the jet is moving on the sky about 20 mas yr^{-1} and proper-motion studies of the inner part of the jet are feasible, with a telescope such as MERLIN[1], over the next few years. If the velocities are comparable to those seen in HH 80-81 (Martí *et al*. 1995), the proper motion could be a factor of four higher than this conservative estimate.

The radio continuum flux is equivalent to a B0→0.5 star with a stellar luminosity of 1.5×10^4 L$_\odot$. This is very close to the fitted infrared luminosity of 1.95×10^4 L$_\odot$. Since this infrared luminosity must include contributions from FIR1 and FIR2b, accounting for FIR2a alone, which is responsible for approximately 60 per cent of the total submm flux, shows that the observed submm flux in this object is entirely consistent with a B0.5 star at its centre.

The averaged ^{12}CO spectrum (Fig. 5.12a), which is a good approximation to observing with a 60 arcsec beam, shows good agreement with the large beam 1-0 spectra of MDPS and LBC. All the spectra show absorption at the line centre and a shoulder of emission at -5 km s^{-1}. The molecular outflow reported by LBC does not show a very large spatial separation in the outflow lobes, given the huge beam size, so it is very difficult to say where the outflow centre should be. The C^{18}O (and CS) spectra do show red- and blue-shifted wings (e.g. Figs 5.12b and 5.13) but the limited map area and poor signal-to-noise make it extremely difficult to see evidence for an outflow in channel maps. All that can be said from the C^{18}O map is that it traces FIR2 extremely well. Indeed the gas mass measured from C^{18}O of 660 M$_\odot$ agrees reasonably well with that derived from the dust of 560 M$_\odot$ (assuming a dust index of 1.0; a dust index of 1.23 is required for the 800 μm flux to be consistent with 660 M$_\odot$). The methanol data is far too noisy to derive quantitative information from; all that can be said is that the methanol line is much stronger and broader at the position of the northern radio source than it is at either FIR1 or FIR2. The symmetric top observations show weak evidence for high temperature gas in FIR2 ($T_{\rm Rot} = 224$ K) with an hydrogen column density approximately three times lower than that derived from the C^{18}O data. This agrees with the general result that the warm gas is only excited towards the centre of the hot core and the C^{18}O is dominated by emission from the cooler gas. The CS data show that it is not surprising that cool propyne was not detected – the 2σ upper limits on the $J = 14 \rightarrow 13$ observations are consistent with a column density in propyne of less than 2.4×10^{18} m^{-2} at 50 K; this upper limit is five times larger than the column density expected if the normal abundance ratio relative to CS is assumed.

Velocity structure is visible in the ^{12}CO data. Fig. 5.14 shows that the red-shifted emission is centred on FIR2 and blue-shifted emission is centred on FIR1 (the velocity intervals have been chosen to coincide with those of LBC). This shift from blue- to red-shifted emission in only 30 arcsec was noticed by LBC but they did not have the resolution to examine the outflow centre in detail. This picture implies that the outflow centre is *between* FIR1 and 2 but no source appears to be there from my observations. This emission could also be explained by large scale rotation of the sources – FIR1 is

[1]The Jodrell Bank Multi-Element-Radio-Linked-Interferometer-Network is operated by the University of Manchester on behalf of PPARC

Figure 5.12. IRAS 20188+3928

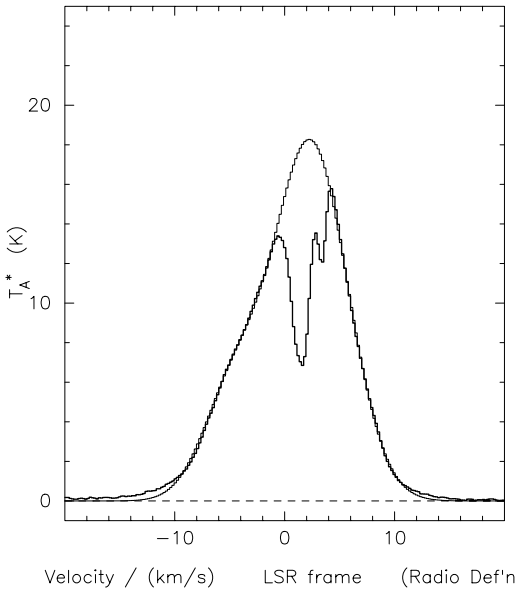

(a) Average ^{12}CO spectrum with two fitted Gaussians (amplitude = 18 K, width = 7.9 km s^{-1} at 2.4 km s^{-1}; amplitude = 5.3 K, width = 6.6 km s^{-1} at −4.5 km s^{-1}).

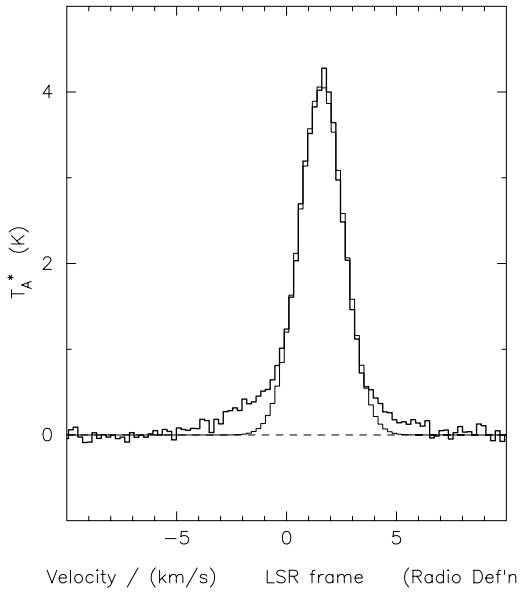

(b) Average C^{18}O spectrum with fitted Gaussian (width = 2.4 km s^{-1} at 1.6 km s^{-1}).

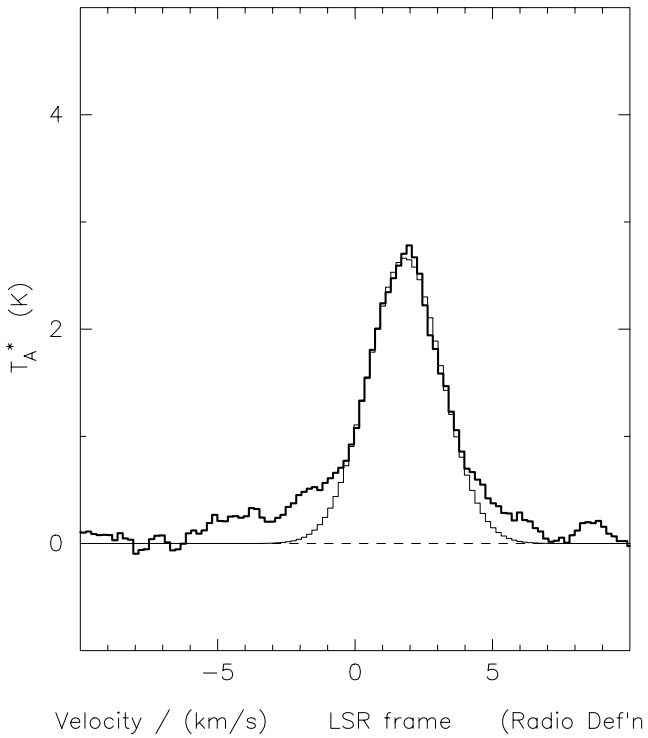

Figure 5.13
IRAS 20188+3928 average CS spectrum with fitted Gaussian (width = 3.1 km s^{-1} at 1.8 km s^{-1}).

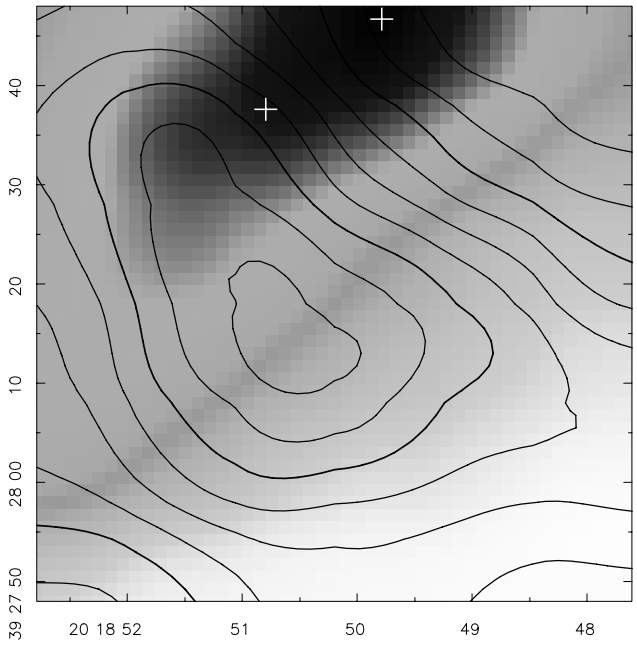

Figure 5.14
IRAS 20188+3928 ^{12}CO channel map. Blue-shifted emission (-15 to -1 km s^{-1}) is shown by the contours and red-shifted emission (4 to 12 km s^{-1}) is shown by the greyscale. The water maser positions are indicated by crosses.

moving away from us and FIR2 is moving towards us with a velocity of approximately 3 km s^{-1}. It would be interesting to map FIR1 in C^{18}O to see if red-shifted emission is present.

Previous water maser observations have all used large beams and so have lacked accurate positional information – previous observations have quoted positional accuracies of no better than 20 arcsec. Palla *et al.* (1991) detected a single component at -1.2 km s^{-1} (with a flux density of 20 Jy) in 1989, Felli *et al.* (1992) detected nothing in 1990 (< 3 Jy), and Xiang & Turner (1992) detected lines at -1 and 4.1 km s^{-1} (with flux densities of 4 and 9.5 Jy respectively) in 1991. My observations, from 1994, show two spatially separated components: a weak (0.21 Jy) maser with a velocity of 4 km s^{-1} associated with the northern radio source, and a stronger two component maser associated with FIR1 (with components at -1 and 7 km s^{-1}). Since the molecular cloud is at a velocity of 1.5 km s^{-1} *and* the maser is directly associated with a submm core, this immediately suggests that the maser is caused by material in an expanding shell caused by a stellar wind. The maser has been present since 1991 (although the red-shifted component is now 3 km s^{-1} faster), but has become approximately three times weaker in three years in both components. This is presumably either because the wind is accelerating and expanding, resulting in a lower pump rate due to lower densities (Elitzur 1992), or the geometry of the gain path has changed and less power is beamed in the direction of the observer. The 20 Jy maser detected by Palla *et al.* (1991) switched off in 1990 and it is unlikely that this maser is related to the more recent component even though it had a similar velocity.

The second maser was either too weak to have been detected by previous observations or made a contribution to the 4 km s^{-1} spectrum detected by Xiang & Turner (1992) and was spatially indistinguishable from the other component. This maser is an order of magnitude weaker than the maser associated with FIR1 and has an isotropic luminosity of 2×10^{-7} L$_\odot$. The location of this maser near

to the end of the radio ridge suggests that this maser is excited near the end of the bow-shock. A high-resolution radio image of the interaction between the bow-shock and the maser would help to support this view, although the lack of any other obvious power source makes it difficult to imagine an alternative.

5.6 IRAS 21078+5211

Previous observations of this object, which is in the direction of the Cyg. OB7 molecular cloud, detected an H II region approximately 1 arcmin in extent (MDPS). More recent observations by Miralles *et al*. (1994) faintly detected the H II region but their observations suffered dramatically from the VLA's inability to detect extended structure in C array at high frequencies. The *IRAS* source 21078+5211 is on the north-eastern edge of the H II region and has colours indicative of a cold dust condensation. IRAS 21078+5209, 2 arcmin to the south, is only visible in the 12 μm *IRAS* band and is therefore too hot to be associated with a pre-main-sequence object – two bright stars are visible on the red POSS plates within 10 arcsec of the nominal position.

Previous line observations have centred on the main *IRAS* source and have used large beams. Water maser observations (Palla *et al*. 1991; Wouterloot *et al*. 1993; Miralles *et al*. 1994) have easily detected this moderately strong maser but always with poor positional accuracy. First detected in 1988 (Wouterloot *et al*. 1993) with peak emission of 3.7 Jy at -21 km s^{-1} (the molecular cloud velocity is approximately -5 km s^{-1}) and weak emission ($\sim$ 1 Jy) at -15 and -5 km s^{-1}, this maser has had a progressively lower velocity over the last five years. In 1989 it had components at -28, -18 and -13 km s^{-1} (fluxes of 10, 41 and 20 Jy respectively), in 1991 it was not detected ($<$5 Jy) and in 1992 there was weak emission at -17 and -15 km s^{-1} (both components were 6 Jy) but the strongest component was at -5 km s^{-1} (i.e. the molecular cloud velocity) with a flux of 60 Jy. Ammonia observations suggest that this source has a rotational temperature of 24 K (Miralles *et al*. 1994) but the large beam size (90 arcsec) and large pointing offset from the submm core imply that this is simply an average temperature for the surrounding medium and not an indication of the actual core temperature.

My observations clarify this picture. Continuum observations show that there is no submm core associated with IRAS 21078+5211 and in fact the submm source is 1.2 arcmin away and has too small an error ellipse to be an association (IRAS 21078+5209 is nearly one arcmin from the submm source and, as mentioned previously, has the wrong colours to be an association). The failure of Wilking *et al*. (1989) to detect 2.7 mm continuum emission at the *IRAS* source is not surprising in the light of this large offset. This large positional discrepancy invalidates the SED fitting for this source. The *IRAS* fluxes used are not solely those of the submm core suggesting that the core is less luminous than the fitted value of 5000 $L_{\odot}$. The large *IRAS* beam seems to be detecting extended emission which would have been chopped out with the observing technique used at the JCMT. There are insufficient continuum data to decide whether the core is cooler than the fitted value of 38 K and line data must be used to determine the temperature.

The RT observations show good morphological agreement with the 5 GHz maps of MDPS but the source is about half the size. The discrepancy is due to the different telescope properties. The RT in extended configuration is sensitive to structure smaller than about 1 arcmin whereas the VLA in C array at 5 GHz is sensitive to structure smaller than about 2 arcmin (less than this in snapshot mode). This would account for the factor of 2 in the observed flux density measured. Observations at both frequencies were performed by Miralles *et al*. (1994) and although these suffered from the compact arrangement of the VLA C array, especially at 15-GHz, a flat radio spectrum was observed suggesting an optically thin H II region. High resolution VLA maps, using B array, resolve out all the radio emission and confirm that the H II region has no structure smaller than 10 arcsec. The good agreement between the *IRAS* luminosity and the luminosity expected from the radio flux (equivalent to a B0.5 star) suggests that the *IRAS* source, probably extended warm dust, is being heated by the same object that created the H II region.

The submm continuum source is point-like in the 18 arcsec JCMT beam, but the high-resolution map (7 arcsec beam FWHM) shows that the source has extended emission resolved in one dimension (with a position angle of 110°) with a point source smaller than 5 arcsec (0.035 pc at the adopted distance of 1.3 kpc from MDPS) at the centre. The extended emission does not appear on the 850 μm map, however, and is probably an artefact of the raster scanning observing mode. The water maser is within 1 arcsec (6 mpc) of the compact 450-μm source but absolute pointing inaccuracies make it impossible to know the relative position accurately, indeed, the separation could be as much as 3 arcsec (0.02 pc).

The ^{12}CO spectra show evidence for absorption by cold foreground gas at a velocity of approximately -4 km s^{-1}. Fig. 5.15a shows a spectrum offset 30 arcsec to the east of the submm core fitted by a Gaussian. Moving across the map to the west the spectra get wider and less Gaussian-like with the line peaks flattening towards the north-west of the map. Fig. 5.15b shows this extremely sharp cut-off in emission at -5 km s^{-1}for selected spectra. All 49 spectra are missing emission at this velocity, and there is also 1.5 K negative feature at -1 km s^{-1} which varies only slightly across the map and so is probably due to a weak source at the reference position (absorption of a background continuum source is not possible since this would require a source with approximately 15 Jy per JCMT beam across the whole map). Mapping optically thin emission with velocities between 0 and 3 km s^{-1} shows a peak approximately 5 arcsec to the south-east of the submm core (Fig. 5.16). The feature seen at 8 km s^{-1} by MDPS is visible and shows only very minor variation across the map. This emission cannot therefore be associated directly with the submm core.

The C^{18}O emission has an average spectrum with no sign of wings and is well approximated by a Gaussian of amplitude 2.8 K, width of 2.4 km s^{-1} and velocity of -6.3 km s^{-1}. No signs of absorption, by e.g. the foreground cloud absorbing the ^{12}CO, are visible but this can be explained by the much smaller abundance of C^{18}O relative to ^{12}CO. Comparing the line strength at the submm position in

Figure 5.15. IRAS 21078+5211

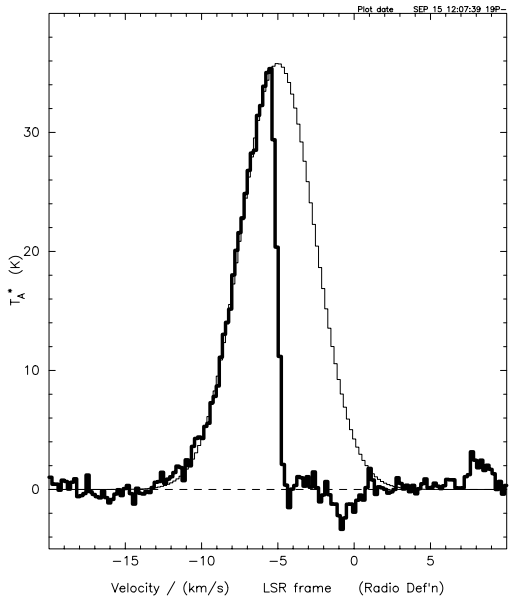

(a) A ^{12}CO spectrum of IRAS 21078+5211, taken at an offset of (30, 0) from the submm source centre, with a fitted gaussian with parameters of $T_A^* = 35.8$ K, $\Delta v = 5.7$ km s^{-1}and $v_{peak} = -5$ km s^{-1}.

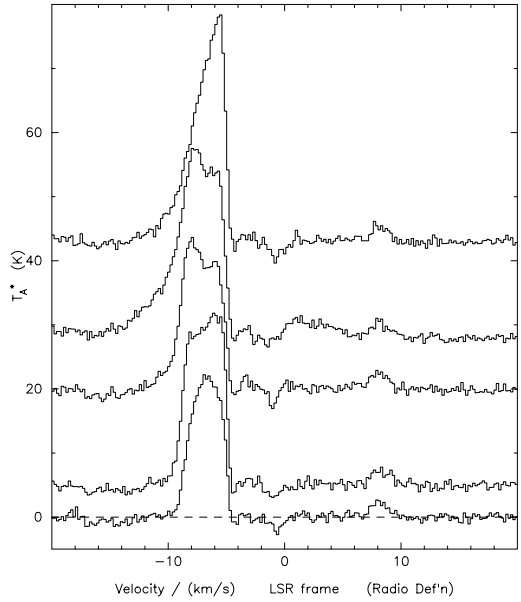

(b) Spectra from (0, 30), (0, -30), (-30, 0), (0,0) and (30, 0)

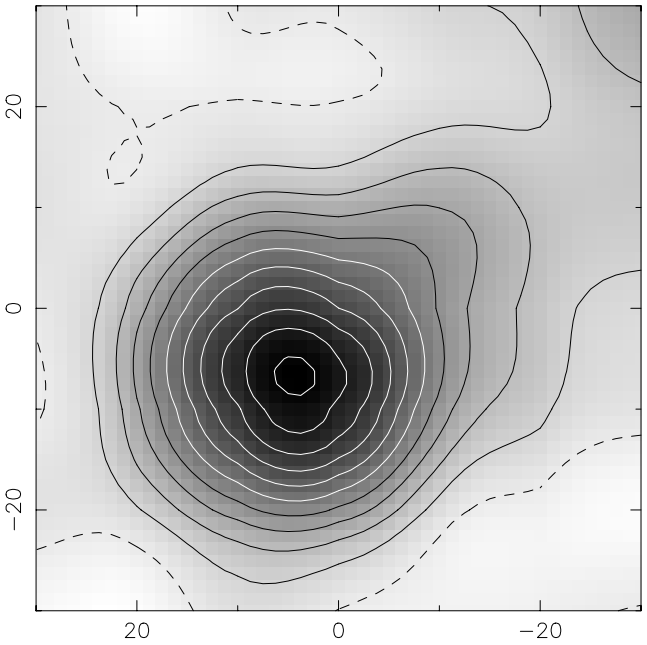

Figure 5.16
IRAS 21078+5211 ^{12}CO integrated intensity 0 to 3 km s^{-1}. Contour levels are every 1 K km s^{-1}. The map is centred on the submm position.

Figure 5.17. IRAS 21078+5211

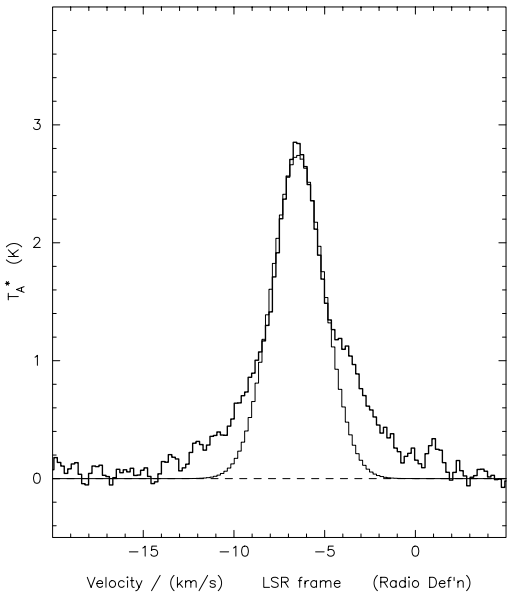

(a) Average CS spectrum with fitted Gaussian (width = 3.4 km s^{-1} at −6.5 km s^{-1}).

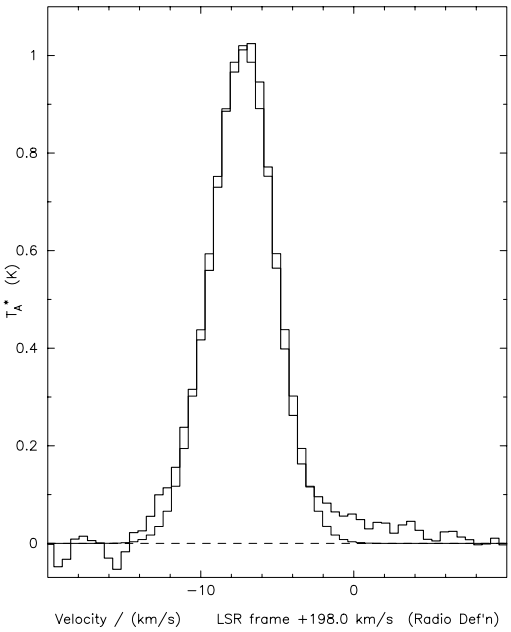

(b) Methanol spectrum of core region with fitted Gaussian (width = 5 km s^{-1}). Note that the velocity scale has been shifted so that the peak coincides with the velocity of the molecular cloud.

^{12}CO to C^{18}O, using

$$\tau(\mathrm{C^{18}O}) = \frac{\tau(^{12}\mathrm{CO})}{490} = -\ln\left(1 - \frac{T_A^*(\mathrm{C^{18}O})}{T_A^*(^{12}\mathrm{CO})}\right),$$

results in an optical depth of approximately 0.16, confirming that this line is indeed optically thin. The C^{18}O integrated intensity map is extended. Peak emission is at the position of the submm core but also extends to the south-east towards the warmest ^{12}CO gas (a trend which is hinted at in the, much smaller, CS map). The total mass of the gas determined from the C^{18}O works out to be 80 M$_\odot$, under the assumption it is optically thin and the gas has an excitation temperature equivalent to the propyne rotation temperature, which is in remarkably good agreement with the mass derived from the submm emission of 74 M$_\odot$. The mass derived from the gas is expected to be larger simply because the C^{18}O map is extended.

The CS observations covered a much smaller area (a 3 by 3 grid); the average spectrum is shown in Fig. 5.17a. Shown along with a fitted Gaussian, excess emission is visible in the blue- and red-shifted wings. Whilst the map is too small to draw any real conclusions about the nature of this possible outflow, the wings are more pronounced in the southern part of the map with the strongest line at the origin. The single methanol spectrum (Fig. 5.17b) also shows a small red-shifted wing although a

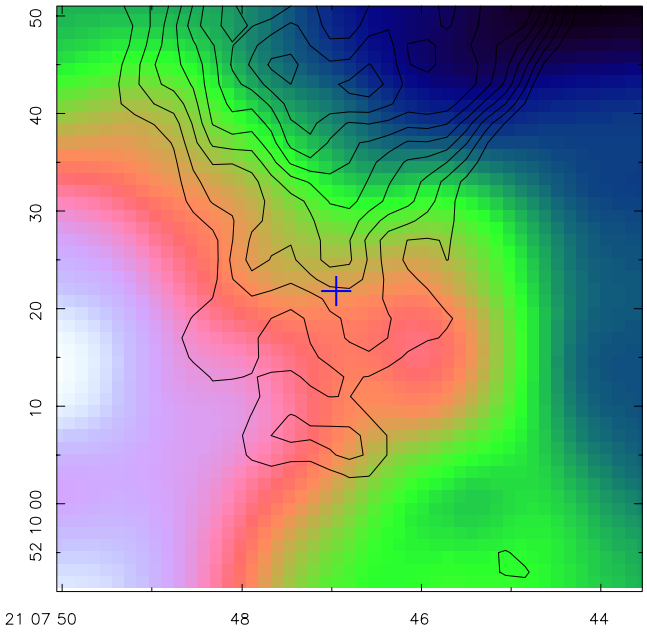

Figure 5.18
Comparison of radio emission with CO temperature in IRAS 21078+5211. The 15-GHz RT map is shown by the contours, which are every 0.5 mJy beam^{-1} excluding the zero level, and peak ^{12}CO temperature is indicated by the greyscale. The location of the water maser and submm core is indicated by the cross.

map in methanol would be needed to say for certain whether a methanol outflow is present. Since the optically thin spectra are offset approximately 1.3 km s^{-1} from the ^{12}CO this gas may not even be associated with the optically thick ^{12}CO.

Comparing the RT map and the peak ^{12}CO temperature map (Fig. 5.18) shows that the edge of the H II region lies along the edge of the warmest gas. This excellent match suggests an ionization front, where ultraviolet photons from the massive star which is responsible for the H II region are warming up the molecular gas along this edge. Projection effects could be responsible for this effect not being present on the western side and a much larger region has to be mapped around the H II region to decide whether this heating is caused by a source in the center of the radio emission or a source to the south-east which is responsible for the temperature gradient to the north-west. The morphology of the RT map suggests there is some radio continuum extending towards the submm source; since the 5-GHz map of MDPS does not show any particular extension to the south, either the source responsible for the H II region has triggered star formation along the ionization front to the south and south-east, as visible in the ^{12}CO temperature map, or the H II region is an unrelated foreground source associated with the molecular material which is absorbing the red-shifted ^{12}CO.

Earlier in this section it was mentioned that deriving the temperature from the dust was unreliable because of the lack of mid-infrared data. Line observations give an alternative method of determining temperature. An optically thick line, such as ^{12}CO, should give a direct indication of the excitation temperature of the gas. Since ^{12}CO is very common and extended it will generally give an indication of the temperature at the point at which the cloud becomes optically thick. At the position of the submm core the ^{12}CO brightness temperature is approximately 43 K giving a lower limit to the excitation temperature of 48 K (using equation 3.19). Whilst this value is consistent with the fitted dust

temperature, 38 K, both these observations are sampling the average temperature because of the large beams used in both cases, and may, in fact, simply be sampling foreground material. A more reliable way of determining the excitation temperature is to use an optically thin symmetric top molecule (such as ammonia) with a small beam. The submm core was observed in methyl cyanide and propyne with a beamsize of 21 arcsec (14 arcsec for the high frequency propyne observations). The rotation diagram (Fig. 3.8) shows evidence of propyne and methyl cyanide at about 75 K, but also evidence for high temperature propyne, 155 K. This higher temperature and smaller column density (about half that seen in the lower temperature propyne) suggests that this emission is coming from a hot core surrounded by a cooler halo. These temperatures are much higher than the temperatures derived from more extended features, such as the ammonia rotation temperature of MDPS, and show that the submm core is indeed warmer than the surrounding medium.

A surprising feature is that the maser spectrum has a line shape very similar to that of the ^{12}CO – including evidence for a weak line at 8 km s^{-1}. Given that the optically thin C^{18}O and propyne spectra are Gaussian, this similarity is probably by chance and a higher resolution maser spectrum is required to see individual velocity components. In keeping with the general trend of the maser emission from this source, the maser is now at the molecular cloud velocity, and the peak flux is 90 per cent weaker than the most recent observation of Miralles *et al.* (1994).

5.7 IRAS 22198+6336

Located in the L1204 molecular cloud complex approximately 37 arcmin to the north of S140, IRAS 22198+6336 has good detections in the three longest wavelength *IRAS* bands but only an upper limit at 12 μm. No radio continuum has been detected by Hughes & MacLeod (1994) (<0.6 mJy at 5 GHz) or Tofani *et al.* (1995) (<0.1 mJy at 8.4 GHz). Continuum has been detected at 2.7 mm (Wilking *et al.* 1989) and a mass of 9.5 M$_\odot$ inferred.

A molecular outflow was inferred by Fukui (1989) on the basis of wings in the CO spectrum. Observations by Wilking *et al.* (1989) detected ^{12}CO ($J = 2 \rightarrow 1$) and also reported the presence of wings as well as self-absorption in the line centre. From ^{13}CO observations they reported a hydrogen column density of 11×10^{25} m^{-2} (equivalent to a visual extinction of 6 mag). ^{12}CO ($J = 2 \rightarrow 1$) observations have also been made by Tafalla *et al.* (1993) (labelled core G), but their low spectral resolution (four times worse than for the Wilking *et al.* observations) smooths out the self-absorption. Ammonia observations show a core centred approximately 40 arcsec to the north-west of the *IRAS* position with a velocity shift across it of 0.82 km s^{-1}. A kinetic temperature of 12 K is derived from the ammonia data. CS ($J = 1 \rightarrow 0$) observations (also by Tafalla *et al.* and with a 2 arcmin beam) show a core near IRAS 22198 and a lower limit to its mass of 200 M$_\odot$ is derived. Slysh *et al.* (1994) failed to detect the $1_0 - 0_0$A$^+$ methanol line (<0.14 K) and Kalenskii & Sobolev (1994) derive an upper limit for the methanol column density of 9×10^{16} m^{-2}.

The water maser has been observed at least eight times since 1988 (Wouterloot *et al.* 1993; Palla

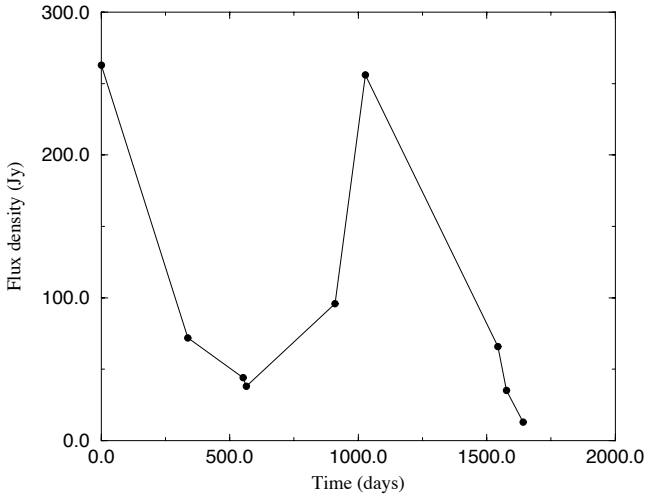

Figure 5.19
Flux density variation of the -20 km s^{-1} maser component in IRAS 22198+6336. The time axis indicates the number of days elapsed since the earliest detection of the maser by Wouterloot *et al*. (1993).

et al. 1991; Felli *et al*. 1992; Xiang & Turner 1992; Tofani *et al*. 1995) and has always shown broad ($\sim$ 3km s^{-1}wide) emission at a LSR velocity of approximately -20 km s^{-1}. Fig. 5.19 shows how the strength of this component has changed since 1988. High-resolution observations by Tofani *et al*. (1995) show four spatially distinct masers each with different velocities and only separated by 0.3 arcsec (30 AU). The masers are aligned north east to south west, from red- to blue-shifted, and the 18 km s^{-1} velocity difference is explained in terms of a bipolar acceleration of the masers in the inner part of the outflow.

My submm continuum observations show a point source at 850 μm but the 450 μm high-resolution image shows a source with a deconvolved size (FWHM) of approximately 8 arcsec (0.05 pc at the adopted distance of 1.3 kpc (Wouterloot *et al*. (1993) but 0.035 pc at the distance adopted by Tofani *et al*. (1995) of 0.9 kpc). The positional accuracy of the submm map means that the data are entirely consistent with the submm core and the water maser cluster being coincident. RT observations slightly improved the upper limit imposed by Wilking *et al*. (1989) but still did not detect any radio continuum (this is not surprising considering the very good upper limit imposed by Tofani *et al*. (1995) on the 8.4 GHz continuum flux). An order of magnitude increase in sensitivity is still required in order to see the dust emission at radio wavelengths. The greybody fit to the submm, *IRAS* and 2.7 mm data is very good; the only point not fitted is the 25 μm *IRAS* flux. Near-infrared observations in J, H and K are required to determine whether this is a class 0 source. The far-infrared luminosity derived from the greybody fit is equivalent to a B3 star and hence a radio flux of 0.3 mJy at 8 GHz would be expected. This is right on the limit of the current observations so the presence of a B3 ZAMS star, or equivalent, at the centre of this core can not be discounted.

Line observations in ^{12}CO show weak evidence for wings and show the self-absorption reported by Wilking *et al*. (1989) (Fig. 5.20a). The integrated intensity and peak temperature maps show compact (i.e. approximately beamsized) cores at the location of the submm source. The equivalent width map (Fig. 5.22) shows that the widest lines are found in the centre of the map on the submm source. The C^{18}O observations (see Fig. 5.20b) show the outflow very clearly (Fig. 5.21) from the north west to

Figure 5.20. IRAS 22198+6336

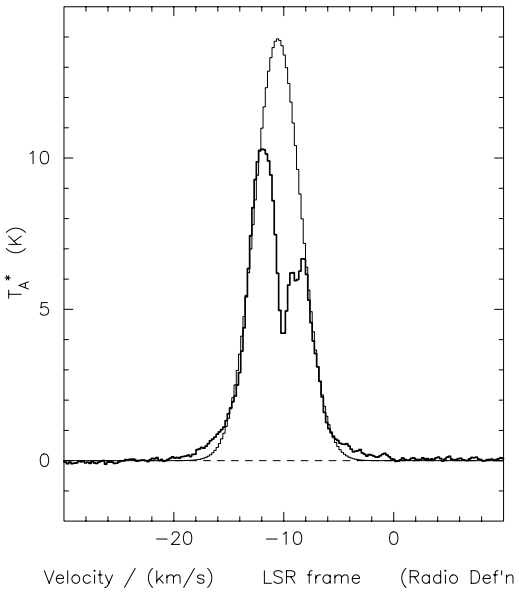

(a) Average ^{12}CO spectrum with fitted Gaussian (width = 5 km s^{-1} at −10.5 km s^{-1}).

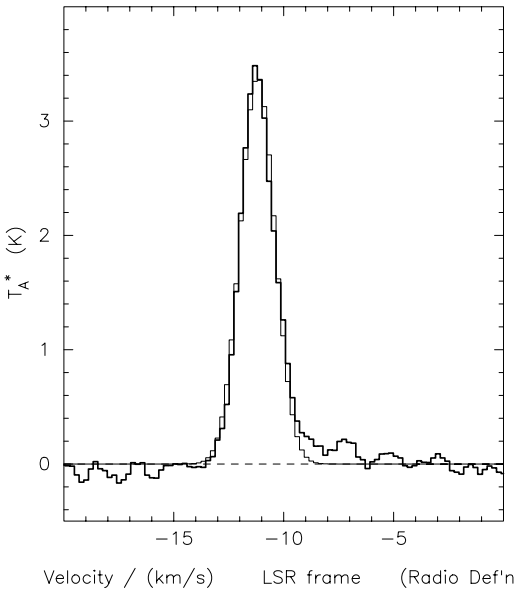

(b) Average C^{18}O spectrum of 9 nearest spectra to the submm position with fitted Gaussian (width = 1.9 km s^{-1} at -11.2 km s^{-1}).

the south.

As expected for an outflow source the widest lines are centred on the submm core. The outflow is highly collimated with an opening angle of less than 30 degrees. The total mass traced by the C^{18}O, of 108 $M_\odot$, is much larger than the mass determined from the dust observations of 34 $M_\odot$, but this indicates that a large fraction of the line emission is from the outflow. On removing the contribution from the central channel, there is approximately 30 $M_\odot$ in the blue-shifted lobe and 50 $M_\odot$ in the red-shifted lobe. These values are extremely uncertain since the outflowing material is not expected to be in LTE and the excitation temperature will be different from that found in the core region. An interesting point is that the outflow is not symmetrical; whereas the redshifted lobe has a position angle of −25 degrees, the blue-shifted lobe is not opposite and is oriented to the south (a position angle of 180 degrees). This is probably caused by density gradients to the east of the southern lobe. The low velocity of this outflow, and the minimal overlap of the lobes suggests that the outflow axis is within 20 degrees of the plane of the sky. For this source, where θ_{max}= 40 arcsec and v_{max} = 2.5 km s^{-1}, placing an upper limit on the inclination angle of 20 degrees, results in an upper limit for τ_D of 3×10^4 yr. The mechanical luminosity of the outflow is extremely sensitive to the inclination angle (equation A.16). For example, for an angle of 5 degrees the mechanical luminosity is approximately 400 $L_\odot$, which is almost 50 per cent of the luminosity seen in the continuum, whereas for an inclination angle of 20 degrees, the mechanical luminosity is 6 $L_\odot$, which is only about 1 per cent of the total luminosity.

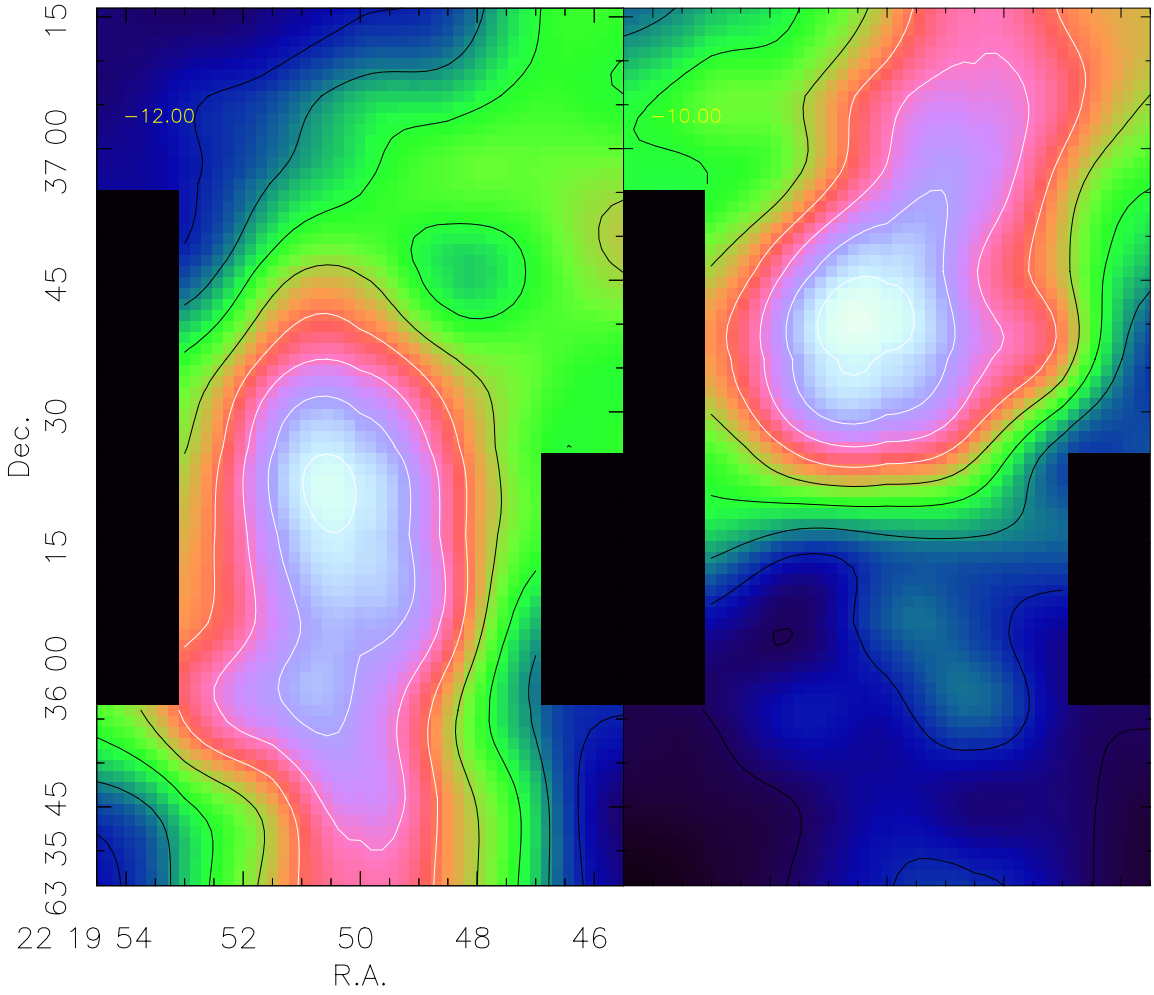

Figure 5.21. IRAS 22198+6336 $C^{18}O$ channel maps of integrated intensity of width 2 km s^{-1} centred at -12 km s^{-1} and -10 km s^{-1}.

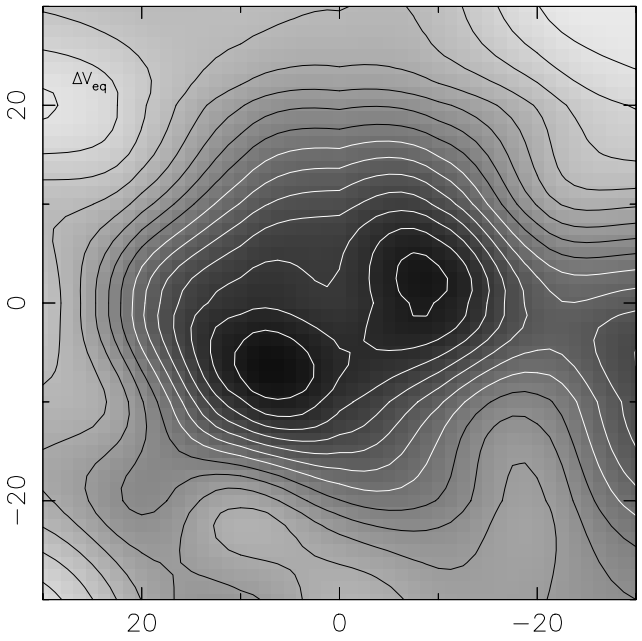

Figure 5.22
IRAS 22198+6336 ^{12}CO equivalent width. Contour levels are 0.25 km s^{-1} starting at 3.25 km s^{-1}. The map is centred on the submm position.

Outflows seen in class 0 sources, such as VLA 1623 (André *et al*. 1990) or L1448-C (Bachiller *et al*. 1990), possess highly-collimated flows, have velocities around 50 km s^{-1}, dynamical lifetimes much less than 10^4 yr, and mechanical luminosities approximately 50 per cent of the bolometric luminosity (André 1995). An inclination angle of approximately 5 degrees for this outflow results in properties extremely similar to those found in other young outflow sources.

The visual extinction through the core, derived from C^{18}O, is 6 times larger than that derived by Wilking *et al*. (1989) but this is almost certainly because their beam area was ten times larger. The 9 CS spectra are very noisy and weak but the strongest line is also the widest and is centred on the core. The abundance of CS relative to C^{18}O is an order of magnitude smaller than is generally assumed; this may be due to chemical depletion onto grains but it is more likely that the high densities necessary to thermalize the *J* level are only present towards the centre of the core, whereas the C^{18}O is more diffuse. Methanol was detected but neither propyne nor methyl cyanide were.

The outflow is aligned in the same orientation as the three blue-shifted water masers and, within the errors, centred on the maser positions and on the submm core. This gives weight to the suggestion by Tofani *et al*. (1995) that the masers are accelerated at the inner part of the outflow. One problem is that the velocity gradient detected in the masers is perpendicular to the direction of the outflow. Since the outflow is thought to be almost in the plane of the sky this then suggests that the water masers are associated with a disk surrounding the forming protostar. The velocity difference of 17 km s^{-1} and maser separation of 1.64 mpc, then imply a central gravitating mass of 7 M$_\odot$.

In summary this source has a central object of 7 M$_\odot$ surrounded by 34 M$_\odot$ of circumstellar matter, with a mean hydrogen density greater than 10^7 cm^{-3}, and an extremely young outflow. This source is an extremely good class 0 candidate. The water masers are thought to arise in a rapidly rotating disk

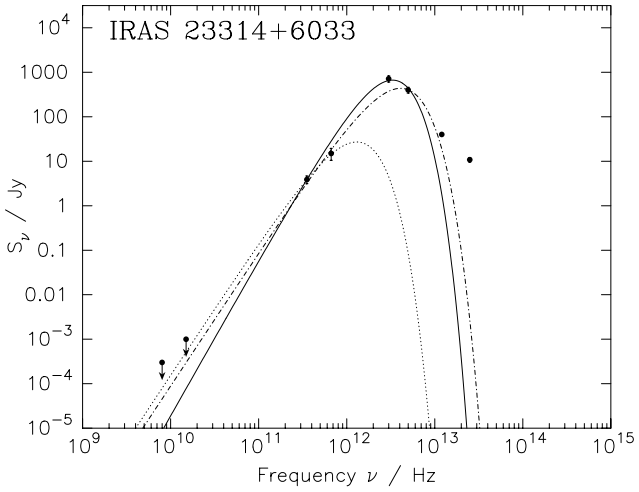

Figure 5.23
SED of IRAS 23314. The solid line is the best fit with β = 1.5, the dotted line is $\beta = 1.0$, $T_{\rm d} = 16$ K, $\Omega = 400$ arcsec^2 and $\lambda_c = 10$ μm, and the dot-dashed line is $\beta = 1.0, T_{\rm d} = 56$ K, $\Omega = 10$ arcsec^2 and $\lambda_c = 66$ μm.

near to the forming star.

5.8 IRAS 23314+6033

This source, discovered by *IRAS*, has not previously been observed in detail and has only been observed for water maser emission on the basis of its *IRAS* colurs. First detected in 1986 February by Wouterloot *et al*. (1993) as part of their extensive survey of *IRAS* sources, this extremely weak maser, with a flux density of only 0.4 Jy, has not been detected subsequently (Comoretto *et al*. 1990; Palla *et al*. 1991; Wouterloot *et al*. 1993). Plume *et al*. (1992) searched this source for CS $J = 7 \rightarrow 6$ but failed to detect a line (<0.3 K).

The low-resolution submm continuum observations show a slightly extended (23 $\times$ 13 arcsec^2) source with peak emission approximately 4 arcsec from the VLA maser position. This extension is explained by the high-resolution 450-μm map which shows two unresolved sources connected by background emission. The *IRAS* source is a few arcseconds to the east of the submm peak so using the *IRAS* fluxes for the grey-body fit should be a reasonable approximation. The fitted size of 240 arcsec^2 is consistent with the observed size of the low-resolution map of 235 arcsec^2. The assumed dust index of 1.5 used for the grey-body fits is too large and the submm fluxes are better fitted by a dust index of 1.0. Using β = 1.0 for the fits of the submm fluxes allows dust temperatures from 16 K (limited by the 450 μm point and resulting in a core mass of 600 $M_\odot$ and a luminosity of 300 $L_\odot$) up to 56 K (limited by the *IRAS* fluxes, with a mass of 94 $M_\odot$and luminosity of 1.5×10^4 $L_\odot$). The different fits are shown in Fig. 5.23 and show that with less than an order of magnitude improvement in sensitivity the embedded core should be visible in the radio at, for example, 15 GHz.

Extended radio continuum has been detected by the RT approximately 20 arcsec to the south-east of the water maser position (Fig. 5.24). VLA observations failed to detect any continuum less than 10 arcsec in extent and the RT observations show that the smallest structure is larger than 30 arcsec

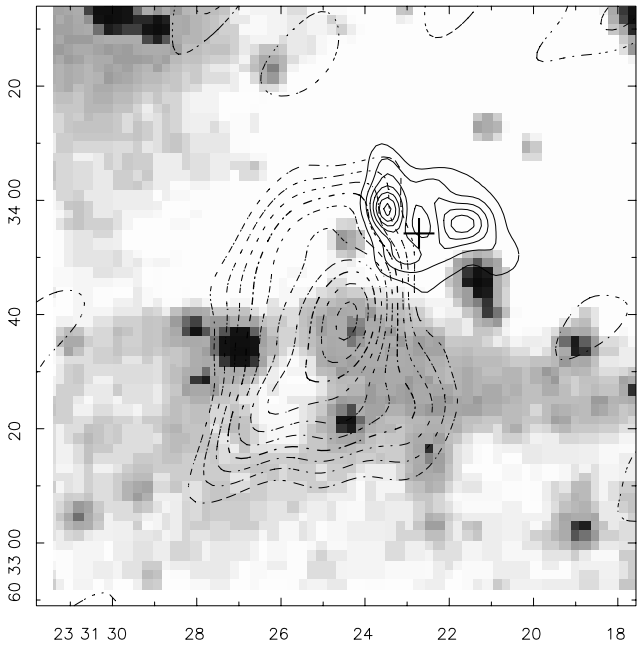

Figure 5.24
IRAS 23314+6033 15 GHz radio continuum contours (dashed) and 450 μm contours (solid) overlayed on the POSS image.

and most of the flux has been resolved out by the RT in its extended configuration. This radio source is probably unrelated to the submm core and water maser and may be a remnant of an earlier stage of star formation.

The average ^{12}CO spectrum (Fig. 5.25a) shows red- and blue-shifted wings but does not show any significant velocity structure across the map. The absorption at -37 km s^{-1} is caused by a source in the reference beam. The ^{12}CO map shows a hotspot a few arcsec to the south-east of the continuum peak with emission streaming back to the north-west. Placing contours of this map onto the POSS plate (Fig. 5.26) shows that the CO is probably externally heated to the south and east by the stars visible on the POSS image along an ionization front and the submm sources may be the sites of triggered star-formation. The peak brightness temperature of 37 K is consistent with the dust temperature of the core but external heating of the ^{12}CO would makes the comparison difficult if the submm sources are internally heated. Symmetric top molecules were searched for but only upper limits could be set on the propyne and methyl cyanide observations. Fig. 5.27 shows the upper limits these observations imposed on the column densities of the two molecules. The expected column density, derived from the C^{18}O data and indicated by the horizontal dotted lines in the figure, can only be attained with extreme temperatures. The propyne column density can still agree with the expected value if the rotation temperature is less than 20 K or greater than 300 K. This is unreasonable considering the observed ^{12}CO temperatures and the temperatures found in propyne in sources for which multiple transitions were detected. A rotational temperature of 50 K, the 'norm' for the detected sources, places an upper limit on the propyne column density of 1.3×10^{17} m^{-2}, which is four times lower than the 'expected' value from C^{18}O.

Line observations show very interesting velocity structure. The C^{18}O integrated intensity map

Figure 5.25. IRAS 23314+6033

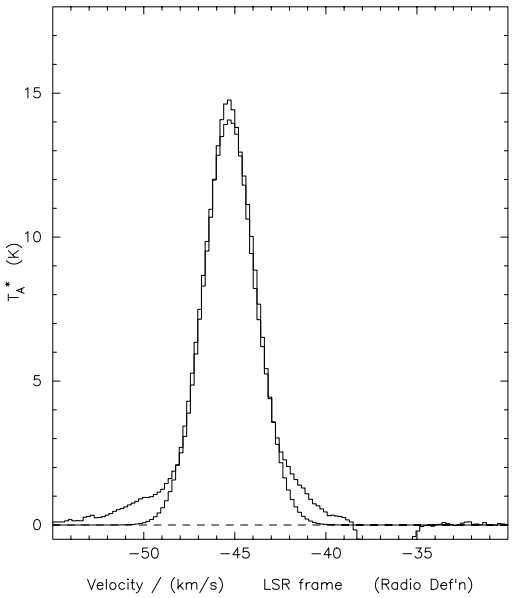

(a) Average ^{12}CO spectrum with fitted Gaussian (width = 3.4 km s^{-1} at −45.3 km s^{-1}).

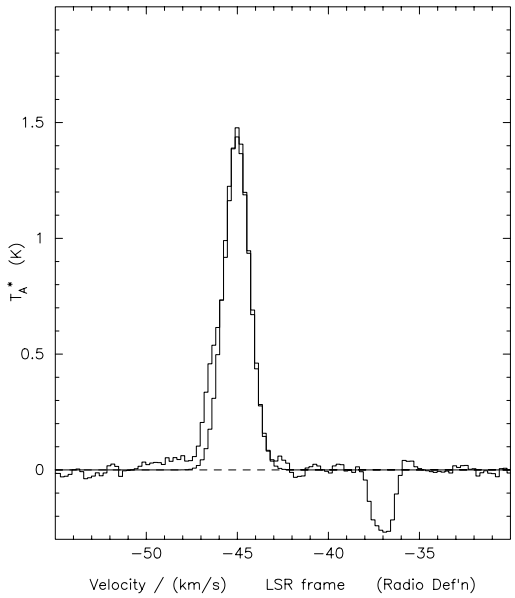

(b) Average C^{18}O spectrum with fitted Gaussian (width = 1.7 km s^{-1} at −45.0 km s^{-1}.)

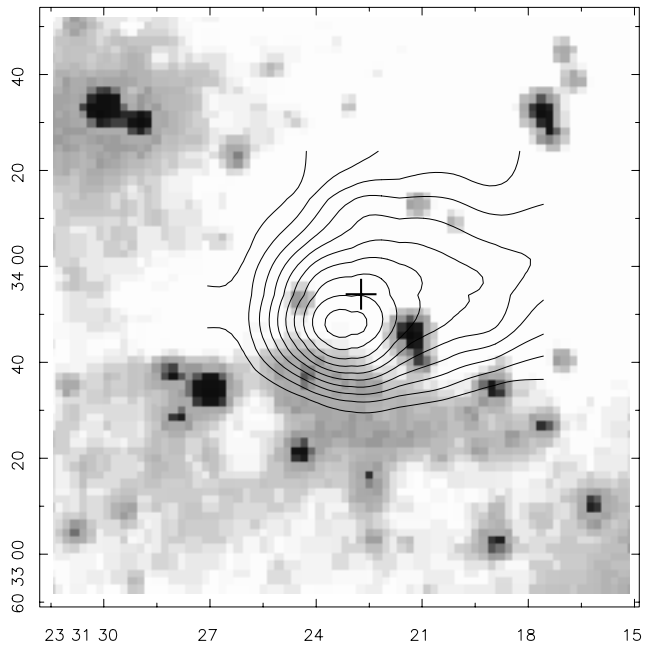

Figure 5.26
IRAS 23314+6033, ^{12}CO contours overlayed on POSS image

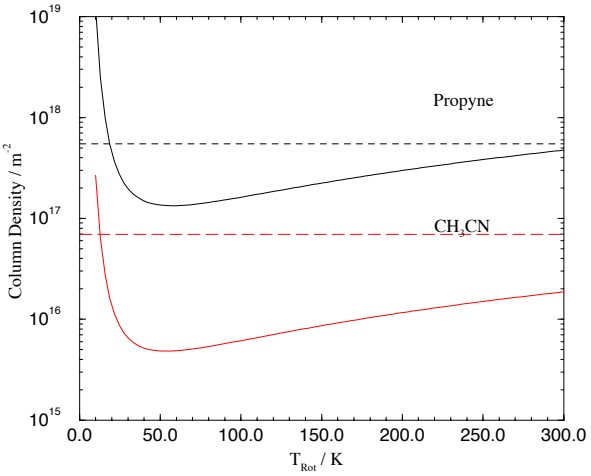

Figure 5.27
Upper limits on propyne and methyl cyanide column densities in IRAS 23314. The horizontal lines indicate the 'expected' values. A line width of 3 MHz has been assumed.

Figure 5.28. IRAS 23314+6033

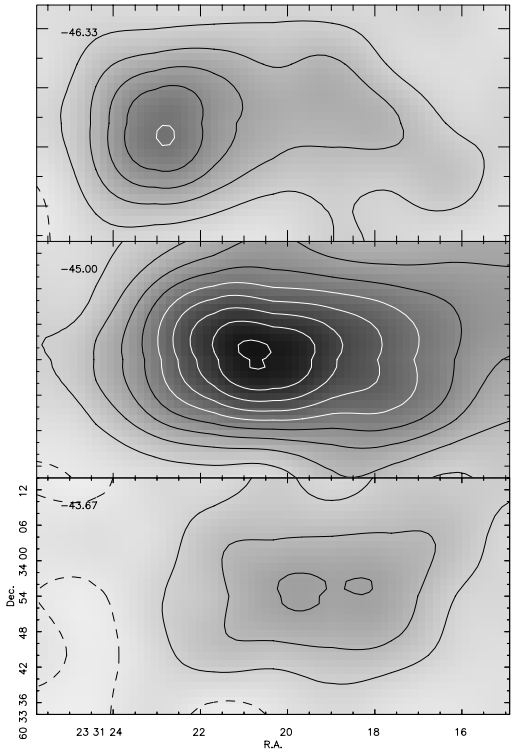

(a) Channel map of width 1.33 km s^{-1} centred on the ambient cloud velocity of −45 km s^{-1}.

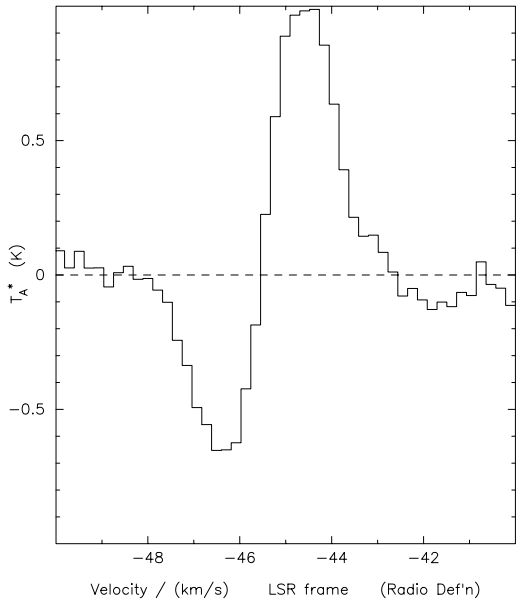

(b) Difference between six spectra from the eastern edge and six spectra from western edge in $C^{18}O$.

Figure 5.29. IRAS 23314+6033 $C^{18}O$ position-velocity diagram along the RA axis at 0 arcsec dec. offset. The ambient emission has not been shown for clarity.

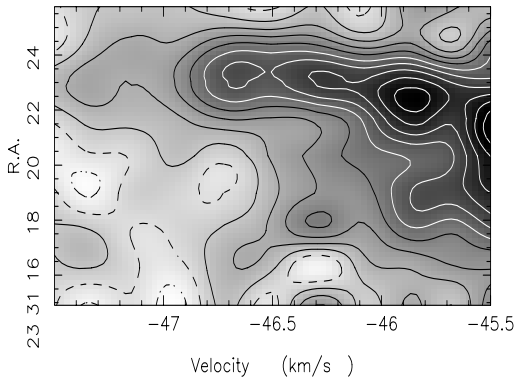

(a) Blue shifted-emission.

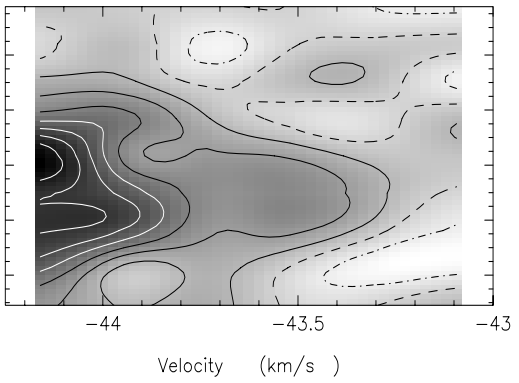

(b) Red-shifted emission (note the slightly different velocity interval).

shows a bar of emission extending east-west for about 30 arcsec. Channel maps of this data (Fig. 5.28a) show a velocity shift between the eastern edge (blue-shifted from the ambient) and the western edge (red-shifted) of approximately 3 km s^{-1}. Fig. 5.28b shows this shift explicitly in the form of a spectrum showing the difference between the average six spectra in the eastern and western extremes of the map. Ambient emission has mostly cancelled out and the resultant spectrum shows the velocity structure. An alternative way of presenting this information is by using a position-velocity diagram (Fig. 5.29) which shows the blue-shifted emission out to -47 km $s^{-1}$and a fairly sharp decrease to the ambient velocity. As seen in the channel maps, the integrated intensity of the red-shifted gas is far weaker than that of the blue-shifted gas and is barely visible in the position-velocity diagram at a velocity of -43.5 km s^{-1}. The edge of the blue-shifted emission, at an RA of $23^h31^m24^s$, coincides with the eastern edge of the 450 μm data; rather suggestively the continuum image looks flattened north-south at this position.

This velocity data can be explained in two ways:

- Large-scale rotation

  The velocity shift across the source could simply be due to large scale rotation of the molecular gas with a rotation velocity of approximately 3 km s^{-1}. This model predicts a central bar at ambient velocity with two lobes equally spaced in position and velocity on either side. This is seen in the channel map (Fig. 5.28a) and the spatial separation between the red and blue lobes of 30 arcsec (0.65 pc) then implies a central gravitating mass, given by

  $$M = \frac{R(\Delta v)^2}{2G}$$

  where Δv is half the velocity difference and R is the radius of the orbit, of 85 $M_\odot$, if the matter is in a stable orbit. From the integrated $C^{18}O$ map a gas mass of 540 $M_\odot$ is derived, assuming

an excitation temperature of 50 K. From the channel maps the central mass should be at an RA of $23^h31^m20.5^s$ but this position is inaccurate because of the difficulty in finding the location of the peak of the red-shifted emission. This position is 7 arcsec to the west of the weaker 450 μm continuum source, FIR2, and it is *just* possible that if all the errors went in the right direction that this source is at the centre. The flux of FIR2 is approximately 5 Jy, and although this number is unreliable due to the background emission, this flux is consistent with a source mass of 85 $M_\odot$ if the dust temperature is approximately 27 K. This hypothesis cannot account for the eastern submm source, FIR1, which seems to be related to FIR2, unless it is also orbiting FIR2. The position-velocity diagram shows that the eastern edge has gas moving at all velocities up to the maximum. This is inconsistent with a disk model which should only have gas at the higher velocities towards the edge. The size of the disk is unreasonable and an alternative hypothesis is required.

- Molecular outflow

  An alternative explanation is that the gas is not in orbit but is flowing away from a central object in the form of a molecular outflow. The outflow can be centred on either of the FIR sources.

  - FIR1 is centred on the highest velocity emission suggesting a low velocity outflow is pointing directly towards the observer. The red-shifted gas, offset from FIR1, cannot be explained by this.
  - Given the pointing errors in the continuum map and the large beam used for the $C^{18}O$, FIR2 may coinicide with the predicted centre of the red- and blue-shifted emission as discussed previously. The position-velocity diagram shows structure consistent with a shock at the location of FIR1. Indeed FIR1 may have been produced (triggered?) by the outflow from FIR2. The red-shifted lobe is weak compared to the blue-shifted lobe because the intervening ambient gas can absorb the low velocity photons. The outflow has a very low velocity and some overlap in the lobes which suggests that the outflow axis is almost in the plane of the sky. This implies an outflow length of approximately 1 pc which is comparable to outflows such as NGC 2024 (Richer 1990) but much smaller than the largest outflows known, such as RNO 43 (Bence *et al*. 1996).

The water maser is located between the two 450-μm sources and, given the poor absolute positional accuracy of the 450-μm map, the separation between the maser and the eastern source is greater than 3 arcsec (0.07 pc at the adopted distance of 4.5 kpc) and is therefore *not* within the submm core (although it is within the FWHM of the low-resolution map) and is possibly excited some distance from an external source. The water maser *is* directly coincident with the column density peak of the blue-shifted $C^{18}O$ but the maser is moving 7 km s^{-1} faster than the gas at this point, although the maser is just within the blue wing of the ^{12}CO. The maser feature is 5 km s^{-1} faster and three times more luminous now than it was back in 1986, but it is impossible to tell whether the maser has been accelerated to this new velocity or that a new maser has been created.

References

André P., 1995, in *The Cold Universe, Proceedings of the XIIIth Rencontres de Moriond*, eds Montmerle T., Lada C. J., Mirabel F., Trân Thanh Vân J.

André P., Martin-Pintado J., Despois D., Montmerle T., 1990, *A&A*, 236, 180

Bachiller R., Cernicharo J., Martin-Pintado J., Tafalla M., Lazareff B., 1990, *A&A*, 231, 180

Bence S. J., Richer J. S., Padman R., 1996, *MNRAS*, submitted

Brand J., *et al*., 1994, *A&AS*, 103, 541

Casoli F., Dupraz C., Gerin M., Combes F., Boulanger F., 1986, *A&A*, 169, 281

Comoretto G., *et al*., 1990, *A&AS*, 84, 179

Condon J. J., Broderick J. J., 1985, *AJ*, 90, 2540

Elitzur M., 1992, *Astronomical Masers*, Astrophysics & Space Science Library, Kluwer Academic Publishers, Dordrecht

Felli M., Palagi F., Tofani G., 1992, *A&A*, 255, 293

Fukui Y., 1989, in *ESO workshop on low mass star formation and pre-main sequence objects*, ed. Reipurth B., p. 95, European Southern Observatory, Garching bei München, Germany

Hughes V. A., MacLeod G. C., 1994, *ApJ*, 427, 857

Jaffe D. T., Güsten R., Downes D., 1981, *ApJ*, 250, 621

Jaffe D. T., Stier M. T., Fazio G. G., 1982, *ApJ*, 252, 601

Kalenskii S. V., Sobolev A. M., 1994, *Pis'ma Astron. Zh.*, 20, 113

Little L. T., Bergman P., Cunningham C. T., Heaton B. D., Knee L. B. G., MacDonald G. H., Richards P. J., Toriseva M., 1988, *A&A*, 205, 129

Martí J., Rodríguez L. F., Reipurth B., 1993, *ApJ*, 416, 208

Martí J., Rodríguez L. F., Reipurth B., 1995, *ApJ*, 449, 184

Matthews H. E., Olnon F. M., Winnberg A., Baud B., 1985, *A&A*, 149, 227

McCutcheon W. H., Dewdney P. E., Purton C. R., Sato T., 1991, *AJ*, 101, 1435

Miralles M. P., Rodríguez L. F., Scalise E., 1994, *ApJS*, 92, 173

Odenwald S. F., 1989, *AJ*, 97, 801

Palla F., Brand J., Cesaroni R., Comoretto G., Felli M., 1991, *A&A*, 246, 249

Plume R., Jaffe D. T., Evans II N. J., 1992, *ApJS*, 78, 505

Poetzel R., Mundt R., Ray T. P., 1992, *A&A*, 262, 229

Ray T. P., Poetzel R., Solf J., Mundt R., 1990, *ApJ*, 357, L45

Richards P. J., Little L. T., Toriseva M., Heaton B. D., 1987, *MNRAS*, 228, 43

Richer J. S., 1990, *MNRAS*, 245, 24P

Schutte A. J., van der Walt D. J., Gaylard M. J., MacLeod G. C., 1993, *MNRAS*, 261, 783

Slysh V. I., *et al*., 1994, *Astron. Zh.*, 71, 37

Stier M. T., Jaffe D. T., Fazio G. G., Roberge W. G., Thum C., Wilson T. L., 1982, *ApJS*, 48, 127

Tafalla M., Bachiller R., Martin-Pintado J., 1993, *ApJ*, 403, 175

Tofani G., Felli M., Taylor G. B., Hunter T. R., 1995, *A&AS*, 112, 299

Wilking B. A., Mundy L. G., Blackwell J. H., Howe J. E., 1989, *ApJ*, 345, 257

Wouterloot J. G. A., Walmsley C. M., Henkel C., 1988, *A&A*, 203, 367

Wouterloot J. G. A., Brand J., Fiegle K., 1993, *A&AS*, 98, 589

Xiang D., Turner B. E., 1992, *Chin. Astron. Astrophys.*, 16, 307

Chapter 6

Water masers and the submm cores

In this chapter I will use the statistical analysis of the complete sample performed in chapter 4 and the detailed source analysis of the previous chapter to discuss the implications for maser excitation and the nature of the submm cores.

6.1 Maser excitation

6.1.1 The water molecule and maser theory

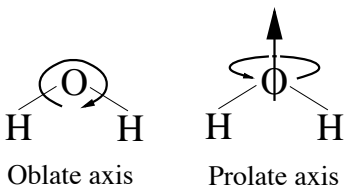

Figure 6.1.

Although water is a planar molecule with an axis of symmetry, it has three different moments of inertia. This means that unlike the molecules dealt with in §3.2.3, the water molecule is an asymmetric rotor with energy levels denoted by $J_{K_-K_+}$ (Townes & Schawlow 1975). Here J is the total angular momentum, and K_- and K_+ its projections on two molecular axes. The K_- quantum number corresponds to the projection of the total angular momentum on the symmetry axis water would have if it was a symmetric prolate rotor; K_+ corresponds to the projection along the symmetry axis water would have if it was a symmetric oblate rotor. The radiative selection rules are that K_- and K_+ must change their evenness and $\Delta J = 0 \pm 1$. These selection rules result in two distinct species that are radiatively uncoupled. Ortho-H_2O has nuclear spin 1 and (K_+, K_-) = (odd, even) or (even, odd), and para-H_2O has nuclear spin 0 and (K_+, K_-) = (odd, odd) or (even, even).

The equation of radiative transfer (equation 3.3) tells us that it is not possible for the observed intensity to exceed the source function. In terms of Rayleigh-Jeans brightness temperature, and ignoring

external radiation, the solution to the radiative transfer equation can be written as

$$T_{\rm b} = (1 - e^{-\tau})T_{\rm ex}, \tag{6.1}$$

and it is clear that $T_{\rm ex}$ must exceed the observed brightness temperature.

The discovery of water lines with extremely large brightness temperatures, i.e. brightness temperatures well in excess of the temperature at which water dissociates, at first sight leads to a problem. The implicit assumption in the previous statement is that temperatures must be positive. If, however, there are more atoms in the upper level than in the lower level, equation (3.15) tells us that the excitation temperature of the system must be negative. In order to have a negative excitation temperature and a positive observed brightness temperature the optical depth must also be negative. This removes any limit to the size of the brightness temperature and means that the material is now amplifying the radiation instead of absorbing it. If a molecule undergoes spontaneous emission and produces a photon, this photon can now cause another molecule to emit a photon of the same frequency through stimulated emission. Both these photons can then stimulate emission in other molecules and, so long as the number of molecules in the upper state exceeds the number in the lower state, the number of photons can continue to increase – the emission is amplified and a maser is in operation.

For an astronomical maser to form, four conditions need to be met:

1. **Population inversion**

   The energy levels of water were first investigated by de Jong (1973), and more recently by Chandra *et al.* (1984) (see Fig. 6.2). These analyses showed that the energy levels divide naturally into two groups. Transitions among the lowest levels of each J-state have larger cross sections and line strengths than the other transitions, and, to a first approximation, are decoupled from each other. The larger collisional cross sections mean that the levels in the first group thermalize easily and the large difference in spontaneous emission rates mean that radiative trapping effects (i.e. where the photons cannot escape from a line because the large line strength keeps the optical depth high) are important. This means that the first group, the lowest levels in each J-state, are known as the *backbone* levels. For example, the Einstein A coefficient for the backbone transition $6_{16} \rightarrow 5_{05}$ is eight orders of magnitude larger than that for the $6_{16} \rightarrow 5_{23}$ maser transition. Downward transitions of backbone levels are dominated by transitions to the next lower backbone levels and the main way of populating the off-backbone levels is from radiative cascades from neighbouring backbone levels; all other excitation processes are much slower. This means that level populations decrease with increasing distance from the backbone and inverted populations are generated easily

2. **Large column density**

   If a negative τ (known as the maser gain (Elitzur 1992), although some authors refer to $e^{|\tau|}$ as the maser gain) is substituted into the solution of the radiative transfer equation (equation 3.3) it can be seen that the intensity of the source increases exponentially with gain and, so long as the

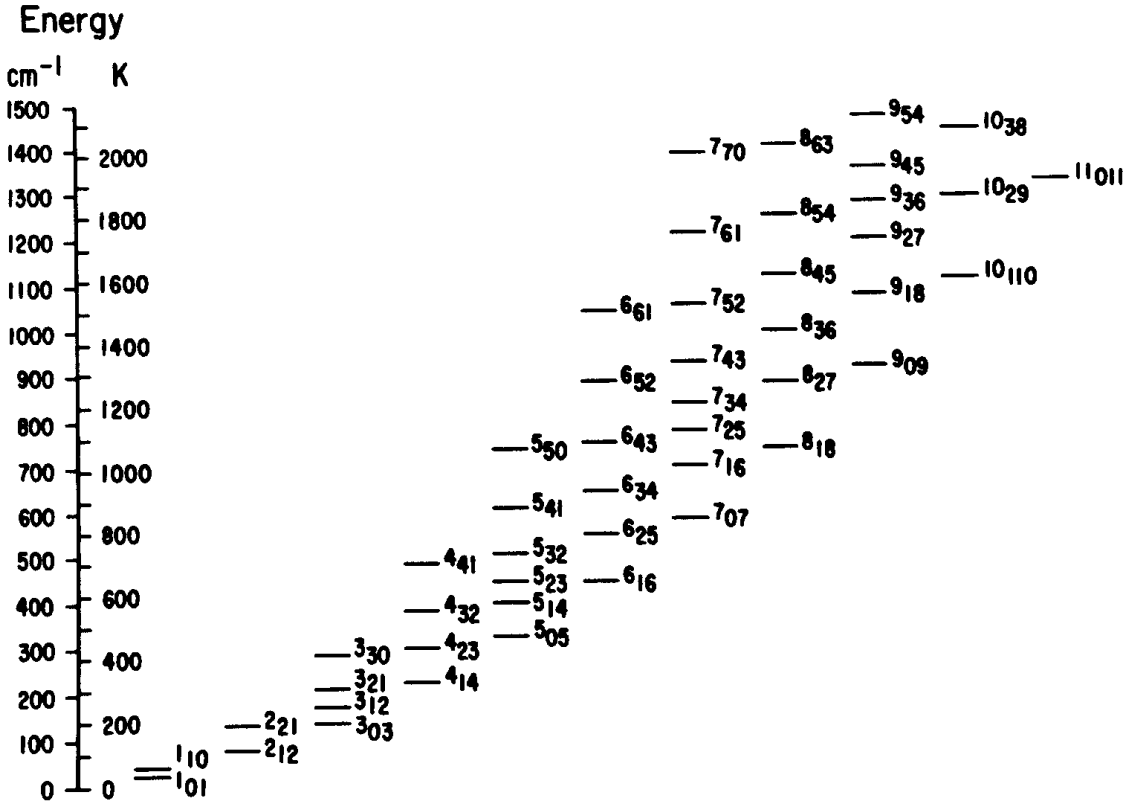

Figure 6.2. Rotation levels of ortho H_2O with energies less than 2150 K. (Fig. taken from Elitzur 1992)

column density is large enough to generate enough stimulated photons, a maser will be formed. A maser which is not using all of the available pumped atoms is said to be unsaturated. However, this exponential growth cannot continue *ad infinitum*, and eventually all of the molecules pumped into the upper level are radiatively de-excited as soon as they enter that state and the maser is then said to be saturated. The strength of a saturated maser can only vary linearly with the pumping conditions and cannot show the huge temporal variations in intensity associated with the exponential gain seen when a maser is in the unsaturated phase.

3. **Small velocity gradient**

Even if a large column density of water is present this will not necessarily produce a maser. Since an incoming photon can only stimulate emission if its frequency is within the natural linewidth of the transition of the 'absorbing' molecule, a large difference in velocity between the two atoms will cause the photon to be Doppler shifted out of the available range of frequencies the second atom can accept. This means that only those atoms with small relative velocities can affect each other so that there must be a small velocity gradient along the line of sight.

4. **Volume density**

   The hydrogen volume density must be large enough such that the upper maser level is collisionally populated, but small enough such that only the backbone levels are thermalized.

Analysing the inversion structure of water (Cooke & Elitzur 1985), it becomes clear that there is nothing special about the $6_{16} \rightarrow 5_{23}$ maser transition at 22 GHz (1.35 cm). This transition is only one of many allowed which may have inverted populations. The 22 GHz line is simply the lowest frequency transition and therefore it is the easiest to observe – low frequency detectors are fairly easy to construct and for a given intensity the brightness temperature will be highest for the longest wavelength transition. Recent detections of water masers at submm wavelengths (Menten *et al*. 1990a, 1990b; Cernicharo *et al*. 1990) have confirmed that many maser transitions are possible. Since each maser transition uses different energy levels, multiple transitions should allow more detailed analyses of the pumping environment to be performed.

6.1.2 Models

Models for maser excitation have had to develop a pump mechanism capable of generating the inverted population. Early models involved radiative pump mechanisms where dust grains are heated by, for example, a hot star which then emit infrared photons. Some of these infrared photons are then absorbed by water molecules. This has the effect of increasing the population of the higher levels above the equilibrium value obtained from collisions with the cold (relative to the dust) molecular hydrogen. The water molecules are then being heated by the warm dust and cooled by the molecular hydrogen. It is for this reason that the model is known as the hot-dust, cool-gas model (Goldreich & Kwan 1974). In this way a population inversion can be achieved until the molecular hydrogen reaches a high enough temperature (from collisions with the dust) sufficient to thermalize the water in the presence of the infrared photons. Strong evidence for radiative pump models has been seen for 1612 MHz OH masers in the hot envelopes of late-type variable stars, where the variability of the stars correlates with variation in the OH masers (Harvey *et al*. 1974). Although water maser emission is much more chaotic in late-type stars, a general trend of maser variability with the star has been seen (Engels *et al*. 1986), but the large delay between the star variability and that of the maser (i.e. much longer than the light travel time) indicates collisional pumping. Further evidence for this is seen when multiple maser transitions are observed simultaneously. Yates & Cohen (1996) find that there is very little correlation between the variability seen in submm and 22 GHz masers.

The first detailed attempt at a radiative pump model for water maser excitation in star forming regions was by Tartar & Welch (1986). Their model involves a collision between two dense ($\sim 10^9$ cm^{-3}) clouds with a relative velocity $\sim$100 km s^{-1}. The powerful dissociative shock which this creates, produces large numbers of infrared photons which diffuse rapidly from the shock and pump the water maser via the hot-dust, cold-gas pump mechanism (Goldreich & Kwan 1974). Whilst this model accounts for the variability seen in water masers, the energy requirements are large. One problem is that

the actual collision rates may be an order of magnitude smaller than those used in this model (Kylafis & Norman 1987; Green 1980). Including the more accurate rates, increases the density required for maser formation to unreasonable values (Elitzur 1986).

Recently, collisional excitation from shock models has been reasonably successful in explaining the maser emission from star-forming regions. Elitzur *et al*. (1989) (hereafter EHM) suggest that the 22 GHz maser emission can be explained by the collisional pumping of dense ($n_{\rm H_2} \sim 10^7$ cm^{-3}), neutral gas which has been compressed and heated by a high velocity ($\geq 40-50$ km s^{-1}) dissociative *J*-shock (*J* signifies a *jump* in the density and temperature across the shock). These shocks have been investigated in detail by Hollenbach & McKee (1989). First they completely dissociate the hydrogen molecules because of the high temperature ($T \sim 10^5$ K) just behind the shock front. Most dust grains survive these high velocity shocks (McKee *et al*. 1987) but, since they are not well coupled to the gas for the conditions found behind the shock, the dust temperature is much lower than the gas (approximately 100 K). As the material cools down hydrogen molecules can form on these dust grains which are then ejected back into the gas due to the exothermic heat of formation. The injection of these high energy molecules into the gas effectively prevents the cooling of the gas and a 400 K temperature plateau is formed behind the shock. It is in this region that other molecules form and the temperatures are high enough so that almost all of the oxygen not tied up in CO is converted to water. It is in this plateau region where the water abundance is enhanced and the velocity gradient is small that the maser can form. Eventually all the H atoms have been converted to H_2 and the gas begins to cool again. A more detailed numerical simulation of maser formation behind dissociative *J*-shocks has been performed by Kylafis & Norman (1991) with essentially the same results. An extensive study of outflow sources by Felli *et al*. (1992) has shown that the mechanical luminosities of the outflows correlate weakly with the H_2O maser luminosities as predicted by EHM. Although the scatter is fairly large, this can be accounted for by variation in the unknown parameters, for example the shock size and velocity. They support the view that there is a direct causal connection between energetic mass motions and H_2O masers.

Melnick *et al*. (1993) have used multiple water maser transitions to impose more stringent limits on the conditions. They conclude that low velocity ($\leq$50 km s^{-1}) non-dissociative shocks (i.e. *C*-shocks, where all the parameters describing the shock are *C*ontinuous (Draine 1980; Draine *et al*. 1983) because the magnetic field can 'warn' the unshocked material that a shock is coming, or slow *J*-shocks (Smith 1994)) with post-shock temperatures in excess of 900 K, are all that is required to produce a water maser. Enhancement of the water abundance occurs naturally behind *C*-shocks since a shock of between 10- and 25-km s^{-1} supplies enough energy for the conversion of O and H_2 to H_2O. High temperatures are required for this neutral-neutral reaction,

$$\mathrm{O} + \mathrm{H_2} \rightarrow \mathrm{OH} + \mathrm{H}$$
$$\mathrm{OH} + \mathrm{H_2} \rightarrow \mathrm{H_2O} + \mathrm{H},$$

because the first reaction is highly endothermic and the second reaction, which is exothermic, requires a large activation energy (Neufeld & Kaufman 1993). Since the shock is non-dissociative, water is

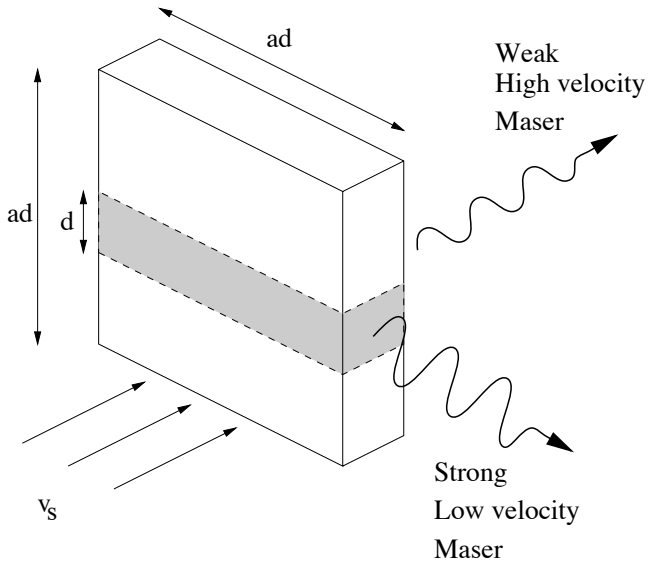

Figure 6.3
Shock geometry used in EHM model. The high velocity masers are weak because the column density is small and the velocity gradient is high. Perpendicular to the shock the velocity gradient is small and the column density is much higher.

not destroyed and can reach the high temperatures necessary for maser operation.

Both *C*- and *J*-shock mechanisms provide natural gain paths since the velocity gradient is small perpendicular to the flow direction of a planar shock. This means that for either mechanism it is most likely that masers will have relatively small (i.e. much less than the shock velocity) observed velocities relative to the molecular cloud (Fig. 6.3). Masers along the shock direction are possible in *J*-shocks because of the small velocity gradient through the shock although the small column density means that these masers are generally weak and unsaturated (Fig. 6.3). *C*-shocks have large velocity gradients through the shock and maser action in this direction is unlikely.

Consider a square planar shock of side ad (where a is the aspect ratio of the maser filament = length/width; Fig. 6.3) requiring mechanical luminosity L_m to exist. This shock subtends a solid angle of

$$\Omega = \frac{(ad)^2}{D^2} \tag{6.2}$$

to a source at a distance D. The energy available to the shock from a source with luminosity L_* is then given by,

$$L_m = \frac{\Omega}{4\pi} L_* \tag{6.3}$$

$$= \frac{1}{4\pi}\left(\frac{ad}{D}\right)^2 L_*. \tag{6.4}$$

Inverting this equation, this means that a shock of mechanical luminosity L_m can exist a distance D from a central source given by

$$\left(\frac{D}{\mathrm{AU}}\right) = \left(\frac{d}{\mathrm{AU}}\right)\sqrt{\frac{a^2}{4\pi}\frac{L_*}{L_m}}, \tag{6.5}$$

assuming all the energy available is used to power the shock. The isotropic maser luminosity of a 22 GHz saturated maser is given by

$$\frac{L_{\mathrm{H_2O}}}{\mathrm{L}_\odot} = 9.5\times10^{-9} a^3 \left(\frac{d}{\mathrm{AU}}\right)^2 \left(\frac{\Delta \mathrm{v}}{\mathrm{km\ s^{-1}}}\right) f, \tag{6.6}$$

from EHM, where Δv is the linewidth and f is the ratio of the solid angle of the filament cap, as viewed from the other end, to the maser beaming angle and is equal to 11/16 (Elitzur *et al*. 1991). A diameter of 1 AU, a linewidth of 1 km s^{-1} and an aspect ratio of 5, result in a maser with luminosity of the order of 10^{-6} L$_\odot$; a typical value for masers in the sample.

The EHM model also gives an expression for the total shock luminosity, $L_{m\mathrm{H_2O}}$, involved in the maser formation, which is also a lower limit to the shock mechanical luminosity:

$$\frac{L_{m\mathrm{H_2O}}}{\mathrm{L}_\odot} = \varepsilon\frac{L_m}{\mathrm{L}_\odot} = 3.2\times10^{-9} \left(\frac{n_{\mathrm{H_2}}}{10^7\ \mathrm{cm^{-3}}}\right) \left(\frac{\mathrm{v}_s}{\mathrm{km\ s^{-1}}}\right)^3 \left(\frac{d}{\mathrm{AU}}\right)^2 a^4 f, \tag{6.7}$$

where $n_{\mathrm{H_2}}$ is the pre-shock density, v$_s$ is the shock velocity and ε is the fraction of the shock energy involved in the maser formation. Substituting this into equation (6.5) eliminates d and results in a maximum distance at which this shock can be excited of,

$$\left(\frac{D}{\mathrm{AU}}\right) \leq 5000\sqrt{\frac{\varepsilon L_*}{n_{\mathrm{H_2}}\mathrm{v}_s^3 f a^2}}, \tag{6.8}$$

where the units are the same as used in previous equations. These equations demonstrate that the shock luminosity is only weakly dependent on the pre-shock hydrogen density whereas the aspect ratio and shock velocity are the critical parameters. It is also possible to write this distance in terms of the isotropic water maser luminosity, defined in equation (6.6),

$$\left(\frac{D}{\mathrm{AU}}\right) \leq 0.5\left(\frac{d}{\mathrm{AU}}\right)\sqrt{\frac{a\Delta \mathrm{v}}{n_{\mathrm{H_2}}\mathrm{v}_s^3}\frac{\varepsilon L_*}{L_{\mathrm{H_2O}}}}. \tag{6.9}$$

6.2 Comparison with observations

The previous two chapters have discussed the sample properties and individual sources. It now has to be investigated whether the results from those chapters are consistent with the collisionally excited shock models discussed in the previous section. The relevant observational results can be summarised as follows:

- High temperature gas has been detected, and most of the submm cores have mean densities greater than 10^6 cm^{-3}.
- The masers have low velocities with respect to the molecular cloud and are uniformly distributed within 6600 AU of the submm core.

- The isotropic maser luminosity is proportional to the far-infrared luminosity over more than 5 orders of magnitude.
- There is no obvious correlation between the near-infrared spectral class and the maser emission.
- Where a radio spectral index is known the majority of sources are optically thin H II regions. The bulk of the remainder are undetected and have a flux density less than 1 mJy.
- Masers not associated directly with a submm core show explicit evidence for shocks.

A necessary first step is to investigate the energetics of the system. The EHM model suggests that the mechanical luminosity required to power a 50 km s^{-1} shock of width 1 AU and aspect ratio of 5, is 0.17 L$_\odot$. Equation (6.5) tells us that this shock can only exist at a maximum distance from a 10^5 L$_\odot$ star of 1000 AU. Since the masers are known to exist at distances much larger than this, a shock of this type cannot be responsible for the bulk of the maser emission from sources in this sample. In order for a shock to exist at a distance of 6600 AU equation (6.8) imposes the constraint

$$\frac{\varepsilon L_*}{\mathrm{L}_\odot} > \left(\frac{n_{\mathrm{H}_2}}{10^7\ \mathrm{cm}^{-3}}\right)\left(\frac{\mathrm{v}_s}{\mathrm{km\ s}^{-1}}\right)^3 a^2. \tag{6.10}$$

This tells us that in the case of a 10^6 L$_\odot$ source powering a shock of aspect ratio 5, passing through material of pre-shock density 10^7 cm^{-3}, the shock velocity can be at most 34 km s^{-1} for $\varepsilon = 1$. This means that it is unlikely that a dissociative shock is responsible for maser emission at these distances.

As stated earlier, the pre-shock density is not a critical parameter. As long as the density is between 10^6 cm^{-3} and 10^8 cm^{-3} the shock will create enough water for the maser without thermalising the energy levels off the backbone. This condition is satisfied indirectly in all the cores in the sample since all the cores have mean densities greater than 10^5 cm^{-3} (§4.2.3). Corroborative evidence for the high densities comes from the CS and CH_3CN observations which require densities of 3×10^6 cm^{-3} and 10^7 cm^{-3} to thermalize. The detection of high temperature gas from these observations could be from two effects. The hot gas could simply be close to the central object or a direct indicator of the hot gas present behind the shocks. The column density measurements suggest that this gas fills only 10 per cent of the volume occupied by the cool gas, indicating that either explanation is plausible. These temperatures simply reflect the ambient conditions at which the transition is thermalized; higher transitions will generally give an indications of conditions in the warmer regions. As an example, IRAS 20275+4001 is known to have gas at temperatures in excess of 1000 K, from CO vibrational transitions (Mitchell *et al*. 1990), whereas the rotation temperature derived from the methyl cyanide observations was only 450 K.

Identifying L_{FIR} as L_* and using the observational result that L_{FIR} is approximately 10 orders of magnitude larger than the isotropic water maser luminosity, equation (6.9) becomes,

$$\left(\frac{D}{\mathrm{AU}}\right) \leq 5 \times 10^4 \left(\frac{d}{\mathrm{AU}}\right)\sqrt{\frac{a\varepsilon\Delta\mathrm{v}}{n_{\mathrm{H}_2}\mathrm{v}_s^3}}. \tag{6.11}$$

At a distance of 6000 AU, the shock velocity is then given by

$$v_s \approx 5 \left(\frac{d^2 a \Delta v}{n_{H_2}} \right)^{\frac{1}{3}}. \quad (6.12)$$

Since all the variables on the right-hand-side are of order unity, the shock velocity must be of order 10 km s^{-1}. This result completely rules out dissociative shocks as the cause for maser excitation at these distances, although there is no reason that dissociative shocks can not be responsible for the masers closer to the centre of the core.

The only way that dissociative *J*-shocks can be responsible is if multiple sources are present in the beam. This would effectively reduce the maser/submm separation and make these *J*-shocks energetically viable. High-resolution ($<$10 arcsec) maps are required to rule out the possibility of multiple power sources and this analysis has assumed that the 850-μm maps contain single sources. The maps of IRAS 23314 and IRAS 20188 show that this assumption is not always valid.

Continuing with the assumption that all the central objects are resolved implies that only non-dissociative shock models can be responsible for the maser emission at these distances. Both *C*-shocks (Melnick *et al*. 1993) and non-dissociative *J*-shocks (Smith 1994) can create a suitable environment for maser activity at distances of a few thousand AU from the power source.

The fact that no obvious correlation of maser properties with near-infrared class is seen suggests that the conditions for water maser emission are present during all phases of protostellar development (up to and including at least class II-D) and that the maser phase of star formation is long ($> 3 \times 10^5$ yr). This implies that it is maser variability, e.g. density inhomogeneities producing variation of the shock luminosity, and geometry effects, e.g. beaming, which prevent the detection of water masers in all young protostars and *not* a particular stage of star formation which preferentially excites water masers. This idea is supported by the observed variability of the masers in the sample (e.g. Fig. 5.19) and the non-detection of half of the masers that I observed with the VLA. Even though a II-D source is thought only to have a remnant of a disk, there must still be enough warm, and dense, gas close to the objects to allow water masers to form. For example, IRAS 18032−2137 has a visual extinction of 200 mag (from the $C^{18}O$ data) so that the source is still deeply embedded even though a near-infrared counterpart is visible; an isotropic model for these objects is obviously an oversimplification. The existence of maser emission for all NIR classes implies that either the masers have a different pump mechanism during the main accretion phase to that pumping the maser when the source is visible in the near-infrared, or the masers are not radiatively pumped. Class 0 sources are still accreting mass and there is not expected to be a high enough intrinsic luminosity in the forming star to radiatively pump the masers. On the other hand, the densities close to the core are more than enough to excite masers collisionally in the presence of shocks.

Of course, an alternative explanation for this lack of correlation is that the SED's are unreliable. Many of the near-infrared observations included in the SED's were made with large beams, 30 arcsec, and it is unclear whether the source included in the SED is the central object. It may well be that the stronger sources, which dominate the flux detected in a large beam, are not directly involved in

the maser process and are evidence of earlier star formation (see e.g. the study of GL 5142 by Hunter *et al*. 1995). Multiple submm sources will also distort the SED, since it is usually not clear to which source the *IRAS* and near-infrared information should be assigned.

In summary, non-dissociative shock models seem to be the most likely cause of maser excitation in these embedded cores, although dissociative shocks cannot be ruled out without higher resolution continuum images. It must also be remembered that the arguments given above to discount dissociative shocks are only valid on the basis of isotropic emission from a central source. Shocks generated via disks (e.g. IRAS 22198+6336), jets (e.g. IRAS 20188+3928 FIR 2) or outflows (e.g. IRAS 23314+6033) are not subject to the same energy constraints. This sample shows that the maser emission is unrelated to the radio source. Most sources have simple compact H II regions or no continuum at all, and an ionised expanding shell model (Panagia & Felli 1975), with a rising radio spectrum, is not required for the maser emission to occur.

The dense, energetic conditions found in the vicinity of a forming star favour the formation of water masers.

References

Cernicharo J., Thum C., Hein H., John D., Garcia P., Mattioco F., 1990, *A&A*, 231, L15
Chandra D. A., Varshalovich D. A., Kegel W. H., 1984, *A&AS*, 55, 51
Cooke B., Elitzur M., 1985, *ApJ*, 295, 175
de Jong T., 1973, *A&A*, 26, 297
Draine B. T., 1980, *ApJ*, 241, 1021
Draine B. T., Roberge W. G., Dalgarno A., 1983, *ApJ*, 264, 485
Elitzur M., 1986, in *Masers, molecules and mass outflows in star forming regions*, ed. Haschick A. D., p. 299, Haystack Observatory, Westford
Elitzur M., 1992, *Astronomical Masers*, Astrophysics & Space Science Library, Kluwer Academic Publishers, Dordrecht
Elitzur M., Hollenbach D. J., McKee C. F., 1989, *ApJ*, 346, 983
Elitzur M., McKee C. F., Hollenbach D. J., 1991, *ApJ*, 367, 333
Engels D., Schmid-Burgk J., Walmsley C. M., 1986, *A&A*, 167, 129
Felli M., Palagi F., Tofani G., 1992, *A&A*, 255, 293
Goldreich P., Kwan J., 1974, *ApJ*, 191, 93
Green S., 1980, *ApJS*, 42, 103
Harvey P. M., Bechis K. P., Wilson W. J., Ball J. A., 1974, *ApJS*, 27, 331
Hollenbach D. J., McKee C. F., 1989, *ApJ*, 342, 306
Hunter T. R., Testi L., Taylor G. B., Tofani G., Felli M., Philips T. G., 1995, *A&A*, 302, 249
Kylafis N. D., Norman C., 1987, *ApJ*, 323, 346
Kylafis N. D., Norman C., 1991, *ApJ*, 373, 525
McKee C. F., Hollenbach D. J., Seab C. G., Tielens A. G. G. M., 1987, *ApJ*, 318, 674
Melnick G. J., Menten K. M., Phillips T. G., Hunter T., 1993, *ApJ*, 416, L40
Menten K. M., Melnick G. J., Phillips T. G., 1990a, *ApJ*, 350, L41
Menten K. M., Melnick G. J., Phillips T. G., Neufeld D. A., 1990b, *ApJ*, 363, L27
Mitchell G. F., Maillard J.-P., Allen M., Beer R., Belcourt K., 1990, *ApJ*, 363, 554
Neufeld D. A., Kaufman M. J., 1993, *ApJ*, 418, 263

Panagia N., Felli M., 1975, *A&A*, 39
Smith M. D., 1994, *MNRAS*, 266, 238
Tartar J. C., Welch W. J., 1986, *ApJ*, 305, 467
Townes C. H., Schawlow A. L., 1975, *Microwave Spectroscopy*, Dover Publications, Inc.
Yates J. A., Cohen R. J., 1996, *MNRAS*, 278, 668

Chapter 7

Conclusions

This research arose from the *observation* that many deeply embedded cores, including those with only a few solar masses, had associated H_2O maser emission. This raises a number of questions which need to be answered:

1. What is it about these sources that enables them to excite masers?
2. Does this constrain the theories of maser excitation in any way?
3. Could the presence of water masers be used to find embedded sources?

Once these questions have been asked it is necessary to determine a sample of maser sources which could be used to extend our knowledge and answer the questions. Looking in the literature for maser sources, it becomes clear that no unbiased sample exists. Most of the existing sources are either from complicated high-luminosity regions such as W51 (Genzel *et al*. 1981) or are associated with *IRAS* point sources (Palagi *et al*. 1993). This immediately implies that any sample constructed with these sources will under-represent cool, young, low-luminosity embedded cores. Despite this fact, the Arcetri atlas (Comoretto *et al*. 1990; Brand *et al*. 1994) was a full list of all water maser sources detected to date and had to be used. Many of the water masers listed have very little information available on them beyond a maser observation and *IRAS* – many of the more recent detections have been found through searching for maser emission from *IRAS* point sources. This means that it may indeed be a useful sample for detecting new, interesting objects. Another problem was that, given the time constraints only a small number of sources could be observed; even though more than 700 masers are known, only 45 were observed from a final sample of approximately 100 (§2.1).

The main task was to observe the resulting sample in the submm continuum with the James Clerk Maxwell Telescope in order to detect cool dust. Once submm cores had been detected it was necessary

to gather more information from the literature on the sources in order to determine their age and physical parameters. Determining the age of the cores was difficult as many sources were lacking near-infrared data and those sources which had been observed previously in the near-infrared sometimes had NIR stars nearby to a core but not directly associated – deciding whether a source was associated or not was hampered by pointing inaccuracies and different beamsizes between observations.

Observations with the VLA were necessary since many maser positions were extremely inaccurate and many sources had no radio continuum data; continuum observations were useful in determining whether H II regions were present. Further observations with the JCMT were also useful in determining the presence of outflows and the line data gives an alternative approach to finding masses and densities.

7.1 The maser environment

This work allows us to focus on the overall environment within which a maser can exist and answer the first of the questions listed at the start of this chapter.

One immediately obvious result of this work is that *it was extremely successful in detecting embedded cores via the presence of a water maser*. Submm continuum emission was detected from 40 of the 44 objects (91 per cent) by using the James Clerk Maxwell Telescope. Whilst this high detection rate is not altogether surprising, given the large fraction of the sources which are known to have *IRAS* counterparts, it is a good confirmation of the hypothesis. The *IRAS* bias in the maser sample immediately increases the chances of the resulting subsample possessing warm dust detectable in the submm, since sources with mid-infrared dust emission have already been pre-selected.

This high detection rate indicates that the masers are *not* related to H II regions (the source selection criteria should have removed evolved stars from the sample (§2.1.1)). This effect can be shown by the radio observations available (Tables 3.2 and 3.3, and Appendix B): 30 per cent have a flux density of less than 1 mJy and 25 per cent have thermal radio spectra indicative of simple compact H II regions. The very weakest radio sources are associated with the weaker masers but the masers with luminosity greater than 10^{-7} $L_{\odot}$ show no correlation with radio flux.

Using the Arcetri Atlas, JCMT line observations and the literature, the maser and molecular cloud velocities differ by less than 25 km s^{-1}. The accurate VLA maser positions also allow us to determine the maser/core separation. The masers are distributed uniformly within a radius of 6600 AU of the core. These two pieces of information indicate that the submm cores are indeed the origin of the masers although the existence of close-binary systems cannot be discounted.

The submm continuum observations also allow us to constrain the densities of the central cores: Most of the cores have mean densities in excess of 10^{6}cm^{-3}. This is reinforced by the detection of symmetric top molecules in many of the cores.

Whilst FIR luminosity does appear to be proportional to the water maser luminosity over 5 orders

of magnitude this is not a new result (Wouterloot & Walmsley 1986; Palagi *et al*. 1993; Tofani *et al*. 1995). It is generally true that the higher luminosity sources tend to have the higher luminosity masers (§4.2.4). Given the large variability of the masers they are at least 10 orders of magnitude weaker than the FIR source.

In summary, the masers are located close to, but still at a separation of a few thousand A.U. from, a high density core and are moving with a speed of a few tens of kilometres per second relative to this object. They also form without any apparent need for a compact radio H II region; some sources have H II regions, others do not. This trend has been noted by Tofani *et al*. (1995) who find that only 40 per cent of their sample have unresolved radio continuum sources. They explain this in terms of a YSO undergoing mass loss; the stellar wind interacts with the high density molecular material to generate shocks but a radio continuum source is only seen once the surrounding envelope becomes fully ionized. This result is different to that seen for OH masers which seem to be always associated with a ultra-compact H II region (Forster & Caswell 1989).

In a sample such as this there are bound to be exceptions. In one case, IRAS 20188 (§5.5), a weak ($10^{-6.7}$ $L_{\odot}$) maser is associated with the end of a radio jet and not with an embedded core – this is evidence for this maser being excited entirely by a shock interaction. Shock excitation at a distance from the central core may also account for the maser (also approximately $10^{-6.7}$ $L_{\odot}$) associated with IRAS 23314 (§5.8) which is located in a molecular outflow. These objects are discussed again later in this chapter (§7.5.1)

7.2 The longevity of the maser phase

The prevalence of masers (bearing in mind that there are many more not pointing towards us at any one time), and the fact that they are associated with cores with all types of infra-red spectral class, suggest that they are present throughout most or even all of a core's evolution.

One explanation of this is that the maser strength is governed entirely by the overall luminosity of the star. Since the stellar luminosity comes out mainly in the IR/FIR the spectral class does not reflect the luminosity, but merely the energy distribution. The maser can continue to operate as long as a significant fraction of the stellar luminosity is reradiated and the shock is still expanding into the ambient cloud. The maser does not care about the presence, or not, of ultra-compact H II regions since these will still be embedded in dust.

An alternative view that the maser emission arises far down in the stellar structure (so that the environment is not greatly changed by the gross evolution that changes the stellar class) is probably not tenable, since water molecules will be dissociated near to the stellar surface.

7.3 Maser excitation

Earlier studies of water maser sources have tended to concentrate on masers associated with massive O stars (Genzel *et al*. 1981; Walker *et al*. 1982). These maser sources are characterized by their complicated multi-component spectra, which show velocities in excess of 100 km s^{-1}, and their high luminosity, with some maser spots being as bright as 0.01 $L_{\odot}$. The presence of massive O stars makes high velocity dissociative shocks common-place and theoretical models have been fairly successful in describing these regions (e.g. Elitzur *et al*. 1989).

More recently, surveys of less complicated maser sources have been undertaken using a variety of approaches (e.g. Tofani *et al*. 1995 examined molecular outflow sources). My approach was to examine less active sites of star formation using the presence of water masers as a signpost to the dominant source. These data show that most masers in these regions are low-velocity (< 25 /kms/ relative to the ambient cloud), with only one or two maser components and are fairly weak ($< 10^{-4}$ $L_{\odot}$). This is different to the properties of those masers found in extremely energetic regions of massive O stars discussed in the previous paragraph. It may well be that high velocity components are present but are simply to weak to be detected – they would be formed in the front or back of an expanding shell where the velocities restrict the gain path and would therefore be much weaker than the low-velocity components.

Given all this, my data do constrain the theories of maser excitation to a certain extent. The relatively large separation of maser and submm core suggests that, at least for an isotropic system, *non-dissociative shocks*, e.g. generated by a low-velocity (< 25 km s^{-1}) stellar wind, *are the most likely sources of maser excitation* (see e.g. Melnick *et al*. 1993 and Smith 1994 for models). High velocity dissociative shocks are still possible for some sources such as those in complicated regions or where multiple unresolved sources in a JCMT beam would reduce the maser/core separation.

It is also likely that focused shocks caused by disks, molecular outflows (e.g. IRAS 23314) or ionized jets (e.g. IRAS 20188 FIR 2) could generate the conditions necessary for maser formation.

7.4 A search for M17 SW-like objects

Whilst this project has been successful in detecting embedded cores, detecting submm emission in 40 of the 44 objects (91 per cent), it has been less successful in detecting M17 SW-like objects. In retrospect this is not altogether surprising. The *IRAS* bias in the maser sample immediately increases the chances of the resulting subsample possessing warm dust detectable in the submm, since sources with mid-infrared dust emission have already been pre-selected. It is also not a surprising result that the masers are more likely to be near the peak of the submm emission since, on energy grounds alone, the masers need to be near to a power source. The sources with slightly offset masers may simply have multiple power sources unresolved by the submm observations – this is especially likely with the more distant sources.

7.5 Future work

There is still much work that needs to be done to confirm and extend the results of this thesis. This section explains some ways in which this can be achieved in the future.

7.5.1 The current sample

Obviously a major difficulty with this analysis has been the lack of near-infrared data. Many sources have no data in this wavelength range and spectral classification has been impossible. High-resolution (1 arcsec) J, H, and K′ images would permit the age of these system to be estimated – the young sources should be deeply embedded and not visible in the NIR, whereas it should be possible to see the maser power source directly for class I and II-D objects. Molecular hydrogen emission has been shown to be useful in probing very young, powerful and heavily obscured outflow phenomena (McCaughrean *et al*. 1994) and observations with the narrow-band H_2 (v=1$\rightarrow$ 0) filter should give direct evidence of shocked regions (see e.g. Geballe 1990; Smith 1991; Davis & Smith 1995). It is unfortunate that all the allocated nights on the TIRGO telescope were lost due to bad weather; a further 14 nights have been allocated and I hope that some useful data will be obtained this time.

Another improvement could be made by completing the observations on the existing sample. Many sources in the sample do not have 450 μm fluxes (and hence don't have a submm spectral index), reliable column density measurements (from $C^{18}O$ or $C^{17}O$ observations) or accurate temperatures (from symmetric top observations). Completing these observations would give a better overview of the types of sources which contain water maser emission.

Individual sources

In terms of individual sources, three are of particular interest and require further study:

- IRAS 20188+3928

  Since the maser associated with FIR 1 was discovered *after* the submm continuum mapping was performed, high-resolution images of the core were not taken. Uncertainty in the position of the outflow centre makes it unclear whether FIR 1 or FIR 2 is the power source; extensive line mapping is required.

  The jet-like ridge of radio emission emerging from FIR 2a requires further study. Multi-frequency observations with the VLA in the compact C and D array should enable spectral index information to be obtained for the whole length rather than just the ends. This will help to determine the emission mechanism and identify optically thick or stellar wind components. Radio-recombination lines would give line-of-sight velocity information for the jet, but long integration times would be required since most of the emission is less than 1 mJy in continuum, while recombination line fluxes are typically only a few percent of this.

Sub-arcsecond resolution images of the radio emission in the vicinity of the weaker of the two water masers, for example with MERLIN, should be able to resolve the end of the radio ridge. Shock structures near the water maser should then become evident. Sub-arcsecond resolution observations of the inner part of the jet should detect newly ejected material and will enable a proper motion study to be carried out.

- IRAS 22198+6336

  This outflow needs to mapped over a larger area in order to determine the full extent. Since the velocity structure was not evident in ^{12}CO it may be worthwhile mapping the source in a less optically-thick line, such as ^{13}CO, in order to improve the signal-to-noise of the detection – the ^{13}CO line should be stronger than the C^{18}O line. Higher-resolution observations (i.e. 345 GHz at the JCMT, or 220 GHz at IRAM) of the outflow centre will also be useful in locating the source accurately (although the continuum source *must* be responsible). The disk hypothesis suggested by the maser observations must also be investigated by using interferometers since the continuum observations are not of a high enough resolution to be able to determine whether the masers in L1204 are associated with the core or with a disk.

- IRAS 23314+6033

  Whilst this source is intriguing, the first step must be to map the C^{18}O outflow with a small beam so that the outflow centre can be determined. With this information it would then be possible to decide which of the two continuum sources was responsible (if any). Of course accurate positions for the two continuum sources are also required – the pointing error on these particular data could be as large as 4 arcsec.

7.5.2 Extending the sample

In order to improve on the statistical significance of the submm/maser association, two steps are necessary:

1. To image those maser sources listed in table 2.3 which were not observed because of time constraints. With SCUBA (the Submm Common-User Bolometer Array) coming on-line at the JCMT in mid-1996, it will soon be possible to image sources simultaneously at 850- and 450-μm with an order of magnitude better sensitivity than that obtainable from UKT14. This will reduce the required observing time dramatically: indeed, it should soon be possible to image *all* the SFR maser sources in only a few shifts

2. Once all this submm continuum data has been taken, the biggest hurdle to improving the statistics is the reduction of the positional errors of the water masers. Since the majority of the masers detected from *IRAS* surveys have used single-dish telescopes the absolute pointing accuracy is

poor ($>$ 20 arcsec). The only way to improve on this is to map all the masers with an instrument such as the VLA. As yet this is a difficult proposal to justify because of the telescope time required (it is possible to map 15 sources in 6 hours with the VLA).

Once high-quality submm continuum data, high-resolution maser data and near-infrared images are available for a large fraction of the maser sources it should then be possible to determine the maser environment to a much greater degree. Knowledge of the position and velocity of each maser relative to the submm core will give information on the shock orientation and position. It will also be necessary to improve the distance constraints on the sample; both the luminosity and the maser-submm separation are dependent on the given distance and errors on this measurement may influence the resulting statistics.

7.5.3 New directions

Since all the sources have been pre-selected to possess maser emission, this type of survey cannot tell us anything about the fraction of embedded cores which go through a maser phase. In order to do this, a survey of a region of the Galactic plane for embedded cores must be complemented by a survey for maser emission. This is not as difficult as it sounds. With SCUBA it should be possible to image a square degree of the sky with a sensitivity of 40 mJy at 850 μm (simultaneously with a map at 450 μm) in only 2 hours. This work has shown that masers are directly associated with an embedded core, therefore, only those cores detected in the SCUBA survey need to be observed for maser emission, preferably with the VLA although an instrument such as the Medicina telescope at Bologna is all that is required to determine whether a source possesses maser emission.

This work has shown that a survey *of a region of sky for maser sources* would *be a good way of finding early-type cores*. A large problem with the present work is the contamination of the maser sample by *IRAS*. A maser survey by a single-dish telescope with modern low-noise receivers should be able to survey a few square degrees of sky in a reasonable time; for example the 32-m Merlin dish, with a 100 arcsec beam, could map a square degree of sky down to a sensitivity of 1 Jy in one night (1300 spectra if the pixels were spaced at one beamwidth[1]) and it would be a simple task to observe a signifcant area (c.f. Matthews *et al*. 1985). Submm mapping of the masers detected in the survey would then raise the possibility of identifying new class 0 cores. Repeating the survey at some later time would also give an idea of the variability of the maser sources and show whether new sources have 'switched on' since the previous survey. Of course, since SCUBA can map large areas of sky much faster than a maser survey the approach of the preceeding chapter would be the most efficient.

[1] A fully-sampled grid would not be necessary if it was only necessary to detect masers. A coarse frequency resolution, e.g. 200 kHz per channel as used for the VLA observations, is more than adequate for this task.

7.6 Closing thoughts

In summary, this survey has shown the potential power of this method for identifying embedded sources but has also shown the complicated nature of these sources. The many different types of maser (e.g. from outflows, stellar winds and molecular shells) makes the excitation conditions unclear but progress can be made. The sample represented by these sources are generally much better behaved and less complicated, which indicates that it should be possible to determine the excitation conditions.

Progress can only be made when the different types can be distinguished. Most of the masers were associated directly with a central source but some were found in outflow systems or jets.

Eventually it should be possible to use water masers as diagnostics of the conditions in a star forming region rather than as a signpost of star formation. The time variation of unsaturated water masers, such as the ones present in much of this sample (or maybe even all of it), is a product of the exponential gain in these systems and reflects small changes in the velocity gradient of the surrounding material. Higher powered, saturated masers would be easier to monitor than an unsaturated maser since the variation will be less pronounced and should simply be proportional to the pumping conditions. The difficulty of assessing the conditions near to star by using unsaturated masers still needs to be addressed.

References

Brand J., *et al*., 1994, *A&AS*, 103, 541
Comoretto G., *et al*., 1990, *A&AS*, 84, 179
Davis C. J., Smith M. D., 1995, *ApJ*, 443, L41
Elitzur M., Hollenbach D. J., McKee C. F., 1989, *ApJ*, 346, 983
Forster J. R., Caswell J. L., 1989, *A&A*, 213, 339
Geballe T. R., 1990, in *Molecular astrophysics: A volume honouring Alexander Dalgarno*, ed. Hartquist T. W., p. 345, Cambridge University Press
Genzel R., *et al*., 1981, *ApJ*, 247, 1039
Matthews H. E., Olnon F. M., Winnberg A., Baud B., 1985, *A&A*, 149, 227
McCaughrean M. J., Rayner J. T., Zinnecker H., 1994, *ApJ*, 436, L189
Melnick G. J., Menten K. M., Phillips T. G., Hunter T., 1993, *ApJ*, 416, L40
Palagi F., Cesaroni R., Comoretto G., Felli M., Natale V., 1993, *A&AS*, 101, 153
Sandell G., 1994, *MNRAS*, 271, 75
Smith M. D., 1991, *MNRAS*, 253, 175
Tofani G., Felli M., Taylor G. B., Hunter T. R., 1995, *A&AS*, 112, 299
Walker R. C., Matsakis D. N., Garcia-Barreto J. A., 1982, *ApJ*, 255, 128
Wouterloot J. G. A., Walmsley C. M., 1986, *A&A*, 168, 237

Appendix A

Useful formulae

This chapter describes some formulae which are used in this work but are not included in the main text so that the flow is not interrupted.

A.1 Luminosity

If a source has a flux density F_ν (flux per unit frequency interval), then the incident power, P, in a given frequency range is

$$P = \int F_\nu \, d\nu, \tag{A.1}$$

whereas if the spectrum is flux against velocity the non-relativistic Doppler equation must be taken into account.

$$\mathrm{v} = \frac{\nu_\circ - \nu}{\nu_\circ} c \tag{A.2}$$

so that

$$d\mathrm{v} = -\frac{c}{\nu_\circ} d\nu \tag{A.3}$$

Combining this with A.1 gives

$$P = \int F_\nu \, d\nu = \frac{c}{\nu_\circ} \int F_\mathrm{v} \, d\mathrm{v} \tag{A.4}$$

where $\nu_\circ$ is the rest frequency of the observation. This is a good approximation provided the bandwidth is small so that the frequency does not vary appreciably across the spectrum.

If it is assumed that the source is radiating isotropically then its luminosity is given by

$$L = 4\pi D^2 P \tag{A.5}$$

where D is the distance to the source. Using convenient astronomical units the luminosity of an isotropically radiating source is then given by

$$L = 3.136 \times 10^{-10} \left(\frac{D}{\mathrm{kpc}}\right)^2 \int \left(\frac{F_\nu}{\mathrm{Jy}}\right) \left(\frac{d\nu}{\mathrm{kHz}}\right) \mathrm{L}_\odot \tag{A.6}$$

or

$$L = 1.046 \times 10^{-9} \left(\frac{D}{\mathrm{kpc}}\right)^2 \left(\frac{\nu_\circ}{\mathrm{GHz}}\right) \int \left(\frac{F_\nu}{\mathrm{Jy}}\right) \left(\frac{d\nu}{\mathrm{km\ s^{-1}}}\right) \mathrm{L}_\odot \tag{A.7}$$

A.2 Fluxes

A long standing problem in astronomy is that astronomers in different wavebands use different units for flux density. A radio astronomer will often use janskys whereas an optical/infra-red astronomer will often use magnitudes. To simplify the construction of spectral energy distributions (see §4.1.1) I decided to convert all flux density units to janskys.

Magnitudes are defined such that, in practice

$$m = -2.5 \log_{10} \left(\frac{S_\nu}{S_\nu(0)}\right) \tag{A.8}$$

where $S_\nu(0)$ is the flux density of a 0^{th} magnitude star and S_ν is the observed flux density (Zombeck 1990). Rearranging this equation gives us

$$S_\nu = S_\nu(0)\ 10^{-m/2.5} \tag{A.9}$$

The values I used for $S_\nu(0)$ are in the following table from Longair (1992)

	λ/μm	$S_\nu(0)$ / Jy
J	1.25	1600
H	1.65	1020
K	2.20	657
L	3.45	290
M	4.70	163
N	10.2	39
Q	20.0	10

From Fig. A.1 these numbers can be approximated by a power law of the form,

$$S_\lambda(0) = 2630\, \lambda^{-1.83}, \tag{A.10}$$

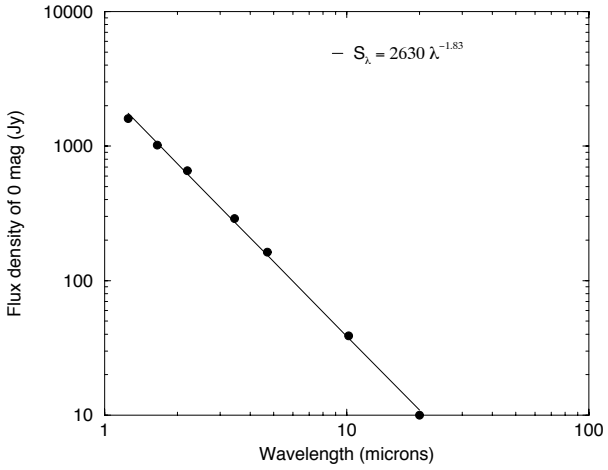

Figure A.1
Flux density variation with wavelength for a mag 0 object

for the near-infrared data. On the rare occasions that magnitudes have been quoted for a wavelength of 27 μm, the value for $S_\nu(0)$, of 6.3 Jy, has been obtained by extrapolating this relation to the longer wavelength.

A.3 Molecular outflows

The dynamical lifetime of an outflow is given by

$$\tau_D \approx \frac{\text{Outflow length}}{\text{Outflow velocity}} \tag{A.11}$$

$$= \frac{R_{\rm max}}{\cos i} \times \frac{\sin i}{\rm v_{max}} \tag{A.12}$$

$$= 4750 \tan i \left(\frac{\theta_{\rm max}}{\rm arcsec}\right)\left(\frac{D}{\rm kpc}\right)\left(\frac{\rm v_{max}}{\rm km\ s^{-1}}\right)^{-1}\ {\rm yr}, \tag{A.13}$$

where $R_{\rm max}$ and $\rm v_{max}$ are the *observed* length and maximum velocity of the outflow respectively. This formula also assumes that the outflow has always been moving at an inclination angle i to the plane of the sky and with the same velocity now that it has always had.

The mechanical luminosity in the outflow is given by

$$L_{mCO} = \frac{\text{Kinetic Energy}}{\text{Lifetime}} \tag{A.14}$$

$$= \frac{\frac{1}{2}M{\rm v}^2}{\tau_D} \tag{A.15}$$

$$= 0.017 \left(\frac{\cos i}{\sin^3 i}\right)\left(\frac{M}{\rm M_\odot}\right)\left(\frac{\rm v_{max}}{\rm km\ s^{-1}}\right)^3\left(\frac{\theta_{max}}{\rm arcsec}\right)^{-1}\left(\frac{D}{\rm kpc}\right)^{-1} {\rm L_\odot}, \tag{A.16}$$

where equation (A.13) has been substituted explicitly. Note that this function is extremely sensitive to the inclination angle.

A.4 Thermal Bremsstrahlung

If an extremely hot, massive and luminous O or B star should form at the centre of one of these deeply embedded objects some fraction of the photons it emits will have energy >13.6 eV, enough to ionise the surrounding hydrogen out to a maximum radius known as a Strömgren sphere – the radius at which the recombination rate balances the ionization rate. As with the case for dust emission dealt with in §3.2.2, the observed flux from an H II region can be written as

$$S_\nu = B_\nu(\nu,T)(1-e^{-\tau_\nu}) \tag{A.17}$$

$$= \frac{2kT}{c^2}\nu^2(1-e^{-\tau_\nu}), \tag{A.18}$$

where the Rayleigh-Jeans approximation has been used.

In the case of free-free emission the optical depth, at a frequency ν, of an H II region of temperature T_e and electron density n_e, is given by

$$\tau_\nu = 8.24\times10^{-2}\left(\frac{T_e}{\mathrm{K}}\right)^{-1.35}\left(\frac{\nu}{\mathrm{GHz}}\right)^{-2.1}\left(\frac{\mathrm{EM}}{\mathrm{pc\ cm^{-6}}}\right), \tag{A.19}$$

where EM is the emission measure, defined as $\int n_e^2 dl$.

In the optically thick limit, the H II region tends to a blackbody and therefore $S_\nu \propto \nu^2$. In the optically thin limit S_ν tends to $B_\nu\tau_\nu$ and hence the flux is only weakly dependent on frequency: $S_\nu \propto \nu^{-0.1}$. If this frequency dependence is ignored, the flux from an H II region can be written simply as

$$\left(\frac{S}{\mathrm{Jy}}\right) = 74\left(\frac{n_e}{\mathrm{cm^{-3}}}\right)^2\left(\frac{V}{\mathrm{pc^3}}\right)\left(\frac{D}{\mathrm{pc}}\right)^{-2}, \tag{A.20}$$

where V is the volume, D is the distance to the source and the electron temperature is 10^4 K.

If a source has a flat-radio spectrum then the H II region must become optically thick at a lower frequency than those observed. This turnover point is taken to be the frequency, $\nu_\circ$, where τ=1, and an upper limit to this frequency is given by the lowest frequency for which data exists. For sources unresolved by the observations it is possible to obtain a lower limit to the source size by combining equations (A.19) and (A.20):

$$\left(\frac{r}{\mathrm{pc}}\right) \geq 4.6\times10^{-2}\left(\frac{S_{\nu_\circ}}{\mathrm{Jy}}\right)^{\frac{1}{2}}\left(\frac{D}{\mathrm{kpc}}\right)\left(\frac{\nu_\circ}{\mathrm{GHz}}\right)^{-1.05}, \tag{A.21}$$

where the H II region is assumed to be spherical and the equality holds if the turnover frequency is known.

It is also possible to calculate the number of Lyman photons required to ionize the H II region,

$$N_{\mathrm{Ly}} = 4.76\times10^{48}\left(\frac{\nu}{\mathrm{GHz}}\right)^{0.1}\left(\frac{T_\mathrm{e}}{\mathrm{K}}\right)^{-0.45}\left(\frac{S_\nu}{\mathrm{Jy}}\right)\left(\frac{D}{\mathrm{kpc}}\right)^2, \tag{A.22}$$

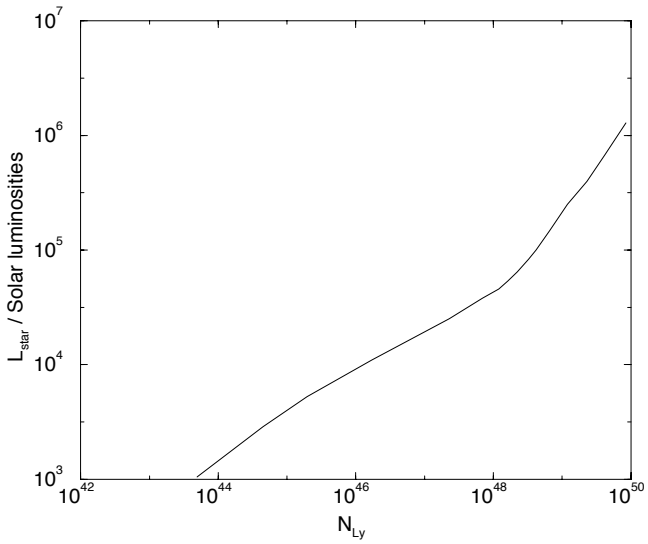

Figure A.2
Calibration of stellar luminosity from Lyman photon number (from data in Panagia 1973).

which assumes that the radio emission is optically thin and is ionization bounded. This number of Lyman photons can then be related to the spectral type and hence to the total stellar luminosity using the calibration of Fig. A.2 from data in Panagia (1973).

For further information and a formal derivation of free-free emission the reader is referred to any of the text books available (e.g. Rybicki & Lightman 1979; Gordon 1988; Longair 1992).

References

Gordon M. A., 1988, in *Galactic and extragalactic radio astronomy*, eds Verschuur G. L., Kellermann K. I., Astronomy & Astrophysics Library, p. 40, Springer-Verlag, 2nd edn.

Longair M. S., 1992, *High Energy Astrophysics*, vol. 1, chap. 8, p. 243, Cambridge University Press, 2nd edn.

Panagia, 1973, *AJ*, 78, 929

Rybicki G. B., Lightman A. P., 1979, *Radiative processes in astrophysics*, Wiley-interscience, New York

Zombeck M. V., 1990, *Handbook of space astronomy and astrophysics*, chap. 2, p. 100, Cambridge University Press, http://adswww.harvard.edu/books/hsaa/, 2nd edn.

Appendix B

Source database

This appendix lists all the observations published in the literature that were found during the course of this thesis. As well as traditional methods of searching the literature (e.g. the *Catalog of Infrared Observations*, Gezari *et al*. 1993) computer-aided literature search systems such as Simbad[1] (Egret *et al*. 1991) and NASA's Astrophysics Data System[2] (Murray *et al*. 1992; Eichhorn *et al*. 1995a, 1995b) have been used. Of course this does not mean that *all* the published data on these sources is included in the following list.

The column marked 'SED' has been used to indicate whether a particular observation has been used for the SED fitting described in §4.1. For cases in which multiple sources have been found which are separated by less than the JCMT beam the source closest to the core has been used.

Where positional accuracy information has not been available from a paper, the beam size has been given instead and is indicated by a superscript *b*.

Where possible, temperatures use the T_R scale (Kutner & Ulich 1981). For my JCMT observations η is taken to be 0.75 and for Wilking *et al*. (1989) $\eta = 0.83$. All other entries have used the temperature scale used in the original paper. For a revised and corrected form of the first Arcetri Atlas (Comoretto *et al*. 1990) please see Palagi *et al*. 1993.

[1]The Simbad astronomical database is operated by the Centre de Données Astronomiques de Strasbourg (CDS) under an agreement between French Institut National des Sciences de l'Univers (INSU) and Université Louis Pasteur, Strasbourg (ULP).

[2]The Astrophysics Data System is funded by the NASA Astrophysics program under grant NCCW-0024

Name	R.A.	Dec	±	ν/λ	flux	±	SED	Ref
IRAS 00338+6312 / L1287								
00338+6312	00 33 52.8	63 12 22	2″	850 μm	17 Jy	20%	Y	Me
00338+6312	53.3	32	4′ [b]	6 cm	0.22 mJy		Y	[1]
00338+6312			3′ [b]	6 cm	<0.3 mJy		N	[2]
VLA 1	52.47	27.4		3.6 cm	0.16 mJy		N	[3]
VLA 2	52.89	20.4		3.6 cm	0.13 mJy		N	[3]
VLA 3	53.15	32.2		3.6 cm	0.49 mJy		Y	[3]
VLA 4	53.18	23.6		3.6 cm	0.19 mJy		N	[3]
00338+6312	53.3	32	14,8,40	100 μm	683 Jy	8%	Y	IRAS
				60 μm	357 Jy	6%	Y	IRAS
				25 μm	21 Jy	4%	Y	IRAS
				12 μm	1.8 Jy	11%	Y	IRAS
GY2	53.3	32.0	27′ [b]	L	6.35 M		Y	[4]
RNO 1B			1	K	7.59 M		N	[5]
RNO 1C			1	K	7.68 M		N	[5]
GY2	53.3	32.0	27′ [b]	K	7.09 M		Y	[4]
RNO 1B			1	H	8.63 M		N	[5]
RNO 1C			1	H	9.15 M		N	[5]
GY2	53.3	32.0	27′ [b]	H	7.88 M		Y	[4]
RNO 1B			1	J	10.22 M		N	[5]
RNO 1C			1	J	11.21 M		N	[5]
GY2	53.3	32.0	27′ [b]	J	9.64 M		Y	[4]
00338+6312	53.3	32	40′ [b]	^{12}CO 1-0	16 K	−18.0		[1]
00338+6312			4.′4 [b]	^{13}CO 1-0	3.8 K	−18		[6]
	53.3	32	40′ [b]	^{13}CO 1-0	9 K			[1]
	53.3	32	40′ [b]	C^{18}O 1-0	1.5 K			[1]
00338+6312	53.3	32.0	20′ [b]	CS 7-6	1.7 K	−17.6		[7]
00338+6312			2″ [b]	CH_3OH	<0.29 Jy			[8]
00338+6312				CH_3OH 6.6-GHz				[2]
00338+6312			7.′8 [b]	OH	0.8 Jy	−22.6		[9]
WB349	52.7	42.0	5	H_2O	0.6 Jy	−28.0		[9]
L1287				H_2O	<13.4 Jy			[10]
L1287				H_2O	<4.0 Jy			[11]
00338+6312			5	H_2O	0.9 Jy	−10.51		[12]
IRAS 00420+5530								
00420+5530	00 42 05.7	55 30 31	2	850 μm	5.7 Jy	20%	Y	Me
00420+5530			4′ [b]	6 cm	< 0,3 mJy		Y	[1]
00420+5530				8 GHz	< 0,3 mJy		Y	Me
00420+5530	05.4	54	19,10,40	100 μm	468 Jy	9%	Y	IRAS
				60 μm	217 Jy	5%	Y	IRAS
				25 μm	15 Jy	8%	Y	IRAS
				12 μm	7.4 Jy	7%	Y	IRAS
Com Neb #2A	05.0	31 00		L	9.19 M		Y	[13]
Com Neb #2A	05.0	00		K	10.00 M		Y	[13]
Com Neb #2A	05.0	00		H	10.49 M		Y	[13]
Com Neb #2A	05.0	00		J	11.51 M		Y	[13]
Com Neb #2A	05.0	00		1.25 μm	spectrum		N	[14]
00420+5530	05.7	30 31	2	^{12}CO 2-1	23 K	−52.0		Me
00420+5530	05.4	54	40′ [b]	^{12}CO 1-0	13 K	−52.0		[1]
00420+5530	05.7	31	2	C^{18}O 2-1	5.7 K	−51.8		Me
00420+5530	05.4	54	40′ [b]	C^{18}O 1-0	0.5 K			[1]
00420+5530	05.4	54	40′ [b]	^{13}CO 1-0	7 K			[1]
00420+5530	05.3	54	20	H_2O	27.2 Jy	−45.75		[15]
00420+5530	05.3	54	20	H_2O	66.0 Jy	−44.74		[16]
00420+5530	06.15	23.8	0.1	H_2O	0.45 Jy	−45		Me
IRAS 03035+5819 / GL 437 / HHL5								
03035+5819	03 03 33.5	58 19 09	2	850 μm	11 Jy	20%	Y	Me

continued on next page

continued from previous page

Name	R.A.	Dec	±	ν/λ	flux	±	SED	Ref
GL 437 N				2.7 GHz	20 mJy	4	Y	[17]
GL 437	31.28	18.9		8 GHz	18 mJy		Y	[18]
GL 437	32.04	11.9		8 GHz	1 mJy		N	[18]
GL 437 W				2 cm	17 mJy		Y	[17]
GL 437 S				2 cm	1 mJy		N	[17]
GL 437 N+W				23 GHz	14 mJy	3	Y	[19]
03035+5819	33.2	21	16,9,68	100 μm	1297 Jy	7%	Y	IRAS
FIRSSE37	37	06	10″	93 μm	1609 Jy		Y	[20]
03035+5819	33.2	21	16,9,68	60 μm	1055 Jy	5%	Y	IRAS
FIRSSE37	37	06	10″	40 μm	388 Jy		Y	[20]
FIRSSE37	37	06	10″	27 μm	612 Jy		Y	[20]
RAFGL 437	31.3	19	10″	27 μm	-4.8 M		N	[21]
03035+5819	33.2	21	16,9,68	25 μm	396 Jy	4%	Y	IRAS
FIRSSE37	37	06	10″	20 μm	299 Jy		Y	[20]
RAFGL 437	31.3	19	10″	20 μm	-3.3 M		N	[21]
RAFGL 437	31.3	19	8.5[b]	18 μm	-2.2 M		N	[22]
03035+5819	33.2	21	16,9,68	12 μm	31 Jy	5%	Y	IRAS
RAFGL 437	31.3	19	10″	11 μm	-0.3 M		N	[21]
RAFGL 437	31.3	19	8.5[b]	10.6 μm	3.0 M		N	[22]
RAFGL 437	31.3	19	12[b]	10.6 μm	6 Jy		Y	[23]
RAFGL 437	31.7	07		10 μm	7.5 Jy		Y	[24]
RAFGL 437	31.3	19	9[b]	7.7 μm	3.7 fW m^{-2}		N	[25]
RAFGL 437	31.3	19	9[b]	6.9 μm	0.07 fW m^{-2}		N	[25]
RAFGL 437	31.3	19	9[b]	6.2 μm	1.9 fW m^{-2}		N	[25]
RAFGL 437	31.3	19	9[b]	5.6 μm	0.13 fW m^{-2}		N	[25]
AFGL 437N	32.0	23	7.8[b]	4.05 μm	<0.5 fW m^{-2}		N	[26]
RAFGL 437	31.3	19	17[b]	3.58 μm	6.0 M		Y	[22]
03035+5819	33.2	21	5[b]	3.51 μm	7 fW m^{-2} μm^{-1}		N	[27]
RAFGL 437	31.8	15		3.5 μm	0.8 fW m^{-2}		N	[28]
03035+5819	33.2	21	5[b]	3.46 μm	12 fW m^{-2} μm^{-1}		N	[27]
03035+5819	33.2	21	5[b]	3.4 μm	18 fW m^{-2} μm^{-1}		N	[27]
03035+5819	33.2	21	5[b]	3.3 μm	6.7 fW m^{-2}		N	[27]
RAFGL 437	31.8	15		3.3 μm	24 fW m^{-2}		N	[28]
RAFGL 437	31.8	15		3.1 μm	spectrum		N	[29]
RAFGL 437	31.3	19	17[b]	2.28 μm	8.0 M		Y	[22]
AFGL 437N	32.0	23	7.8[b]	2.17 μm	0.11 fW m^{-2}		N	[26]
RAFGL 437	31.3	19	17[b]	1.65 μm	9.4 M		Y	[22]
RAFGL 437	31.3	19	17[b]	1.25 μm	10.6 M		Y	[22]
AFGL 437S	32.2	13		1.00 μm	0.012 fW m^{-2}		N	[30]
03035+5819	33.5	09	2	^{12}CO 2-1	75 K	−40.0		Me
WB 466				CO		−39.7		[9]
				CO		−40.0		[31]
03035+5819	33.2	20	10	NH$_3$ 1,1	0.64 K	−40.0		[32]
03035+5819	33.2	20	10	NH$_3$ 2,2	0.37 K	−40.0		[32]
AFGL 437			2″	CH_3OH	<0.29 Jy			[8]
	34.2	13	90[b]	H_2O	2,3,3 Jy	−28,-39,-49		[33]
GL 437	33.2	21	20	H_2O	12.7 Jy	−28.1		[10]
WB 466			7	H_2O	1.1 Jy	−50.4		[9]
03035+5819	33.2	20	10	H_2O	156.7 Jy	−31.5		[32]
GL 437 W	31.3	19.5	0.1	H_2O	2.2 Jy	−37.7		[18]
GL437 N	32.2	21.6	0.1	H_2O	6.7 Jy	−25.2		[18]
03035+5819			5	H_2O	4.1 Jy	−24.9		[12]

IRAS 03262+3108 / HH 6

03262+3108	03 26 05.6	31 08 16	2	850 μm	5.6 Jy	20%	Y	Me
	05.63	13.3	0.1	5 GHz	0.9 mJy		Y	[34]
03262+3108	14.7	16	61,10,73	100 μm	<947 Jy		N	IRAS
NGC1333 IRAS7	06.9	28		100 μm	107 Jy		Y	[35]
03262+3108	14.7	16	61,10,73	60 μm	<0.4 Jy		N	IRAS
NGC1333 IRAS7	06.9	28		50 μm	55 Jy		Y	[35]

continued on next page

continued from previous page

Name	R.A.	Dec	±	ν/λ	flux	±	SED	Ref
03262+3108	14.7	16	61,10,73	25 μm	1.0 Jy	35%	Y	IRAS
03262+3108	14.7	16	61,10,73	12 μm	0.49 Jy	38%	Y	IRAS
H-H 6	06.6	20		2.12 μm	0.22 fW m^{-2}		N	[36]
03262+3108	05.6	16	2	C^{18}O 2-1	5.1 K	8.3		Me
HH 6	05.6	13	2^{tb}	CH_3OH	0.2 K	8.3		[37]
HH 6	05.6	12.8	0.1	H_2O	20 Jy	8		[38]
HH 6				H_2O	<9.7 Jy			[10]
IRAS 05274+3345 / GL 5142								
05274+3345	05 27 29.7	33 45 38	2	850 μm	21 Jy	20%	Y	Me
05274+3345				6 cm	<0.3 mJy		Y	[1]
AFGL 5142	29.99	40.0		8 GHz	1 mJy		N	[18]
AFGL5142	29.99	40.1	0.1	8.4 GHz	0.83 mJy	0.12	Y	[39]
05274+3345	27.6	37	22,9,100	100 μm	905 Jy	10%	Y	IRAS
RAFGL 5142	26	54	10^{tb}	93 μm	390 Jy		Y	[20]
05274+3345	27.6	37	22,9,100	60 μm	449 Jy	8%	Y	IRAS
RAFGL 5142	25.7	55	10^{tb}	27 μm	-3.3 M		Y	[21]
RAFGL 5142	26	54	10^{tb}	27 μm	127 Jy		Y	[20]
05274+3345	27.6	37	22,9,100	25 μm	69.4 Jy	4%	Y	IRAS
RAFGL 5142	25.7	55	10^{tb}	20 μm	-1.4 M		Y	[21]
RAFGL 5142	26	54	10^{tb}	20 μm	39 Jy		Y	[20]
05274+3345	27.6	37	22,9,100	12 μm	6.89 Jy	5%	Y	IRAS
GL5142 IRS1	29.92	40.2	2.5	K	13.2 M		Y	[40]
GL5142 IRS1	29.92	40.2	2.5	H	15.1 M	0.14	Y	[40]
GL5142 IRS1	29.92	40.2	2.5	J	17.5 M	0.3	Y	[40]
WB 652				CO		−3.9		[9]
AFGL 5142	27.6	37	45^{b}	^{12}CO 1-0	12.6 K	-4.1		[41]
AFGL 5142	27.6	37	40^{b}	^{12}CO 1-0	18 K	-4.0		[1]
AFGL 5142	27.6	37	40^{b}	^{13}CO 1-0	4.0 K			[1]
AFGL 5142	27.6	37	40^{b}	C^{18}O 1-0	1.3 K			[1]
AFGL 5142	27.6	37	15	NH_3 1,1	0.26 K	-3.43		[42]
AFGL 5142	27.6	37	15	NH_3 2,2	<0.09 K			[42]
174.20-0.08	32.4	52		CH_3OH 6.6-GHz	84.9 Jy	0,5		[43]
AFGL 5142	30.8	12	40	H_2O	43 Jy	0.4		[42]
	27.6	37	25	H_2O	51.5 Jy	-5.18		[15]
05274+3345	30.8	12	25	H_2O	105.7 Jy	4.30		[16]
05274+3345	30.8	12	25	H_2O	47.8 Jy	3.15		[16]
05274+3345	30.8	12	25	H_2O	81.1 Jy	-5.11		[16]
05274+3345	30.8	12	25	H_2O	87.4 Jy	-5.04		[16]
WB 652				H_2O	22.7 Jy	-4.9		[9]
WB 652				H_2O	81.3 Jy	-5.1		[9]
WB 652				H_2O	89.2 Jy	-5.0		[9]
AFGL 5142	27.6	37		H_2O	284 Jy	23.3		[11]
AFGL 5142			60^{b}	H_2O	9.4 Jy	−7.4		[39]
AFGL 5142			60^{b}	H_2O	50.3 Jy	−5.3		[39]
AFGL 5142			60^{b}	H_2O	49.8 Jy	−3.2		[39]
AFGL 5142			60^{b}	H_2O	6.6 Jy	−1.4		[39]
AFGL 5142-C1	29.94	38.49	0.1	H_2O	0.62 Jy	-8.3		[40, 39]
AFGL 5142-C2	29.99	38.87	0.1	H_2O	18.8 Jy	-5		[40, 39]
AFGL 5142-C3	29.99	40.20	0.1	H_2O	10.3 Jy	-1.7		[40, 39]
AFGL 5142-C4	30.00	39.93	0.1	H_2O	23.1 Jy	-9.6		[40, 39]
AFGL 5142-C5	30.17	40.16	0.1	H_2O	7.63 Jy	-5.7		[40, 39]
AFGL 5142	29.99	38.9	0.1	H_2O	62.1 Jy	-4.8		[18]
AFGL 5142	29.99	40.1	0.1	H_2O	56.5 Jy	4.4		[18]
AFGL 5142	30.10	40.1	0.1	H_2O	30.0 Jy	-5.5		[18]
IRAS 05302−0537 / Orion A-west								
05302–0537	05 30 14.8	−05 37 56	2	850 μm	3.3 Jy	20%	Y	Me
OriA-west	14.41	51.0	0.1	8.4 GHz	0.86 mJy	0.15	Y	[39]
05302–0537	14.5	52	26,9,87	100 μm	82.4 Jy	27 %	Y	IRAS
05302–0537	14.5	52	26,9,87	60 μm	55.3 Jy	14 %	Y	IRAS

continued on next page

continued from previous page

Name	R.A.	Dec	±	ν/λ	flux	±	SED	Ref
05302–0537	14.5	52	26,9,87	25 μm	19.4 Jy	7 %	Y	IRAS
05302–0537	14.5	52	26,9,87	12 μm	4.3 Jy	5 %	Y	IRAS
05302–0537	14.5	52	2.′7[b]	CO outflow				[44]
05302–0537	14.5	52	20	H_2O	18.9 Jy	7.5		[11]
05302–0537	14.5	52	20	H_2O	20.6 Jy	7.4		[16]
05302–0537	14.5	52	20	H_2O	<6 Jy			[16]
OriA-west-C1	14.41	50.9	0.01	H_2O	2.09 Jy	8		[39]
OriA-west			60[b]	H_2O	17.5 Jy	0.0		[39]
OriA-west			60[b]	H_2O	4.6 Jy	7.4		[39]
IRAS 05373+2349 / HH 4								
05373+2349	05 37 21.4	23 49 18	2	850 μm	2.1 Jy	20%	Y	Me
05373+2349	21.3	22		2 cm	<0.69 mJy		Y	[45]
GGD 4	21.8	24		4.9 GHz	<4.8 mJy		N	[46]
GGD 4			0.2[b]	8.4 GHz	<0.1 mJy		N	[39]
05373+2349	21.3	22		6 cm	<0.28 mJy		Y	[45]
05373+2349	21.3	22		2.7 mm	<82 mJy		Y	[45]
05373+2349	21.3	22	30,6,88	100 μm	192 Jy	16%	Y	IRAS
05373+2349	21.3	22	30,6,88	60 μm	125 Jy	12%	Y	IRAS
05373+2349	21.3	22	30,6,88	25 μm	26.5 Jy	5%	Y	IRAS
05373+2349	21.3	22	30,6,88	12 μm	9.0 Jy	7%	Y	IRAS
05373+2349	21.0	39.0	8[b]	10 μm	2.35 M		N	[47]
GGD 4 IRS	21.7	23.0	11[b]	4.8 μm	4.14 M		Y	[48]
05373+2349	21.0	39.0	8[b]	4.8 μm	4.63 M		N	[47]
GGD 4 IRS	21.7	23.0	11[b]	3.5 μm	5.33 M		Y	[48]
05373+2349	21.0	39.0	8[b]	3.5 μm	6.33 M		N	[47]
GGD 4 ANON	21.3	20.0	34[b]	K	7.8 M		N	[49]
GGD 4 IRS	21.7	23.0	11[b]	K	7.56 M		Y	[48]
05373+2349	21.0	39.0	4.6[b]	K	8.77 M		N	[47]
GGD 4	21.8	24.0		2.12 μm	<0.7 fW m^{-2}		N	[49]
GGD 4 ANON	21.3	20.0	34[b]	H	9.8 M		N	[49]
GGD 4 IRS	21.7	23.0	11[b]	H	9.88 M		Y	[48]
05373+2349	21.0	39.0	8[b]	H	11.42 M		N	[47]
GGD 4 ANON	21.3	20.0	34[b]	J	12.6 M		N	[49]
GGD 4 IRS	21.7	23.0	11[b]	J	11.46 M		Y	[48]
05373+2349	21.0	39.0	8[b]	J	14.43 M		N	[47]
GGD 4				CO outflow				[6]
05373+2349	21.3	22	1.′2[b]	^{12}CO 2-1	7.5 K	3		[45]
05373+2349			4.′4[b]	^{12}CO 1-0	6.2 K			[6]
05373+2349				^{12}CO 2-1	4.0 K			[6]
05373+2349			4.′4[b]	^{13}CO 1-0	2.7 K	3		[6]
05373+2349	21.3	22	1.′2[b]	^{13}CO 2-1	3.3 K	3		[45]
WB 685				^{12}CO		2.7		[9]
GGD 4	21.8	24	44[b]	^{12}CO 1-0	7 K	3		[46]
GGD 4	21.8	24	1.′4	NH_3 1,1	0.08 K	3		[46]
GGD 4	21.3	22	2.″[b]	CH_3OH	0.10 K	2.5		[37]
GGD 4	21.8	24	44[b]	SiO maser	<170 Jy			[46]
GGD 4	21	24	2′	1612 MHz	<0.07 K	OH		[46]
GGD 4	21	24	2′	1665 MHz	0.12 K	OH	2	[46]
GGD 4	21	24	2′	1667 MHz	0.20 K	OH	2	[46]
GGD 4	21	24	2′	1720 MHz	<0.08 K	OH		[46]
GGD 4	21.8	24	20	H_2O	variable	-10 to +5		[46]
05363+2349				H_2O	<10.8 Jy			[10]
	21.3	22	20	H_2O	35.2 Jy	4.7		[15]
WB 685	21.3	22.0	5	H_2O	19.3 Jy	3.6		[9]
WB 685	21.3	22.0	5	H_2O	13.9 Jy	-4.5		[9]
GGD 4			60[b]	H_2O	19.0 Jy	5.2		[39]
GGD 4			60[b]	H_2O	29.2 Jy	4.5		[39]
GGD 4-C1	21.04	22.8	0.01	H_2O	0.41 Jy	-2.4		[39]
GGD 4-C2	21.10	22.5	0.01	H_2O	18.65 Jy	2.8		[39]

continued on next page

continued from previous page

Name	R.A.	Dec	±	ν/λ	flux	±	SED	Ref
IRAS 05375–0731 / L1641								
05375–0731	05 37 31.0	−07 32 04	2	850 μm	6.5 Jy	20%	Y	Me
05375–0731	31.1	31 59		6 cm	<1.2 mJy		N	[45]
05375–0731				6 cm	<0.3 mJy		Y	[2]
05375–0731	31.1	31 59		2 cm	<0.69 mJy		Y	[45]
05375–0731	31.1	31 59		2.7 mm	112 mJy	31	Y	[45]
05375–0731	31.1	31 59		1.3 mm	944 mJy	54	Y	[50]
L1641 #59	28.5	31 43		100 μm	298 Jy		N	[51]
05375–0731	31.1	31 59	27,10,89	100 μm	269 Jy	23%	Y	IRAS
L1641 #59	28.5	31 43		60 μm	159 Jy		N	[51]
05375–0731	31.1	31 59	27,10,89	60 μm	157 Jy	15%	Y	IRAS
L1641 #59	28.5	31 43		25 μm	10.8 Jy		N	[51]
05375–0731	31.1	31 59	27,10,89	25 μm	8.9 Jy	9%	Y	IRAS
L1641 #59	28.5	31 43		12 μm	0.18 Jy		N	[51]
05375–0731	31.1	31 59	27,10,89	12 μm	<0.25 Jy		Y	IRAS
L1641 #59	28.5	31 43		K	>13.8 M		N	[51]
L1641 KMS 59	31.0	32 02	3.9[b]	K	15.5 M		Y	[52]
L1641-south3	31.1	31 59		bipolar CO outflow				[53]
05375–0731			21	^{12}CO 1-0	14.8 K	5.1		[54]
05375–0731	31.1	31 59	1.′2[b]	^{12}CO 2-1	10.8 K	5.1		[45]
L1641.S3#108	27	31 37		^{13}CO				[55]
05375–0731			21	^{13}CO 1-0	6.6 K	4.6		[54]
05375–0731	31.1	31 59	1.′2[b]	^{13}CO 2-1	3.5 K	5.1		[45]
05375–0731				NH_3		5.4		[56]
05375–0731	31.1	31 59	2″[b]	CH_3OH	<0.16 K			[37]
05375–0731				H_2O	<11.6 Jy			[10]
L1641-south3				H_2O	<5.6 Jy			[11]
05375–0731	30.9	31 51	5	H_2O	2.7 Jy	6		[57]
05375–0731				H_2O				[58]
IRAS 05413–0104 / L1630								
05413–0104	05 41 18.9	−01 04 11	2	850 μm	2.3 Jy	20%	Y	Me
05413–0104				23.7 GHz	<0.04 Jy		Y	[56]
05413–0104	19.0	08	33,10,91	100 μm	58.5 Jy	14%	Y	IRAS
05413–0104	19.0	08	33,10,91	60 μm	17.1 Jy	10%	Y	IRAS
05413–0104	19.0	08	33,10,91	25 μm	0.38 Jy	15%	Y	IRAS
05413–0104	19.0	08	33,10,91	12 μm	<0.25 Jy		Y	IRAS
05413–0104			21	^{12}CO 1-0	14.9 K	8.7		[54]
05413–0104			21	^{13}CO 1-0	6.3 K	1.62		[54]
05413–0104			21	C^{18}O	1.1 K	1.59		[54]
05413–0104				NH_3		1.72		[56]
05413–0104				3264 MHz	<0.12 K	CH		[54]
05413–0104				3335 MHz	0.30 K	CH	2.7	[54]
05413–0104				3335 MHz	0.26 K	CH	6.6	[54]
05413–0104				3335 MHz	0.29 K	CH	9.1	[54]
05413–0104				3349 MHz	<0.14 K	CH		[54]
05413–0104				HC_5N 9-8	<0.03 K			[54]
05413–0104				H_2CO	-0.17 K	1.66		[54]
05413–0104				H_2CO	-0.11 K	5.00		[54]
05413–0104				H_2CO	-0.11 K	8.28		[54]
05413–0104				1612 MHz	<0.04 K	OH		[54]
05413–0104				1665 MHz	0.09 K	OH	8.4	[54]
05413–0104				1667 MHz	0.18 K	OH	9.0	[54]
05413–0104				1720 MHz	<0.04 K	OH		[54]
05413–0104	18.6	17	5	H_2O	162 Jy	3		[57]
05413–0104				H_2O	87.9 Jy	2.6		[54]
05413–0104				H_2O	74.0 Jy	1.8		[54]
05413–0104				H_2O	41.4 Jy	0.7		[54]
05413–0104				H_2O	76.3 Jy	2.9		[54]
05413–0104				H_2O	56.2 Jy	2.6		[54]

continued on next page

continued from previous page

Name	R.A.	Dec	±	ν/λ	flux	±	SED	Ref
G20601–1548	18.6	17	25	H_2O	48.5 Jy	2.4		[10]
05413–0104				H_2O				[58]
IRAS 06053–0622 / Mon R2 IRS3								
06053–0622	06 05 19.9	−06 22 44	2	850 μm	21 Jy	20%	Y	Me
Mon R2	20.1	40	5	2.695 GHz	5300 mJy	200	Y	[59]
Mon R2	20.2	46	5	2.695 GHz	1220 mJy	100	N	[59]
Mon R2				5 GHz	7.5 Jy		N	[60]
Mon R2 IRS3	21.8	26		5 GHz	<1 mJy		N	[60]
06053–0622	20.4	31		6 cm	6.0 Jy		Y	[45]
Mon R2	20.1	40	5	8 GHz	5600 mJy	400	Y	[59]
Mon R2	20.2	46	5	8 GHz	1850 mJy	300	N	[59]
Mon R2			0.3″	8.4 GHz	<3 mJy		N	[39]
06053–0622	20.4	31		2 cm	6.1 Jy		Y	[45]
213.7–12.6	20.2	53	5	14.8 GHz	6.1 Jy	5%	Y	[59]
213.7–12.6	20.2	53	5	86 GHz	4.27 Jy	15%	Y	[59]
06053–0622	20.4	31		2.7 mm	2320 mJy	30	Y	[45]
Mon R2	23	24	3.″9	1 mm	58 Jy		N	[61]
Mon R2	19	17	80″	390 μm	660 Jy		Y	[62]
Mon R2	19	17	50″	140 μm	7200 Jy		Y	[62]
06053–0622	20.4	31	23,6,95	100 μm	20200 Jy	10%	Y	IRAS
FIRSSE 126	18	36	10″	93 μm	18825 Jy		Y	[20]
06053–0622	20.4	31	23,6,95	60 μm	13070 Jy	999%	Y	IRAS
FIRSSE 126	18	36	10″	40 μm	12976 Jy		Y	[20]
FIRSSE 126	18	36	10″	27 μm	5866 Jy		Y	[20]
RAFGL 877	18.6	57	10″	27 μm	-7.8 M		Y	[21]
06053–0622	20.4	31	23,6,95	25 μm	4095 Jy	4%	Y	IRAS
FIRSSE 126	18	36	10″	20 μm	2275 Jy		Y	[20]
RAFGL 877	18.6	57	10″	20 μm	-6.0 M		N	[21]
Mon R2 IRS3				20 μm	500 Jy	50%	N	[63]
06053–0622	20.4	31	23,6,95	12 μm	470 Jy	3%	Y	IRAS
RAFGL 877	18.6	57	10″	11 μm	-2.7 M		N	[21]
Mon R2 IRS3				10 μm	100 Jy	50%	Y	[63]
RAFGL 877	18.6	57	10″	4.2 μm	0.5 M		N	[21]
Mon R2 IRS3	21.5	26	32″	3.5 μm	8 Jy		Y	[64]
Mon R2 IRS3	21.6	25	6″	2.2 μm	1.64 Jy		Y	[65]
Mon R2 IRS3				2.2 μm	2 Jy	50%	N	[63]
Mon R2 IRS3				1.65 μm	0.25 Jy	50%	Y	[63]
06053–0622	20.4	31	1.″2	^{12}CO 2-1	33.7 K	10		[45]
06053–0622	20.4	31	1.″2	^{12}CO 2-1	10.8 K	10		[45]
Mon R2	17.0	40.0	20″	CS 7-6	3.1 K	10.9		[7]
MonR2 IRS3	21.7	35.0	20″	CS 7-6	2.3 K	10.4		[7]
Mon R2	17.0	40	2″	CH_3OH	<0.35 K			[66, 37]
Mon R2	20.0	40		CH_3OH 6.6 GHz	160 Jy	9,14		[67]
Mon R2				CH_3OH 6.6 GHz	330 Jy	9,14		[68]
Mon R2				CH_3OH 12.2 GHz	4.8 Jy	6,13		[68]
213.7–12.6	20.2	53	5	H76α	0.88 K	12.0		[59]
213.7–12.6	20.2	53	5	He76α	<0.02 K			[59]
213.7–12.6	20.2	53	5	C76α	0.10 K	10.1		[59]
Mon R2 IRS3	21.8	26		Bα	<4.5 fW m^{-2}			[69, 60]
Mon R2 IRS3	21.8	26		Bα	<0.2 fW m^{-2}			[70, 60]
Mon R2(1)	17.0	40	5	H_2O	12 Jy	11.2		[71]
Mon R2(2)	21.7	35	5	H_2O	8 Jy	11.8		[71]
MONR2	16.9	47.9	25	H_2O	47.3 Jy	11.8		[10]
MONR2 IRS3	21.7	35.0	25	H_2O	214.8 Jy	18.1		[10]
Mon R2			60″	H_2O	754 Jy	11.7		[39]
Mon R2			60″	H_2O	605 Jy	11.7		[39]
Mon R2-C1	21.58	27.79	0.1	H_2O	227 Jy	12		[39]
06053–0622	20.3	54	20	H_2O	500 Jy	11.8		[72]
IRAS 06084–0611 / GGD 12-15								

continued on next page

continued from previous page

Name	R.A.	Dec	±	ν/λ	flux	±	SED	Ref
06084–0611	06 08 23.7	−06 11 06	2	850 μm	26 Jy	20%	Y	Me
GGD 12–15	24.1	11 08	1	20 cm	98 mJy	1	Y	[73]
GGD 12–15	24.1	11 08		4.9 GHz	120 mJy		N	[46]
GGD 12–15	24.1	11 08	1	6 cm	108 mJy	0.6	Y	[73]
06084–0611	24.5	11 12		6 cm	108 mJy		Y	[45]
GGD 12–15	25.6	10 49	0.3[b]	8.4 GHz	<0.2 mJy		N	[39]
GGD12–15 HII	24.15	11 8		8.4 GHz	∼105 mJy		N	[39]
GGD 12–15	24.1	11 08	1	2 cm	102 mJy	4	Y	[73]
06084–0611	24.5	11 12		2 cm	102 mJy		Y	[45]
06084–0611	24.5	11 12		2.7 mm	245 mJy	45	Y	[45]
IPC 41008	24.5	11 12	90[b]	1300 μm	11.8 Jy		Y	[74]
IPC 41008	24.5	11 12	67[b]	800 μm	44.7 Jy		Y	[75]
IPC 41008	24.5	11 12	86[b]	350 μm	500 Jy		Y	[75]
06084–0611	12	11 12	25,10,93	100 μm	4837 Jy	7%	Y	IRAS
06084–0611	12	11 12	25,10,93	60 μm	3607 Jy	9%	Y	IRAS
RAFGL 890	21.4	12 27	10*[b]	27 μm	-5.5 M		N	[21]
06084–0611	12	11 12	25,10,93	25 μm	602 Jy	5%	Y	IRAS
RAFGL 890	21.4	12 27	10*[b]	20 μm	-4.5 M		N	[21]
GGD 12–15	25.7	10 49.0	50[b]	19.5 μm	-3.6 M		N	[76]
06084–0611	12	11 12	25,10,93	12 μm	27 Jy	5%	Y	IRAS
GGD 12–15 VLA	24.7	10 50	34[b]	2.2 μm	8.3 M		N	[49]
GGD 12–15 #1	24.0	11 22	29[b]	100 μm	2100 Jy		N	[77]
GGD 12–15 #1	24.0	11 22	27[b]	50 μm	2200 Jy		N	[77]
GGD 12–15 #1	24.0	11 22	3.8[b]	Q	2.7 M	0.28	N	[77]
GGD 12–15 #1	24.0	11 22	3.8[b]	N	6.9 M	0.25	N	[77]
GGD 12–15 #1	24.0	11 22	3.6[b]	L	10.95 M	0.1	N	[77]
GGD 12–15 #1	24.0	11 22	3.6[b]	K	11.57 M	0.1	N	[77]
GGD 12–15 #1	24.0	11 22	3.6[b]	H	12.25 M	0.1	N	[77]
GGD 12–15 #1	24.0	11 22	3.6[b]	J	13.36 M	0.1	N	[77]
GGD 12–15 #2	23.8	11 15	3.8[b]	Q	-1.47 M	0.2	N	[77]
GGD 12–15 #2	23.8	11 15	3.8[b]	20.0 μm	39 Jy		N	[77]
GGD 12–15 #2	23.8	11 15	3.8[b]	12.5 μm	7.92 Jy		N	[77]
GGD 12–15 #2	23.8	11 15	3.8[b]	11.6 μm	5.94 Jy		N	[77]
GGD 12–15 #2	23.8	11 15	3.8[b]	10.3 μm	3.31 Jy		N	[77]
GGD 12–15 #2	23.8	11 15	3.8[b]	N	2.58 M	0.15	N	[77]
GGD 12–15 #2	23.8	11 15	3.8[b]	9.7 μm	2.53 Jy		N	[77]
GGD 12–15 #2	23.8	11 15	3.8[b]	8.7 μm	2.27 Jy		N	[77]
GGD 12–15 #2	23.8	11 15	3.6[b]	L	8.99 M	0.1	N	[77]
GGD 12–15 #2	23.8	11 15	3.6[b]	K	11.01 M	0.1	N	[77]
GGD 12–15 #2	23.8	11 15	3.6[b]	H	12.58 M	0.1	N	[77]
GGD 12–15 #2	23.8	11 15	3.6[b]	J	14.23 M	0.1	N	[77]
GGD 12–15 #3	24.3	11 12	3.8[b]	Q	-0.86 M	0.2	N	[77]
GGD 12–15 #3	24.3	11 12	3.8[b]	N	4.72 M	0.15	N	[77]
GGD 12–15 #3	24.3	11 12	3.6[b]	L	13.27 M	0.1	N	[77]
IRS 4	24.5	11 16	12[b]	L	7.77 M		N	[78]
GGD 12–15 #3	24.3	11 12	3.6[b]	K	12.04 M	0.1	N	[77]
IRS 4	24.5	11 16	12[b]	K	9.97 M		N	[78]
GGD 12–15 #3	24.3	11 12	3.6[b]	H	13.20 M	0.1	N	[77]
IRS 4	24.5	11 16	12[b]	H	11.00 M		N	[78]
GGD 12–15 #3	24.3	11 12	3.6[b]	J	14.95 M	0.1	N	[77]
IRS 4	24.5	11 16	12[b]	J	11.56 M		N	[78]
GGD 12–15 #4	24.0	11 07	3.8[b]	Q	-2.82 M	0.2	N	[77]
GGD 12–15 #4	24.0	11 07	3.8[b]	20	134 Jy		N	[77]
GGD 12–15 #4	24.0	11 07	3.8[b]	12.5 μm	12.9 Jy		N	[77]
GGD 12–15 #4	24.0	11 07	3.8[b]	11.6 μm	7.71 Jy		N	[77]
GGD 12–15 #4	24.0	11 07	3.8[b]	10.3 μm	2.33 Jy		N	[77]
GGD 12–15 #4	24.0	11 07	3.8[b]	N	2.46 M	0.15	N	[77]
GGD 12–15 #4	24.0	11 07	3.8[b]	9.7 μm	1.21 Jy		N	[77]
GGD 12–15 #4	24.0	11 07	3.8[b]	8.7 μm	1.36 Jy		N	[77]

continued on next page

continued from previous page

Name	R.A.	Dec	±	ν/λ	flux	±	SED	Ref
GGD 12–15 #4	24.0	11 07	3.6[b]	L	11.04 M	0.1	N	[77]
GGD 12–15 #4	24.0	11 07	3.6[b]	K	14.28 M	0.1	N	[77]
GGD 12–15 #4	24.0	11 07	3.6[b]	H	15.42 M	0.1	N	[77]
GGD 12–15 #4	24.0	11 07	3.6[b]	J	16.72 M	0.1	N	[77]
GGD 12–15 #5	23.4	11 03	3.8[b]	Q	2.8 M	0.25	N	[77]
GGD 12–15 #5	23.4	11 03	3.8[b]	N	6.2 M	0.25	N	[77]
GGD 12–15 #5	23.4	11 03	3.6[b]	L	10.26 M	0.1	N	[77]
GGD 12–15 #5	23.4	11 03	3.6[b]	K	11.40 M	0.1	N	[77]
GGD 12–15 #5	23.4	11 03	3.6[b]	H	12.51 M	0.1	N	[77]
GGD 12–15 #5	23.4	11 03	3.6[b]	J	13.80 M	0.1	N	[77]
GGD 12–15 #6	23.0	10 59	3.8[b]	Q	3.2 M	0.3	N	[77]
GGD 12–15 #6	23.0	10 59	3.8[b]	N	6.2 M	0.25	N	[77]
GGD 12–15 #6	23.0	10 59	3.6[b]	L	9.79 M	0.1	N	[77]
GGD 12–15 #6	23.0	10 59	3.6[b]	K	11.68 M	0.1	N	[77]
GGD 12–15 #6	23.0	10 59	3.6[b]	H	14.02 M	0.1	N	[77]
GGD 12–15 #6	23.0	10 59	3.6[b]	J	>17.02 M		N	[77]
GGD 12–15 #7	24.3	10 57	3.8[b]	Q	>3.0 M		N	[77]
GGD 12–15 #7	24.3	10 57	3.6[b]	L	10.39 M	0.1	N	[77]
GGD 12–15 #7	24.3	10 57	3.6[b]	K	12.19 M	0.1	N	[77]
GGD 12–15 #7	24.3	10 57	3.6[b]	H	14.42 M	0.1	N	[77]
GGD 12–15 #7	24.3	10 57	3.6[b]	J	17.12 M	0.1	N	[77]
GGD 12–15 #8	24.1	10 53	3.8[b]	Q	>2.8 M		N	[77]
GGD 12–15 #8	24.1	10 53	3.6[b]	L	11.07 M	0.1	N	[77]
IRS 3	23.6	10 55	12[b]	L	8.60 M		N	[78]
GGD 12–15 #8	24.1	10 53	3.6[b]	K	12.43 M	0.1	N	[77]
IRS 3	23.6	10 55	12[b]	K	10.69 M		N	[78]
GGD 12–15 #8	24.1	10 53	3.6[b]	H	14.26 M	0.1	N	[77]
IRS 3	23.6	10 55	12[b]	H	12.75 M		N	[78]
GGD 12–15 #8	24.1	10 53	3.6[b]	J	16.61 M	0.1	N	[77]
GGD 12–15 #9E	26.0	10 51	3.8[b]	Q	>3.0 M		N	[77]
GGD 12–15 #9E	26.0	10 51	3.8[b]	N	6.6 M	0.3	N	[77]
GGD 12–15 #9E	26.0	10 51	3.6[b]	L	10.92 M	0.1	N	[77]
GGD 12–15 #9E	26.0	10 51	3.6[b]	K	12.03 M	0.1	N	[77]
GGD 12–15 #9E	26.0	10 51	3.6[b]	H	13.15 M	0.1	N	[77]
GGD 12–15 #9E	26.0	10 51	3.6[b]	J	15.13 M	0.1	N	[77]
GGD 12–15 #9M	25.8	10 50	3.8[b]	Q	1.85 M	0.2	N	[77]
GGD 12–15	25.7	10 49	11[b]	19.5 μm	-2.6 M		Y	[76]
GGD 12–15 #9M	25.8	10 50	3.8[b]	N	5.9 M	0.25	Y	[77]
GGD 12–15	25.7	10 49	11[b]	N	1.9 M		N	[76]
GGD 12–15 #9M	25.8	10 50	3.6[b]	L	13.10 M	0.1	Y	[77]
GGD 12–15	25.7	10 49	11[b]	L	7.8 M		N	[76]
GGD 12–15 #9M	25.8	10 50	3.6[b]	K	14.40 M	0.1	Y	[77]
GGD 12–15	25.7	10 49	4.9[b]	K	11.07 M		N	[76]
GGD 12–15	25.7	10 49	7.5[b]	K	10.94 M		N	[76]
GGD 12–15	25.7	10 49	11[b]	K	10.1 M		N	[76]
GGD 12–15 #9M	25.8	10 50	3.6[b]	H	16.29 M	0.1	Y	[77]
GGD 12–15	25.7	10 49	7.5[b]	H	11.98 M		N	[76]
GGD 12–15 #9M	25.8	10 50	3.6[b]	J	>17.29 M		Y	[77]
GGD 12–15 #10	24.0	10 37	3.8[b]	Q	>3.0 M		N	[77]
GGD 12–15 #10	24.0	10 37	3.8[b]	N	5.6 M	0.2	N	[77]
GGD 12–15 IRS5	23.9	10 33	12[b]	M	7.12 M		N	[78]
GGD 12–15 #10	24.0	10 37	3.6[b]	L	8.07 M	0.1	N	[77]
GGD 12–15 IRS5	23.9	10 33	12[b]	L	7.85 M		N	[78]
GGD 12–15 #10	24.0	10 37	3.6[b]	K	9.57 M	0.1	N	[77]
GGD 12–15 IRS5	23.9	10 33	12[b]	K	9.66 M		N	[78]
GGD 12–15 #10	24.0	10 37	3.6[b]	H	11.54 M	0.1	N	[77]
GGD 12–15 IRS5	23.9	10 33	12[b]	H	11.28 M		N	[78]
GGD 12–15 #10	24.0	10 37	3.6[b]	J	13.99 M	0.1	N	[77]

continued on next page

continued from previous page

Name	R.A.	Dec	±	ν/λ	flux	±	SED	Ref
GGD 12–15 IRS5	23.9	10 33	12[b]	J	12.73 M		N	[78]
GGD 12–15 #11	25.1	10 53	3.8[b]	Q	>2.0 M		N	[77]
GGD 12–15 #11	25.1	10 53	3.8[b]	N	>6.5 M		N	[77]
GGD 12–15 #11	25.1	10 53	3.6[b]	L	12.19 M	0.1	N	[77]
GGD 12–15 #11	25.1	10 53	3.6[b]	K	13.51 M	0.1	N	[77]
GGD 12–15 #11	25.1	10 53	3.6[b]	H	15.27 M	0.1	N	[77]
GGD 12–15 #11	25.1	10 53	3.6[b]	J	17.77 M	0.1	N	[77]
GGD 12–15 #12	22.8	10 47	3.6[b]	L	11.67 M	0.1	N	[77]
GGD 12–15 #12	22.8	10 47	3.6[b]	K	12.15 M	0.1	N	[77]
GGD 12–15 #12	22.8	10 47	3.6[b]	H	12.76 M	0.1	N	[77]
GGD 12–15 #12	22.8	10 47	3.6[b]	J	14.39 M	0.1	N	[77]
06084–0611	24.5	11 12	1.′2[b]	^{12}CO 2-1	15.5 K	11.6		[45]
06084–0611	24.5	11 12	1.′2[b]	^{12}CO 2-1	8.2 K	11.6		[45]
GGD 12–15	27.8	10 46	44[b]	^{12}CO 1-0	9 K	10		[46]
GGD 12–15	27.8	10 46	1.′4	NH_3 1,1	0.37 K	12		[46]
GGD 12–15				NH_3				[79]
GGD 12–15	24.5	11 12	2″[b]	CH_3OH	<0.23 K			[66, 37]
GGD 12–15	27.8	10 46	44[b]	SiO maser	<130 Jy			[46]
GGD 12–15	28	10 46	2′	1612 MHz	<0.08 K	OH		[46]
GGD 12–15	28	10 46	2′	1665 MHz	0.10 K	OH	11	[46]
GGD 12–15	28	10 46	2′	1667 MHz	0.10 K	OH	11	[46]
GGD 12–15	28	10 46	2′	1720 MHz	<0.07 K	OH		[46]
GGD 12–15	25.66	10 49.5	1	H_2O	variable	-20 to -5		[46]
GGD 12–15	25.66	10 49.5	0.2	H_2O	10,4 Jy	-15,-9		[73]
06084–0611	25.6	10 49	25	H_2O	<14.7 Jy			[10]
GGD 12-15	25.6	10 49	25	H_2O	40.0 Jy	-20.3		[11]
GGD 12–15			60[b]	H_2O	209 Jy	-22.5		[39]
GGD 12–15			60[b]	H_2O	81.0 Jy	-22.9		[39]
GGD 12–15-C1	25.66	10 49.6	0.01	H_2O	14.7 Jy	-22.6		[39]

IRAS 06103–0612 / GGD 16-17

GGD 16–17	06 10 23.4	−06 12 45	2	850 μm	2.6 Jy	20%	Y	Me
06103–0612	21.8	12 28	23,9,92	100 μm	121 Jy	21%	Y	IRAS
06103–0612	21.8	12 28	23,9,92	60 μm	70 Jy	12%	Y	IRAS
06103–0612	21.8	12 28	23,9,92	25 μm	21 Jy	5%	Y	IRAS
06103–0612	21.8	12 28	23,9,92	12 μm	4 Jy	12%	Y	IRAS
Bretz 4	23	13		3.6 μm	>7.5 M		N	[80]
GGD 16–17 IRS1	24.2	12 16.0		L	9.59 M		N	[78]
GGD 16–17 IRS1	23.0	12 55.0		L	7.4 M		Y	[48]
GGD 16–17 IRS2	24.0	12 20.0		K	10.07 M		N	[48]
GGD 16–17 IRS1	24.2	12 16.0		K	10.10 M		N	[78]
GGD 16–17 IRS1	23.0	12 55.0		K	10.50 M		Y	[48]
Bretz 4	23	13		K	>8.7 M		N	[80]
GGD 16–17 IRS2	24.0	12 20.0		H	10.79 M		Y	[48]
GGD 16–17 IRS1	24.2	12 16.0		H	10.79 M		Y	[78]
GGD 16–17 IRS2	24.0	12 20.0		J	11.81 M		Y	[48]
GGD 16–17 IRS1	24.2	12 16.0		J	11.29 M		N	[78]
GGD 17	23.56	12 06.8	1	optical				[81, 46]
GGD 16–17	21.0	13 00	1.′4	NH_3 1,1	<0.16 K			[46]
GGD 16–17	23	12 55	2′	1612 MHz	<0.08 K	OH		[46]
GGD 16–17	23	12 55	2′	1665 MHz	<0.07 K	OH	2	[46]
GGD 16–17	23	12 55	2′	1667 MHz	0.10 K	OH	12	[46]
GGD 16–17	23	12 55	2′	1720 MHz	<0.07 K	OH		[46]
Mon R2-east	23.0	12 55	25	H_2O	<5 Jy			[11]
GGD 16–17	23.0	55	20	H_2O	12 Jy	7		[46]
HH 16–17	23.0	12 54.9		H_2O	<13.9 Jy			[10]

IRAS 06291+0421

06291+0421	06 29 10.0	04 21 35		850 μm	<5.4 Jy		Y	Me
06291+0421	09	50	3[b]	6 cm	10.12 mJy		Y	[2]
06291+0421	09.3	44		2.7 mm	<57 mJy		Y	[45]

continued on next page

continued from previous page

Name	R.A.	Dec	±	ν/λ	flux	±	SED	Ref
06291+0421	09.3	44	25,7,95	100 μm	496 Jy	11%	Y	IRAS
06291+0421	09.3	44	25,7,95	60 μm	253 Jy	14%	Y	IRAS
06291+0421	09.3	44	25,7,95	25 μm	21.5 Jy	6%	Y	IRAS
06291+0421	09.3	44	25,7,95	12 μm	8.5 Jy	4%	Y	IRAS
Mon OB2	09.3	44	1.′2[b]	^{12}CO 2-1	10.8 K	13		[45]
WB 817				CO		14.0		[9]
	09.3	44	25	H_2O	12.85 Jy	10.0		[15]
06291+0421	09.3	44	25	H_2O	3.1 Jy	9.65		[16]
WB 817	09.3	44	10	H_2O	2.3 Jy	9.2		[9]
06291+0421	09.3	44	25	H_2O	13.2 Jy	9.59		[16]
06291+0421	09.3	44	25	H_2O	13.7 Jy	10.06		[16]
WB 817	09.3	44	10	H_2O	<2.3 Jy			[9]
IRAS 17441−2910								
17441–2910	17 44 09.2	−29 10 59	2	850 μm	11 Jy	20%	Y	Me
17441–2910	09.2	59	7[b]	450 μm	54 Jy	30%	Y	Me
17441–2910	09.6	58	22,4,93	100 μm	3687 Jy	19%	Y	IRAS
17441–2910	09.6	58	22,4,93	60 μm	1741 Jy	11%	Y	IRAS
17441–2910	09.6	58	22,4,93	25 μm	228 Jy	4%	Y	IRAS
17441–2910	09.6	58	22,4,93	12 μm	27.5 Jy	5%	Y	IRAS
17441–2910	08.91	53.1		M	3.89 M	0.06	Y	[82]
17441–2910	08.91	53.1		L	5.56 M	0.04	Y	[82]
17441–2910	08.91	53.1		K	7.49 M	0.04	Y	[82]
17441–2910	08.91	53.1		H	9.74 M	0.04	Y	[82]
17441–2910	08.91	53.1		J	12.66 M	0.04	Y	[82]
17441–2910	09.2	59	2	C^{18}O 2-1	14.1 K	18.5		Me
17441–2910	09.2	59	2	CS 5-4	5.3 K	18.2		Me
17441–2910	09.17	56.4	0.1	OH maser	13.0 Jy	14.5		[83]
17441–2910	09.22	57.7	0.1	H_2O	12.6 Jy	19.0		[83]
	10.3	11 02.9	25	H_2O	64.8 Jy	20.1		[10]
IRAS 18032−2137								
18032–2137FIR2	18 03 18.6	−21 37 52	2	850 μm	49 Jy	20%	Y	Me
18032–2137FIR1	23.2	36	2	850 μm	20 Jy	20%	N	Me
G8.67–0.36	18.75	53.2	0.2	6 cm			N	[84]
G8.67–0.36	18.4	56	2.′6	4.875 GHz	1.41 Jy	5%	Y	[85, 59]
G8.67–0.36	18.4	56	1.′5	8.875 GHz	1.38 Jy	5%	Y	[59]
G8.67–0.36	18.75	53.2	0.2	2 cm			N	[84]
G8.67–0.36	18.4	56	1.′0	14.8 GHz	1.42 Jy	5%	Y	[59]
8.67–0.36				22 GHz	890 mJy	50%	Y	[83]
G8.67–0.36	18.4	56	1.′3	86 GHz	1.49 Jy	15%	Y	[59]
IPC 165563	18.5	54	4	1300 μm	7.1 Jy		Y	[74]
18032–2137FIR1	23.2	36	18[b]	450 μm	123 Jy	25%	N	Me
18032–2137FIR2	18.6	52	18[b]	450 μm	390 Jy	25%	Y	Me
18032–2137FIR2	18.6	47	7[b]	450 μm	320 Jy	30%	Y	Me
18032–2137	14.6	54	21,7,89	100 μm	5125 Jy	22%	Y	IRAS
18032–2137	14.6	54	21,7,89	60 μm	1895 Jy	16%	Y	IRAS
18032–2137	14.6	54	21,7,89	25 μm	154 Jy	5%	Y	IRAS
18032–2137	14.6	54	21,7,89	12 μm	19 Jy	5%	Y	IRAS
IPC 165563	18.5	54	4	4.6 μm	0 mJy		N	[86]
IPC 165563	18.5	54	4	3.8 μm	262 mJy		Y	[86]
IPC 165563	18.5	54	4	2.2 μm	145 mJy		Y	[86]
IPC 165563	18.5	54	4	1.6 μm	63.8 mJy		Y	[86]
IPC 165563	18.5	54	4	1.2 μm	7.1 mJy		Y	[86]
18032–2137FIR2	18.6	52	2	C^{18}O 2-1	14 K	34		Me
8.67–0.36	18.60	59.0	20[b]	CS 7-6	4.5 K	36.0		[7]
G8.67–0.36	18.75	53.2	5	NH_3 1,1	6.8 K	35.3		[32]
G8.67–0.36	18.75	53.2	5	NH_3 2,2	4.1 K	35.1		[32]
G8.67–0.36			2″[b]	CH_3OH	<0.40 Jy			[8]
8.67–0.36	18.9	59		CH_3OH 6.6 GHz	117 Jy	38,45		[67]
G8.67–0.36	18.4	56		H90α	0.146 K	42		[59]
G8.67–0.36				H110α				[87]

continued on next page

continued from previous page

Name	R.A.	Dec	±	ν/λ	flux	±	SED	Ref
8.67–0.36	18.81	52.6	0.5	OH	1.7 Jy	41.1		[83]
8.67–0.36	18.6	59	5	H_2O	35 Jy	35		[88]
00868–0036	21.5	39.9	25	H_2O	320.1 Jy	33.2		[10]
G8.67–0.36	18.75	53.2	5	H_2O	25.10 Jy	38.6		[32]
8.67–0.36	18.75	53.4	0.5	H_2O	6.8 Jy	31.0		[83]
18032–2137	17.2	55	20	H_2O	60 Jy	34.0		[72]

IRAS 18089−1732 / RAFGL 5451

18089–1732	18 08 56.4	−17 32 15	2	850 μm	17 Jy	20%	Y	Me
12.9+0.5	57.0	20		6 cm	<0.8 mJy	point src		[89]
18089-1732				6 cm	70.49 mJy	diffuse		[2]
12.89+0.48	58.4	24.0	9	10.7 GHz	<27 mJy		Y	[90]
18089–1732				450 μm	200 Jy	25%	Y	Me
12.9+0.5	56.6	22	10	400 μm	240 Jy	25%	Y	[89]
12.9+0.5	56.6	22	10	180 μm	2300[1] Jy	50%	Y	[89]
12.9+0.5	56.6	22	10	140 μm	2500[1] Jy	50%	Y	[89]
12.9+0.5	56.6	22	10	100 μm	2250[1] Jy	50%	N	[89]
18089-1732	56.4	14	40,7,88	100 μm	3146 Jy	22%	Y	IRAS
12.89+0.48	58.4	24.0	1[tb]	70 μm	2400 Jy	30%	Y	[91]
18089-1732	56.4	14	40,7,88	60 μm	1242 Jy	17%	Y	IRAS
12.9+0.5	56.6	22	10	60 μm	1050[1] Jy	50%	N	[89]
12.9+0.5	56.6	22	10	40 μm	260[1] Jy	50%	Y	[89]
RAFGL 5451	56.2	09	10[tb]	27 μm	-3.5 M		N	[21]
18089-1732	56.4	14	40,7,88	25 μm	45.3 Jy	8%	Y	IRAS
RAFGL 5451	56.2	09	10[tb]	Q	-2.1 M		N	[21]
18089-1732	56.4	14	40,7,88	12 μm	<6.1 Jy		Y	IRAS
RAFGL 5451	56.2	09	10[tb]	N	-0.5 M		N	[21]
12.9+0.5	58.4	26		10 μm	<8 Jy		Y	[89]
12.89+0.49	56.4	02.0	1[tb]	M	5.75 M	0.3	Y	[92]
12.89+0.49	56.4	02.0	1[tb]	L	7.62 M	0.2	Y	[92]
12.89+0.49	56.4	02.0	1[tb]	K	11.88 M	0.1	Y	[92]
12.89+0.48	58.4	24.0	20	^{12}CO 1-0	8 K	34		[90]
12.9+0.5				$C^{18}O$ 1-0	3.1 K	33.2		[89]
12.89+0.49	56.4	14		CH_3OH 6.6 GHz	75 Jy	32,41		[67]
12.89+0.49	56.40	14.0	15	CH_3OH	20 Jy	31.44		[93]
12.89+0.49	56.30	09.0	20[b]	CS 7-6	3.7 K	33.7		[7]
				OH maser				[94, 95]
01289+0049	56.2	16.0	25	H_2O	51.5 Jy	31.6		[10]
01289+0049	56.2	16.0	25	H_2O	15.9 Jy	30.75		[15]
12.89+0.49	56.3	16	10	H_2O	60 K	28,32,37		[96]

IRAS 18117−1753 / W33 A

18117–1753	18 11 44.1	−17 52 57	2	850 μm	45 Jy	20%	Y	Me
W33A				5 GHz	<5 mJy		Y	[97]
G12.91-0.28	48.9	53 15		10.7 GHz	1 Jy		N	[91, 98]
12.91-0.26				22 GHz	80 mJy		Y	[83]
IPC 169695	43.6	53 04		1300 μm	10.8 Jy		Y	[74]
W33A	43.7	53 02	1[tb]	1 mm	41 Jy	20%	Y	[99]
12.9-0.3				400 μm	460 Jy	25%	Y	[89]
18117–1753				450 μm	240 Jy	25%	Y	Me
12.9-0.3	44.2	52 56	25	180 μm	2900[1] Jy	50%	Y	[89]
12.9-0.3	44.2	52 56	25	140 μm	4000[1] Jy	50%	Y	[89]
W33 A	44.8	52 40		135 μm	6000 Jy	25%	Y	[100]
18117−1753	43.7	53 01	36,8,88	100 μm	6183 Jy	23%	Y	IRAS
W33 A	44.8	52 40		77 μm	4100 Jy	25%	Y	[100]
W33 A	44.8	52 40		73 μm	3400 Jy	25%	Y	[100]
G12.91-0.26	44.8	52 40		70 μm	3800 Jy	25%	Y	[91]
18117−1753	43.7	53 01	36,8,88	60 μm	2206 Jy	24%	Y	IRAS
W33 A	44.8	52 40		42 μm	1300 Jy	25%	Y	[100]
12.9-0.3	44.2	52 56	25	40 μm	1000 Jy	50%	Y	[89]
W33A	43.7	53 02		33 μm	1500 fW m^{-2}μm^{-1}		N	[101]

continued on next page

continued from previous page

Name	R.A.	Dec	±	ν/λ	flux	±	SED	Ref
18117−1753	43.7	53 01	36,8,88	25 μm	268 Jy	8%	Y	IRAS
W33A	43.7	53 02		25 μm	1800 fW m^{-2}μm^{-1}		N	[101]
12.9-0.3	43.7	53 02		20 μm	114 Jy	25%	Y	[89]
W33A	43.7	53 02		20 μm	850 fW m^{-2}μm^{-1}		N	[101]
18117−1753	43.7	53 01	36,8,88	12 μm	21.2 Jy	7%	Y	IRAS
12.9-0.3	43.7	53 02		10 μm	15 Jy	25%	Y	[89]
IPC 169695	43.6	53 04	4	4.6 μm	19.4 Jy		N	[86]
IPC 169695	43.6	53 04	4	3.8 μm	641 mJy		Y	[86]
IPC 169695	43.6	53 04	4	2.2 μm	169 mJy		Y	[86]
IPC 169695	43.6	53 04	4	1.6 μm	23.0 mJy		Y	[86]
IPC 169695	43.6	53 04	4	1.2 μm	6.2 mJy		Y	[86]
W33 A				CO v=0-1				[102]
12.91-0.26				H109α		30.0		[87]
12.91-0.26				^{12}CO 1-0	11 K	36		[90]
12.91-0.26	44.0	53 09	20[b]	CS 7-6	1.5 K	37.6		[7]
G12.9-0.3			2[#b]	CH_3OH	<0.43 Jy			[8]
W33 A	44.2	52 58		CH_3OH 6.6 GHz	327 Jy	35,41		[67]
12.91-0.26	44.24	52 58.8	0.4	OH	27 Jy	38.5		[103]
				OH				[104]
12.91-0.26	44.21	52 58.0	0.5	OH	3.4 Jy	35.2		[83]
W33A				H_2O	<13.2 Jy			[10]
W33A	44.0	53 08.5	5	H_2O	30 Jy	40		[71]
12.91-0.26	44.0	53 09	5	H_2O	3.6 K	38		[96]
12.91-0.26	44.18	52 57.8	0.5	H_2O	7.7 Jy	37.7		[83]
18117–1753	48.0	53 25	20	H_2O	<5.3 Jy	37.7		[72]
G14.45−0.11								
G14.45-0.11 FIR1	18.6	−16 26 49	2	850 μm	3.6 Jy	20%	N	Me
G14.45-0.11 FIR2	15.3	27 12	2	850 μm	5.7 Jy	20%	Y	Me
G14.45-0.11 FIR3	17.4	27 17	2	850 μm	2.4 Jy	20%	N	Me
G14.45-0.11				8 GHz	<0.3 mJy		N	Me
14.44-0.11	15	28 14	68[b]	10.7 GHz	270 mJy		Y	[91]
G14.45-0.11 FIR1				450 μm	25 Jy	25%	N	Me
G14.45-0.11 FIR2				450 μm	37 Jy	25%	Y	Me
G14.45-0.11 FIR3				450 μm	18 Jy	25%	N	Me
14.47-0.11	18.6	26 16	40	70 μm	2200 Jy	25%	Y	[91]
14.45-0.11	17.6	27 50	15[b]	K	10.40 M	0.10	Y	[92]
14.45-0.11	17.6	27 50	15[b]	H	10.65 M	0.08	Y	[92]
14.45-0.11	17.6	27 50	15[b]	J	11.52 M	0.10	Y	[92]
G14.45-0.11				^{12}CO 2-1	20.4 K	42.3		Me
14.47-0.11	18.6	26 16	64[b]	^{12}CO 1-0	13 K	41		[91, 90]
G14.45-0.11				C^{18}O 2-1	10.1 K	40.5		Me
14.45-0.11	16.4	27 20.0	20[b]	CS 7-6	<0.5 K			[7]
14.45-0.11	16.4	27 20	10	H_2O	8 K	37.0		[96]
01445-0010	16.4	27 20.0	25	H_2O	13.6 Jy	37		[10]
G14.45-0.11				H_2O	<0.05 Jy			Me
IRAS 18162−2048 / GGD 27–28								
18162–2048	18 16 13.0	−20 48 47	2	850 μm	21 Jy	20%	Y	Me
HH 80-81				Radio jet				[105, 106]
GGD 27–28	13.0	48 48	1	20 cm	<17 mJy		Y	[73]
GGD 27–28	13.0	48 48	1	6 cm	7 mJy	0.6	Y	[73]
GGD 27–28	13.0	48 48	1	4.9 GHz	6.0 mJy	1	N	[46]
18162–2048				6 cm	4.1 mJy		N	[1]
18162–2048				6 cm	9.2 mJy		N	[45]
GGD 27–28	13.0	48 48	1	2 cm	<14 mJy		N	[73]
18162–2048				2 cm	7.6 mJy		Y	[45]
18162–2048				2.7 mm	193 mJy	45	Y	[45]
18162–2048				800 μm	24 Jy	20%	Y	Me
18162–2048				450 μm	130 Jy	20%	Y	Me
18162–2048	12.8	48 51	29,6,88	100 μm	3714 Jy	12%	Y	IRAS

continued on next page

continued from previous page

Name	R.A.	Dec	±	ν/λ	flux	±	SED	Ref
18162–2048	12.8	48 51	29,6,88	60 μm	2767 Jy	10%	Y	IRAS
18162–2048	12.8	48 51	29,6,88	25 μm	346 Jy	4%	Y	IRAS
RAFGL 2121	11.2	47 40	$10''^{b}$	27 μm	-5.1 M		N	[21]
RAFGL 2121	11.2	47 40	$10''^{b}$	20 μm	-3.1 M		Y	[21]
18162–2048	12.8	48 51	29,6,88	12 μm	26 Jy	5%	Y	IRAS
RAFGL 2121	11.2	47 40	$10''^{b}$	11 μm	-0.2 M		N	[21]
GGD27 IRS 1	13.0	49 09	3	M	4.9 M		N	[107]
GGD27 IRS 1	13.0	49 09	3	L′	5.9 M		N	[107]
GGD27 IRS 1	13.0	49 09	3	K	8.1 M		N	[107]
GGD27 IRS 1	13.0	49 09	3	H	10.3 M		N	[107]
GGD27 IRS 1	13.0	49 09	3	J	13.1 M		N	[107]
GGD27 IRS 2				nbM	0.96 Jy		N	[108]
GGD27 IRS 2	13.2	48 46	3	M	4.7 M		Y	[107]
GGD27 IRS 2				L′	0.73 Jy		N	[108]
GGD27 IRS 2	13.2	48 46	3	L′	5.9 M		Y	[107]
GGD27 IRS 2				K	48 mJy		N	[108]
GGD27 IRS 2	13.2	48 46	3	K	9.4 M		Y	[107]
GGD27 IRS 2				H	4 mJy		N	[108]
GGD27 IRS 2	13.2	48 46	3	H	12.1 M		Y	[107]
GGD27 IRS 2				J	0.7 mJy		N	[108]
GGD27 IRS 2	13.2	48 46	3	J	13.9 M		Y	[107]
GGD27 IRS 3	15.8	49 04	3	K	9.9 M		N	[107]
GGD27 IRS 4	11.7	48 16	3	K	10.1 M		N	[107]
GGD27 IRS 5	11.7	49 13	3	K	10.3 M		N	[107]
GGD27 IRS 6	10.0	47 54	10	K	7.7 M		N	[107]
GGD 27a	10.86	48 29.7	1.8		optical		N	[46, 81]
GGD 27b	12.53	48 44.0	1.8		optical		N	[46, 81]
GGD 27c	12.69	49 08.3	1.8		optical		N	[46, 81]
GGD 27d	12.93	48 23.9	1.8		optical		N	[46, 81]
18162-2048			40^{b}	^{12}CO 1-0	20 K	12		[1]
GGD 27–28	14.6	48 41.0		^{12}CO 1-0	4 K	11		[46]
GGD 27			$1\farcm2^{b}$	^{12}CO 2-1	18 K	12.2		[45]
18162-2048			40^{b}	^{13}CO 1-0	12 K	12		[1]
GGD 27			$1\farcm2^{b}$	^{13}CO 2-1	8.8 K	12.2		[45]
18162-2048			40^{b}	C^{18}O 1-0	1.5 K	12		[1]
GGD 27				Hα				[109]
GGD 27–28	14.6	48 41.0	$1\farcm4^{b}$	NH_3 1,1	0.14 K	10		[46]
GGD 27–28	14.6	48 41.0	44^{b}	SiO maser	<220 Jy			[46]
GGD 27	12.8	48 51	$2''^{b}$	CH_3OH	<0.34 K			[37]
18162-2048				CH_3OH 6.6-GHz	<3 Jy			[110]
GGD 27–28	15	48 41	$2'$	1612 MHz	0.1,-0.1 K	OH	-7,12	[46]
GGD 27–28	15	48 41	$2'$	1665 MHz	<0.08 K	OH		[46]
GGD 27–28	15	48 41	$2'$	1667 MHz	0.13 K	OH	14	[46]
GGD 27–28	15	48 41	$2'$	1720 MHz	-0.1,0.1 K	OH	-8,14	[46]
GGD 27–28	14.6	48 41.0	20	H_2O	7-70 Jy	−70		[46]
HH27–28	14.6	48 40.9	25	H_2O	<9.9 Jy			[10]

IRAS 18164−1631

18164–1631	18 16 21.8	−16 31 21	2	850 μm	22 Jy	20%	Y	Me
18164–1631	21.8	21	3^{b}	6 cm	<0.3 mJy		N	[2]
14.63–0.69				10.7 GHz	<27 mJy		Y	[91]
18164–1631				23.7 GHz	0.09 Jy	50%	Y	[56]
18164–1631			17^{b}	450 μm	100 Jy	25%	Y	Me
18164–1631			7^{b}	450 μm	90 Jy	30%	Y	Me
18164–1631	24.0	39	37,7,88	100 μm	<2976 Jy		Y	IRAS
14.63–0.69	24.1	32	40	70 μm	1200 Jy	25%	Y	[91]
18164–1631	24.0	39	37,7,88	60 μm	735 Jy	24%	Y	IRAS
18164–1631	24.0	39	37,7,88	25 μm	22.5 Jy	18%	Y	IRAS
18164–1631	24.0	39	37,7,88	12 μm	<9.9 Jy		Y	IRAS
14.63–0.69			64^{b}	^{12}CO 1-0	12 K	20		[90]
18164–1631			21^{b}	^{12}CO 2-1	29 K	15.9		Me

continued on next page

continued from previous page

Name	R.A.	Dec	±	ν/λ	flux	±	SED	Ref
18164–1631			21[b]	$C^{18}O$ 2-1	6 K	18		Me
18164–1631			21[b]	CS 5-4	4 K	17.2		Me
14.63-0.58	21.20	24	20[b]	CS 7-6	1.5 K	18.8		[7]
18164–1631	21.0	24	2′[b]	CH_3OH	<0.28 K			[37]
18164–1631				NH_3		18.72		[56]
01463–0058	21.2	23.9	25	H_2O	<10.9 Jy			[10]
14.63–0.58	21.2	23.9	6	H_2O	20 K	26		[96]
IRAS 18273+0113 / GGD 29 / SERPENS								
18273+0113	18 27 17.5	01 13 15	2	850 μm	13 Jy	20%	Y	Me
Serpens NW				20 cm	2.2 mJy	0.2	N	[111]
Serpens NW				6 cm	2.1 mJy	0.2	N	[111]
GGD 29	17.2	19		4.9 GHz	3.0 mJy		N	[46]
Serpens NW				3.6 cm	2.0 mJy	0.1	N	[111]
18273+0113 VLA1	17.11	20.0	0.1	8 GHz	1.2 mJy		Y	Me
Serpens NW				2 cm	2.0 mJy	0.2	N	[111]
Serpens Cen				20 cm	2.6 mJy	0.4	N	[111]
Serpens Cen				6 cm	2.7 mJy	0.2	N	[111]
Serpens Cen				3.6 cm	2.8 mJy	0.1	N	[111]
18273+0113 VLA2	17.44	15.6	0.1	8 GHz	2.8 mJy		Y	Me
Serpens Cen				2 cm	4.0 mJy	0.2	N	[111]
Serpens SE				20 cm	4.7 mJy	0.2	N	[111]
Serpens SE				6 cm	2.8 mJy	0.1	N	[111]
GGD 29	17.7	13		4.9 GHz	3.4 mJy		N	[46]
Serpens SE				3.6 cm	2.7 mJy	0.1	N	[111]
18273+0113 VLA3	17.75	12.4	0.1	8 GHz	2.2 mJy		Y	Me
Serpens SE				2 cm	2.3 mJy	0.1	N	[111]
FIRS 1				2000 μm	0.91 Jy b^{-1}	0.2	N	[112]
FIRS 1				1300 μm	2.52 Jy b^{-1}	0.1	N	[112]
FIRS 1				1100 μm	3.47 Jy b^{-1}	0.1	N	[112]
FIRS 1				800 μm	8.16 Jy b^{-1}	0.2	N	[112]
18273+0113				800 μm	17 Jy	20%	Y	Me
18273+0113			7[b]	450 μm	60 Jy	30%	Y	Me
18273+0113			17[b]	450 μm	80 Jy	25%	Y	Me
Serpens/FIRS1				160 μm	500[1] Jy	50%	Y	[113]
18273+0113	18.0	14	37,6,85	100 μm	<744 Jy		N	IRAS
Serpens/FIRS1				100 μm	400[1] Jy	50%	Y	[113]
18273+0113	18.0	14	37,6,85	60 μm	153 Jy	13%	Y	IRAS
Serpens/FIRS1				60 μm	100[1] Jy	50%	N	[113]
18273+0113	18.0	14	37,6,85	25 μm	<3.2 Jy		Y	IRAS
Serpens/FIRS1				20 μm	2[1] Jy	50%	N	[113]
18273+0113	18.0	14	37,6,85	12 μm	<0.25 Jy		Y	IRAS
Serpens/FIRS1				10 μm	<80[1] mJy	50%	Y	[113]
Serpens/FIRS1				2.2 μm	<1[1] mJy	50%	N	[113]
Serpens/FIRS1	17.4	24	2	K	14.6 M	0.1	N	[114]
Serpens/FIRS1	17.3	23	4	K	14.76 M		Y	[115]
Serpens/FIRS1	17.4	24	2	H	<16.0 M	0.1	Y	[114]
Serpens/FIRS1	17.4	24	2	J	<18.0 M	0.1	Y	[114]
SMM1				CO isotopes				[116]
FIRS1				Lines				[117]
18273+0113				^{12}CO 2-1	19 K	10.4		Me
GGD 29	19.2	06	44[b]	^{12}CO 1-0	12 K	8		[46]
18273+0113				$C^{18}O$ 2-1	6.4 K	8.3		Me
18273+0113				CS 5-4	1.9 K	9.8		Me
FIRS 1				H_2CO 3-2	5 K	8		[118]
GGD 29	19.2	06	1.′4[b]	NH_3 1,1	0.40 K	8		[46]
FIRS1			0.3	NH_3 1,1				[119]
GGD 29	19.2	06	44[b]	SiO	<360 Jy			[46]
GGD 29	19	06	2′	1612 MHz	<0.08 K	OH		[46]
GGD 29	19	06	2′	1665 MHz	0.10 K	OH	8	[46]
GGD 29	19	06	2′	1667 MHz	0.14 K	OH	8	[46]

continued on next page

continued from previous page

Name	R.A.	Dec	±	ν/λ	flux	±	SED	Ref
GGD 29	19	06	2[f]	1720 MHz	−0.10 K	OH	9	[46]
GGD 29	19.2	06	20	H_2O	Jy	∼38		[46]
GGD 29	21.5	20	25	H_2O	<7.7 Jy			[10]
18273+0113	17.44	15.6	0.1	H_2O	0.74 Jy	35		Me
Serpens	17.43	15.8	0.1	H_2O	7 Jy	8		[111]
IRAS 18316−0602 / RAFGL 7009S								
18316−0602	18 31 40.2	−06 02 06	2	800 μm	28 Jy	20%	Y	Me
18316–0602	39.0	08		6 cm	2.7 mJy		Y	[1]
18316–0602	40.14	05.7	0.1	8 GHz	3.8 mJy		Y	Me
18316–0602				450 μm	180 Jy	25%	Y	Me
18316–0602	39.0	08	20,5,85	100 μm	2137 Jy	12%	Y	IRAS
18316–0602	39.0	08	20,5,85	60 μm	963 Jy	12%	Y	IRAS
RAFGL 7009S	41.6	35	10[tb]	27 μm	-3.6 M		Y	[21]
18316–0602	39.0	08	20,5,85	25 μm	138 Jy	5%	Y	IRAS
18316–0602	39.0	08	20,5,85	12 μm	23 Jy	6%	Y	IRAS
18316–0602	39.0	08		^{12}CO 1-0	15 K	43.5		[1]
18316–0602	39.0	08		^{13}CO 1-0	9 K	42		[1]
18316–0602	39.0	08		C^{18}O 1-0	2 K	42		[1]
	39.0	07	25	H_2O	726 Jy	45.2		[15]
18316–0602	39.0	07	25	H_2O	734 Jy	45.2		[16]
18316–0602	40.15	05.4	0.1	H_2O	109, 0.23Jy	45,74		Me
IRAS 18455−0149								
18455–0149	18 45 34.8	−01 48 51	2	850 μm	4.1 Jy	20%	Y	Me
18455–0149				8 GHz	<0.3 Jy		Y	Me
18455–0149			17[b]	450 μm	26 Jy	25%	Y	Me
18455–0149			7[b]	450 μm	17 Jy	30%	Y	Me
18455–0149	35.0	03	42,6,82	100 μm	<5534 Jy		Y	IRAS
18455–0149	35.0	03	42,6,82	60 μm	<503 Jy		Y	IRAS
18455–0149	35.0	03	42,6,82	25 μm	<12.4 Jy		Y	IRAS
18455–0149	35.0	03	42,6,82	12 μm	2.9 Jy	12%	Y	IRAS
18455–0149	34.8	51	2	C^{18}O 1-0	7.6 K	81.5		Me
18455–0149	34.8	51	2	CS 5-4	1.9 K	81.8		Me
03100–0007	34.9	35.0	25	H_2O	<4.4 Jy			[10]
H_2O 31.000-0.075	34.9	35.0	45	H_2O	1.6 Jy	74		[120]
H_2O 31.000-0.075	34.9	35.0	45	H_2O	3.5 Jy	74		[120]
18455–0149	34.86	51.2	0.1	H_2O	1.01 Jy	82		Me
IRAS 18537+0749 / S76 E								
18537+0749	18 53 46.1	07 49 19	2	850 μm	33 Jy	20%	Y	Me
18537+0749	54 40.0	53 40		6 cm	43 mJy		N	[2]
18537+0749			17[b]	450 μm	215 Jy	25%	Y	Me
18537+0749	46.2	30	26,5,80	100 μm	4227 Jy	14%	Y	IRAS
18537+0749	46.2	30	26,5,80	60 μm	2351 Jy	5%	Y	IRAS
18537+0749	46.2	30	26,5,80	25 μm	242 Jy	4%	Y	IRAS
RAFGL 2284	47	51 06	10[tb]	20 μm	-4.4 M		N	[21]
18537+0749	46.2	30	26,5,80	12 μm	31.9 Jy	5%	Y	IRAS
RAFGL 2284	47	51 06	10[tb]	11 μm	-1.7 M		N	[21]
18537+0749	46.5	18.5		M	4.74 M	0.1	Y	[82]
18537+0749	46.5	18.5		L	7.19 M	0.1	Y	[82]
18537+0749	46.5	18.5		K	10.32 M	0.1	Y	[82]
18537+0749	46.5	18.5		H	12.68 M	0.1	Y	[82]
18537+0749	46.5	18.5		J	14.25 M	0.1	Y	[82]
S76 E	45.6	16.0	20[b]	CS 7-6	4.3 K	31.9		[7]
18537+0749				HCO^+ 1-0	<0.8 K			[121]
18537+0749				CH_3OH 6.6-GHz	<3 Jy			[110]
S76E	47.0	26	30	H_2O	4.5 K	26,31,33		[122]
S76E	47.0	26	25	H_2O	126 Jy	32		[10]
S76 E(1)	45.6	16.0	5	H_2O	50 Jy	30,40		[38]
S76 E(2)	45.9	16.0	5	H_2O		25,32,35		[38]

continued on next page

continued from previous page

Name	R.A.	Dec	±	ν/λ	flux	±	SED	Ref
18537+0749	47.9	41	20	H_2O	10 Jy	31.6		[72]
IRAS 18592+0108 / W48								
18592+0108	18 59 13.8	01 09 03	2	850 μm	50 Jy	20%	Y	Me
35.195-1.745	14.3	08 40		4.875 GHz	13.77 Jy	5%	Y	[59]
35.195-1.745	14.3	08 40		14.8 GHz	7.70 Jy	5%	Y	[59]
35.20-1.74				22 GHz	1.29 Jy	50%	N	[83]
35.195-1.745	14.3	08 40		86 GHz	6.94 Jy	15%	Y	[59]
IPC 191989	14.9	08 46		1.3 mm	10.1 Jy		Y	[74]
IPC 191989	09	08 16	3.9^{tb}	1.0 mm	49 Jy		Y	[61]
18592+0108			17^{b}	450 μm	250 Jy	25%	Y	Me
18592+0108	14.5	08 46	18,8,48	100 μm	13920 Jy	8%	Y	IRAS
18592+0108	14.5	08 46	18,8,48	60 μm	10150 Jy	10%	Y	IRAS
W48	14.2	08 41		33 μm	2200 fW m^{-2}μm^{-1}		N	[101]
RAFGL 2304	20	08 39	10^{tb}	27 μm	-6.7 M		N	[21]
18592+0108	14.5	08 46	18,8,48	25 μm	1023 Jy	4%	Y	IRAS
W48	14.2	08 41		25 μm	2500 fW m^{-2}μm^{-1}		N	[101]
W48	14.2	08 41		20 μm	1900 fW m^{-2}μm^{-1}		N	[101]
RAFGL 2304	20	08 39	10^{tb}	20 μm	-5.0 M		N	[21]
IR 35.2-1.7	13.6	09 01		20 μm	100 Jy		Y	[123]
IR 35.2-1.7	13.6	09 01		12.5 μm	38 Jy		Y	[123]
18592+0108	14.5	08 46	18,8,48	12 μm	115 Jy	5%	N	IRAS
IR 35.2-1.7	13.6	09 01		11.2 μm	17 Jy		Y	[123]
RAFGL 2304	20	08 39	10^{tb}	11 μm	-2.2 M		N	[21]
IR 35.2-1.7	13.6	09 01		10.1 μm	17 Jy		Y	[123]
IR 35.2-1.7	13.6	09 01		9.5 μm	8 Jy		Y	[123]
IR 35.2-1.7	13.6	09 01		8.7 μm	8 Jy		Y	[123]
IR 35.2-1.7	13.6	09 01		4.8 μm	1.7 Jy		Y	[123]
IPC 191989	14.9	08 46		4.6 μm	0 mJy		N	[86]
IPC 191989	14.9	08 46		3.8 μm	192 mJy		Y	[86]
IPC 191989	14.9	08 46		2.2 μm	66 mJy		Y	[86]
IPC 191989	14.9	08 46		1.6 μm	32.3 mJy		y	[86]
IPC 191989	14.9	08 46		1.2 μm	3.6 mJy		Y	[86]
W48 IRS 1	14.7	08 53		3.5 μm	1.8 Jy		Y	[124]
W48 IRS 2	12.2	08 20		3.5 μm	1.2 Jy		N	[124]
G35.2-1.7	14.1	09 00		2.2 μm	spectrum			[125]
W48			3^{tb}	CO 1-0	20 K	41		[124]
W 48	15	08 18	8^{tb}	H158α	0.26 K	45.2		[126]
W 48	15	08 18	8^{tb}	He158α	0.04 K	45		[126]
W 48	15	08 18	8^{tb}	C158α	0.17 K	42.9		[126]
W 48	15	08 18	8^{tb}	H166α	0.21 K	44		[126]
W 48	15	08 18	8^{tb}	C166α	0.14 K	42.4		[126]
35.20–0.73	13.8	09 20	CH_3OH 6.6 GHz		556 Jy	39,47		[67]
35.20-1.74	13.16	09 11.8	0.5	OH	0.6 Jy	32.1		[83]
W48				H_2O				[127]
W48	12.7	09 13.0	25	H_2O	17.0 Jy	43.8		[10]
W48	12.8	09 13	10	H_2O	30 Jy	46		[71]
W48				H_2O				[123]
W48				H_2O				[128]
35.20-1.74	13.24	09 13.5	0.5	H_2O	15.5 Jy	46.6		[83]
18592+0108	15.3	08 29	20	H_2O	40.0 Jy	46.0		[72]
IRAS 19374+2352								
19374+2352	19 37 27.8	23 52 49	2	800 μm	7.1 Jy	20%	Y	Me
19374+2352	27.80	51.4	0.1	8 GHz	79.3 mJy		Y	Me
19374+2352			30^{b}	15 GHz	75 mJy		Y	Me
19374+2352			17^{b}	450 μm	55 Jy	25%	N	Me
19374+2352			7^{b}	450 μm	30 Jy	30%	N	Me
19374+2352	26.4	57	29,8,70	100 μm	767 Jy	15%	Y	IRAS
19374+2352	26.4	57	29,8,70	60 μm	422 Jy	10%	Y	IRAS
19374+2352	26.4	57	29,8,70	25 μm	24.4 Jy	6%	Y	IRAS

continued on next page

continued from previous page

Name	R.A.	Dec	±	ν/λ	flux	±	SED	Ref
19374+2352	26.4	57	29,8,70	12 μm	4.57 Jy	7%	Y	IRAS
19374+2352				^{12}CO 2-1	21 K	35.4		Me
19374+2352				C^{18}O 2-1	5.2 K	37		Me
19374+2352				CH_3OH 6.6-GHz	<3 Jy			[110]
19374+2352	27.69	52.2	0.1	H_2O	0.19 Jy	34		Me
19374+2352	26.4	57	25	H_2O	40.8 Jy	38.83		[15]
19374+2352	26.4	57	25	H_2O	33.1 Jy	38.98		[16]
IRAS 19442+2427 / S87								
19442+2427 FIR1	19 44 16.0	24 28 36	2	850 μm	6.5 Jy	20%	Y	Me
19442+2427 FIR2	19 44 14.0	24 28 12	2	850 μm	17 Jy	20%	Y	Me
S87	14.0	27 58.0		5 GHz	0.4 Jy		Y	[129]
S87 FIR1				5 GHz	Jy		N	[129]
IPC 208471	13.5	28 00		1300 μm	3.6 Jy		Y	[74]
19442+2427 FIR1			17^b	450 μm	18 Jy	25%	Y	Me
19442+2427 FIR2			17^b	450 μm	110 Jy	25%	Y	Me
19442+2427	13.5	28 00	30,6,73	100 μm	5158 Jy	9%	Y	IRAS
19442+2427	13.5	28 00	30,6,73	60 μm	3446 Jy	9%	Y	IRAS
19442+2427	13.5	28 00	30,6,73	25 μm	425 Jy	6%	Y	IRAS
RAFGL 2454	10	27 18	10^{tb}	20 μm	-4.2 M		N	[21]
19442+2427	13.5	28 00	30,6,73	12 μm	47.5 Jy	8%	Y	IRAS
RAFGL 2454	10	27 18	10^{tb}	11 μm	-1.7 M		N	[21]
RAFGL 2454	10	27 18	17^b	M	4.9 M		Y	[22]
RAFGL 2454	10	27 18	17^b	L	3.5 M		Y	[22]
19442+2427	13.7	27 59		3.4 μm	0.7 fW m^{-2}		N	[28]
19442+2427	13.7	27 59		3.3 μm	50.0 fW m^{-2}		N	[28]
RAFGL 2454	10	27 18	17^b	3.3 μm	6.4 M		Y	[22]
19442+2427	13.7	27 59		3.1 μm	spectrum			[28]
RAFGL 2454	10	27 18	17^b	3.08 μm	7.7 M		Y	[22]
RAFGL 2454	10	27 18	17^b	K	9.0 M		Y	[22]
RAFGL 2454	10	27 18	17^b	H	10.7 M		Y	[22]
RAFGL 2454	10	27 18	17^b	J	11.6 M		Y	[22]
S87	14.0	28 10.0	20^b	CS 7-6	2.6 K	22.8		[7]
19442+2427	13.5	28 00		NH_3 1,1	?1.77 K	21.1		[32]
19442+2427	13.5	28 00		NH_3 2,2	0.74 Jy	21.6		[32]
19442+2427				CH_3OH 6.6-GHz	<3 Jy			[110]
S87 (1)	14.0	28 10	7	H_2O	3 Jy	22		[38]
S87 (2)	15.5	28 25	5	H_2O	1 Jy	12		[38]
	14.0	27 58	30	H_2O		25.5		[122]
19442+2427	13.5	28 00		H_2O	?0.22 Jy	?29.6		[32]
S87	14.0	27 58	25	H_2O	<9.7 Jy			[10]
19442+2427	13.9	28 20	20	H_2O	<2.1 Jy			[72]
IRAS 20056+3350								
20056+3350	20 05 35.8	33 50 56	2	800 μm	6.2 Jy	20%	Y	Me
20056+3350	35.69	56.2	0.1	8 GHz	0.93 mJy		Y	Me
20056+3350	35.79	56.7	0.1	8 GHz	0.60 mJy		Y	Me
20056+3350			30^b	15 GHz	3 mJy		Y	Me
20056+3350			17^b	450 μm	48 Jy	25%	Y	Me
20056+3350			7^b	450 μm	33 Jy	30%	Y	Me
20056+3350	36	53	20,9,63	100 μm	755 Jy	16%	Y	IRAS
20056+3350	36	53	20,9,63	60 μm	422 Jy	15%	Y	IRAS
20056+3350	36	53	20,9,63	25 μm	24.7 Jy	8%	Y	IRAS
20056+3350	36	53	20,9,63	12 μm	4.34 Jy	22%	Y	IRAS
20056+3350	36	53	4.′4^b	^{13}CO 1-0	1.5 K	10		[6]
20056+3350	35.8	56	2	C^{18}O 2-1	5.3 K	9		Me
20056+3350	35.8	56	2	CS 5-4	2.5 K	9		Me
20056+3350	36.0	53		HCO^+ 1-0	0.6 K	8.5		[121]
20056+3350				CH_3OH 6.6-GHz	<3 Jy			[110]
20056+3350	35.70	55.8	0.1	H_2O	0.46 Jy	10		Me
20056+3350	35.76	55.8	0.1	H_2O	0.28 Jy	2		Me

continued on next page

continued from previous page

Name	R.A.	Dec	±	ν/λ	flux	±	SED	Ref
	36.0	53	25	H_2O	67.43 Jy		10.36	[15, 130]
20056+3350	36.0	53	25	H_2O	80.3 Jy	10.42		[16]
20056+3350	36.0	53	25	H_2O	111.2 Jy	8.43		[16]
20056+3350	36.0	53	25	H_2O	124.8 Jy	8.43		[16]
IRAS 20188+3928								
20188+3928 FIR2	20 18 50.4	39 28 18	2	800 μm	21 Jy	20%	Y	Me
20188+3928 FIR1	20 18 50.0	39 28 45	2	800 μm	9.8 Jy	20%	Y	Me
20188+3928	50.7	18	4[b]	6 cm	29 mJy		Y	[1]
20188+3928	50.8	40	4[b]	6 cm	3 mJy		N	[1]
20188+3928	50.71	17.1	0.1	8 GHz	24.1 mJy		Y	Me
20188+3928	50.77	19.1	0.1	8 GHz	2.2 mJy		Y	Me
20188+3928	50.92	38.7	0.1	8 GHz	3.4 mJy		Y	Me
20188+3928	50.4	19	30[b]	15 GHz	28 mJy		Y	Me
20188+3928	50.7	17	1[b]	15 GHz	26 mJy		Y	Me
20188+3928	50.9	38	1[b]	15 GHz	2.8 mJy		N	Me
	58.0	26 04	30[b]	15 GHz	14.5 mJy		N	Me
20188+3928 FIR1			17[b]	450 μm	48 Jy	25%	Y	Me
20188+3928 FIR2			17[b]	450 μm	144 Jy	25%	Y	Me
20188+3928 FIR2			7[b]	450 μm	130 Jy	30%	Y	Me
20188+3928	50.7	18	20,4,66	100 μm	1441 Jy	14%	Y	IRAS
20188+3928	50.7	18	20,4,66	60 μm	1051 Jy	12%	Y	IRAS
20188+3928	50.7	18	20,4,66	25 μm	241 Jy	5%	Y	IRAS
20188+3928	50.7	18	20,4,66	12 μm	11.5 Jy	6%	Y	IRAS
20188+3928				POSS				[131]
20188+3928				Outflow				[132]
20188+3928			40[b]	^{12}CO 1-0	15.9 K	2.0		[1]
20188+3928			33[b]	^{12}CO 1-0	35 K	4		[132]
20188+3928 FIR2				^{12}CO 2-1	36.7 K	4.7		Me
20188+3928			40[b]	^{13}CO 1-0	12 K	2.0		[1]
20188+3928			33[b]	^{13}CO 1-0	20 K	3		[132]
20188+3928			40[b]	C^{18}O 1-0	2.2 K	2.0		[1]
20188+3928 FIR2				C^{18}O 2-1	8.3 K	1.5		Me
20188+3928 FIR2				CS 5-4	5.5 K	2.2		Me
20188+3928	50.7	18		HCO^+ 1-0	4.2 K	2.0		[121]
20188+3928			50[b]	HCO^+ 1-0	5 K	3		[132]
20188+3928			66[b]	HCO^+ 3-2	2.5 K	2		[132]
20188+3928			2[b]	CH_3OH	<2.0 Jy			[8]
20188+3928				CH_3OH 6.6-GHz	<3 Jy			[110]
20188+3928	49.79	46.7	0.1	H_2O	3.20 Jy	7		Me
20188+3928	50.81	37.6	0.1	H_2O	0.21 Jy	4		Me
	50.7	18	25	H_2O	19.7 Jy	-1.24		[15]
20188+3928	50.7	18	25	H_2O	<3.3 Jy			[11]
20188+3928	50.4	20	15	H_2O	9.5 Jy	4.1		[133]
20188+3928	50.7	18		H_2O	21.2 Jy	-1.14		[16]
20188+3928	50.7	18	25	H_2O	<3 Jy			[16]
IRAS 20275+4001 / GL 2591								
20275+4001	20 27 35.9	40 01 14	2	850 μm	19 Jy	20%	Y	Me
CRL 2591	35.7	10.6		6 cm	74 mJy	1	N	[60]
IR source	35.9	16		5 GHz	2.5 mJy	1	Y	[60]
IR source	36	16		5 GHz	<4 mJy		N	[97]
GL 2591 N1	35.66	10.4	0.1	8.4 GHz	81.9 mJy	8.0	N	[39]
GL 2591 N2	35.60	14.9	0.1	8.4 GHz	3.44 mJy	0.15	Y	[39]
GL 2591 N3	35.98	14.7	0.1	8.4 GHz	0.54 mJy	0.14	N	[39]
GL 2591 N4	35.36	23.3	0.1	8.4 GHz	1.61 mJy	0.20	N	[39]
CRL 2591	35.7	10.6		2 cm	100 mJy	5	N	[60]
IR source	35.9	16		15 GHz	8 mJy	1	Y	[60]
20275+4001				23.7 GHz	0.11 Jy		N	[56]
GL 2591				1.1 mm	3.0 Jy		Y	JCMT
20275+4001			17[b]	450 μm	170 Jy	25%	Y	Me

continued on next page

continued from previous page

Name	R.A.	Dec	±	ν/λ	flux	±	SED	Ref
AFCRL	34	54	63[b]	350 μm	250 Jy	80	Y	[134]
AFGL 2591	35.8	14		160 μm	3400 Jy	20%	Y	[135]
AFGL 2591	35.8	14		110 μm	5500 Jy	20%	Y	[135]
20275+4001	35.2	09	30,9,62	100 μm	5689 Jy	15%	Y	IRAS
AFGL 2591	35.8	14		95 μm	5800 Jy	20%	Y	[135]
AFGL 2591	35.8	14		60 μm	4600 Jy	20%	Y	[135]
20275+4001	35.2	09	30,9,62	60 μm	5314 Jy	8%	Y	IRAS
20275+4001	35.2	09	30,9,62	25 μm	1112 Jy	6%	Y	IRAS
AFGL 2591	35.8	14		23.0 μm	920 Jy	10%	Y	[135]
AFGL 2591	35.8	14		19.5 μm	630 Jy	10%	Y	[135]
AFGL 2591	35.8	14		12.6 μm	680 Jy	10%	Y	[135]
20275+4001	35.2	09	30,9,62	12 μm	439 Jy	6%	Y	IRAS
AFGL 2591	35.8	14		11.4 μm	270 Jy	10%	Y	[135]
AFGL 2591	35.8	14		11.0 μm	190 Jy	10%	Y	[135]
AFGL 2591	35.8	14		10.0 μm	330 Jy	10%	Y	[135]
AFGL 2591	35.8	14		8.7 μm	320 Jy	10%	Y	[135]
AFGL 2591	35.8	14		7.9 μm	610 Jy	10%	Y	[135]
AFGL 2591	35.8	14		4.9 μm	230 Jy	5%	Y	[135]
RAFGL 2591	35.9	5.0	10[tb]	4.2 μm	0.5 M		Y	[21, 22]
AFGL 2591	35.8	14		3.6 μm	70 Jy	5%	Y	[135]
AFGL 2591	35.8	14		2.3 μm	2.8 Jy	5%	Y	[135]
20275+4001				POSS				[131]
AFGL 2591				HH jet				[136]
GL2591				^{12}CO 2-1	44 K			[137]
GL2591				CO v=0-1				[138]
20275+4001				NH_3		−5.68		[56]
20275+4001	35.2	08		NH_3 1,1	0.58 K	−6.2		[32]
20275+4001	35.2	08		NH_3 2,2	0.49 K	−6.3		[32]
IR source	35.9	16		Bα	<2.3 fW m^{-2}			[69, 60]
IR source	35.9	16		Bγ	<0.14 fW m^{-2}			[139, 60]
GL 2591				Brγ, H_2				[140]
GL 2591				H_2O				[141]
GL 2591	35.93	15.4	0.2	H_2O	18,21 Jy	-10,-8		[73]
20275+4001	35.2	08		H_2O	57.0 K	−24.8		[32]
AFGL 2591	36.0	16	25	H_2O	35.0 Jy	−8.8		[11]
GL 2591	36.0	16	25	H_2O	35.1 Jy	−8.8		[10]
AFGL 2591			60[b]	H_2O	93.5 Jy	−7.2		[39]
AFGL 2591			60[b]	H_2O	62.7 Jy	−7.6		[39]
AFGL2591-C1	35.63	16.09	0.01	H_2O	0.71 Jy	-6.6		[39]
AFGL2591-C2	35.90	14.31	0.01	H_2O	0.59 Jy	1.2		[39]
AFGL2591-C3	35.95	14.74	0.01	H_2O	22.9 Jy	-21.8		[39]
AFGL2591-C4	35.95	15.12	0.01	H_2O	54.99 Jy	-7.3		[39]

IRAS 21007+4951 / L988-A

21007+4951	21 00 45.1	49 51 17	2	850 μm	1.7 Jy	20%	Y	Me
21007+4951			0.5[b]	8 GHz	<0.3 mJy		Y	Me
21007+4951			30[b]	15 GHz	<0.6 mJy		Y	Me
21007+4951			17[b]	450 μm	10 Jy	25%	Y	Me
21007+4951	44.9	13	9,9,38	100 μm	31.2 Jy	8%	Y	IRAS
21007+4951	44.9	13	9,9,38	60 μm	21.6 Jy	9%	Y	IRAS
21007+4951	44.9	13	9,9,38	25 μm	5.1 Jy	7%	Y	IRAS
21007+4951	44.9	13	9,9,38	12 μm	0.92 Jy	13%	Y	IRAS
WB23				^{12}CO		−84.9		[9]
21007+4951	44.70	15.2	0.1	H_2O	0.07 Jy	−1		Me
L988-a	44.9	13	25	H_2O	25.0 Jy	4		[11]
WB23			40[b]	H_2O	<1.0 Jy			[9]
21007+4951				H_2O	<10 Jy			[15]
21007+4951	44.9	13	25	H_2O	12.5 Jy	3.73		[16]
21007+4951	44.9	13	25	H_2O	27.6 Jy	3.95		[16]
21007+4951	44.9	13	25	H_2O	15.4 Jy	3.51		[16]
21007+4951	44.9	13	25	H_2O	19.2 Jy	3.91		[16]

continued on next page

continued from previous page

Name	R.A.	Dec	±	ν/λ	flux	±	SED	Ref
21007+4951	44.9	13	25	H_2O	<3 Jy			[16]

IRAS 21078+5211

21078+5211	21 07 46.8	52 10 21	2	850 μm	18 Jy	20%	Y	Me
21078+5211			4[b]	6 cm	236 mJy	ext[2]	Y	[1]
21078+5211	46.22	10 44.5		6 cm	40 mJy	1	N	[142]
21078+5211			0.5[b]	8 GHz	<0.3 mJy		N	Me
21078+5211	46.22	10 44.5		2 cm	31 mJy	1	N	[142]
21078+5211			5[b]	15 GHz	118 mJy[2]		N	Me
21078+5211			35[b]	2.7 mm	<130? mJy		Y	[45]
21078+5211			17[b]	450 μm	110 Jy	25%	Y	Me
21078+5211			7[b]	450 μm	113 Jy	30%	Y	Me
21078+5211	50.2	11 29	20,10,44	100 μm	3486 Jy	11%	Y	IRAS
21078+5211	50.2	11 29	20,10,44	60 μm	1453 Jy	6%	Y	IRAS
21078+5211	50.2	11 29	20,10,44	25 μm	86.6 Jy	15%	Y	IRAS
21078+5211	50.2	11 29	20,10,44	12 μm	8.23 Jy	5%	Y	IRAS
21078+5209	50.9	09 37	8,7,147	100 μm	<3486 Jy		Y	IRAS
21078+5209	50.9	09 37	8,7,147	60 μm	<1665 Jy		Y	IRAS
21078+5209	50.9	09 37	8,7,147	25 μm	<14.7 Jy		Y	IRAS
21078+5209	50.9	09 37	8,7,147	12 μm	3.77 Jy	6%	Y	IRAS
21078+5211			40[b]	^{12}CO 1-0	20.0 K	−6.5		[1]
21078+5211				^{12}CO 2-1	21.7 K	−6.1		[45]
21078+5211				^{12}CO 2-1	47.2 K	−5.5		Me
WB43				^{12}CO		−6.8		[9]
21078+5211			40[b]	^{13}CO 1-0	9 K	−6.5		[1]
21078+5211			40[b]	^{13}CO 2-1	11.8 K	−6.5		[45]
21078+5211			40[b]	C^{18}O 1-0	1 K	−6.5		[1]
21078+5211				C^{18}O 2-1	6.3 K	−6.6		Me
21078+5211				CS 5-4	5.6 K	−6.8		Me
21078+5211	50.2	11 29		HCO^+ 1-0	1.7 K	−6.7		[121]
21078+5211				NH_3		−6.5		[142]
21078+5211	46.65	10 22.8	0.1	H_2O	6.53 Jy	−5		Me
	50.2	11 29	25	H_2O	40.57 Jy	−17.71		[15]
WB43			40[b]	H_2O	3.7 Jy	−21.4		[9]
21078+5211	50.2	11 29	25	H_2O	39.1 Jy	−17.6		[16]
21078+5211	50.2	11 29	25	H_2O	<4.5 Jy			[16]
21078+5211	50.2	11 29	90[b]	H_2O	59 Jy	−4.0		[142]

HH 32-35 [1]

HH32-35[1]	21 41 51.5	65 49 37	2	800 μm	5.2 Jy	20%	Y	Me
HH 33-35			1	4.9 GHz	<3 mJy		Y	[46]
^{13}CO peak	57.2	50 02		1000 μm	1.5 Jy	1	Y	[143]
HH32-35[1]			17[b]	450 μm	30 Jy	25%	Y	Me
^{13}CO peak	57.2	50 02	20	160 μm	78 Jy	24	Y	[143]
^{13}CO peak	57.2	50 02	20	110 μm	58 Jy	28%	Y	[143]
	57.2	50 32	20	110 μm	22 Jy	9	N	[143]
	42 01.2	50 02	20	110 μm	17 Jy	8	N	[143]
	53.2	50 02	20	80 μm	-8 Jy	15	N	[143]
NGC 7129#6	50.4	50 48	30[b]	L	>8.5 M		N	[144]
NGC 7129#6	50.4	50 48	30[b]	K	11.32 M		N	[144]
NGC7129				CO				[145]
^{13}CO peak	57.2	50 02	20	^{13}CO	9 K	−11		[143]
^{13}CO peak	57.2	50 02	20	^{12}CO	14 K	−11		[143]
				CO		8		[46]
GGD 32-35	55	51 25	2′	1612 MHz	<0.07 K	OH		[46]
GGD 32-35	55	51 25	2′	1665 MHz	<0.07 K	OH		[46]
GGD 32-35	55	51 25	2′	1667 MHz	<0.07 K	OH		[46]
GGD 32-35	55	51 25	2′	1720 MHz	<0.08 K	OH		[46]
NGC 7129(1)	52.0	49 40	10	H_2O	12,5 Jy	28,38		[146]
HH 32-35[1]	52.0	49 40	10	H_2O	65 Jy	−9.0		[46]
Bs40[3]	52.0	49 40	10	H_2O	58.2 Jy	−6.0		[147]

continued on next page

continued from previous page

Name	R.A.	Dec	±	ν/λ	flux	±	SED	Ref
IRAS 21418+6552 / LkHα234								
21418+6552	21 41 57.8	65 53 08	2	850 μm	3.4 Jy	20%	Y	Me
HH 33-35			1	4.9 GHz	<3 mJy		N	[46]
LkHα234	57.38	53 08.1	0.1	8.4 GHz	2.1 mJy		Y	[39]
LkHα234				GHz				[148]
CO peak	58	52 50	20	1.0 mm	3.2 Jy	2.2	Y	[143]
LkHα234				1.1 mm	1.2 Jy		Y	JCMT
21418+6552			2	800 μm	4.2 Jy	20%	Y	Me
21418+6552			17[b]	450 μm	60 Jy	25%	Y	Me
CO peak	58	52 50	20	175 μm	410 Jy	110	Y	[143]
21418+6552	53.2	52 42	10,9,40	100 μm	1215 Jy	8%	Y	IRAS
FIR peak	57.8	53 04	6	100 μm	520 Jy	25%	N	[143]
FIR peak	57.8	53 04	6	80 μm	650 Jy	25%	N	[143]
21418+6552	53.2	52 42	10,9,40	60 μm	688 Jy	11%	Y	IRAS
FIR peak	57.8	53 04	6	53 μm	390 Jy	25%	N	[143]
FIR peak	57.8	53 04	6	40 μm	200 Jy	74	N	[143]
21418+6552	53.2	52 42	10,9,40	25 μm	79.0 Jy	6%	Y	IRAS
LkHα234	57.5	53 03	4[b]	20 μm	11.4 Jy	2.0	N	[113]
LkHα234	57.5	53 03	8[b]	20 μm	21.0 Jy	4.0	N	[113]
LkHα234	57.5	53 03		20 μm	2.5 Jy	1.0	N	[143]
21418+6552	53.2	52 42	10,9,40	12 μm	14.7 Jy	87%	Y	IRAS
LkHα234	57.5	53 03		10.4 μm	2.3 Jy	25%	N	[143]
LkHα234	57.5	53 03	4[b]	10 μm	3.7 Jy	0.4	N	[113]
LkHα234	57.5	53 03	8[b]	10 μm	4.8 Jy	0.5	N	[113]
LkHα234	57.5	53 03		10 μm	2.2 Jy	25%	N	[143]
LkHα234	57.5	53 03		M	4.7 M		Y	[149]
NGC 7129#12	57.5	53 07	30[b]	L	5.31 M		Y	[144]
LkHα234	57.5	53 03	3	L	5.86 M	0.07	N	[113]
NGC 7129#12	57.5	53 07	30[b]	K	6.84 M		Y	[144]
LkHα234	57.5	53 03	3	K	7.18 M	0.07	N	[113]
LkHα234	57.5	53 03		K	6.8 M		N	[149]
IRS 1				K	7.72 M		N	[150]
LkHα234	57.1	53 09		2.12 μm	25 ??		N	[151]
NGC 7129#12	57.5	53 07	30[b]	H	8.11 M		Y	[144]
LkHα234	57.5	53 03	3	H	8.22 M	0.07	N	[113]
LkHα234	57.5	53 03		H	8.1 M		N	[149]
IRS 1				H	8.75 M		N	[150]
NGC 7129#12	57.5	53 07	30[b]	J	9.41 M		Y	[144]
LkHα234	57.5	53 03	3	J	9.50 M	0.07	N	[113]
LkHα234	57.5	53 03		J	9.3 M		N	[149]
Bs40				optical				[152]
LkHα234				opt. jet				[153]
NGC7129				CO				[145]
BFS 11	47	53		CO	21 K	−10.1		[154]
BFS 11				^{12}CO 1-0		−10		[155]
WB114				^{12}CO		−10.3		[9]
FIR peak	57.5	53 03		^{12}CO	15 K	−11		[143]
FIR peak	57.5	53 03		^{13}CO	7 K	−11		[143]
LkHα234				^{12}CO 3-2	22 K	−11		[156]
LkHα234				^{13}CO 3-2	14 K	−10		[156]
HH 32-35	58.3	53 10	88[b]	NH_3 1,1	0.17 K	−10		[46]
GGD 32-35	55	51 25	2′	1612 MHz	<0.07 K	OH		[46]
GGD 32-35	55	51 25	2′	1665 MHz	<0.07 K	OH		[46]
GGD 32-35	55	51 25	2′	1667 MHz	<0.07 K	OH		[46]
GGD 32-35	55	51 25	2′	1720 MHz	<0.08 K	OH		[46]
LkHα234			2′[b]	CH_3OH	<0.33 Jy			[8]
BFS 11-A	48.8	52 02	5	H_2O	4.98 Jy	−8		[155]
BFS 11-A	48.8	52 02	5	H_2O	<0.36 Jy			[155]
BFS 11-A	48.7	52 02	25	H_2O	<7.4 Jy			[10]
Bs40[2]	55	52 10	25	H_2O	10 Jy	−13.7		[147]

continued on next page

continued from previous page

Name	R.A.	Dec	±	ν/λ	flux	±	SED	Ref
Bs40[2]	55	52 10	25	H_2O	<4.1 Jy			[147]
Bs40[2]	54.9	52 10	25	H_2O	38.5 Jy	−31.2		[10]
NGC 7129(2)	58.3	53 10	10	H_2O	4,25 Jy	21,34		[146]
HH32-35[2]	58.3	53 10	20	H_2O	7 Jy	−15,−10		[46]
Bs40[1]	58.3	53 10	10	H_2O	43.1 Jy	−8.3		[147]
Bs40[1]	58.3	53 10	10	H_2O	14.1 Jy	−16.9		[147]
BFS 11-B	57.6	53 17	5	H_2O	39.3 Jy	−19		[155]
BFS 11-B	57.6	53 17	5	H_2O	3.21 Jy	−13		[155]
BFS 11-B	57.0	53 10	25	H_2O	12.5 Jy	−14.9		[10]
LkHα234				H_2O	3,2 Jy	−10, 0		[157]
WB114			40[b]	H_2O	13 Jy	−16.6		[9]
LkHα234	57.03	53 10.8	0.2	H_2O	3.11 Jy	−15,-7		[73, 158]
LkHα234	57.22	53 08.6	0.2	H_2O	6 Jy	−19		[73, 158]
LkHα234	53.2	52 42	25	H_2O	231.8 Jy	−20.7		[11]
LkHα234			60[b]	H_2O	31.8 Jy	-9.6		[39]
LkHα234-C1	57.22	53 08.85	0.01	H_2O	23.7 Jy	-9.6		[39]
LkHα234-C2	57.28	53 01.39	0.01	H_2O	0.59 Jy	1.5		[39]
LkHα234-C3	57.37	53 08.24	0.01	H_2O	8.34 Jy	-7		[39]
LkHα234			60[b]	H_2O	50.0 Jy	-6.9		[39]
IRAS 21432+4719 / HHL 73								
21432+4719	21 43 15.2	47 18 58	2	800 μm	<1.1 Jy	20%	Y	Me
21432+4719			0.5[b]	8 GHz	<0.3 mJy		Y	Me
21432+4719			30[b]	15 GHz	<0.6 mJy		Y	Me
21432+4719	17.3	30	24,10,53	100 μm	23 Jy	17%	Y	IRAS
21432+4719	17.3	30	24,10,53	60 μm	12 Jy	11%	Y	IRAS
21432+4719	17.3	30	24,10,53	25 μm	1.4 Jy	9%	Y	IRAS
21432+4719	17.3	30	24,10,53	12 μm	<0.25 Jy	%	Y	IRAS
WB121				^{12}CO		4.8		[9]
21432+4719				^{12}CO 2-1	<1 K	3		Me
HHL 73	13.6	19 45	1.″4[b]	NH_3 1,1	0.48 K	3.87		[42]
HHL 73	13.6	19 45	1.″4[b]	NH_3 2,2	<0.12 K	3.87		[42]
21432+4719			0.5[b]	H_2O	<0.05 Jy			Me
HHL-73	14.0	19 15	1.″5[b]	H_2O	16 Jy	−2		[33]
WB121				H_2O	<0.6 Jy			[9]
HHL-73	14.0	15	25	H_2O	<7.2 Jy			[10]
IRAS 22142+5206								
22142+5206	22 14 14.4	52 06 37	2	850 μm	<1.2 Jy	20%	Y	Me
22142+5206	14.7	26	10,9,14	100 μm	138 Jy	32%	Y	IRAS
22142+5206	14.7	26	10,9,14	60 μm	171 Jy	7%	Y	IRAS
22142+5206	14.7	26	10,9,14	25 μm	92.4 Jy	3%	Y	IRAS
22142+5206	14.7	26	10,9,14	12 μm	20.8 Jy	4%	Y	IRAS
22142+5206	14.7	36	8	10 μm	1.05 M		Y	[47]
22142+5206	14.7	36	8	4.8 μm	5.09 M		Y	[47]
22142+5206	14.7	36	8	3.5 μm	7.73 M		Y	[47]
22142+5206	14.7	36	8	2.2 μm	10.60 M		Y	[47]
22142+5206	14.7	36	8	1.65 μm	13.15 M		Y	[47]
22142+5206	14.7	36	8	1.25 μm	15.24 M		Y	[47]
22142+5206			2.″2[b]	^{12}CO 2-1	3.0 K	−37.4		[9]
22142+5206				C^{18}O 2-1	4.7 K	−37.6		Me
22142+5206	14.5	33	20[b]	CS 7-6	<0.8 K			[7]
22142+5206			7.″8[b]	OH LCP	0.14 Jy	−32.0		[9]
22142+5206	16.1	32	7.″8[b]	OH RCP	0.28 Jy	−33.3		[9]
22142+5206			2.″5[b]	CH_3OH	<10 Jy			[9]
22142+5206	14.5	33	8	H_2O	72.9 Jy	−46.3		[9]
22142+5206			40[b]	H_2O	69.6 Jy	−35.5		[9]
22142+5206			40[b]	H_2O	24.8 Jy	−15.0		[9]
22142+5206			40[b]	H_2O	18.1 Jy	−36.9		[9]
22142+5206			40[b]	H_2O	24.3 Jy	−36.8		[9]
22142+5206	14.5	32.9	25	H_2O	76 Jy	−20.5		[10]

continued on next page

continued from previous page

Name	R.A.	Dec	±	ν/λ	flux	±	SED	Ref
IRAS 22198+6336 / L1204-A								
22198+6336	22 19 50.0	63 36 26	2	850 μm	5.2 Jy	20%	Y	Me
22198+6336			35[b]	6 cm	<0.8 mJy		N	[45]
22198+6336			3[b]	6 cm	<0.6 mJy		Y	[2]
22198+6336			35[b]	2 cm	<1.0 mJy		N	[45]
L1204-G			0.1	8.4 GHz	<0.1 mJy		Y	[39]
22198+6336			30[b]	15 GHz	<0.6 mJy		Y	Me
22198+6336			35[b]	2.7 mm	82 mJy	24	Y	[45]
22198+6336			7[b]	450 μm	35 Jy	30%	Y	Me
22198+6336	50.7	33	13,9,29	100 μm	400 Jy	24%	Y	IRAS
22198+6336	50.7	33	13,9,29	60 μm	189 Jy	16%	Y	IRAS
22198+6336	50.7	33	13,9,29	25 μm	25.6 Jy	22%	Y	IRAS
22198+6336	50.7	33	13,9,29	12 μm	<0.27 Jy		Y	IRAS
22198+6336				^{12}CO		−10.5		[9]
22198+6336				^{12}CO 2-1	14.5 K	−10.9		[45]
22198+6336				^{12}CO 2-1	18.4 K	−10.5		Me
22198+6336				^{13}CO 2-1	7.5 K	−10.9		[45]
22198+6336				C^{18}O 2-1	5.9 K	−10.5		Me
L1204 Core G	45	37 45	4[tb]	CS 1-0	1.2 K	-10.8		[159]
22198+6336				CS 5-4	1.2 K	−10.5		Me
L1204 Core G	45	37 03	40	NH_3 1,1	1.6 K	-11.08		[159]
L1204 Core G	45	37 03	40	NH_3 2,2	0.3 K	-11.08		[159]
22198+6336	50.7	33	2[tb]	CH_3OH	<0.14 K			[66, 37]
	50.7	36	25	H_2O	4.03 Jy	−21.14		[15]
22198+6336	50.7	36	25	H_2O	37.9 Jy	−21.2		[15]
WB 176			40[b]	H_2O	262.7 Jy	−20.7		[9]
WB 176			40[b]	H_2O	255.9 Jy	−22.2		[9]
L1204-A	45.6	04	15	H_2O	96.0 Jy	−22.0		[133]
L1204-A			25	H_2O				[11]
22198+6336	50.7	36	25	H_2O	36.9 Jy	−21.31		[16]
22198+6336	50.7	36	25	H_2O	71.6 Jy	−20.91		[16]
22198+6336	50.7	36	25	H_2O	37.7 Jy	−20.59		[16]
22198+6336	50.7	36	25	H_2O	60.5 Jy	−21.14		[16]
22198+6336	50.7	36	25	H_2O	237.8 Jy	−22.27		[16]
22198+6336	50.7	36	25	H_2O	255.3 Jy	−22.18		[16]
L1204-G			60[b]	H_2O	65 Jy	-20		[39]
L1204-G-C1	49.81	28.98	0.1	H_2O	0.3 Jy	-11.6		[39]
L1204-G-C2	49.82	28.75	0.1	H_2O	35.1 Jy	-19.5		[39]
L1204-G-C3	49.83	28.64	0.1	H_2O	7.2 Jy	-16.2		[39]
L1204-G-C4	49.86	28.84	0.1	H_2O	3.5 Jy	-1.7		[39]
L1204-G			60[b]	H_2O	12.5 Jy	-19.3		[39]
IRAS 22475+5939 / S146								
22475+5939 FIR1	22 47 31.8	59 39 50	2	800 μm	2.0 Jy	20%	Y	Me
22475+5939 FIR2	22 47 29.8	59 38 59	2	800 μm	6.5 Jy	20%	Y	Me
				2.8 cm	0.7 Jy		Y	[160]
22475+5939 FIR2			7[b]	450 μm	16 Jy	30%	Y	Me
22475+5939	30.9	39 03	12,9,23	100 μm	1066 Jy	10%	Y	IRAS
22475+5939	30.9	39 03	12,9,23	60 μm	832 Jy	6%	Y	IRAS
22475+5939	30.9	39 03	12,9,23	25 μm	151 Jy	4%	Y	IRAS
RAFGL 2963	23.0	40 30	10[tb]	20 μm	−3.2 M		N	[21]
22475+5939	30.9	39 03	12,9,23	12 μm	25.0 Jy	4%	Y	IRAS
RAFGL 2963	23.0	40 30	10[tb]	11 μm	−0.9 M		N	[21]
S146 IRS1	14.1	38 55	15[b]	4.8 μm	7.4 M		N	[161]
S146 IRS1	14.1	38 55	15[b]	3.4 μm	8.8 M		N	[161]
S146 IRS1	14.1	38 55	15[b]	2.2 μm	10.17 M		N	[161]
S146 IRS1	14.1	38 55	15[b]	1.65 μm	11.36 M		N	[161]
				CO		−49.5		[160]
WB 212				^{12}CO		−49.4		[9]
22475+5939			21	^{12}CO 1-0	42.8 K	−48.4		[54]

continued on next page

continued from previous page

Name	R.A.	Dec	±	ν/λ	flux	±	SED	Ref
22475+5939			21	^{13}CO 1-0	9.9 K	−50.5		[54]
22475+5939 FIR2			21	C^{18}O 2-1	2.4 K	−51		Me
22475+5939				NH_3	<			[56]
WB 212			40[b]	H_2O	<0.2 Jy			[9]
22475+5939	30.5	39 00	20	H_2O	14 Jy	−54.4		[72]
22475+5939	30.5	39 00	20	H_2O	<2 Jy			[72]
S146	31.0	39 43	25	H_2O	14.1 Jy	−54.4		[10]
S146				H_2O	0.3 K	−61,−50		[160]
S146	31.0	39 40	10	H_2O	7 Jy	−59		[38]
IRAS 22506+5944								
22506+5944	22 50 39.2	59 44 47	2	850 μm	8.1 Jy	20%	Y	Me
22506+5944	38.85	44 42.3	0.5[b]	8 GHz	1.7 mJy		Y	Me
22506+5944			3[b]	15 GHz	<1.0 mJy		Y	Me
22506+5944				23.7 GHz	<0.03 Jy		Y	[56]
22506+5944	38.7	44 58	10,9,39	100 μm	294 Jy	13%	Y	IRAS
22506+5944	38.7	44 58	10,9,39	60 μm	187 Jy	14%	Y	IRAS
22506+5944	38.7	44 58	10,9,39	25 μm	34.7 Jy	4%	Y	IRAS
22506+5944	38.7	44 58	10,9,39	12 μm	6.39 Jy	4%	Y	IRAS
WB 214				^{12}CO		−51.0		[9]
22506+5944			21	^{12}CO 1-0	35.3 K	−50.4		[54]
22506+5944	38.7	44 58	4.′4[b]	^{12}CO 1-0	10.8 K	−52		[6]
22506+5944			21	^{13}CO 1-0	13.6 K	−51.2		[54]
22506+5944	38.7	44 58	4.′4[b]	^{13}CO 1-0	2.0 K	−52		[6]
22506+5944				NH_3		−51.4		[56]
22506+5944	38.66	52.6	0.1	H_2O	21.6 Jy	−53		Me
22506+5944	38.36	54.5	0.1	H_2O	2.16 Jy	−53		Me
22506+5944	38.74	53.3	0.1	H_2O	5.26 Jy	−53		Me
	38.7	50	25	H_2O	294.35 Jy	−47.87		[15]
	38.7	50	5	H_2O	105.8 Jy	−48.2		[57]
WB 214			40[b]	H_2O	155.5 Jy	−47.8		[9]
WB 214			40[b]	H_2O	390.6 Jy	−48.1		[9]
			25	H_2O		−47.9		[15]
G10860+0049	37.0	44 50	25	H_2O	357.0 Jy	−48.3		[10]
IRAS 22528+5936								
22528+5936	22 52 48.6	59 36 58	2	850 μm	<3.1 Jy	20%	Y	Me
22528+5936			0.5[b]	8 GHz	<0.3 mJy		Y	Me
22528+5936				23.7 GHz	<0.03 Jy		Y	[56]
22528+5936	48.7	48	13,9,21	100 μm	99.2 Jy	18%	Y	IRAS
22528+5936	48.7	48	13,9,21	60 μm	66.6 Jy	16%	Y	IRAS
22528+5936	48.7	48	13,9,21	25 μm	13.4 Jy	5%	Y	IRAS
22528+5936	48.7	48	13,9,21	12 μm	3.37 Jy	5%	Y	IRAS
WB 219				^{12}CO		−53.0		[9]
22528+5936			21	^{12}CO 1-0	30.8 K	−53.1		[54]
22528+5936	48.7	36 48	4.′4[b]	^{12}CO 1-0	10.1 K	−52		[6]
22528+5936			21	^{13}CO 1-0	8.0 K	−53.3		[54]
22528+5936	48.7	36 48	4.′4[b]	^{13}CO 1-0	2.8 K	−52		[6]
22528+5936				NH_3		−53.2		[56]
22528+5936			0.5[b]	H_2O	<0.05 Jy			Me
	49.6	40	5	H_2O	2.4 Jy	−47.0		[57]
WB 219			40[b]	H_2O	0.5 Jy	−51.3		[9]
G10879+0025	49.6	36 40	25	H_2O	<6.9 Jy			[10]
IRAS 22539+5758 / S147								
22539+5758 FIR1	22 54 00.7	57 59 06	2	850 μm	5.7 Jy	20%	N	Me
22539+5758 FIR2	22 53 56.4	57 58 36	2	850 μm	6.8 Jy	20%	Y	Me
22539+5758	53 55.99	58 41.1	0.5[b]	8 GHz	2.6 mJy		Y	Me
22539+5758				23.7 GHz	<0.03 Jy		Y	[56]
22539+5758	56.3	58 44	10,9,17	100 μm	399 Jy	12%	Y	IRAS
22539+5758	56.3	58 44	10,9,17	60 μm	319 Jy	9%	Y	IRAS

continued on next page

continued from previous page

Name	R.A.	Dec	±	ν/λ	flux	±	SED	Ref
22539+5758	56.3	58 44	10,9,17	25 μm	61.1 Jy	6%	Y	IRAS
22539+5758	56.3	58 44	10,9,17	12 μm	6.81 Jy	5%	Y	IRAS
22539+5758	55.9	58 41	8[b]	10 μm	4.15 M		Y	[47]
22539+5758	55.9	58 41	8[b]	4.8 μm	7.20 M		Y	[47]
22539+5758	55.9	58 41	8[b]	3.5 μm	8.11 M		Y	[47]
22539+5758	55.9	58 41	8[b]	2.2 μm	9.95 M		Y	[47]
22539+5758	55.9	58 41	8[b]	1.65 μm	11.14 M		Y	[47]
22539+5758	55.9	58 41	8[b]	1.25 μm	12.52 M		Y	[47]
WB 221				^{12}CO		−54.8		[9]
22539+5758			21	^{12}CO 1-0	24.6 K	−55.4		[54]
22539+5758	56.3	58 44	4.′4[b]	^{12}CO 1-0	10.1 K	−55		[6]
22539+5758	56.3	58 44	1.′4[b]	^{12}CO 2-1	8.6 K	−55		[6]
22539+5758			21	^{13}CO 1-0	19.3 K	−54.42		[54]
22539+5758	56.3	58 44	4.′4[b]	^{13}CO 1-0	2.8 K	−55		[6]
22539+5758				NH_3		−53.8		[56]
22539+5758			0.5[b]	H_2O	<0.05 Jy			Me
	56.0	58 48	5	H_2O	1.6 Jy	−36.4		[57]
WB 221			40[b]	H_2O	<0.2 Jy			[9]
G10822-0129	56.0	58 48	25	H_2O	<14.8 Jy			[10]

IRAS 22566+5830 / S152

22566+5830 FIR1	22 56 39.8	58 31 47	2	850 μm	7.2 Jy	20%	Y	Me
22566+5830 FIR2	22 56 38.4	58 31 04	2	850 μm	6.8 Jy	20%	N	Me
S152	36.3	30 50		1.4 GHz	1.30 Jy		Y	[162]
S152	36.4	30 46		4.89 GHz	1.38 Jy[2]		N	[162]
22566+5830	37.0	30 52	13,9,23	100 μm	2228 Jy	9%	Y	IRAS
22566+5830	37.0	30 52	13,9,23	60 μm	1184 Jy	10%	Y	IRAS
22566+5830	37.0	30 52	13,9,23	25 μm	111 Jy	4%	Y	IRAS
22566+5830	37.0	30 52	13,9,23	12 μm	23.8 Jy	9%	Y	IRAS
S152	34	31	116[b]	3.5 μm	4.77 M		Y	[163]
S152	34	31	85[b]	3.5 μm	4.92 M		N	[163]
S152	34	31	55[b]	3.5 μm	5.60 M		N	[163]
S152	34	31	40[b]	3.5 μm	6.07 M		N	[163]
S152	34	31	27[b]	3.5 μm	7.45 M		N	[163]
S152	34	31	22[b]	3.5 μm	7.70 M		N	[163]
S152	34	31	15[b]	3.5 μm	8.27 M		N	[163]
S152	34	31	116[b]	2.2 μm	7.22 M		Y	[163]
S152	34	31	85[b]	2.2 μm	7.32 M		N	[163]
S152	34	31	57[b]	2.2 μm	7.57 M		N	[163]
S152	34	31	55[b]	2.2 μm	7.60 M		N	[163]
S152	34	31	40[b]	2.2 μm	7.92 M		N	[163]
S152	34	31	27[b]	2.2 μm	8.38 M		N	[163]
S152	34	31	22[b]	2.2 μm	8.57 M		N	[163]
S152	34	31	15[b]	2.2 μm	9.02 M		N	[163]
S152	34	31	116[b]	1.65 μm	8.17 M		Y	[163]
S152	34	31	85[b]	1.65 μm	8.10 M		N	[163]
S152	34	31	55[b]	1.65 μm	8.40 M		N	[163]
S152	34	31	40[b]	1.65 μm	8.60 M		N	[163]
S152	34	31	27[b]	1.65 μm	9.00 M		N	[163]
S152	34	31	22[b]	1.65 μm	9.16 M		N	[163]
S152	34	31	15[b]	1.65 μm	9.36 M		N	[163]
WB 228				^{12}CO		−50.5		[9]
22566+5830			21	^{12}CO 1-0	26.5 K	−49.8		[54]
22566+5830			21	^{13}CO 1-0	11.3 K	−50.9		[54]
22566+5830				NH_3		−50.3		[56]
	38.3	31 40	5	H_2O	34 Jy	−43		[57]
WB 228			40[b]	H_2O	21.5 Jy	−58.7		[9]
WB 228			40[b]	H_2O	25.8 Jy	−58.6?		[9]
WB 228			40[b]	H_2O	10.4 Jy	−47.8		[9]
WB 228			40[b]	H_2O	45.2 Jy	−56.5		[9]

continued on next page

continued from previous page

Name	R.A.	Dec	±	ν/λ	flux	±	SED	Ref
22566+5830	37.6	30 52	20	H_2O	47 Jy	−56.4		[72]
22566+5830	37.6	30 52	20	H_2O	9 Jy	−55.9		[72]
G10877-0094	38.3	31 40	25	H_2O	36.8 Jy	−46.6		[10]
IRAS 23138+5945 / S157								
23138+5945 FIR1	23 13 51.7	59 45 47	2	850 μm	3.5 Jy	20%	N	Me
23138+5945 FIR2	23 13 53.5	59 45 24	2	850 μm	5.9 Jy	20%	Y	Me
23138+5945	53.5	37	13,9,29	100 μm	2164 Jy	14%	Y	IRAS
23138+5945	53.5	37	13,9,29	60 μm	1759 Jy	7%	Y	IRAS
23138+5945	53.5	37	13,9,29	25 μm	233 Jy	5%	Y	IRAS
RAFGL 3057	53	45 42	10″[b]	20 μm	−3.3 M		N	[21]
23138+5945	53.5	37	13,9,29	12 μm	28.7 Jy	9%	Y	IRAS
RAFGL 3057	53	45 42	10″[b]	11 μm	−0.3 M		N	[21]
RAFGL 3057	53	45 42	10″[b]	4.2 μm	2.8 M		N	[21]
S 157A	52	46	84[b]	3.45 μm	0.85 Jy		Y	[164]
S 157A	52	46	84[b]	2.22 μm	0.46 Jy		Y	[164]
S 157A	52	46	36[b]	2.22 μm	0.170 Jy		Y	[164]
S 157A	52	46	18[b]	2.22 μm	0.090 Jy		Y	[164]
S 157A	52	46	12[b]	2.22 μm	0.061 Jy		Y	[164]
S 157A	52	46	84[b]	1.67 μm	0.37 Jy		Y	[164]
S 157A	52	46	84[b]	1.25 μm	0.37 Jy		Y	[164]
WB 263				^{12}CO		−44.8		[9]
23138+5945			21	^{12}CO 1-0	63.5 K	−44.6		[54]
23138+5945			21	^{13}CO 1-0	17.9 K	−44.66		[54]
S157	53.1	45 18.0	20[b]	CS 7-6	0.8 K	−43.7		[7]
23138+5945				NH_3		−44.2		[56]
WB 263			40[b]	H_2O	1.0 Jy	−45.7		[9]
WB 263			40[b]	H_2O	<0.6 Jy			[9]
S157	53.0	45 18	25	H_2O	8.4 Jy	−44.0		[10]
S157	53.1	45 18	10	H_2O	30 Jy	−46.0		[71]
IRAS 23314+6033								
23314+6033	23 31 23.2	60 33 52	2	850 μm	3.9 Jy	20%	Y	Me
23314+6033			0.5[b]	8 GHz	<0.3 mJy		Y	Me
23314+6033			19[b]	15 GHz	19 mJy[2]		N	Me
23314+6033			5[b]	15 GHz	<1 mJy		Y	Me
23314+6033			7[b]	450 μm	15 Jy	30%	Y	Me
23314+6033	24.8	55	13,8,27	100 μm	716 Jy	16%	Y	IRAS
23314+6033	24.8	55	13,8,27	60 μm	401 Jy	15%	Y	IRAS
23314+6033	24.8	55	13,8,27	25 μm	40.0 Jy	4%	Y	IRAS
23314+6033	24.8	55	13,8,27	12 μm	10.8 Jy	12%	Y	IRAS
WB 284				^{12}CO		−45.5		[9]
23314+6033				^{12}CO 2-1	37.3 K	−45		Me
23314+6033				$C^{18}O$ 2-1	6.1 K	−45		Me
23314+6033	24.8	55.0	20[b]	CS 7-6	<0.3 K			[7]
23314+6033	22.73	54.2	0.1	H_2O	0.14 Jy	−54		Me
WB 284			40[b]	H_2O	0.4 Jy	−49.4		[9]
WB 284			40[b]	H_2O	<0.4 Jy			[9]
			25	H_2O	<10 Jy			[15]
23314+6033	24.8	55	25	H_2O	<14.6 Jy			[10]

Notes

[1] taken from figure not table

[2] Extended emission

References

[1] McCutcheon W. H., Dewdney P. E., Purton C. R., Sato T., 1991, AJ, 101, 1435

[2] Hughes V. A., MacLeod G. C., 1994, ApJ, 427, 857

[3] Anglada G., Rodríguez L. F., Girart J. M., Estella R., Torrelles J. M., 1994, ApJ, 420, L91

[4] Persi P., Ferrari-Toniolo M., Busso M., Robberto M., Scaltriti F., Silvestro G., 1988, AJ, 95, 1167

[5] Weintraub D. A., Kastner J., 1993, ApJ, 411, 767

[6] Casoli F., Dupraz C., Gerin M., Combes F., Boulanger F., 1986, A&A, 169, 281

[7] Plume R., Jaffe D. T., Evans II N. J., 1992, ApJS, 78, 505

[8] Kalenskii S. V., Berulis I. I., Val'tts I. E., Dzyura A. M., Slysh V. I., Vasil'kov V. I., 1994, Astron. Zh., 71, 51

[9] Wouterloot J. G. A., Brand J., Fiegle K., 1993, A&AS, 98, 589

[10] Comoretto G., et al., 1990, A&AS, 84, 179

[11] Felli M., Palagi F., Tofani G., 1992, A&A, 255, 293

[12] Henning T., Cesaroni R., Walmsley M., Pfau W., 1992, A&AS, 93, 525

[13] Neckel T., Staude H. J., 1984, A&A, 131, 200

[14] White G. J., Gee G., 1986, A&A, 156, 301

[15] Palla F., Brand J., Cesaroni R., Comoretto G., Felli M., 1991, A&A, 246, 249

[16] Brand J., et al., 1994, A&AS, 103, 541

[17] Wynn-Williams C. G., Becklin E. E., Beichman C. A., Capps R., Shakeshaft J. R., 1981, ApJ, 246, 801

[18] Torrelles J. M., Gomez J. F., Anglada G., Estalella R., Mauersberger R., Eiroa C., 1992, ApJ, 392, 616

[19] Henning T., Pfau W., Altenhoff W. J., 1990, A&A, 227, 542

[20] Price S. D., Murdock T. L., Shivanandan K., 1983, Far infrared sky survey experiment. final report. AFGL-TR-83-0055. Air Force Geophysics Laboratory, Hanscom AFB, Ma.

[21] Price S. D., Murdock T. L., 1983, The revised AFGL infrared sky survey catalog. AFGL-TR-83-0161. Air Force Geophysics Laboratory, Hanscom AFB, Ma.

[22] Ney E. P., Merrill K. M., 1980, Study of sources in AFGL rocket infrared study. AFGL-TR-80-0050, Air Force Geophysics Laboratory, Hanscom AFB, Ma.

[23] Lebofsky M. J., Sargent D. G., Kleinmann S. G., Rieke G. H., 1978, ApJ, 219, 487

[24] Kleinmann S. G., Sargent D. G., Gillett F. C., Grasdalen G. L., Joyce R. R., 1977, ApJ, 215, L79

[25] Cohen M., Allamandola L., Tielens A. G. G. M., , Bregman J., Simpson J. P., Witteborn F. C., Wooden D., Rank D., 1986, ApJ, 302, 737

[26] Suto H., Mizutani K., Maihara T., 1989, MNRAS, 239, 139

[27] Jourdain De Muizon M., D'Hendecourt L. B., Geballe T. R., 1990, A&A, 235, 367

[28] Jourdain De Muizon M., D'Hendecourt L. B., Geballe T. R., 1990, A&A, 227, 526

[29] Jourdain De Muizon M., Geballe T. R., D'Hendecourt L. B., Baas F., 1986, ApJ, 306, L105

[30] McGregor P. J., Persson S. E., Cohen J. G., 1984, ApJ, 286, 609

[31] Schneps M. H., Martin R. N., Ho P. T. P., Barrett A. H., 1978, ApJ, 221, 124

[32] Churchwell E., Walmsley C. M., Cesaroni R., 1990, A&AS, 83, 119

[33] Gyulbudaghian A. L., Rodríguez L. F., Mendoza-Torres E., 1987, Rev. Mex. Astron. Astrofís., 15, 53

[34] Snell R. L., Bally J., 1986, ApJ, 303, 683

[35] Jennings R. E., Cameron D. H. M., Cudlip W., Hirst C. J., 1987, MNRAS, 226, 461

[36] Schwartz R. D., Cohen M., Williams P. M., 1987, ApJ, 322, 403

[37] Slysh V. I., et al., 1994, Astron. Zh., 71, 37

[38] Henkel C., Haschick A. D., Güsten R., 1986, A&A, 165, 197

[39] Tofani G., Felli M., Taylor G. B., Hunter T. R., 1995, A&AS, 112, 299

[40] Hunter T. R., Testi L., Taylor G. B., Tofani G., Felli M., Philips T. G., 1995, A&A, 302, 249

[41] Snell R. L., Huang Y., Dickman R. L., Claussen M. J., 1988, ApJ, 325, 853

[42] Verdes-Montenegro L., Torelles J. M., Rodríguez L. F., Anglada G., López R., Estalella R., Cantó J., Ho P. T. P., 1989, ApJ, 346, 193

[43] Gaylard M. J., MacLeod G. C., 1993, MNRAS, 262, 43

[44] Fukui Y., Sugitani K., Takaba H., Iwata T., Mizuno A., Ogawa H., Kawabata K., 1986, ApJ, 311, L85

[45] Wilking B. A., Mundy L. G., Blackwell J. H., Howe J. E., 1989, ApJ, 345, 257

[46] Rodríguez L. F., Moran J. M., Ho P. T. P., Gottlieb E. W., 1980, ApJ, 235, 845

[47] Campbell B., Persson S. E., Matthews K., 1989, AJ, 98, 643

[48] Carballo R., Eiroa C., Mampaso A., 1988, MNRAS, 232, 497

[49] Simon T., Joyce R. R., 1983, ApJ, 265, 748

[50] Saraceno P., Andre P., Ceccarelli C., Griffin M., Molinari S., Russell S., 1994, A&A, in prep

[51] Strom K. M., Newton G., Strom S. E., Seaman R. L., Carrasco L., Cruz-Gonzalez I., Serrano A., Grasdalen G. L., 1989, ApJS, 71, 183

[52] Strom K. M., Margulis M., Strom S. E., 1989, ApJ, 345, L79

[53] Fukui Y., 1989, In Reipurth B. (ed.), ESO workshop on low mass star formation and pre-main sequence objects, p. 95. European Southern Observatory, Garching bei München, Germany, 1989

[54] Wouterloot J. G. A., Henkel C., Walmsley C. M., 1989, A&A, 215, 131

[55] Chen H., Tokunaga T., Fukui Y., 1993, ApJ, 416, 235

[56] Wouterloot J. G. A., Walmsley C. M., Henkel C., 1988, A&A, 203, 367

[57] Wouterloot J. G. A., Walmsley C. M., 1986, A&A, 168, 237

[58] Wilking B. A., Claussen M. J., Myers P. J. B. P. C., Tereby S., Wotten A., 1994, ApJ, 431, L119

[59] Wink J. E., Altenhoff W. J., Mezger P. G., 1982, A&A, 108, 227

[60] Simon M., Righini-Cohen G., Felli M., Fischer J., 1981, ApJ, 245, 552

[61] Chini R., Kreysa E., Mezger P. G., Gemünd H.-P., 1984, A&A, 137, 117

[62] Thronson Jr. H. A., Harper D. A., Keene J., Loewenstein R. F., Moseley S. H., Telesco C. M., 1978, AJ, 83, 492

[63] Beckwith S., Evans II N. J., Becklin E. E., Neugebauer G., 1976, ApJ, 208, 390

[64] Monin J. L., Vauglin I., Audaire L., 1987, A&A, 172, 368

[65] Hodapp K. W., 1987, A&A, 172, 304

[66] Kalenskii S. V., Sobolev A. M., 1994, Pis'ma Astron. Zh., 20, 113

[67] Menten K. M., 1991, ApJ, 380, L75

[68] MacLeod G. C., Gaylard M. J., Kemball A. J., 1993, MNRAS, 262, 343

[69] Simon T., Simon M., Joyce R. R., 1979, ApJ, 230, 127

[70] Thompson R. I., Tokunaga A. T., 1979, ApJ, 229, 153

[71] Genzel R., Downes D., 1977, A&AS, 30, 145

[72] Codella C., Felli M., Natale V., Palagi F., Palla F., 1994, A&A, 291, 261

[73] Rodríguez L. F., Cantó J., 1983, Rev. Mex. Astron. Astrofís., 8, 163

[74] Chini R., Kreysa E., Mezger P. G., Gemünd H.-P., 1986, A&A, 154, L8

[75] Gear W. K., Robson E. I., Griffin M. J., 1988, MNRAS, 231, 55P

[76] Olofsson G., Koornneef J., 1985, A&A, 146, 337

[77] Harvey P. M., Wilking B. A., Joy M., Lester D. F., 1985, ApJ, 288, 725

[78] Reipurth B., Wamsteker W., 1983, A&A, 119, 14

[79] Torrelles J. M., Ho P. T. P., Rodríguez L. F., Cantó J., Verdes-Montenegro L., 1989, ApJ, 346, 756
[80] Cohen M., 1974, MNRAS, 169, 257
[81] Gyulbudaghian A. L., Glushkov Y. I., Denisyuk E. K., 1978, ApJ, 224, L137
[82] Persson S. E., Campbell B., 1987, AJ, 94, 416
[83] Forster J. R., Caswell J. L., 1989, A&A, 213, 339
[84] Wood D. O. S., Churchwell E., 1989, ApJS, 69, 831
[85] Altenhoff W. J., Downes D., Pauls T., Schraml J., 1978, A&AS, 35, 23
[86] Chini R., Krügel E., Wargau W., 1987, A&A, 181, 378
[87] Downes D., Wilson T. L., Bieging J., Wink J., 1980, A&AS, 40, 379
[88] Genzel R., Downes D., 1979, A&A, 72, 234
[89] Jaffe D. T., Hildebrand R. H., Keene J., Harper D. A., Loewenstein R. F., Moran J. M., 1984, ApJ, 281, 225
[90] Stier M. T., Jaffe D. T., Fazio G. G., Roberge W. G., Thum C., Wilson T. L., 1982, ApJS, 48, 127
[91] Jaffe D. T., Stier M. T., Fazio G. G., 1982, ApJ, 252, 601
[92] Braz M. A., Epchtein N., 1987, A&A, 176, 245
[93] Slysh V. I., Kalenskii S. V., Otrupcek I. E. V. R., 1994, MNRAS, 268, 464
[94] Cohen R. J., Baart E., Jonas J., 1988, MNRAS, 231, 205
[95] Cohen R. J., Masheder M. R. W., Walker R. N. F., 1991, MNRAS, 250, 611
[96] Jaffe D. T., Güsten R., Downes D., 1981, ApJ, 250, 621
[97] Wynn-Williams C. G., Beichman C. A., Downes D., 1981, AJ, 86, 565
[98] Bieging J. H., Pankonin V., Smith L. F., 1978, A&A, 64
[99] Cheung L. H., Frogel J. A., Gezari D. Y., Hauser M. G., 1980, ApJ, 240, 74
[100] Stier M. T., et al., 1984, ApJ, 283, 573
[101] Dyck H. M., Simon T., 1977, ApJ, 211, 421
[102] Mitchell G. F., Allen M., Maillard J.-P., 1988, ApJ, 333, L55
[103] Caswell J. L., Vaile R. A., Forster J. R., 1995, MNRAS, 277, 210
[104] Wynn-Williams C. G., Werner M. W., Wilson W. J., 1974, ApJ, 187, 41
[105] Martí J., Rodríguez L. F., Reipurth B., 1993, ApJ, 416, 208
[106] Martí J., Rodríguez L. F., Reipurth B., 1995, ApJ, 449, 184
[107] Yamashita T., Sato S., Nagata T., Suzuki H., Hough J. H., McLean I. S., Garden R., Gatley I., 1987, A&A, 177, 258
[108] Aspin C., et al., 1994, A&A, 292, L9
[109] Hartigan P., Lada C. J., 1985, ApJS, 59, 383
[110] Schutte A. J., van der Walt D. J., Gaylard M. J., MacLeod G. C., 1993, MNRAS, 261, 783
[111] Curiel S., Rodríguez L. F., Moran J. M., Cantó J., 1993, ApJ, 415, 191
[112] Casali M. M., Eiroa C., Duncan W. D., 1993, A&A, 275, 195
[113] Harvey P. M., Wilking B. A., Joy M., 1984, ApJ, 278, 156
[114] Eiroa C., Casali M. M., 1992, A&A, 262, 468
[115] Eiroa C., Casali M. M., 1989, A&A, 223, L17
[116] White G. J., Casali M. M., Eiroa C., 1995, A&A, 298, 594
[117] McMullin J. P., Mundy L. G., Wilking B. A., Hezel T., Blake G. A., 1994, ApJ, 424, 222
[118] Hurt R. L., Barsony M., Wootten A., 1995, In Circumstellar Matter, Royal Observatory, Edinburgh
[119] Torrelles J. M., Gómez J. F., Curiel S., Eiroa C., Rodríguez L. F., Ho P. T. P., 1992, ApJ, p. L59
[120] Matthews H. E., Olnon F. M., Winnberg A., Baud B., 1985, A&A, 149, 227

[121] Richards P. J., Little L. T., Toriseva M., Heaton B. D., 1987, MNRAS, 228, 43
[122] Blair G. N., Dinger A. S. C., Dickinson D. F., 1980, AJ, 85, 161
[123] Evans II N. J., Beckwith S., Brown R. L., Gilmore W., 1979, ApJ, 227, 450
[124] Zeilik II M., Lada C. J., 1978, ApJ, 222, 896
[125] Moorwood A. F. M., Salinari P., 1981, A&A, 94, 299
[126] Pankonin V., Thomasson P., Barsuhn J., 1977, A&A, 54, 335
[127] Turner B. E., Rubin R. H., 1977, ApJ, 170, L113
[128] Caswell J. L., Batchelor R. A., Forster J. R., Wellington K. J., 1983, Aust. J. Phys, 36, 443
[129] Felli M., Harten R., Habing H., Israel F., 1978, A&AS, 32, 423
[130] Palumbo G. G. C., Scappini F., Codella G. P. C., Caselli P., Attolini M. R., 1994, MNRAS, 266, 123
[131] Odenwald S. F., 1989, AJ, 97, 801
[132] Little L. T., Bergman P., Cunningham C. T., Heaton B. D., Knee L. B. G., MacDonald G. H., Richards P. J., Toriseva M., 1988, A&A, 205, 129
[133] Xiang D., Turner B. E., 1992, Chin. Astron. Astrophys., 16, 307
[134] Rieke G. H., Harper D. A., Low F. J., Armstrong K. R., 1973, ApJ, 183, L67
[135] Lada C. J., Thronson, Jr. H. A., Smith H. A., Schwartz P. R., Glaccum W., 1984, ApJ, 286, 302
[136] Poetzel R., Mundt R., Ray T. P., 1992, A&A, 262, 229
[137] Mitchell G. F., Hasegawa T. I., Schella J., 1992, ApJ, 386, 604
[138] Mitchell G. F., Maillard J.-P., Allen M., Beer R., Belcourt K., 1990, ApJ, 363, 554
[139] Thompson R. I., Tokunaga A. T., 1979, ApJ, 231, 736
[140] Tamura M., Yamashita T., 1992, ApJ, 391, 710
[141] White G. J., Little L. T., Parker E. A., Nicholson P. S., Macdonald G. H., Bale F., 1975, MNRAS, 170, 37P
[142] Miralles M. P., Rodríguez L. F., Scalise E., 1994, ApJS, 92, 173
[143] Bechis K. P., Harvey P. M., Campbell M. F., Hoffman W. F., 1978, ApJ, 226, 439
[144] Strom S. E., Vrba F. J., Strom K. M., 1976, AJ, 81, 638
[145] Loren R. B., 1977, ApJ, 218, 716
[146] Cesarsky C. J., Cesarsky D. A., Churchwell E., Lequeux J. A., 1978, ApJ, 68, 33
[147] Sandell G., Olofsson H., 1981, A&A, 99, 80
[148] Skinner S. L., Brown A., Stewart R. T., 1993, ApJS, 87, 217
[149] Lorenzetti D., Saraceno P., Strafella F., 1983, ApJ, 276, 554
[150] Weintraub D. A., Kastner J. H., Mahesh A., 1994, ApJ, 420, L87
[151] Wilking B. A., Schwartz R. D., Mundy L. G., Schultz A. S. B., 1990, AJ, 99, 344
[152] Bernes C., 1977, A&AS, 29, 65
[153] Ray T. P., Poetzel R., Solf J., Mundt R., 1990, ApJ, 357, L45
[154] Blitz L., Fich M., Stark A. A., 1982, ApJS, 49, 183
[155] Wouterloot J. G. A., Brand J., Henkel C., 1988, A&A, 191, 323
[156] Mitchell G. F., Matthews H. E., 1994, ApJ, 423, L55
[157] Schwartz P. R., Buhl D., 1975, ApJ, 201, L27
[158] Rodríguez L. F., Hashick A. D., Torrelles J. M., Myers P. C., 1987, A&A, 186, 319
[159] Tafalla M., Bachiller R., Martin-Pintado J., 1993, ApJ, 403, 175
[160] Blair G. N., Davis J. H., Dickinson D. F., 1978, ApJ, 226, 435
[161] Eiroa C., Neckel T. H., Sanchez Magro C., Selby M. J., 1983, A&A, 95, 206
[162] Fich M., 1993, ApJS, 86, 475
[163] Frogel J. A., Persson S. E., 1972, ApJ, 178, 667
[164] Zeilik II M., 1976, A&A, 46, 319

List of publications

This is the list of my work which has been published during my time at MRAO.

- *Embedded FIR sources in the vicinity of H_2O masers I. Observations*
  Jenness T., Scott P.F., Padman R. *MNRAS*, 1995, **276**, 1024
- *Embedded FIR sources in the vicinity of H_2O masers II. Analysis*
  Jenness T., Scott P.F., Padman R. *MNRAS*, 1996 in preparation
- *High Resolution $C^{17}O$ observations of M17SW*
  Hobson M.P., Jenness T., Padman R., Scott P.F. *MNRAS*, 1994, **266**, 972
- *Limitations on detecting faint broad lines: Low-level instrumental ripples*
  Röttgering H., Miley G., Jenness T., Sleath J.P., van Ojik R., van der Werf P. *The JCMT Newsletter*, 1995, Number **4**, March, p32
- *Clumping in M17SW*
  Jenness T., 1995, in *The physics and chemistry of interstellar molecular clouds: proceedings of the 2nd Cologne-Zermatt symposium held at Zermatt, Switzerland, 21-24 September 1993*, eds Winnewisser G., Pelz G. C., p. 150, Springer-Verlag
- *Studies of embedded FIR cores in the vicinity of H_2O masers*
  Jenness T. 1996, in *Disks and outflows around young stars*, ed. S. Beckwith, in press
- *Sub-mm and radio observations of water maser sources*[online]
  Jenness T. 1995, Available WWW (World Wide Web):
  <URL:http://www.cup.cam.ac.uk/onlinepubs/YERAC/jenness/jennessab.html> In *XXVIIth Young European Radio Astronomers Conference*, eds D. A. Green and W. Steffen in association with Cambridge University Press: <URL:http://www.cup.cam.ac.uk/onlinepubs/YERAC/YERACtop.html>

Bibliography

Adams F. C., Shu F. H., 1986, *ApJ*, 308, 836
Adams F. C., Lada C. J., Shu F. H., 1987, *ApJ*, 312, 788
Altenhoff W. J., Downes D., Pauls T., Schraml J., 1978, *A&AS*, 35, 23
André P., 1995, in *The Cold Universe, Proceedings of the XIIIth Rencontres de Moriond*, eds Montmerle T., Lada C. J., Mirabel F., Trân Thanh Vân J.
André P., Martin-Pintado J., Despois D., Montmerle T., 1990, *A&A*, 236, 180
André P., Ward-Thompson D., Barsony M., 1993, *ApJ*, 406, 122
Anglada G., Rodríguez L. F., Girart J. M., Estella R., Torrelles J. M., 1994, *ApJ*, 420, L91
Aspin C., *et al*., 1994, *A&A*, 292, L9

Bachiller R., Cernicharo J., Martin-Pintado J., Tafalla M., Lazareff B., 1990, *A&A*, 231, 180
Bally J., Lada C. J., 1983, *ApJ*, 265, 824
Bechis K. P., Harvey P. M., Campbell M. F., Hoffman W. F., 1978, *ApJ*, 226, 439
Beckwith S., Evans II N. J., Becklin E. E., Neugebauer G., 1976, *ApJ*, 208, 390
Beichman C. A., Neugebauer G., Habing H. J., Clegg P. E., Chester T. J. (eds), 1988, *Infrared Astronomical Satellite (IRAS) Catalogs and Atlases*, The Joint IRAS Science Working Group, NASA RP–1190
Bence S. J., Richer J. S., Padman R., 1996, *MNRAS*, submitted
Benson P. J., *et al*., 1990, *ApJS*, 74, 911
Bernes C., 1977, *A&AS*, 29, 65
Bieging J. H., Pankonin V., Smith L. F., 1978, *A&A*, 64
Blair G. N., Davis J. H., Dickinson D. F., 1978, *ApJ*, 226, 435
Blair G. N., Dinger A. S. C., Dickinson D. F., 1980, *AJ*, 85, 161
Blitz L., Fich M., Stark A. A., 1982, *ApJS*, 49, 183
Bohlin R. C., Savage B. D., Drake J. F., 1978, *ApJ*, 224, 132
Bos A., 1988, The DAS: System Description, Tech. Rep. 187, Netherlands Foundation for Radio Astronomy
Brand J., *et al*., 1994, *A&AS*, 103, 541
Braz M. A., Epchtein N., 1987, *A&A*, 176, 245
Braz M. A., Scalise Jr. E., Gregorio Hetem J. C., *et al*., 1989, *A&AS*, 77, 465
Burke B. F., Papa D. C., Papadopoulos G. D., Schwartz P. R., Knowles S. H., Sullivan W. T., Meeks M. L., Moran J. M., 1970, *ApJ*, 160, L63

Campbell B., Persson S. E., Matthews K., 1989, *AJ*, 98, 643
Carballo R., Eiroa C., Mampaso A., 1988, *MNRAS*, 232, 497
Casali M. M., Eiroa C., Duncan W. D., 1993, *A&A*, 275, 195
Casanova S., Montmerle T., Feigelson E. D., André P., 1995, *ApJ*, 439, 752
Casoli F., Dupraz C., Gerin M., Combes F., Boulanger F., 1986, *A&A*, 169, 281
Caswell J. L., Batchelor R. A., Forster J. R., Wellington K. J., 1983, *Aust. J. Phys*, 36, 443
Caswell J. L., Vaile R. A., Forster J. R., 1995, *MNRAS*, 277, 210
Cernicharo J., Thum C., Hein H., John D., Garcia P., Mattioco F., 1990, *A&A*, 231, L15
Cesarsky C. J., Cesarsky D. A., Churchwell E., Lequeux J. A., 1978, *ApJ*, 68, 33
Chandra D. A., Varshalovich D. A., Kegel W. H., 1984, *A&AS*, 55, 51
Chapman J. M., Cohen R. J., 1986, *MNRAS*, 220, 513
Chen H., Tokunaga T., Fukui Y., 1993, *ApJ*, 416, 235
Cheung A. C., Rank D. M., Townes C. H., Thornton D. D., Welch W. J., 1969, *Nature*, 221, 626
Cheung L. H., Frogel J. A., Gezari D. Y., Hauser M. G., 1980, *ApJ*, 240, 74
Chini R., Elsässer H., Neckel T., 1980, *A&A*, 91, 186
Chini R., Kreysa E., Mezger P. G., Gemünd H.-P., 1984, *A&A*, 137, 117
Chini R., Kreysa E., Mezger P. G., Gemünd H.-P., 1986, *A&A*, 154, L8
Chini R., Krügel E., Wargau W., 1987, *A&A*, 181, 378
Churchwell E., Hollis J. M., 1983, *ApJ*, 272, 591
Churchwell E., Walmsley C. M., Cesaroni R., 1990, *A&AS*, 83, 119
Clayton G. C., Mathis J. S., 1988, *ApJ*, 327, 911
Codella C., Felli M., Natale V., Palagi F., Palla F., 1994, *A&A*, 291, 261
Cohen J. G., 1991, *AJ*, 101, 734
Cohen M., 1974, *MNRAS*, 169, 257
Cohen M., Allamandola L., Tielens A. G. G. M., , Bregman J., Simpson J. P., Witteborn F. C., Wooden D., Rank D., 1986, *ApJ*, 302, 737
Cohen R. J., Baart E., Jonas J., 1988, *MNRAS*, 231, 205
Cohen R. J., Masheder M. R. W., Walker R. N. F., 1991, *MNRAS*, 250, 611
Comoretto G., *et al.*, 1990, *A&AS*, 84, 179
Condon J. J., Broderick J. J., 1985, *AJ*, 90, 2540
Cooke B., Elitzur M., 1985, *ApJ*, 295, 175
Cunningham C. T., Hayward R. H., Wade J. D., Davies S. R., Matheson D. N., 1992, *Int. J. Infrared Millim. Waves*, 13, 1827
Curiel S., Rodríguez L. F., Moran J. M., Cantó J., 1993, *ApJ*, 415, 191

Dame T. M., Thaddeus P., 1985, *ApJ*, 297, 751
Davies S. R., Cunningham C. T., Little L. T., Matheson D. N., 1992, *Int. J. Infrared Millim. Waves*, 13, 647
Davis C. J., Smith M. D., 1995, *ApJ*, 443, L41
de Jong T., 1973, *A&A*, 26, 297
Dent W. R. F., Matthews H. E., 1995, *User's guide to the DAS*, Joint Astronomy Centre, Hilo, HI, http://www.jach.hawaii.edu/JCMT/das-guide/das-guide.html
Downes D., Wilson T. L., Bieging J., Wink J., 1980, *A&AS*, 40, 379
Draine B. T., 1980, *ApJ*, 241, 1021
Draine B. T., Roberge W. G., Dalgarno A., 1983, *ApJ*, 264, 485
Duncan W. D., Robson E. I., Ade P. A. R., Griffin M. J., Sandell G., 1990, *MNRAS*, 243, 126

Dyck H. M., Simon T., 1977, *ApJ*, 211, 421

E

Egret D., Wenger M., Dubois P., 1991, in *Databases and On-line Data in Astronomy*, eds Egret D., Albrecht M., p. 89, Kluwer
Eichhorn G., Murray S. S., Accomazzi A., Kurtz M. J., Grant C. S., 1995, in *Databases and On-line Data: II*, eds Egret D., Albrecht M., in press, The NASA Astrophysics Data System, http://adswww.harvard.edu/adswww/adshomepg.html
Eichhorn G., Murray S. S., Kurtz M. J., Accomazzi A., Grant C. S., 1995, in *Astronomical Data Analysis Software and Systems IV*, eds Shaw R. A., Payne H. E., Hayes J. J. E., vol. 77, ASP Conference Series, http://www.stsci.edu/meetings/adassIV/eichhorng.html
Eiroa C., Casali M. M., 1989, *A&A*, 223, L17
Eiroa C., Casali M. M., 1992, *A&A*, 262, 468
Eiroa C., Neckel T. H., Sanchez Magro C., Selby M. J., 1983, *A&A*, 95, 206
Elitzur M., 1986, in *Masers, molecules and mass outflows in star forming regions*, ed. Haschick A. D., p. 299, Haystack Observatory, Westford
Elitzur M., 1992, *Astronomical Masers*, Astrophysics & Space Science Library, Kluwer Academic Publishers, Dordrecht
Elitzur M., Hollenbach D. J., McKee C. F., 1989, *ApJ*, 346, 983
Elitzur M., McKee C. F., Hollenbach D. J., 1991, *ApJ*, 367, 333
Emerson D. T., Klein U., Haslam C. G. T., 1979, *ApJ*, 76, 92
Emerson J. P., 1987, in *Star Forming Regions*, eds Peimbert M., Jugaku J., p. 19, IAU Symp. No. 115, Reidel, Dordrecht
Emerson J. P., 1988, in *Formation and Evolution of Low Mass Stars*, eds Dupree A. K., Lago M. T. V. T., p. 21, Kluwer Academic Publishers, Dordrecht
Engels D., Schmid-Burgk J., Walmsley C. M., 1986, *A&A*, 167, 129
Evans II N. J., Beckwith S., Brown R. L., Gilmore W., 1979, *ApJ*, 227, 450

F

Felli M., Harten R., Habing H., Israel F., 1978, *A&AS*, 32, 423
Felli M., Palagi F., Tofani G., 1992, *A&A*, 255, 293
Fich M., 1993, *ApJS*, 86, 475
Forster J. R., Caswell J. L., 1989, *A&A*, 213, 339
Frogel J. A., Persson S. E., 1972, *ApJ*, 178, 667
Fukui Y., 1989, in *ESO workshop on low mass star formation and pre-main sequence objects*, ed. Reipurth B., p. 95, European Southern Observatory, Garching bei München, Germany
Fukui Y., Sugitani K., Takaba H., Iwata T., Mizuno A., Ogawa H., Kawabata K., 1986, *ApJ*, 311, L85

G

Gaylard M. J., MacLeod G. C., 1993, *MNRAS*, 262, 43
Gear W. K., Robson E. I., Griffin M. J., 1988, *MNRAS*, 231, 55P
Geballe T. R., 1990, in *Molecular astrophysics: A volume honouring Alexander Dalgarno*, ed. Hartquist T. W.,

p. 345, Cambridge University Press
Genzel R., 1986, in *Masers, Molecules and Mass Outflows in Star Forming Regions*, ed. Haschick A. D., p. 233, Haystack Observatory, Westford, MA
Genzel R., Downes D., 1977, *A&AS*, 30, 145
Genzel R., Downes D., 1979, *A&A*, 72, 234
Genzel R., *et al*., 1981, *ApJ*, 247, 1039
Gezari D. Y., Scmitz M., Pitts P. S., Mead J. M., 1993, *Catalog of Infrared Observations*, NASA RP–1294, 3rd edn.
Goldreich P., Kwan J., 1974, *ApJ*, 189, 441
Goldreich P., Kwan J., 1974, *ApJ*, 191, 93
Gordon M. A., 1988, in *Galactic and extragalactic radio astronomy*, eds Verschuur G. L., Kellermann K. I., Astronomy & Astrophysics Library, p. 40, Springer-Verlag, 2nd edn.
Gordon M. A., 1995, *A&A*, 301, 853
Green S., 1980, *ApJS*, 42, 103
Greisen E. (ed.), 1994, *AIPS Cookbook (15JUL94)*, NRAO, Socorro, New Mexico
Gyulbudaghian A. L., Glushkov Y. I., Denisyuk E. K., 1978, *ApJ*, 224, L137
Gyulbudaghian A. L., Rodríguez L. F., Mendoza-Torres E., 1987, *Rev. Mex. Astron. Astrofís.*, 15, 53

H

Harris S., Clegg P., Hughes J., 1988, *MNRAS*, 235, 441
Hartigan P., Lada C. J., 1985, *ApJS*, 59, 383
Harvey P. M., Bechis K. P., Wilson W. J., Ball J. A., 1974, *ApJS*, 27, 331
Harvey P. M., Wilking B. A., Joy M., 1984, *ApJ*, 278, 156
Harvey P. M., Wilking B. A., Joy M., Lester D. F., 1985, *ApJ*, 288, 725
Henkel C., Haschick A. D., Güsten R., 1986, *A&A*, 165, 197
Henning T., Pfau W., Altenhoff W. J., 1990, *A&A*, 227, 542
Henning T., Cesaroni R., Walmsley M., Pfau W., 1992, *A&AS*, 93, 525
Herzberg G., 1945, *Infrared and Raman Spectra*, New York: Van Nostrand Reinhold
Hildebrand R. H., 1983, *QJRAS*, 24, 267
Hobson M. P., Padman R., Scott P. F., Prestage R. M., Ward-Thompson D., 1993, *MNRAS*, 264, 1025
Hobson M. P., Jenness T., Padman R., Scott P. F., 1994, *MNRAS*, 266, 972
Hodapp K. W., 1987, *A&A*, 172, 304
Hollenbach D. J., McKee C. F., 1989, *ApJ*, 342, 306
Hughes V. A., MacLeod G. C., 1994, *ApJ*, 427, 857
Hunter T. R., Testi L., Taylor G. B., Tofani G., Felli M., Philips T. G., 1995, *A&A*, 302, 249
Hurt R. L., Barsony M., Wootten A., 1995, in *Circumstellar Matter*, Royal Observatory, Edinburgh

J

Jaffe D. T., Güsten R., Downes D., 1981, *ApJ*, 250, 621
Jaffe D. T., Stier M. T., Fazio G. G., 1982, *ApJ*, 252, 601
Jaffe D. T., Hildebrand R. H., Keene J., Harper D. A., Loewenstein R. F., Moran J. M., 1984, *ApJ*, 281, 225
Jenness T., 1995, in *The physics and chemistry of interstellar molecular clouds: proceedings of the 2nd Cologne-Zermatt symposium held at Zermatt, Switzerland, 21-24 September 1993*, eds Winnewisser G., Pelz G. C., p. 150, Springer-Verlag
Jenness T., Scott P. F., Padman R., 1995, *MNRAS*, 276, 1024

Jennings R. E., Cameron D. H. M., Cudlip W., Hirst C. J., 1987, *MNRAS*, 226, 461
Jones M., 1991, in *IAU Colloq. 131, Radio Interferometry: Theory, Techniques and Applications*, eds Cornwell T. J., Perley R., p. 395, Astron. Soc. Pac., San Francisco
Jourdain De Muizon M., Geballe T. R., D'Hendecourt L. B., Baas F., 1986, *ApJ*, 306, L105
Jourdain De Muizon M., D'Hendecourt L. B., Geballe T. R., 1990a, *A&A*, 235, 367
Jourdain De Muizon M., D'Hendecourt L. B., Geballe T. R., 1990b, *A&A*, 227, 526

Kalenskii S. V., Sobolev A. M., 1994, *Pis'ma Astron. Zh.*, 20, 113
Kalenskii S. V., Berulis I. I., Val'tts I. E., Dzyura A. M., Slysh V. I., Vasil'kov V. I., 1994, *Astron. Zh.*, 71, 51
Kleinmann S. G., Sargent D. G., Gillett F. C., Grasdalen G. L., Joyce R. R., 1977, *ApJ*, 215, L79
Knowles S. H., Mayer C. H., Cheung A. C., Rank D. M., Townes C. H., 1969, *Science*, 163, 1055
Kömpe C., Joncas G., Baudry A., Wouterloot J. G. A., 1989, *A&A*, 221, 295
Krügel E., Chini R., 1994, *A&A*, 287, 947
Kuiper N. H., 1962, *Proc. Koninklijke Nederlandse Akademie van Wetenschappen, ser. A*, 63, 38
Kuiper T. B. H., Rodriguez Kuiper E. N., Dickinson D. F., Turner B. E., Zuckerman B., 1984, *ApJ*, 276, 211
Kutner M. L., Ulich B. L., 1981, *ApJ*, 250, 341
Kylafis N. D., Norman C., 1987, *ApJ*, 323, 346
Kylafis N. D., Norman C., 1991, *ApJ*, 373, 525

Lada C. J., Wilking B. A., 1984, *ApJ*, 287
Lada C. J., Thronson, Jr. H. A., Smith H. A., Schwartz P. R., Glaccum W., 1984, *ApJ*, 286, 302
Ladd E. F., Lada E. A., Myers P. C., 1993, *ApJ*, 410, 168
Lebofsky M. J., Sargent D. G., Kleinmann S. G., Rieke G. H., 1978, *ApJ*, 219, 487
Little L. T., Bergman P., Cunningham C. T., Heaton B. D., Knee L. B. G., MacDonald G. H., Richards P. J., Toriseva M., 1988, *A&A*, 205, 129
Litvak M. M., McWhorter A. L., Meeks M. L., Zeiger H. J., 1966, *Phys. Rev. Lett.*, 17, 821
Longair M. S., 1992, *High Energy Astrophysics*, vol. 1, chap. 8, p. 243, Cambridge University Press, 2nd edn.
Loren R. B., 1977, *ApJ*, 218, 716
Lorenzetti D., Saraceno P., Strafella F., 1983, *ApJ*, 276, 554

MacLeod G. C., Gaylard M. J., Kemball A. J., 1993, *MNRAS*, 262, 343
Martí J., Rodríguez L. F., Reipurth B., 1993, *ApJ*, 416, 208
Martí J., Rodríguez L. F., Reipurth B., 1995, *ApJ*, 449, 184
Massi M., Churchwell E., Felli M., 1988, *A&A*, 194
Mathis J. S., 1990, *Ann. Rev. Astron. Astrophys.*, 28, 37
Matthews H. E., Olnon F. M., Winnberg A., Baud B., 1985, *A&A*, 149, 227
McCaughrean M. J., Rayner J. T., Zinnecker H., 1994, *ApJ*, 436, L189
McCutcheon W. H., Dewdney P. E., Purton C. R., Sato T., 1991, *AJ*, 101, 1435
McGregor P. J., Persson S. E., Cohen J. G., 1984, *ApJ*, 286, 609

McKee C. F., Hollenbach D. J., Seab C. G., Tielens A. G. G. M., 1987, *ApJ*, 318, 674
McMullin J. P., Mundy L. G., Wilking B. A., Hezel T., Blake G. A., 1994, *ApJ*, 424, 222
Melnick G. J., Menten K. M., Phillips T. G., Hunter T., 1993, *ApJ*, 416, L40
Menten K. M., 1991, *ApJ*, 380, L75
Menten K. M., Melnick G. J., Phillips T. G., 1990a, *ApJ*, 350, L41
Menten K. M., Melnick G. J., Phillips T. G., Neufeld D. A., 1990b, *ApJ*, 363, L27
Mihalas D., Binney J., 1981, *Galactic Astronomy*, p. 531, W. H. Freeman, San Francisco, 2nd edn.
Miralles M. P., Rodríguez L. F., Scalise E., 1994, *ApJS*, 92, 173
Mitchell G. F., Matthews H. E., 1994, *ApJ*, 423, L55
Mitchell G. F., Allen M., Maillard J.-P., 1988, *ApJ*, 333, L55
Mitchell G. F., Maillard J.-P., Allen M., Beer R., Belcourt K., 1990, *ApJ*, 363, 554
Mitchell G. F., Hasegawa T. I., Schella J., 1992, *ApJ*, 386, 604
Monin J. L., Vauglin I., Audaire L., 1987, *A&A*, 172, 368
Moorwood A. F. M., Salinari P., 1981, *A&A*, 94, 299
Moran J. M., *et al*., 1973, *ApJ*, 185, 535
Moran J. M., Burke B. F., Barrett A. H., Rogers A. E. E., Carter J. C., Ball J. A., Cudaback D. D., 1968, *ApJ*, 152, L98
Murray S. S., Bruegel E. W., Eichhorn G., Farris A., Good J. C., Kurtz M. J., Nousek J. A., Stoner J. L., 1992, in *Astronomy from Large Databases, II*, eds Heck A., Murtagh F., p. 387, European Southern Observatory
Murtagh F., Heck A., 1987, *Multivariate Data Analysis*, Astrophysics & Space Science Library, Reidel, Dordrecht
Myers P. C., Ladd E. F., 1993, *ApJ*, 413, L47

Neckel T., Staude H. J., 1984, *A&A*, 131, 200
Neufeld D. A., Kaufman M. J., 1993, *ApJ*, 418, 263
Neugebauer G., *et al*., 1984, *ApJ*, 278, L1
Ney E. P., Merrill K. M., 1980, Study of Sources in AFGL rocket infrared study, AFGL-TR-80-0050, Air Force Geophysics Laboratory, Hanscom AFB, Ma.

Odenwald S. F., 1989, *AJ*, 97, 801
Olofsson G., Koornneef J., 1985, *A&A*, 146, 337

Palagi F., Cesaroni R., Comoretto G., Felli M., Natale V., 1993, *A&AS*, 101, 153
Palla F., Brand J., Cesaroni R., Comoretto G., Felli M., 1991, *A&A*, 246, 249
Palumbo G. G. C., Scappini F., Codella G. P. C., Caselli P., Attolini M. R., 1994, *MNRAS*, 266, 123
Panagia, 1973, *AJ*, 78, 929
Panagia N., Felli M., 1975, *A&A*, 39
Pankonin V., Thomasson P., Barsuhn J., 1977, *A&A*, 54, 335
Perkins F., Gold T., Salpeter E. E., 1966, *ApJ*, 145, 361

Persi P., Ferrari-Toniolo M., Busso M., Robberto M., Scaltriti F., Silvestro G., 1988, *AJ*, 95, 1167
Persson S. E., Campbell B., 1987, *AJ*, 94, 416
Plume R., Jaffe D. T., Evans II N. J., 1992, *ApJS*, 78, 505
Poetzel R., Mundt R., Ray T. P., 1992, *A&A*, 262, 229
Poynter R. L., Pickett H. M., 1985, *Applied Optics*, 24, 2335, http://spec.jpl.nasa.gov/
Pratchett T., 1987, *Equal Rites*, A Discworld novel, Victor Gollancz
Press W. H., Teukolsky S. A., Vetterling W. T., Flannery B. P., 1992, *Numerical Recipes in* FORTRAN, Cambridge University Press, Cambridge, 2nd edn.
Price S. D., Murdock T. L., 1983, The Revised AFGL Infrared Sky Survey Catalog, AFGL-TR-83-0161. Air Force Geophysics Laboratory, Hanscom AFB, Ma.
Price S. D., Murdock T. L., Shivanandan K., 1983, Far infrared Sky Survey Experiment. Final Report, AFGL-TR-83-0055. Air Force Geophysics Laboratory, Hanscom AFB, Ma.

Ray T. P., Poetzel R., Solf J., Mundt R., 1990, *ApJ*, 357, L45
Reipurth B., Wamsteker W., 1983, *A&A*, 119, 14
Richards P. J., Little L. T., Toriseva M., Heaton B. D., 1987, *MNRAS*, 228, 43
Richer J. S., 1990, *MNRAS*, 245, 24P
Richer J. S., 1991, *Molecular line and continuum studies of high-mass star formation*, Ph.D. thesis, University of Cambridge
Richer J. S., 1992, *MNRAS*, 254, 165
Richer J. S., Padman R., Ward-Thompson D., Hills R. E., Harris A. I., 1993, *MNRAS*, 262, 839
Rieke G. H., Harper D. A., Low F. J., Armstrong K. R., 1973, *ApJ*, 183, L67
Rodríguez L. F., Cantó J., 1983, *Rev. Mex. Astron. Astrofís.*, 8, 163
Rodríguez L. F., Moran J. M., Ho P. T. P., Gottlieb E. W., 1980, *ApJ*, 235, 845
Rodríguez L. F., Hashick A. D., Torrelles J. M., Myers P. C., 1987, *A&A*, 186, 319
Röttgering H., Miley G., Jenness T., Sleath J. P., van Ojik R., van der Werf P., 1995, *The JCMT Newsletter*, 4, 32
Rybicki G. B., Lightman A. P., 1979, *Radiative processes in astrophysics*, Wiley-interscience, New York

Sandell G., 1994, *MNRAS*, 271, 75
Sandell G., Olofsson H., 1981, *A&A*, 99, 80
Saraceno P., Andre P., Ceccarelli C., Griffin M., Molinari S., Russell S., 1994, *A&A*, in prep
Scalise Jr. E., Rodríguez L. F., Mendoza-Torres E., 1989, *A&A*, 221, 105
Schneps M. H., Martin R. N., Ho P. T. P., Barrett A. H., 1978, *ApJ*, 221, 124
Schutte A. J., van der Walt D. J., Gaylard M. J., MacLeod G. C., 1993, *MNRAS*, 261, 783
Schwartz P. R., Buhl D., 1975, *ApJ*, 201, L27
Schwartz R. D., Cohen M., Williams P. M., 1987, *ApJ*, 322, 403
Simon M., Righini-Cohen G., Felli M., Fischer J., 1981, *ApJ*, 245, 552
Simon T., Joyce R. R., 1983, *ApJ*, 265, 748
Simon T., Simon M., Joyce R. R., 1979, *ApJ*, 230, 127
Skinner S. L., Brown A., Stewart R. T., 1993, *ApJS*, 87, 217
Sleath J. P., 1995, *A new model of spiral galaxies based on propagating star formation*, Ph.D. thesis, University of Cambridge

Slysh V. I., *et al*., 1994, *Astron. Zh*., 71, 37
Slysh V. I., Kalenskii S. V., Otrupcek I. E. V. R., 1994, *MNRAS*, 268, 464
Smith M. D., 1991, *MNRAS*, 253, 175
Smith M. D., 1994, *MNRAS*, 266, 238
Snell R. L., Bally J., 1986, *ApJ*, 303, 683
Snell R. L., Scoville N. Z., Sanders D. B., Erickson N. R., 1984, *ApJ*, 284, 176
Snell R. L., Huang Y., Dickman R. L., Claussen M. J., 1988, *ApJ*, 325, 853
Stevens J. A., Robson E. I., 1994, *MNRAS*, 270, L75
Stier M. T., *et al*., 1984, *ApJ*, 283, 573
Stier M. T., Jaffe D. T., Fazio G. G., Roberge W. G., Thum C., Wilson T. L., 1982, *ApJS*, 48, 127
Strom K. M., Newton G., Strom S. E., Seaman R. L., Carrasco L., Cruz-Gonzalez I., Serrano A., Grasdalen G. L., 1989a, *ApJS*, 71, 183
Strom K. M., Margulis M., Strom S. E., 1989b, *ApJ*, 345, L79
Strom S. E., Vrba F. J., Strom K. M., 1976, *AJ*, 81, 638
Stutzki J., Güsten R., 1990, *ApJ*, 356, 513
Stutzki J., Ungerechts H., Winnewisser G., 1982, *A&A*, 111, 201
Suto H., Mizutani K., Maihara T., 1989, *MNRAS*, 239, 139

Tafalla M., Bachiller R., Martin-Pintado J., 1993, *ApJ*, 403, 175
Tamura M., Yamashita T., 1992, *ApJ*, 391, 710
Tartar J. C., Welch W. J., 1986, *ApJ*, 305, 467
Tereby S., Vogel S. N., Myers P. C., 1992, *ApJ*, 390, 181
Thompson R. I., Tokunaga A. T., 1979, *ApJ*, 229, 153
Thompson R. I., Tokunaga A. T., 1979, *ApJ*, 231, 736
Thronson Jr. H. A., Harper D. A., Keene J., Loewenstein R. F., Moseley S. H., Telesco C. M., 1978, *AJ*, 83, 492
Tofani G., Felli M., Taylor G. B., Hunter T. R., 1995, *A&AS*, 112, 299
Torrelles J. M., Ho P. T. P., Rodríguez L. F., Cantó J., Verdes-Montenegro L., 1989, *ApJ*, 346, 756
Torrelles J. M., Gomez J. F., Anglada G., Estalella R., Mauersberger R., Eiroa C., 1992, *ApJ*, 392, 616
Torrelles J. M., Gómez J. F., Curiel S., Eiroa C., Rodríguez L. F., Ho P. T. P., 1992, *ApJ*, p. L59
Townes C. H., Schawlow A. L., 1975, *Microwave Spectroscopy*, Dover Publications, Inc.
Turner B. E., Rubin R. H., 1977, *ApJ*, 170, L113

Verdes-Montenegro L., Torelles J. M., Rodríguez L. F., Anglada G., López R., Estalella R., Cantó J., Ho P. T. P., 1989, *ApJ*, 346, 193

Walker R. C., Matsakis D. N., Garcia-Barreto J. A., 1982, *ApJ*, 255, 128
Wang T. Y., Wouterloot J. G. A., Wilson T. L., 1993, *A&A*, 277, 205
Weaver H., Williams D. R. W., Dieter N. H., Lum W. T., 1965, *Nature*, 208, 29
Weinreb S., Barrett A. H., Meeks M. L., Henry J. C., 1963, *Nature*, 200, 829

Weintraub D. A., Kastner J., 1993, *ApJ*, 411, 767
Weintraub D. A., Kastner J. H., Mahesh A., 1994, *ApJ*, 420, L87
White G. J., Gee G., 1986, *A&A*, 156, 301
White G. J., Little L. T., Parker E. A., Nicholson P. S., Macdonald G. H., Bale F., 1975, *MNRAS*, 170, 37P
White G. J., Casali M. M., Eiroa C., 1995, *A&A*, 298, 594
Wilking B. A., Mundy L. G., Blackwell J. H., Howe J. E., 1989, *ApJ*, 345, 257
Wilking B. A., Schwartz R. D., Mundy L. G., Schultz A. S. B., 1990, *AJ*, 99, 344
Wilking B. A., Claussen M. J., Myers P. J. B. P. C., Tereby S., Wotten A., 1994, *ApJ*, 431, L119
Wink J. E., Altenhoff W. J., Mezger P. G., 1982, *A&A*, 108, 227
Wood D. O. S., Churchwell E., 1989, *ApJS*, 69, 831
Wouterloot J. G. A., Walmsley C. M., 1986, *A&A*, 168, 237
Wouterloot J. G. A., Walmsley C. M., Henkel C., 1988, *A&A*, 203, 367
Wouterloot J. G. A., Brand J., Henkel C., 1988, *A&A*, 191, 323
Wouterloot J. G. A., Henkel C., Walmsley C. M., 1989, *A&A*, 215, 131
Wouterloot J. G. A., Brand J., Fiegle K., 1993, *A&AS*, 98, 589
Wu N., 1993, in *The restoration of HST images and spectra – II*, eds Hanisch R. J., White R. L., p. 58, Space Telescope Science Institute, http://iris.stsci.edu/proceedings/wun.html
Wynn-Williams C. G., Werner M. W., Wilson W. J., 1974, *ApJ*, 187, 41
Wynn-Williams C. G., Becklin E. E., Beichman C. A., Capps R., Shakeshaft J. R., 1981, *ApJ*, 246, 801
Wynn-Williams C. G., Beichman C. A., Downes D., 1981, *AJ*, 86, 565

Xiang D., Turner B. E., 1992, *Chin. Astron. Astrophys.*, 16, 307

Yamashita T., Sato S., Nagata T., Suzuki H., Hough J. H., McLean I. S., Garden R., Gatley I., 1987, *A&A*, 177, 258
Yates J. A., Cohen R. J., 1996, *MNRAS*, 278, 668

Zeilik II M., 1976, *A&A*, 46, 319
Zeilik II M., Lada C. J., 1978, *ApJ*, 222, 896
Zombeck M. V., 1990, *Handbook of space astronomy and astrophysics*, chap. 2, p. 100, Cambridge University Press, http://adswww.harvard.edu/books/hsaa/, 2nd edn.